Simulations of Polymer Crystals: New Methods and Applications

Thesis by

Naoki Karasawa

In Partial Fulfillment of the Requirements

for the Degree of

Doctor of Philosophy

California Institute of Technology

Pasadena, California

1992

(Submitted November 5, 1991)

To my parents

Acknowledgments

I would like to thank my research advisor, Bill Goddard, for his patient guidance and support, both academically and financially. His enthusiasm for chemistry,physics,materials science, and computer programming have impressed me throughout my stay in Caltech.

I would like to thank Hong-Qiang Ding for writing the Cell Multipole Method programs by which most results in Chapter III were obtained. Also I would like to thank Siddharth Dasgupta, who developed valence force-field parameters for polyethylene crystals used in Chapter IV. Jean-Marc Langlois and Murco Ringnalda helped me by running a pseudospectral program used in Chapter VI.

I would like to thank all the members of the Goddard group; I would especially like to thank Yuejin Guo and Guanhua Chen for stimulating discussions. Also, many thanks go to Takashige Maekawa, Terumasa Yamasaki, and Hiroshi Yamamoto.

Finally, I would like to thank my parents Keiko and Tetsuo for supporting me during my stay in the United States. Also I would like to thank my cousin Takuro Tsukatani, who recommended that I study in the United States.

Abstract

The most important applications for simulations of polymers involve composites or blends with extensive, amorphous regions. To simulate such materials we use a very large unit cell, so that the polymer can have random behavior within the cell, but periodic boundary conditions to keep the problem tractable. The major difficulties in carrying out such calculations are: (a) accurate calculation of the lattice sums for the nonbond interactions (electrostatic and dispersion), which converge very slowly; (b) computational time for systems large enough to simulate real materials (1 million atoms); (c) procedures for calculating the properties of interest (energy, force, stress, curvature, phonons, elastic constants, dielectric constants, and piezoelectric constants).

We describe herein significant progress on each of these three issues. Concerning (a) we developed the Accuracy-Bounded Convergence Acceleration (ABCA) procedure, which finds the optimal Ewald parameters to achieve a given accuracy in minimum computation time. Concerning (b) the critical bottleneck in atomic-level simulations of the structure and dynamics of very large molecules is the calculation of N^2 nonbond interactions. Here a major advance is the development of the Cell Multipole Method (CMM), which involves no steps scaling a higher order than N. CMM treats the interactions in terms of a far field (which is evaluated in terms of multipole expansions) and a near field (which involves only approximately 50 near neighbors). The far field can be evaluated infrequently so that the full calculation for a million-atom system involves only the effort of calculation to interactions of each atom with about 50 near neighbors. This leads to a dramatic increase in efficiency, and systematic calculations have been carried out in realistic polymers with up to 1 million atoms (on a workstation). The CMM is 1500 times faster than the exact method for 1 million atoms. For periodic systems the cell multipole method

is extended, using a reduced set that reproduces low-order multipoles of an original unit cell (CMMX). For a polymer with 1 million atoms, the CMMX calculation is 1000 times faster than either the Ewald or Minimum Image Methods (the standards currently in use).

A major issue in carrying out simulations for materials is the force field. We have developed general procedures for obtaining empirical force fields and have applied this to systematic development of force-field parameters for polyethylene and poly (vinylidene fluoride) crystals. van der Waals parameters for carbon and hydrogen are empirically determined from experimental lattice constants, elastic constants and lattice frequencies utilizing Ewald/ABCA procedures. Various mechanical properties are calculated and compared with experimental data. For polyethylene, valence terms are determined by a biased-Hessian method for n-butane, and yield stress and surface energy are obtained from calculations of stress-strain relations in directions perpendicular to polymer chains. For poly (vinylidene fluoride) crystals, a shell model is introduced to include atomic polarizabilities into the simulation. Properties of five different forms (including a new form suggested by Lovinger) are computed using the same parameter sets. We find that using the shell model leads to significant improvement in the agreement between calculated and experimental piezoelectric and dielectric constants. In addition we find that the new form (not yet observed form) is mechanically stable with comparable energy with other forms.

Table of Contents

Introduction

Computer simulations of molecular systems are becoming important because of recent developments of computer hardware and software as well as techniques of simulations[1]. Computer hardware includes computer-graphics terminals, which are important for visualizing molecular systems. Simulations provide a direct route from the microscopic details of a system to macroscopic properties of experimental interest. This type of information is technologically as well as academically useful. The results of computer simulations may be compared with those of real experiments or may be compared with those of approximate theoretical predictions. In the first place, this is a test of an underlying model used in a computer simulation. If the model is a good one, it offers insights to the experimentalist and assists in the interpretation of new results. Also in the simulation, it is possible to realize situations where experiments are difficult or impossible (for example, high pressure or high temperature). For complex materials like polymers, the role of computer simulations is becoming very important for designing new materials.

In this thesis, polymer crystals are treated, and the simulation method employed is a molecular mechanics[2] or a force-field method. In this method, each atom is treated as a classical particle and chemical bonds between atoms are represented by two-body terms like springs. Angle interactions are represented by three-body interactions, and torsion and inversion interactions are represented by four-body interactions, and so on. Adding these valence interactions, there are nonbond interactions, which are van der Waals and Coulomb interactions. Thus, total energy (E_{total}) of an N-atom system, whose atomic coordinates are $\mathbf{r}_1, \ldots, \mathbf{r}_N$, is a sum of valence energy (E_{val}) and nonbond energy (E_{nb}) as follows:

$$E_{total}(\mathbf{r}_1, \ldots, \mathbf{r}_N) = E_{val}(\mathbf{r}_1, \ldots, \mathbf{r}_N) + E_{nb}(\mathbf{r}_1, \ldots, \mathbf{r}_N), \qquad (1)$$

where the valence energy is a sum of bond, angle, torsion, and inversion-energy terms,

$$E_{val} = E_{bond} + E_{angle} + E_{torsion} + E_{inversion}, \tag{2}$$

and the nonbond energy is a sum of van der Waals and Coulomb energy terms,

$$E_{nb} = E_{vdW} + E_{Coulomb}. \tag{3}$$

Within the Born-Oppenheimer approximation, the Hamiltonian of a system can be expressed as a function of nuclear variables only. The motion of electrons has been averaged out in this approximation.

This approximate treatment has both advantages and disadvantages. The main advantage of molecular mechanics is the size of the system that can be treated in energy minimizations, molecular dynamics, vibrational analysis, and thermodynamic-property calculations. Systems with a thousand atoms are treated routinely, which is quite important since many interesting systems require a large number of atoms to simulate. This number can be increased up to one million if we use the Cell Multipole Method described in Chapter III. Also, molecular mechanics can handle systems with periodic boundary conditions so that it can easily calculate bulk properties of the system. If we treat a wave function explicitly as in the Hartree-Fock methods, it is quite expensive to calculate properties of systems of more than about 100 atoms.

On the other hand, there are several problems in this approach. The first problem is the question of how to determine parameters (equilibrium bond lengths, force constants, etc.). Conventionally, these are empirically determined. Since validity of a simulation depends strongly on these parameters, it is quite important to obtain good parameters for the system of interest. There are several force-field parameter sets widely used, for example, DREIDING[3], MM3[4], AMBER[5], all of which assume transferability of parameters. In Chapters IV and V, problems of

parameter determination are discussed for polyethylene and poly (vinylidene fluoride) crystals. Also in Appendix I, the parameter determination for graphite is discussed. In Chapter IV, for the simulation of polyethylene crystal, the valence parameters are developed by using a biased Hessian method[6], which utilizes the Hartree-Fock calculations of n-butane. Because of the difficulty of obtaining van der Waals parameters by the *ab initio* method, van der Waals parameters for all cases are empirically determined. The second problem is the difficulty of including the effect of polarizability in molecular-mechanics simulations. Conventionally, rigid ion models are used. In Chapter V, calculations of a poly (vinylidene fluoride) crystal using the force-field parameters that include explicitly atomic polarizabilities are shown. The third problem is the inconvenience of treating systems where electronic structure can change dramatically during the simulation. For example, bond breakings and bond formings during simulations are not easily handled in molecular mechanics. The fourth problem is the inaccuracies that are due to the neglect of the quantum mechanical nature of the system. For example, specific heat calculated by molecular dynamics would be a classical value but in the real system, the value can be quite different even at room temperature, since vibrational motions are quantized[7].

In this thesis, the third and fourth problems listed above are not treated. For the third problem, it may be necessary to modify force-field parameters during the dynamics and the Car-Parrinello method[8] may be more suitable in this situation. For the fourth problem, quantum correction can be calculated in the simulation if the quantum effect is small[1]. For a quantum solid or liquid (like helium), the classical method cannot be used.

In Part I of this thesis, periodic systems are discussed mainly and the calculation of nonbond interactions are treated in detail. In Chapter I and part of Chapter II, Ewald-type, nonbond calculations are discussed and various equations

are derived. It is well known that the electrostatic potential inside a crystal is conditionally convergent. Let us consider a repeating unit of point charges, build a crystal using the repeating units and calculate the potential at a point far from the surface. If the repeating unit has a net charge, the potential simply does not converge as we add new repeating units on the surface. If the repeating unit has a net dipole, a surface-charge layer is created and a macroscopic field is observed inside the crystal so that the potential is not a periodic function and depends on the shape of the sample. If the repeating unit has a quadruple moment, a dipole layer is created on the surface, and the potential still depends on the shape of the sample. If the repeating unit has no dipoles or quadruples, the potential does not depend on the sample shape since interactions fall off faster than or equal to $1/R^4$ (R is the distance between the point and the repeating unit). Even in this case, if the repeating unit has a nonzero trace of second moments, it still creates the dipole layer on the surface, and a constant potential difference is created between the samples built by different repeating units with different traces of second moments[9]. It is possible to create a repeating unit with zero-dipole, zero-quadruple and zero-second moment by utilizing the periodicity of the lattice and fractional charges; therefore, it is most natural to choose the repeating unit that has these properties. The Ewald potential corresponds to the limiting value of the potential, using the repeating unit with this property[10]. Following the derivation of Tosi[11], the Ewald potential can be derived from the combination of periodic point charges and uniform cancelling-charge distributions. We introduce the Gaussian-charge distribution with a width parameter η and think that the potential at $\mathbf{r}$ is due to (1) periodic Gaussian-charge distributions plus uniform background charges

$$\rho^{(1)}(\mathbf{r}) = \frac{1}{\eta^3 \pi^{3/2}} \sum_{\mathrm{l}} \exp\left[-\frac{(\mathbf{r}-\mathbf{r}_{\mathrm{l}})^2}{\eta^2}\right] - \Omega^{-1}, \tag{4}$$

and (2) original charges plus the negative of the Gaussian-charge distributions

$$\rho^{(2)}(\mathbf{r}) = \sum_{\mathrm{l}} \left\{ \delta(\mathbf{r} - \mathbf{r}_{\mathrm{l}}) - \frac{1}{\eta^3 \pi^{3/2}} \exp\left[-\frac{(\mathbf{r} - \mathbf{r}_{\mathrm{l}})^2}{\eta^2} \right] \right\}. \tag{5}$$

Here Ω is the volume of a unit cell and $\mathbf{r}_{\mathrm{l}}$ is a cell translation vector. The first term can be Fourier-transformed and summed in the reciprocal space, and the use of Poisson's equation yields the potential,

$$\phi^{(1)}(\mathbf{r}) = \frac{4\pi}{\Omega} \sum_{\mathbf{h}}{}' \mathrm{h}^{-2} \exp(-\eta^2 \mathrm{h}^2/4 + \mathrm{i}\mathbf{h} \cdot \mathbf{r}), \tag{6}$$

where $\mathbf{h}$ is a reciprocal vector. The prime on the summation sign indicates that $\mathbf{h} = 0$ is excluded in the sum. The potential from the second term is given by using the Gauss' theorem and integration by parts:

$$\phi^{(2)}(\mathbf{r}) = \sum_{\mathrm{l}} \frac{\mathrm{erfc}(|\mathbf{r} - \mathbf{r}_{\mathrm{l}}|/\eta)}{|\mathbf{r} - \mathbf{r}_{\mathrm{l}}|} - \frac{\pi \eta^2}{\Omega}. \tag{7}$$

The second term is added to make the average potential inside the cell vanish. The potential from the periodic unit charge plus the uniform background charge is then

$$\begin{aligned} \phi(\mathbf{r}) &= \phi^{(1)}(\mathbf{r}) + \phi^{(2)}(\mathbf{r}) \\ &= \frac{4\pi}{\Omega} \sum_{\mathbf{h}}{}' \mathrm{h}^{-2} \exp(-\eta^2 \mathrm{h}^2/4 + \mathrm{i}\mathbf{h} \cdot \mathbf{r}) \\ &\quad + \sum_{\mathrm{l}} \frac{\mathrm{erfc}(|\mathbf{r} - \mathbf{r}_{\mathrm{l}}|/\eta)}{|\mathbf{r} - \mathbf{r}_{\mathrm{l}}|} - \frac{\pi \eta^2}{\Omega}. \end{aligned} \tag{8}$$

For the crystals with N charges inside the cell, q_1, q_2,..., q_{N}, we separately consider each charge as a periodic point charge plus a uniform backgroud charge and add these together using the same η. The total potential is given by taking into account the neutrality of charges,

$$\begin{aligned} \phi_{\mathrm{tot}}(\mathbf{r}) &= \sum_{\mathrm{p}} \mathrm{q}_{\mathrm{p}} \phi(\mathbf{r} - \mathbf{r}_{\mathrm{p}}) \\ &= \frac{4\pi}{\Omega} \sum_{\mathbf{h}}{}' \mathrm{S}(\mathbf{h}) \mathrm{h}^{-2} \exp(-\eta^2 \mathrm{h}^2/4 + \mathrm{i}\mathbf{h} \cdot \mathbf{r}) \\ &\quad + \sum_{\mathrm{l}} \sum_{\mathrm{p}} \mathrm{q}_{\mathrm{p}} \frac{\mathrm{erfc}(|\mathbf{r} - \mathbf{r}_{\mathrm{l}} - \mathbf{r}_{\mathrm{p}}|/\eta)}{|\mathbf{r} - \mathbf{r}_{\mathrm{l}} - \mathbf{r}_{\mathrm{p}}|}, \end{aligned} \tag{9}$$

where

$$S(\mathbf{h}) = \sum_{p} q_p \exp(-i\mathbf{h} \cdot \mathbf{r}_p). \tag{10}$$

The above equations show that the Ewald potential has a period of a lattice, $\phi_{tot}(\mathbf{r} + \mathbf{r}_l) = \phi_{tot}(\mathbf{r})$, since $\exp(i\mathbf{h} \cdot \mathbf{r}_l) = 1$. Also it is shown that an average potential inside the unit cell is zero,

$$\frac{1}{\Omega} \int_{cell} \phi(\mathbf{r}) d^3\mathbf{r} = 0, \tag{11}$$

since $\int_{cell} \exp(i\mathbf{h} \cdot \mathbf{r}) d^3\mathbf{r} = 0 (\mathbf{h} \neq 0)$ and $\sum_p q_p = 0$. These two properties are characteristics of the potential calculated by the Ewald method.

For dispersion interactions $\sum_{i>j} A_{ij}/r_{ij}^6$, the sum is absolutely convergent, and a similar method is used only for the purpose of accelerating the convergence. By using the Ewald-type summation, convergences are speeded up substantially. We developed the Accuracy-Bounded Convergence Acceleration (ABCA) procedures to determine the optimal η to minimize a calculation time while retaining a specified accuracy. This procedure is used in all the calculations involving the Ewald sums in this thesis.

Once the total potential energy expression is determined, force at an atom is obtained by calculating a first derivative of the total energy with respect to the atomic coordinate and the Hessian is obtained by calculating second derivatives, and so on. Structure optimizations and molecular dynamics are performed by using force, while vibrational frequencies are calculated by the Hessian at the optimized structure. For periodic systems, stress components are obtained by calculating strain derivatives of the total energy. Phonon frequencies, elastic constants, dielectric constants, and piezoelectric constants are calculated at the optimized structure from various second-derivative components. Born and Huang[12] derived these properties by using the method of long waves. Our equations based on strain derivatives

are compared with theirs and and equivalence at zero force and zero stress is shown in Chapter II. Also in this chapter, various equations involving dispersion sums are shown.

In Chapter III, a new method of nonbond energy calculation, the Cell Multipole Method (CMM) is shown. In this method, a calculation time scales as N (N is the number of atoms in the simulation) as opposed to N^2 in the exact calculation. Since the nonbond calculations are the most time-consuming part of simulations, it enables the use of very large number of atoms, e.g., 1 million atoms in simulations. The basic idea of this method is to divide the system into cells and use the multipole expansions for interactions from far cells. This method has been developed for the gravitational problems but has not been applied for molecular simulations. For both finite and periodic systems, this method is more accurate and faster than conventional approximation methods. For a periodic system (CMMX), a reduced set that reproduces up to hexadecapoles of the original unit cell is created and the Ewald method is used to evaluate the potential inside the unit cell that is due to the charges of all cells except for the 26 nearest neighbor cells. The potential from these 26 nearest neighbor cells is evaluated by using the Cell Multipole Method. In this way, the Ewald potential of a very large unit cell is calculated efficiently.

In Part II, polymer crystals studied by using methods developed in Part I are shown. To study the properties of polymer crystals, accurate van der Waals parameters are required. To obtain these parameters, a graphite crystal is treated in Appendix I. Here, experimental cell parameters and elastic constants are used to obtain the van der Waals parameters for carbon. Recently, graphite force-field parameters are used to calculate properties of C_{60} crystals[13].

In Chapter IV, the force-field parameters of a polyethylene crystal are developed, and various properties are calculated. One of the focuses in this study is the van der Waals parameters of hydrogen, since experimental values are enough

to determine these parameters accurately at low temperature. Valence force-field parameters are obtained by using n-butane, the repeating unit of polyethylene. By using the Hessian from the Hartree-Fock calculations as well as an experimental geometry and vibrational frequencies, force-field parameters of n-butane are obtained and these are used for larger, normal hydrocarbons and polyethylene. Elastic constants along the chain direction are determined accurately by a calculation. By using fixed-cell minimization techniques, a surface creation process is simulated, and surface energy is calculated.

In Appendix II, van der Waals parameters for carbon and hydrogen derived for graphite and polyethylene are used to calculate structure, cohesive energy, lattice frequencies, and elastic constants of hydrocarbon crystals (n-hexane, n-octane, benzene, naphthalene, and anthracene), and these are compared with available experimental data. As expected, newly derived van der Waals parameters give a better agreement between calculated and experimental properties than that obtained by using previously published van der Waals parameters.

In Chapter V, properties of poly (vinylidene fluoride) crystals are calculated. This polymer is technologically and scientifically important because of its piezoelectric properties. One aim of the simulation is to calculate piezoelectric constants of this polymer crystal. There are four observed forms for this polymer and a new form has been proposed by Lovinger[14]. Force-field parameters describing all forms are developed and used to calculate relative energy and various properties. Calculations show that the new form is mechanically stable and that its energy is comparable to other forms. To examine the effect of atomic polarizabilities to piezoelectric properties, force-field parameters, including explicitly atomic polarizabilities by using a shell model previously used for ionic crystals[15], are developed for this polymer. To determine parameters including atomic polarizabilities, Hartree-Fock calculations of 1,1,1,3,3 - pentafluorobutane are used. By using the shell model for

atomic polarizabilities, the agreement between theoretical and experimental values for piezoelectric constants and dielectric constants is improved significantly.

References

(1) Allen, M. P.; Tildesley, D. J. *Computer Simulation of Liquids* (Oxford Univ. Press, Oxford, 1987).

(2) Burkert, U.; Allinger, N. L. *Molecular Mechanics* (American Chemical Society, Washington, D. C., 1982).

(3) Mayo, S. L.; Olafson, B. D.; Goddard III, W. A. *J. Phys. Chem.* **1990,** *94,* 8897.

(4) Allinger, N. L.; Yuh, Y. H.; Lii, J.-H. *J. Am. Chem. Soc.* **1989,** *111,* 8551.

(5) Weiner, S. J.; Kollman, P. A.; Case, D. A.; Singh, U. C.; Ghio, C.; Alagona, G.; Profeta, Jr., S.; Weiner, P. *J. Am. Chem. Soc.* **1984,** *106,* 765.

(6) Dasgupta, S.; Goddard III, W. A. *J. Chem. Phys.* **1989,** *90,* 7207.

(7) Berens, P. H.; Mackay, D. H. J.; White, G. M.; Wilson, K. R. *J. Chem. Phys.* **1983,** *79,* 2375.

(8) Car, P.; Parrinello, M. *Phys. Rev. Lett.* **1985,** *55,* 2471.

(9) Euwema, R. N.; Surratt, G. T. *J. Phys. Chem. Solids.* **1975,** *36,* 67. A potential difference that is due to the use of a charge-repeating unit with nonzero trace of second moments (but zero dipole and quadruple moments) is given by $V - V_{Ewald} = -(2\pi/3\Omega)\sum_i q_i r_i^2$. Here, Ω is a volume of the unit cell, q_i is a charge and $\mathbf{r_i}$ is a position of ith charge in the repeating unit.

(10) Harris, F. E. , in *Theoretical Chemistry Advances and Perspective,* Eyring, H. and Henderson, D. eds. (Academic Press, New York, 1975).

(11) Tosi, M. P. *Solid State Physics* **1964,** *16,* 107.

(12) Born, M.; Huang, K. *Dynamical Theory of Crystal Lattices* (Oxford Univ. Press, Oxford, 1954).

(13) Guo, Y.; Karasawa, N.; Goddard III, W. A. *Nature* **1991,** *351,* 464.

(14) Lovinger, A. J. *Macromolecules* **1980,** *13,* 1317.

(15) Brüesch, P. *Phonons: Theory and Experiment I* (Springer-Verlag, Berlin, 1982).

Part I

Nonbond Energy Calculations in Molecular Simulations

Chapter I

Acceleration of Convergence for Lattice Sums

Reprinted from The Journal of Physical Chemistry, 1989, 93, 7320.

Acceleration of Convergence for Lattice Sums

Naoki Karasawa and William A. Goddard III*

Arthur Amos Noyes Laboratory of Chemical Physics,† California Institute of Technology, Pasadena, California 91125 *(Received: January 6, 1989; In Final Form: May 10, 1989)*

The lattice sums of nonbond interactions (electrostatic and dispersion) for computer simulations of periodic systems typically coverge very slowly. Here, we examine the accelerated convergence of these sums based on Ewald procedures and derive equations for the energies, forces, stresses, and curvatures. A method is proposed and tested for selecting the convergence acceleration parameter η on the basis of minimum calculation time. As an illustration and check, the properties of argon and NaCl crystals are calculated by using these equations and compared with values obtained analytically.

I. Introduction

To carry out molecular mechanics and molecular dynamics calculations, it is necessary to sum various nonbonded interactions over all pairs of atoms. Thus, the electrostatic energy for a collection of point charges, $\{q_i\}$, is

$$E_Q = \frac{1}{2}\sum_{ij}{}' \frac{Q_{ij}}{R_{ij}} \tag{1}$$

where $Q_{ij} = (\text{Cunit}/\epsilon)q_iq_j$ and q_i is the charge of the atom i. Here the prime indicates that $i = j$ terms are excluded, ϵ is the dielectric constant (which we take as 1.0), and Cunit = 332.0647 puts the final energy in kcal/mol if distances are in angstroms (Cunit = 14.400 if the energy is in electronvolts). Similarly, the dispersion part of the vdw interaction has the form

$$E_{\text{disp}} = \frac{1}{2}\sum_{ij}{}' \frac{B_{ij}}{R_{ij}^6} \tag{2}$$

where B_{ij} is negative.

These sums are notoriously slow to converge. This is illustrated in Table I for NaCl and polyethylene (PE) crystals. To obtain an electrostatic energy good to 0.01 kcal/mol by this procedure would require calculating all terms larger than 0.001 kcal/mol, which for unit charges would require a cutoff distance of 332 000 Å! With a typical density of 10^{22} atoms/cm^3 this would require 10^{15} atoms! Clearly such large cutoffs are untenable.

The convergence is speeded by grouping together all atoms of a cell and summing complete unit cells as illustrated in Table II. However, the convergence is still far too slow.

The general solution to this problem originated with Ewald in 1921 using convergence functions for $1/R$ interactions.[1] Nijboer and de Wette[2] generalized this approach to include all cases where the interactions are proportional to negative powers of distance for a single atom in a cell. Williams[3] extended the formulas to allow multiple atoms in a cell.

Consider a general lattice sum of the type

$$S_m = \frac{1}{2}\sum_{L,i,j} \frac{A_{ij}}{|\mathbf{r}_i - \mathbf{r}_j - \mathbf{R}_L|^m} \tag{3}$$

where $\mathbf{r}_i$ and $\mathbf{r}_j$ are the basis vectors of atoms i and j in the cell and $\mathbf{R}_L$ is the lattice translation vector. The sums over i and j each go over all atoms inside the cell except that $i \neq j$ when $L = 0$. The total electrostatic energy is given by S_1, while the dispersion term is given by S_6. Multiplying every term in (3) by the convergence function ϕ_m and then by $(1 - \phi_m)$, we obtain

$$S_m = \frac{1}{2}\sum_{L,i,j} \frac{A_{ij}\phi_m(|\mathbf{r}_i - \mathbf{r}_j - \mathbf{R}_L|)}{|\mathbf{r}_i - \mathbf{r}_j - \mathbf{R}_L|^m} + \frac{1}{2}\sum_{L,i,j} \frac{A_{ij}[1 - \phi_m(|\mathbf{r}_i - \mathbf{r}_j - \mathbf{R}_L|)]}{|\mathbf{r}_i - \mathbf{r}_j - \mathbf{R}_L|^m} \tag{4}$$

If $\phi_m(r)$ is a rapidly decreasing function, then the first term of (4) converges much faster than (3). The second term converges slowly, but by taking the Fourier transform, the resulting sum (over the reciprocal lattice vectors) converges much faster. Following Nijboer and de Wette[2] and Williams,[3] we choose ϕ_m as

$$\phi_m(r) = \frac{1}{\Gamma(m/2)}\int_{r^2/\eta^2}^{\infty} t^{m/2-1}e^{-t}\,dt \tag{5}$$

II. Coulomb Sums

For the Coulomb case (5) becomes

$$\phi_1(r) = \text{erfc}\,(r/\eta) = 1 - \text{erf}\,(r/\eta) \tag{6}$$

where erf is the error function. In this case, the Coulomb interaction with infinite range is replaced by an interaction of range η and summed in the real space, while the long range corrections are summed in the reciprocal space. The parameter η determines how much of the real space sum is converted to the reciprocal space sum (large η leads to a larger real space sum).

A. Total Energy. The energy sum is

$$S_1 = \frac{1}{2\eta}\sum_{L,i,j} Q_{ij}\frac{\text{erfc}\,(a)}{a} + \frac{2\pi}{\Omega}\sum_{\mathbf{h}}{}' S(\mathbf{h})S(-\mathbf{h})h^{-2}e^{-b^2} - \frac{1}{\pi^{1/2}\eta}\left(\sum_i Q_{ii}\right) \tag{7}$$

where it is assumed that each cell is neutral

$$\sum_i q_i = 0 \tag{8}$$

and the prime indicates that the term at the origin is excluded. Here $\mathbf{h}$ is the reciprocal lattice vector, Ω is the volume of the unit cell, $a = |\mathbf{r}_i - \mathbf{r}_j - \mathbf{R}_L|/\eta$, $b = {}^1/_2h\eta$, and $h = |\mathbf{h}|$. The first term in (7) is just the first term of (4). The last term in (7) arises from the exclusion of $i = j$ terms when $L = 0$, since in the reciprocal space sum, these terms are included.

The second term of (7) arises from the expansion of the second term of (4) in terms of Fourier transforms of the point charge δ function distribution

$$\sum_{i,j,L} Q_{ij}\delta(\mathbf{r} - \mathbf{r}_i + \mathbf{r}_j + \mathbf{R}_L) = \frac{1}{\Omega}\sum_{\mathbf{h}} S(\mathbf{h})S(-\mathbf{h})e^{i\mathbf{h}\cdot\mathbf{r}} \tag{9a}$$

where

$$S(\mathbf{h}) = \left(\frac{\text{Cunit}}{\epsilon}\right)^{1/2}\sum_j q_j e^{-i\mathbf{h}\cdot\mathbf{r}_j} \tag{9b}$$

is referred to as the structure factor. The quantity $S(\mathbf{h})S(-\mathbf{h})$ in (7) has the form

$$S(\mathbf{h})S(-\mathbf{h}) = \sum_{ij} Q_{ij}\cos\,[\mathbf{h}\cdot(\mathbf{r}_i - \mathbf{r}_j)] \tag{10}$$

which Cowley et al.[4] have shown can be rewritten as

$$S(\mathbf{h})S(-\mathbf{h}) = \frac{\text{Cunit}}{\epsilon}\{[\sum_i q_i \cos\,(\mathbf{h}\cdot\mathbf{r}_i)]^2 + [\sum_i q_i \sin\,(\mathbf{h}\cdot\mathbf{r}_i)]^2\} \tag{11}$$

† Contribution No. 7902.

(1) Tosi, M. P. *Solid State Phys.* **1964**, *16*, 107.
(2) Nijboer, B. R. A.; de Wette, F. W. *Physica* **1957**, *23*, 309.
(3) (a) Williams, D. E. *Acta Crystallogr., Sect. A* **1971**, *27*, 452. (b) Williams, D. E. In *Crystal Cohesion and Conformational Energies*; Metzger, R. M., Ed.; Springer-Verlag: Berlin–Heidelberg–New York, 1981; pp 3–40.

0022-3654/89/2093-7320$01.50/0

TABLE I: Convergence of Nonbond Interactions Using Atom-Based Cutoffs[a]

		NaCl[d]			polyethylene		
R_{outer},[b] Å	R_{inner},[b] Å	terms	E_Q	E_{disp}	terms	E_Q	E_{disp}
10	8	608	-981.65	-20.330	3072	-51.870	-797.687
10	9	608	-1556.20	-20.413	3072	-2.343	-797.798
10	10	608	-1492.67	-20.445	3072	-111.998	-797.863
15	14	2152	1446.83	-20.726	10394	-40.272	-798.184
15	15	2152	1281.61	-20.735	10394	-52.972	-798.198
20	19	5296	-1743.32	-20.794	24615	-79.905	-798.275
20	20	5296	1207.33	-20.800	24615	-63.080	-798.280
25	24	10320	1210.98	-20.821	48015	-107.974	-798.306
25	25	10320	109.11	-20.822	48015	-54.830	-798.308
Ewald[c]			-824.59	-20.846		-65.685	-798.338

[a] Energies are in kcal/mol. [b] Each term of (1) or (2) is multiplied by the cubic cutoff function $S(R_{ij})$, where $S(R) = 1.0$ if $R < R_{inner}$, $S(R) = 0.0$ if $R > R_{outer}$, and $S(R) = [R^2_{outer} - R^2]^2[R^2_{outer} + 2R^2 - 3R^2_{inner}]/[R^2_{outer} - R^2_{inner}]^3$, otherwise. [c] $\eta = 2.5$ for NaCl and $\eta = 2.0$ for polyethylene. [d] Parameters used are $B_{NaNa} = -24.180$, $B_{NaCl} = -161.20$, $B_{ClCl} = -1669.58$ kcal Å^6 mol^{-1}. $q_{Na} = e$, $q_{Cl} = -e$, $A = 5.63$ Å.

TABLE II: Convergence of Nonbond Interactions Using Cell-Based Cutoffs[a]

	NaCl[e]			polyethylene		
r_{cut}, Å	terms[b]	E_Q	E_{disp}	terms[b]	E_Q	E_{disp}
6	3500 (2 2 2)	-824.5563	-20.7615	6930 (1 3 2)	-65.6032	-798.0302
8	3500 (2 2 2)	-824.5563	-20.7615	14850 (2 4 2)	-65.6402	-798.1933
10	3500 (2 2 2)	-824.5563	-20.7615	20790 (2 4 3)	-65.6521	-798.2312
15	9604 (3 3 3)	-824.5768	-20.8161	54054 (3 6 4)	-65.6655	-798.3005
20	20412 (4 4 4)	-824.5836	-20.8323	86394 (3 8 5)	-65.6669	-798.3176
25	37268 (5 5 5)	-824.5852	-20.8387	162162 (4 10 6)	-65.6725	-798.3274
Ewald[c]	512 + 2240[d]	-824.5861		1748 + 1584[d]	-65.6836	
	296 + 2240[d]		-20.8463	1044 + 6204[d]		-798.3383

[a] Energies are in kcal/mol. [b] The numbers in parentheses show the (a b c) index for the last shell considered. [c] $\eta = 2.5$ for NaCl and $\eta = 2.0$ for polyethylene. $\delta_Q = 0.001$ kcal/mol. $\delta_{disp} = 10^{-4}$ kcal/mol. [d] The number of terms in real space and reciprocal space sums, respectively (eq 10 is used). [e] Parameters are given in Table I.

Since the summation in (11) runs only over single atoms rather than pairs, the computations for the reciprocal space sum are significantly reduced.

B. Force and Stress. The force at atom p is given by

$$\mathbf{f}_{1,p} = -\frac{\partial S_1}{\partial \mathbf{r}_p} = \frac{1}{\eta^3}\sum_L\sum_i Q_{pi}(\mathbf{r}_p - \mathbf{r}_i - \mathbf{R}_L)\left[\frac{\operatorname{erfc}(a_p)}{a_p^3} + \frac{2\pi^{-1/2}e^{-a_p^2}}{a_p^2}\right] + \frac{4\pi}{\Omega}\sum_{\mathbf{h}}{}'\mathbf{h}[\sum_i Q_{pi}\sin(\mathbf{h}\cdot(\mathbf{r}_p - \mathbf{r}_i))]h^{-2}e^{-b^2} \quad (12)$$

where $a_p = |\mathbf{r}_p - \mathbf{r}_i - \mathbf{R}_L|/\eta$. By use of (11), the second term can be rewritten as

$$\frac{\text{Cunit}}{\epsilon}\frac{4\pi}{\Omega}q_p\sum_h{}'\mathbf{h}\{\sin(\mathbf{h}\cdot\mathbf{r}_p)[\sum_i q_i\cos(\mathbf{h}\cdot\mathbf{r}_i)] - \cos(\mathbf{h}\cdot\mathbf{r}_p)\times[\sum_i q_i\sin(\mathbf{h}\cdot\mathbf{r}_i)]\}h^{-2}e^{-b^2} \quad (13)$$

To calculate the stress, consider the matrix $\mathbf{H}$ that contains the real space unit cell vectors in Cartesian coordinates, i.e., $\mathbf{H} = [\mathbf{a},\mathbf{b},\mathbf{c}]$, where $\mathbf{a},\mathbf{b},\mathbf{c}$ are the unit cell vectors.[5] Then we have

$$\Omega = \det(\mathbf{H}) \quad (14)$$

$$\mathbf{r}_i - \mathbf{r}_j - \mathbf{R}_L = \mathbf{H}(\mathbf{s}_i - \mathbf{s}_j - \mathbf{L}) \quad (15)$$

and

$$\mathbf{h} = 2\pi\tilde{\boldsymbol{H}}^{-1}\mathbf{n} \quad (16)$$

where $\mathbf{s}_i$ is the fractional coordinate vector of the atom i, and $\mathbf{n}$ and $\mathbf{L}$ are vectors whose elements are the integers specifying the reciprocal lattice and real lattice vectors, and $\tilde{\boldsymbol{H}}$ is the transpose of $\boldsymbol{H}$. The stress $\Pi_{\alpha\beta}$ is given by the relation[5]

$$-\frac{\partial E}{\partial \boldsymbol{H}_{\alpha\gamma}} = \sum_\beta \Pi_{\alpha\beta}\Omega\boldsymbol{H}^{-1}_{\gamma\beta} \quad (17)$$

where E is the total (potential) energy of the system. For the electrostatic stress, we have

$$\Omega\Pi_{\alpha\beta} = \frac{1}{2\eta^3}\sum_{L,i,j}Q_{ij}\left[\frac{\operatorname{erfc}(a)}{a^3} + \frac{2\pi^{-1/2}e^{-a^2}}{a^2}\right](\mathbf{r}_i - \mathbf{r}_j - \mathbf{R}_L)_\alpha(\mathbf{r}_i - \mathbf{r}_j - \mathbf{R}_L)_\beta + \frac{2\pi}{\Omega}\sum_{\mathbf{h}}{}'S(\mathbf{h})S(-\mathbf{h})\frac{e^{-b^2}}{h^2}\left[\delta_{\alpha\beta} - 2\frac{(1+b^2)}{h^2}\mathbf{h}_\alpha\mathbf{h}_\beta\right] \quad (18)$$

The stresses can also be obtained by differentiating the energy with respect to strains. The strain tensor is defined by[6]

$$\epsilon = \frac{1}{2}(\tilde{\boldsymbol{H}}_0^{-1}\tilde{\boldsymbol{H}}\boldsymbol{H}\boldsymbol{H}_0^{-1} - 1) \quad (19)$$

where $\boldsymbol{H}_0$ contains the original cell vectors and $\boldsymbol{H}$ contains the deformed cell vectors. ϵ is symmetric so we define six independent strain components e_i such that $e_1 = \epsilon_{11}$, $e_2 = \epsilon_{22}$, $e_3 = \epsilon_{33}$, $e_4 = 2\epsilon_{23}$, $e_5 = 2\epsilon_{31}$, and $e_6 = 2\epsilon_{12}$. Then we have

$$\Omega\Pi_k = -\left(\frac{\partial E}{\partial e_k}\right)_{e_i=0} \qquad (k = 1, \ldots, 6) \quad (20)$$

where $\Pi_1 = \Pi_{11}$, $\Pi_2 = \Pi_{22}$, $\Pi_3 = \Pi_{33}$, $\Pi_4 = \Pi_{23}$, $\Pi_5 = \Pi_{31}$, and $\Pi_6 = \Pi_{12}$. To derive this equation, we use the relations

$$\frac{\partial \boldsymbol{H}_{\alpha\gamma}}{\partial \epsilon_{ii}} = \sum_k \boldsymbol{H}^{-1}_{k\alpha}\boldsymbol{H}_{0i\gamma}\boldsymbol{H}_{0ik} = \delta_{i\alpha}\boldsymbol{H}_{i\gamma} \qquad (e_i = 0) \quad (21a)$$

(4) Cowley, E. R.; Jacucci, G.; Klein, M. L.; McDonald, I. R. *Phys. Rev. B* **1976**, *14*, 1758. In this paper, $A_n(\eta)$ in eq 3 must be multiplied by a factor $(1/\pi L)$.

(5) Nosé, S.; Klein, M. L. *Mol. Phys.* **1983**, *50*, 1055.

(6) Parrinello, M.; Rahman, A. *J. Appl. Phys.* **1981**, *52*, 7182.

(7) Kittel, C. *Introduction to Solid State Physics*, 5th ed.; John Wiley & Sons: New York, 1976.

(8) Born, M.; Huang, K. *Dynamical Theory of Crystal Lattices*; Oxford University Press: London, 1954.

$$\frac{\partial H_{\alpha\gamma}}{\partial \epsilon_{ij}} = \sum_k H_{k\alpha}^{-1}(H_{0i\gamma}H_{0jk} + H_{0j\gamma}H_{0ik}) = \delta_{j\alpha}H_{i\gamma} + \delta_{i\alpha}H_{j\gamma} \qquad (e_i = 0) \tag{21b}$$

derived from (19).

C. Curvatures. The second derivatives with respect to XX and YY strains have the form

(i)

$$\frac{\partial^2 S_1}{\partial e_1 \partial e_1} = -\frac{1}{2\eta^3}\sum_{L,i,j} Q_{ij}\left[F'\frac{1}{a\eta^2}(\mathbf{r}_i - \mathbf{r}_j - \mathbf{R}_L)_1^4 + 2F(\mathbf{r}_i - \mathbf{r}_j - \mathbf{R}_L)_1^2\right] + \frac{2\pi}{\Omega}\sum_{\mathbf{h}}' S(\mathbf{h})S(-\mathbf{h})\left[\frac{1}{2}\eta^2\mathbf{h}_1^4 H' + 4H\mathbf{h}_1^2 + G\right] \tag{22a}$$

(ii)

$$\frac{\partial^2 S_1}{\partial e_1 \partial e_2} = -\frac{1}{2\eta^3}\sum_{L,i,j} Q_{ij}\left[F'\frac{1}{a\eta^2}(\mathbf{r}_i - \mathbf{r}_j - \mathbf{R}_L)_1^2(\mathbf{r}_i - \mathbf{r}_j - \mathbf{R}_L)_2^2\right] + \frac{2\pi}{\Omega}\sum_{\mathbf{h}}' S(\mathbf{h})S(-\mathbf{h})\left[\frac{1}{2}\eta^2\mathbf{h}_1^2\mathbf{h}_2^2 H' + H(\mathbf{h}_1^2 + \mathbf{h}_2^2) + G\right] \tag{22b}$$

where

$$F = [\text{erfc}\ (a) + 2\pi^{-1/2}ae^{-a^2}]/a^3$$

$$G = \eta^2 e^{-b^2}/4b^2$$

$$H = -\eta^4(1 + b^2)e^{-b^2}/8b^4$$

$$F' = \frac{dF}{da}, \quad H' = \frac{dH}{db^2}$$

III. Dispersion Sums

For the dispersion sum with $m = 6$ in (3), the form for ϕ_6 is

$$\phi_6 = \left[1 + (r/\eta)^2 + \frac{1}{2}(r/\eta)^4\right]e^{-(r/\eta)^2} \tag{23}$$

A. Energy. This leads to an energy of

$$S_6 = \frac{1}{2\eta^6}\sum_{L,i,j} B_{ij}\left(a^{-6} + a^{-4} + \frac{1}{2}a^{-2}\right)e^{-a^2} + \frac{\pi^{3/2}}{24\Omega}\sum_{\mathbf{h}}'\sum_{i,j} B_{ij}\cos[\mathbf{h}\cdot(\mathbf{r}_i - \mathbf{r}_j)]h^3\left[\pi^{1/2}\,\text{erfc}\,(b) + \left(\frac{1}{2b^3} - \frac{1}{b}\right)e^{-b^2}\right] + \frac{\pi^{3/2}}{6\Omega\eta^3}\sum_{i,j} B_{ij} - \frac{1}{12\eta^6}\sum_i B_{ii} \tag{24}$$

where $b = {}^1/_2 h\eta$, $a = |\mathbf{r}_i - \mathbf{r}_j - \mathbf{R}_L|/\eta$, and $h = |\mathbf{h}|$. The first term in (24) arises from the first term in (4) and can be written as

$$\frac{1}{\eta^6}\sum_L\left[\sum_{j>i} B_{ij}a^{-2}e^{-a^2}\left(a^{-4} + a^{-2} + \frac{1}{2}\right) + \frac{1}{2}a_L^{-2}e^{-a_L^2}\left(a_L^{-4} + a_L^{-2} + \frac{1}{2}\right)\sum_i B_{ii}\right] \tag{25}$$

where $a_L = |\mathbf{R}_L|/\eta$. The second term arises from the second term in (4) using (9) and (10). The third term is from $\mathbf{h} = 0$ in the second term, while the fourth term is from exclusion of $i = j$ terms when $L = 0$.

Often the dispersion terms are assumed to satisfy the geometric combination rules

$$-B_{ij} = (B_{ii}B_{jj})^{1/2} \tag{26}$$

and expressions similar to (24) are based on this form.[3] However, in the above derivation, *no* such assumptions are made. When (26) is satisfied, we can use

$$\sum_{i,j} B_{ij}\cos[\mathbf{h}\cdot(\mathbf{r}_i - \mathbf{r}_j)] = -[\sum_i (|B_{ii}|)^{1/2}\cos(\mathbf{h}\cdot\mathbf{r}_i)]^2 - [\sum_i (|B_{ii}|)^{1/2}\sin(\mathbf{h}\cdot\mathbf{r}_i)]^2 \tag{26'}$$

in the reciprocal space sum of (24) to reduce the computing time.

B. Force and Stress. The force on atom p is

$$\mathbf{f}_{6,p} = -\frac{\partial S_6}{\partial \mathbf{r}_p} = \frac{1}{\eta^8}\sum_L\sum_i B_{pi}(\mathbf{r}_p - \mathbf{r}_i - \mathbf{R}_L) \times (6a_p^{-8} + 6a_p^{-6} + 3a_p^{-4} + a_p^{-2})e^{-a_p^2} + \frac{\pi^{3/2}}{12\Omega}\sum_{\mathbf{h}}'\mathbf{h}[\sum_i B_{pi} \times \sin[\mathbf{h}\cdot(\mathbf{r}_p - \mathbf{r}_i)]]h^3\left[\pi^{1/2}\,\text{erfc}\,(b) + \left(\frac{1}{2b^3} - \frac{1}{b}\right)e^{-b^2}\right] \tag{27}$$

The stress term is

$$\Omega\Pi_{\alpha\beta} = \frac{1}{2\eta^8}\sum_L\sum_{i,j} B_{ij}(6a^{-8} + 6a^{-6} + 3a^{-4} + a^{-2})e^{-a^2}(\mathbf{r}_i - \mathbf{r}_j - \mathbf{R}_L)_\alpha \times (\mathbf{r}_i - \mathbf{r}_j - \mathbf{R}_L)_\beta + \frac{\pi^{3/2}}{24\Omega}\sum_{\mathbf{h}}'\sum_{i,j} B_{ij}\cos[\mathbf{h}\cdot(\mathbf{r}_i - \mathbf{r}_j)] \times \left[h^3\left\{\pi^{1/2}\,\text{erfc}\,(b) + \left(\frac{1}{2b^3} - \frac{1}{b}\right)e^{-b^2}\right\}\delta_{\alpha\beta} + 3h\left(\pi^{1/2}\,\text{erfc}\,(b) - \frac{e^{-b^2}}{b}\right)\mathbf{h}_\alpha\mathbf{h}_\beta\right] + \frac{\pi^{3/2}}{6\eta^3\Omega}\sum_{i,j} B_{ij}\delta_{\alpha\beta} \tag{28}$$

Here we have used

$$\frac{\partial a}{\partial H_{\alpha\beta}} = \frac{1}{\eta}\frac{1}{|\mathbf{r}_i - \mathbf{r}_j - \mathbf{R}_L|}(\mathbf{r}_i - \mathbf{r}_j - \mathbf{R}_L)_\alpha(\mathbf{s}_i - \mathbf{s}_j - \boldsymbol{L})_\beta \tag{29}$$

where $\mathbf{r}_i - \mathbf{r}_j - \mathbf{R}_L$ is given in (15) and

$$\frac{\partial b^2}{\partial H_{\alpha\beta}} = -\frac{1}{2}\eta^2\mathbf{h}_\alpha\sum_\gamma H_{\beta\gamma}^{-1}\mathbf{h}_\gamma \tag{30}$$

C. Curvatures. The second derivatives with respect to XX and YY strains have the form

(i)

$$\frac{\partial^2 S_6}{\partial e_1 \partial e_1} = -\frac{1}{2\eta^8}\sum_{L,i,j} B_{ij}\left[F'\frac{1}{a\eta^2}(\mathbf{r}_i - \mathbf{r}_j - \mathbf{R}_L)_1^4 + 2F(\mathbf{r}_i - \mathbf{r}_j - \mathbf{R}_L)_1^2\right] + \frac{\pi^{3/2}}{24\Omega}\sum_{\mathbf{h}}'\sum_{i,j} B_{ij}\cos[\mathbf{h}\cdot(\mathbf{r}_i - \mathbf{r}_j)] \times \left[\frac{1}{2}\eta^2\mathbf{h}_1^4 H' + 4H\mathbf{h}_1^2 + G\right] + \frac{\pi^{3/2}}{6\eta^3\Omega}\sum_{i,j} B_{ij} \tag{31a}$$

(ii)

$$\frac{\partial^2 S_6}{\partial e_1 \partial e_2} = -\frac{1}{2\eta^8}\sum_{L,i,j} B_{ij}\left[F'\frac{1}{a\eta^2}(\mathbf{r}_i - \mathbf{r}_j - \mathbf{R}_L)_1^2(\mathbf{r}_i - \mathbf{r}_j - \mathbf{R}_L)_2^2\right] + \frac{\pi^{3/2}}{24\Omega}\sum_{\mathbf{h}}'\sum_{i,j} B_{ij}\cos[\mathbf{h}\cdot(\mathbf{r}_i - \mathbf{r}_j)] \times \left[\frac{1}{2}\eta^2\mathbf{h}_1^2\mathbf{h}_2^2 H' + H(\mathbf{h}_1^2 + \mathbf{h}_2^2) + G\right] + \frac{\pi^{3/2}}{6\eta^3\Omega}\sum_{i,j} B_{ij} \tag{31b}$$

where

$$F = (6a^{-8} + 6a^{-6} + 3a^{-4} + a^{-2})e^{-a^2}$$

$$G = \frac{8b^3}{\eta^3}\left\{\pi^{1/2}\,\text{erfc}\,(b) + \left(\frac{1}{2b^3} - \frac{1}{b}\right)e^{-b^2}\right\}$$

$$H = \frac{6b}{\eta}\left(\pi^{1/2}\,\text{erfc}\,(b) - \frac{e^{-b^2}}{b}\right)$$

$$F' = \frac{dF}{da}, \quad H' = \frac{dH}{db^2}$$

TABLE III: Predicted Values of η_{opt} (Using (34))

crystal	$\lvert R_{L,min}\rvert$, Å	$\lvert h_{min}\rvert$, Å^{-1}	η_{opt}, Å
NaCl (8 atoms/cell)	5.63	1.116	3.18
NaCl (2 atoms/cell)	3.98	1.933	2.03
Ar (4 atoms/cell)	5.31	1.183	3.00
Ar (1 atom/cell)	3.755	2.050	1.91
polyethylene (12 atoms/cell)	2.54	0.8656	2.42
orthorhombic poly(oxymethylene) (16 atoms/cell)	3.56	0.8212	2.94

IV. Selection of η

A. Choice of η from Cell Parameters. The parameter η should be chosen to optimize the convergence of both the real lattice and reciprocal lattice sums. If η is too small, the reciprocal lattice sum does not converge quickly since $b = {}^1/_2 h\eta$ remains small when h becomes large. Similarly, if η is too large, the real space sum does not converge quickly since $a = |\mathbf{r}_i - \mathbf{r}_j - \mathbf{R}_L|/\eta$ remains small for large $|\mathbf{R}_L|$.

Since both sums are multiplied by terms like e^{-x^2} or erfc (x) (where $x = a$ for real space and $x = b$ for reciprocal space), a simple estimate of the optimum parameter η for rapid convergence of both sums can be obtained as follows. These terms decrease rapidly for large x, so that both sums converge similarly when $a = b$. This leads to

$$\eta_{opt}^2 = \frac{|\mathbf{r}_i - \mathbf{r}_j - \mathbf{R}_L|}{{}^1/_2 h} \simeq \frac{|\mathbf{R}_L|}{{}^1/_2 h} \tag{32}$$

which determines η in terms of L and h. The simplest choice of η is to use the minimum length of $\mathbf{R}_L$ and of h so that we have the same orders of magnitude of a and b when these have the minimum values (of course, $|\mathbf{R}_L| \neq 0$ and $h \neq 0$). Then

$$\eta_{opt}^2 = \frac{|\mathbf{R}_{L,min}|}{{}^1/_2 h_{min}} \tag{33}$$

Assuming $a < b,c$ and $h_c < h_a, h_b$ (33) leads to

$$\eta_{opt}^2 = \frac{a\Omega}{\pi|\mathbf{a} \times \mathbf{b}|} = \frac{\Omega}{\pi b \sin \gamma} \tag{34}$$

This determines η_{opt} in terms of the crystal structure. The η_{opt} thus obtained may not be the optimum η for minimizing computation time, since we assumed that the computation time per each term is the same for both real and reciprocal space sums. Table III shows the calculated η_{opt} for various systems.

B. Accuracy Specified Cutoffs. With η specified there is still an infinite number of terms in the sums over the real space and reciprocal space lattices, and we use an accuracy criteria to specify limits on these sums. To this end we specify a tolerance δ and carry out the sums until the neglected terms have a total contribution smaller than this tolerance.

1. Electrostatic Sums. (a) Real Space Sum. Using a cutoff distance R_{cut} introduces an error in the total energy for the real space sum of

$$E_{Q,real} = \frac{1}{2} \sum_{L,i,j}' Q_{ij} \frac{\text{erfc}\,(R_{ijL}/\eta)}{R_{ijL}} \Theta(R_{ijL} - R_{cut}) \tag{35}$$

where $\Theta(x)$ is the step function [$\Theta(x) = 1$ when $x > 0$ and $\Theta(x) = 0$ when $x < 0$]. To estimate this error, we replace discrete sum (35) by a continuous integral. Defining the average interaction as $\langle q^2 \rangle = \sum_i q_i^2/N$, we obtain

$$E_{Q,real} \simeq \frac{1}{2} \frac{N^2\langle q^2\rangle}{\epsilon} \frac{\text{Cunit}}{\Omega} \int_{R_{cut}}^{\infty} 4\pi R^2 \frac{\text{erfc}\,(R/\eta)}{R}\, dR$$

Since

$$\text{erfc}\left(\frac{R}{\eta}\right) = \frac{1}{\pi^{1/2}} \int_{R^2/\eta^2}^{\infty} \frac{1}{t^{1/2}} e^{-t}\, dt \leq \frac{1}{\pi^{1/2}} \int_{R^2/\eta^2}^{\infty} \frac{\eta}{R} e^{-t}\, dt = \frac{\eta}{\pi^{1/2} R} e^{-R^2/\eta^2}$$

we obtain

$$E_{Q,real} \leq \frac{1}{2} \frac{N^2\langle q^2\rangle}{\epsilon} \frac{\text{Cunit}}{\Omega} \int_{R_{cut}}^{\infty} 4\pi^{1/2} \eta e^{-R^2/\eta^2}\, dR = \pi \frac{N^2\langle q^2\rangle}{\epsilon\Omega} \text{Cunit}\, \eta^2\, \text{erfc}\left(\frac{R_{cut}}{\eta}\right) \tag{36}$$

(b) Reciprocal Space Sum. The error in the reciprocal space sum due to a cutoff at H_{cut} is given by

$$E_{Q,real} = \frac{2\pi}{\Omega} \sum_{\mathbf{h}}' S(\mathbf{h})S(-\mathbf{h}) \frac{e^{-b^2}}{h^2} \Theta(h - H_{cut}) \tag{37}$$

Replacing the sum by an integral and replacing $S(\mathbf{h})S(-\mathbf{h})$ by Cunit $N^2\langle q^2\rangle/\epsilon$, we obtain

$$E_{Q,recip} \simeq \frac{2\pi}{\Omega} \frac{N^2\langle q^2\rangle}{\epsilon} \text{Cunit} \frac{\Omega}{8\pi^3} \int_{H_{cut}}^{\infty} 4\pi h^2 \frac{e^{-(h\eta/2)^2}}{h^2}\, dh = \frac{N^2\langle q^2\rangle}{\epsilon\pi^{1/2}} \text{Cunit} \frac{1}{\eta}\, \text{erfc}\left(\eta \frac{H_{cut}}{2}\right) \tag{38}$$

Using (36) and (38), we can evaluate the cutoff distances R_{cut} and H_{cut} to obtain a given accuracy δ_Q (for given η). Because of the neutrality of the cell, there will be a great deal of cancellation in (35) and (37) that is ignored in (36) and (38). Consequently, eq (36) and (38) generally overestimate the error by a factor of 10 or so.

2. Dispersion Sums. (a) Real Space Sum. The total error in the real space dispersion sum is given by

$$E_{6,real} = \frac{1}{2} \sum_{L,i,j}' |B_{ij}| \left(\frac{1}{R_{ijL}^6} + \frac{1}{R_{ijL}^4 \eta^2} + \frac{1}{2R_{ijL}^2 \eta^4} \right) e^{-(R_{ijL}/\eta)^2} \Theta(R_{ijL} - R_{cut}) \tag{39}$$

Approximating this by an integral, we have

$$E_{6,real} \simeq \frac{1}{2} N^2\langle B\rangle \frac{1}{\Omega} \int_{R_{cut}}^{\infty} \left(\frac{1}{R^6} + \frac{1}{R^4\eta^2} + \frac{1}{2R^2\eta^4} \right) 4\pi R^2 e^{-(R/\eta)^2}\, dR = 2\pi \frac{N^2\langle B\rangle}{\Omega} \int_{R_{cut}}^{\infty} \left(\frac{1}{R^4} + \frac{1}{R^2\eta^2} + \frac{1}{2\eta^4} \right) e^{-(R/\eta)^2}\, dR$$

where $N^2\langle B\rangle = \sum_{i,j}' |B_{ij}|$ is the sum of coefficients of dispersion terms. We approximate the above equation as

$$E_{6,real} \leq 2\pi \frac{N^2\langle B\rangle}{\Omega} \left(\frac{1}{R_{cut}^4} + \frac{1}{R_{cut}^2\eta^2} + \frac{1}{2\eta^4} \right) \int_{R_{cut}}^{\infty} e^{-(R/\eta)^2}\, dR = \frac{\pi^{3/2} N^2\langle B\rangle}{\Omega} \eta \left(\frac{1}{R_{cut}^4} + \frac{1}{R_{cut}^2\eta^2} + \frac{1}{2\eta^4} \right) \text{erfc}\left(\frac{R_{cut}}{\eta}\right) \tag{40}$$

(b) Reciprocal Space Sum. The total error in the reciprocal space sum is given by

$$E_{6,recip} = \frac{\pi^{3/2}}{24\Omega} \sum_{\mathbf{h}}' \sum_{ij}' |B_{ij}| \cos\,[\mathbf{h}\cdot(\mathbf{r}_i - \mathbf{r}_j)] h^3 \left[\pi^{1/2}\, \text{erfc}\,(b) + \left(\frac{1}{2b^3} - \frac{1}{b} \right) e^{-b^2} \right] \Theta(h - H_{cut}) \tag{41}$$

Approximating this sum as an integral leads to

$$E_{6,recip} \simeq \frac{\pi^{3/2}}{24\Omega} N^2\langle B\rangle \frac{\Omega}{8\pi^3} \int_{H_{cut}}^{\infty} h^3 \left[\pi^{1/2}\, \text{erfc}\,(b) + \left(\frac{1}{2b^3} - \frac{1}{b} \right) e^{-b^2} \right] 4\pi h^2\, dh$$

By using $\pi^{1/2}\,\mathrm{erfc}\,(b) \le (1/b)e^{-b^2}$, we have

$$E_{6,\mathrm{recip}} \le \frac{\pi^{3/2}}{24\Omega}N^2\langle B\rangle\,\frac{\Omega}{8\pi^3}\int_{H_{\mathrm{cut}}}^{\infty}4\pi h^5\frac{1}{2b^3}e^{-b^2}\,\mathrm{d}h = \frac{2N^2\langle B\rangle}{3\pi^{1/2}}\,\frac{1}{\eta^6}\int_{(H_{\mathrm{cut}}\eta)/2}^{\infty}b^2e^{-b^2}\,\mathrm{d}b = \frac{N^2\langle B\rangle}{6\pi^{1/2}}\,\frac{1}{\eta^6}\left[H_{\mathrm{cut}}\eta e^{-(H_{\mathrm{cut}}\eta/2)^2} + \pi^{1/2}\,\mathrm{erfc}\left(\frac{H_{\mathrm{cut}}\eta}{2}\right)\right] \quad (42)$$

Using (40) and (42), we can calculate the cutoff distances R_{cut} and H_{cut} that lead to a total error δ_V for given η.

3. Repulsive Terms. The repulsive terms in simulations generally have the form

$$E_{12} = \frac{1}{2}\sum_{i,j}{}' A_{ij}R_{ij}^{-12} \quad (43)$$

or

$$E_{\mathrm{ex}} = \frac{1}{2}\sum_{i,j}{}' A_{ij}e^{-\lambda_{ij}R_{ij}} \quad (44)$$

We can estimate the R_{cut} for these cases in a similar way. The results are

$$E_{12,\mathrm{real}} = \frac{2\pi N^2\langle A\rangle}{9\Omega}\,\frac{1}{R_{\mathrm{cut}}{}^9} \quad (45)$$

$$E_{\mathrm{ex,real}} = \frac{2\pi N^2\langle A\rangle}{\Omega}\,\frac{e^{-\langle\lambda\rangle R_{\mathrm{cut}}}}{\langle\lambda\rangle}\left(R_{\mathrm{cut}}{}^2 + \frac{2R_{\mathrm{cut}}}{\langle\lambda\rangle} + \frac{2}{\langle\lambda\rangle^2}\right) \quad (46)$$

where $N^2\langle A\rangle = \sum_{i,j}A_{ij}$ and $\langle\lambda\rangle$ is determined by the relation

$$N^2\langle A\rangle e^{-\langle\lambda\rangle R_{\mathrm{cut}}} = \sum_{i,j}A_{ij}e^{-\lambda_{ij}R_{\mathrm{cut}}}$$

4. Implementations of the Limits. The limit on the real space sum, L, is chosen so that all cells containing any atoms within R_{cut} of any atom in the unit cell are included.[9] This leads to

$$L_a = \frac{R_{\mathrm{cut}}bc\,\sin\alpha}{\Omega} + 1$$

and similarly for L_b, L_c. The sum over the reciprocal lattice has limits of $H_a = (a/2\pi)H_{\mathrm{cut}}$ and similarly for H_b and H_c. Within this set of cells, we eliminate any terms for which $R > R_{\mathrm{cut}}$. This leads to a considerable reduction in effort, as indicated in Table IV.

C. Time Minimized η. Since the choice of η affects the R_{cut} and H_{cut} and thereby the number of terms in real and reciprocal space sums, we can choose η so as to minimize calculation time while retaining prespecified computational accuracy. This is illustrated in Table V for the case of poly(oxymethylene). In this table the electrostatic energy using (11) (a2) as well as those using (10) (a1) are shown. On the basis of several test calculations, we estimate that $t_{\mathrm{real}}/t_{\mathrm{recip}} \approx 4$ in (a1) and (b) and $t_{\mathrm{real}}/t_{\mathrm{recip}} \approx 10$ in (a2), where t_{real} is the time per term for the real space calculation, while t_{recip} is the time per term for the reciprocal space calculation. Of course, these values will depend on the actual program and computer used. The reason that the evaluation of the reciprocal space term is much faster than the real space term is that the reciprocal space lattice sum involves a factor that only depends on h, which is calculated only once, while in the real space sum, all factors depend on atomic distances and must be calculated for each pair.

Excluding the interactions between the same atoms in different cells (since there are easy to evaluate) and using (10), the number of terms in the real space and reciprocal space sums can be estimated as follows (assuming constant atomic density)

$$N_{\mathrm{real}} = \frac{4\pi}{3}R_{\mathrm{cut}}{}^3\frac{N(N-1)}{2\Omega} \quad (47)$$

$$N_{\mathrm{recip}} = \left(\frac{4\pi}{3}H_{\mathrm{cut}}{}^3\frac{\Omega}{(2\pi)^3} - 1\right)\frac{N(N-1)}{2} \quad (48)$$

where N is the number of atoms in the unit cell. When (11) is used, $N(N-1)/2$ in (48) should be replaced by $2N$. Since there is a cancellation of terms in the electrostatic sum due to the charge neutrality in the unit cell, we use $\delta_Q = 10\delta_{\mathrm{disp}}$ to obtain similar accuracy in both sums. By using the estimated number of terms and the values of $t_{\mathrm{real}}/t_{\mathrm{recip}}$, we select η so that $N_{\mathrm{real}} + N_{\mathrm{rec}}/m$ is minimized where m is the ratio $t_{\mathrm{real}}/t_{\mathrm{recip}}$.

In Table V we show the results for poly(oxymethylene). In this system, there are 24 centers of which 16 are charged. In (a1) and (b), the η leading to the fastest calculation is $\eta \approx 2.5$ Å, while in (a2), the η leading to the fastest calculation is $\eta \approx 2.0$ Å. The η predicted using (33) is 2.94 Å, in reasonable agreement with (a1) and (b). In (a2), it is shown that the computing times are shorter than those in (a1) for any η due to the smaller number of terms in the reciprocal space sum. Also, the computing time for each term in the reciprocal space sum is shorter in (a2) than in (a1). Therefore, the time-minimized η in this case is smaller than for other cases. The accuracy here is 10^{-3} kcal/mol for electrostatic and 10^{-4} kcal/mol for dispersion. Note that the error in the energy is independent of η in these calculations, showing the effectiveness of accuracy-specified cutoffs.

V. Application to Ar Crystal

As a test case for the Ewald dispersion sum formlas, we will calculate the structure and properties of argon face-centered cubic (fcc) crystal analytically and compare with those obtained by using the lattice sums.

A. Model. We will describe the Ar–Ar interactions with the Lennard–Jones 12–6 form

$$U(R) = D_0\left[\left(\frac{R_0}{R}\right)^{12} - 2\left(\frac{R_0}{R}\right)^6\right] \quad (49)$$

where $R_0 = 3.8666$ Å, and $D_0 = 0.2351$ kcal/mol are adjusted to reproduce the experimental lattice spacing and heat of vaporization. For an fcc crystal structure, the total energy E_{tot} is[7]

$$E_{\mathrm{tot}}(R) = \frac{1}{2}ND_0\left[p_{12}\left(\frac{R_0}{R}\right)^{12} - 2p_6\left(\frac{R_0}{R}\right)^6\right] \quad (50)$$

where, R is the nearest-neighbor distance, $N = 4$ is the number of atoms in the conventional fcc cell, $p_{12} = 12.131\,88$, and $p_6 = 14.453\,92$.

B. Equilibrium Lattice Constants. Requiring $\partial E_{\mathrm{tot}}/\partial R = 0$ leads to the equilibrium nearest-neighbor distance

$$R_e = \left(\frac{p_{12}}{p_6}\right)^{1/6}R_0 = 0.97123R_0 \quad (51a)$$

The lattice constant at equilibrium becomes

$$A_e = 2^{1/2}R_e = 1.37353R_0 = 5.3109\ \text{Å} \quad (51b)$$

the experimental value[10] at 0 K.

C. Cohesive Energy. Substituting (51) into (50) leads to

$$U_{\mathrm{tot}}(R_e) = -\frac{1}{2}ND_0\frac{p_6{}^2}{p_{12}} \quad (52)$$

so that the cohesive energy (per atom) is

$$U_{\mathrm{coh}} = 8.6102D_0 \quad (53)$$

This leads to $U_{\mathrm{coh}} = 2.0244$ kcal/mol (of atoms), the experimental heat of vaporization at 0 K (after correcting for zero point energy).[11]

(9) Calculations optimizing the cell parameters and internal coordinates of crystals were carried out using the PolyGraf polymer simulation program from Molecular Simulations, Inc. (BioDesign Division), Pasadena, CA 91101.

(10) Donohue, J. *Structures of the Elements*; R. E. Krieger Publishing Co., Malabar, FL, 1982. For argon, $A = 5.3109$ Å at 0 K.

(11) Hultgren, R.; et al. *Selected Values of the Thermodynamic Properties of the Elements*; American Society for Metals: Metals Park, OH, 1973. For argon, $\Delta H_v = 1.848$ kcal/mol at 0 K. Estimating the zero point energy as 0.1764 kcal/mol (from our calculations) leads to $U_{\mathrm{coh}} = 2.0244$ kcal/mol

TABLE IV: Number of Terms in the Sum for Given Ewald (η) and Accuracy (δ) Parameters

(a) Electrostatic Sum

		NaCl				polyethylene			
η, Å	δ_Q, kcal/mol	R_{cut}, Å	H_{cut}, Å^{-1}	real terms	recip terms[a]	R_{cut}, Å	H_{cut}, Å^{-1}	real terms	recip terms[a]
1.5	10^{-2}	4.645	4.568	72	7168	4.226	4.090	212	7128
1.5	10^{-3}	5.152	4.983	104	10192	4.773	4.549	344	9372
1.5	10^{-4}	5.617	5.366	104	12880	5.269	4.964	468	11088
2.5	10^{-2}	8.127	2.683	296	1568	7.460	2.394	1264	924
2.5	10^{-3}	8.938	2.934	512	2240	8.332	2.670	1748	1584
2.5	10^{-4}	9.686	3.173	608	2576	9.126	2.922	2342	2904
3.5	10^{-2}	11.721	1.891	1088	504	10.814	1.678	3820	528
3.5	10^{-3}	12.828	2.073	1328	728	11.999	1.879	5322	660
3.5	10^{-4}	13.852	2.243	1616	896	13.084	2.061	6824	660

(b) Dispersion Sum

		NaCl				polyethylene			
η, Å	δ_{disp}, kcal/(mol Å)	R_{cut}, Å	H_{cut}, Å^{-1}	real terms	recip terms[a]	R_{cut}, Å	H_{cut}, Å^{-1}	real terms	recip terms[a]
1.5	10^{-3}	4.819	5.089	72	10864	4.867	5.001	372	11880
1.5	10^{-4}	5.304	5.485	104	13552	5.348	5.410	480	16104
1.5	10^{-5}	5.752	5.856	104	17304	5.793	5.787	628	20328
2.5	10^{-3}	7.453	2.695	296	1568	7.539	2.639	1302	1584
2.5	10^{-4}	8.310	2.966	296	2240	8.387	2.915	1816	2376
2.5	10^{-5}	9.096	3.217	512	2576	9.168	3.167	2390	3432
3.5	10^{-3}	9.872	1.740	608	504	9.997	1.690	3066	528
3.5	10^{-4}	11.122	1.954	896	728	11.235	1.910	4326	660
3.5	10^{-5}	12.262	2.143	1232	728	12.366	2.105	5854	660

[a] The number of atom pairs in the sum.

D. Bulk Modulus. The bulk modulus, a measure of the stiffness of the crystal, is defined by

$$B = -V\frac{dP}{dV} = V\frac{d^2U_{tot}}{dV^2} \tag{54}$$

Writing the volume of the crystal as $V = NR^3/2^{1/2}$, we have

$$U_{tot}(V) = \frac{b_{12}}{V^4} - \frac{b_6}{V^2} \tag{55}$$

where $b_{12} = (1/8)p_{12}N^5D_0R_0^{12}$ and $b_6 = (1/2)p_6N^3D_0R_0^6$. The equilibrium volume is $V_e = (1/2^{1/2})NR_0^3(p_{12}/p_6)^{1/2}$, leading to

$$B = \frac{20b_{12}}{V_e^5} - \frac{6b_6}{V_e^3} = 2^{1/2}\frac{b_6^{5/2}}{b_{12}^{3/2}} = 4(2^{1/2})\left(\frac{p_6^{5/2}}{p_{12}^{3/2}}\right)\left(\frac{D_0}{R_0^3}\right) = 106.328\left(\frac{D_0}{R_0^3}\right) \tag{56}$$

E. Elastic Constants. The elastic constants have the form[8]

$$C_{11} = \frac{2}{V_e}\sum_L\left[\frac{d^2U}{d(R^2)^2}\right]_L x_L^4 \tag{57a}$$

and

$$C_{12} = \frac{2}{V_e}\sum_L\left[\frac{d^2U}{d(R^2)^2}\right]_L x_L^2y_L^2 \tag{57b}$$

(For a two-body potential such as (49), the shear constant C_{44} is equal to C_{12}.) This leads to

$$C_{11} = 96(2^{1/2})\left(\frac{D_0}{R_0^3}\right)\left(\frac{p_6}{p_{12}}\right)^{3/2}\left[56\left(\frac{p_6}{p_{12}}\right)s_{1,8} - 4s_{1,5}\right] \tag{58a}$$

$$C_{12} = 96(2^{1/2})\left(\frac{D_0}{R_0^3}\right)\left(\frac{p_6}{p_{12}}\right)^{3/2}\left[56\left(\frac{p_6}{p_{12}}\right)s_{2,8} - 4s_{2,5}\right] \tag{58b}$$

where lattice sum constants $s_{1,m}$ and $s_{2,m}$ are given by

$$s_{1,m} = \sum_l \frac{l_1^4}{(l_1^2 + l_2^2 + l_3^2)^m} \tag{59}$$

$$s_{2,m} = \sum_l \frac{l_1^2l_2^2}{(l_1^2 + l_2^2 + l_3^2)^m} \tag{60}$$

Here the sum is over all integer values of l_1, l_2, l_3 where $l_1 + l_2 + l_3$ must be even. The constants $s_{1,8} = 0.031\,840\,01$, $s_{2,8} = 0.015\,673\,32$, $s_{1,5} = 0.320449$, and $s_{2,5} = 0.140\,899$ were obtained by numerical computations. The result is

$$C_{11} = 148.762\left(\frac{D_0}{R_0^3}\right)$$

$$C_{12} = C_{44} = 85.123\left(\frac{D_0}{R_0^3}\right)$$

The Poisson ratio σ for this cubic system

$$\sigma = -\frac{e_2}{e_1} = \frac{C_{12}}{C_{11} + C_{12}} = 0.3640 \tag{61}$$

is independent of R_0 and D_0.

If D_0 is expressed in kcal/mol and R_0 is expressed in Å, then a conversion factor of 6.947 80 is needed to obtain pressures in GPa. Thus the above expressions lead to

$$C_{11} = 4.2031 \text{ GPa}$$

$$C_{12} = 2.4051 \text{ GPa}$$

and

$$B = \frac{1}{3}(C_{11} + 2C_{12}) = 3.0044 \text{ GPa}$$

These can be compared to the experimental values at 0 K of[12]

$$C_{11} = 4.0 \text{ GPa}$$

$$C_{12} = 2.0 \text{ GPa}$$

$$C_{44} = 2.0 \text{ GPa}$$

F. Results. In Table VI we compare the results of optimizing the unit cell parameters of Ar with various ways of carrying out the lattice sums (all of which used periodic boundary conditions). In these calculations we used conjugate gradient minimization to optimize both cell parameters and atomic coordinates inside

(12) Meixner, H.; Leideren, P.; Berberich, P.; Lüscher, E. *Phys. Lett. A* **1972**, *40*, 257.

TABLE V: Dependence of Timing on Choice of η for Orthorhombic Poly(oxymethylene)[a]

(a1) Electrostatic Sum. δ_Q = 0.001 kcal/mol. Equation 10 is used. Use of $\delta_Q = 10^{-5}$ kcal/mol leads to E = −51.19144 kcal/mol.

η, Å	E, kcal/mol	N_{real}	N_{rec}	t_{real}/t_{recip}	t_{est}	t_{calc}, s
1.0	−51.1916	116	92160	8.3	23156	7.38
1.5	−51.1914	443	27360	6.9	7283	2.25
2.0	−51.1916	1154	10320	4.4	3734	1.08
2.25	−51.1915	1656	6720	5.9	3336	1.11
2.5	−51.1915	2306	4800	5.1	3506	1.13
3.0	−51.1914	4232	2880	4.6	4952	1.47
3.5	−51.1915	6928	1440	4.3	7288	2.02
4.0	−51.1914	10830	960	3.9	11070	2.67
4.5	−51.1914	15795	480	4.4	15915	4.35
5.0	−51.1914	22136	480	4.0	22256	5.55

(a2) Electrostatic Sum. δ_Q = 0.001 kcal/mol. Equation 11 is used.

η, Å	E, kcal/mol	N_{real}	N_{rec}	t_{real}/t_{recip}	t_{est}	t_{calc}, s
0.75	−51.1919	36	61312	35.3	6168	3.10
1.0	−51.1916	116	24576	13.6	2573	1.32
1.25	−51.1915	234	12608	12.7	1494	0.74
1.5	−51.1914	443	7296	12.1	1172	0.57
1.75	−51.1914	741	4160	8.5	1157	0.49
2.0	−51.1916	1154	2752	7.3	1429	0.50
2.25	−51.1915	1656	1792	9.4	1835	0.75
2.5	−51.1915	2306	1280	7.8	2434	0.86
3.0	−51.1914	4232	768	7.8	4308	1.32

(b) Dispersion Sum. $\delta_{disp} = 10^{-4}$ kcal/mol. Use of $\delta_{disp} = 10^{-5}$ kcal/mol leads to E = −8085.194 05 kcal/mol.

η, Å	E, kcal/mol	N_{real}	N_{rec}	t_{real}/t_{recip}	t_{est}	t_{calc}, s
1.0	−8085.1939	440	416760	6.6	104630	33.93
1.5	−8085.1939	1479	104880	4.0	27699	8.39
2.0	−8085.1940	3209	35880	2.6	12179	3.17
2.25	−8085.1940	4261	23736	3.8	10195	1.78
2.5	−8085.1939	5656	15456	3.2	9520	2.29
3.0	−8085.1940	9136	8832	3.1	11344	2.41
3.5	−8085.1940	13741	4416	2.8	14845	2.83
4.0	−8085.1940	19501	2208	2.5	20053	3.15
4.5	−8085.1940	26581	1104	2.5	26857	4.04
5.0	−8085.1940	34738	552	2.7	34876	6.03

[a] E is the energy, N_{real} and N_{rec} are the numbers of terms in the real space and reciprocal space sums, t_{real}/t_{recip} is the actual ratio of calculation time per term for real and reciprocal space, t_{est} is the estimated relative time, and t_{calc} is the actual calculation time. The estimated relative time is calculated from $N_{real} + N_{rec}/m$, where m = 4 in (a1) and (b) and m = 10 in (a2).

the cell.[9] In each case the final root mean square (RMS) force per atomic degree of freedom is less than 0.001 kcal/mol, and the RMS stress for the six cell parameters is less than 0.0001 kcal/mol.

Using traditional distance cutoffs with R_{cut} = 9 Å leads to an error in the lattice constant of 0.006 Å or 0.1%, an error in the cohesive energy of 0.68 kcal/mol (of cells) or 8.4%, and an error in the bulk modulus of 0.09 GPa or 3.0%.

In the Ewald calculations, we evaluated the repulsive terms by using direct sums and used the error bounding procedures of section IV.B with several energy criteria, where $\delta_Q = 10\delta_v$. We also carried out calculations as a function of strain by introducing a finite strain to the system, optimizing the atomic coordinates, and calculating the stresses.[9] The highly repulsive nature of the atomic interactions for short R (due to the Pauli principle that requires orthogonalization of the overlapping atomic orbitals) leads to a quite nonlinear stress–strain relation. Using the stress versus strain results for small strains (±0.005, ±0.01), we obtained numerical estimates of C_{11} and C_{12} to compare with the analytic values. The results agreed to two decimal places in each case.

VI. Application to NaCl Crystal

As a test case for the Ewald Coulomb sum formula, we will calculate the structure and properties of NaCl crystal analytically and compare with those obtained by using the lattice sums.

A. Model. For the atom–atom interactions, we use the form

$$U_{ij} = \lambda e^{-R/\rho} - \frac{q^2}{R} \quad \text{(nearest neighbors)} \qquad (62)$$

$$\pm \frac{q^2}{P_{ij}R} \quad \text{(otherwise)}$$

The total energy E_{tot} (relative to free ions) is given by[7]

$$E_{tot}(R) = N\left(z\lambda e^{-R/\rho} - \frac{\alpha q^2}{R}\right) \qquad (63)$$

Here R is the nearest neighbor distance, N = 4 is the number of pairs of NaCl atoms in the unit cell, and z = 6 is the number of nearest neighbors. The Madelung constant is α = 1.747 565, while unit charges on each ion lead to q^2 = 332.0647 Å kcal/mol (allowing R to be in Å and E in kcal/mol).

B. Parameters. We will choose the parameters λ and ρ in (62) to obtain the experimental lattice constant[13]

$$A = 5.578 \text{ Å}$$

and cohesive energy[13]

$$E_{tot}(R_e) = -740.0 \text{ kcal/mol}$$

at 0 K.

The equilibrium nearest neighbor distance $R_e = (1/2)A_e$ is obtained by requiring that $\partial E_{tot}/\partial R = 0$, leading to

$$R_e^2 e^{-R_e/\rho} = \frac{\rho\alpha q^2}{z\lambda} \qquad (64)$$

Substituting R_e into (63) leads to

$$E_{tot}(R_e) = -\frac{N\alpha q^2}{R_e}\left(1 - \frac{\rho}{R_e}\right) \qquad (65)$$

Using these results leads to

$$\rho = 0.309\,223 \text{ Å}$$

$$\lambda = 3.84485e^{R_e/\rho} = 31\,765.8 \text{ kcal/mol}$$

C. Bulk Modulus and Elastic Constants. The volume of the crystal V is given by $V = 2NR^3$; hence

$$E_{tot}(V) = N\left(z\lambda \exp\left[-\left(\frac{V}{2N}\right)^{1/3}/\rho\right] - \left(\frac{2N}{V}\right)^{1/3}\alpha q^2\right) \qquad (66)$$

Using eq 54, we have

$$B = \left(V\frac{d^2E_{tot}}{dV^2}\right)_{V_e} = \frac{\alpha q^2}{18R_e^3}\left(\frac{1}{\rho} - \frac{2}{R_e}\right) = 25.9858 \text{ GPa} \qquad (67)$$

where the equilibrium volume V_e is $2NR_e^3$ and the conversion factor 1 kcal/(mol Å^3) = 6.947 80 GPa was used. This can be compared with the experimental value of[13] 26.60 GPa.

Since each atom in the NaCl crystal is at a point of inversion symmetry, no internal strain is induced when external stress is applied. Hence, the two independent elastic constants are given by

$$C_{11} = \frac{\alpha q^2}{zR_e^4}\left(\frac{R_e}{\rho} - 1\right) + \frac{1}{V_e}\frac{\partial^2 S_1}{\partial e_1 \partial e_1} \qquad (68)$$

$$C_{12} = \frac{1}{V_e}\frac{\partial^2 S_1}{\partial e_1 \partial e_2} \qquad (69)$$

where e_1 and e_2 are strains (XX and YY components) and the first term in C_{11} arises from the repulsive part of the potential. The lattice sums for the second partial derivatives of the elec-

(13) (a) Sangster, M. J. L.; Schröder, U.; Atwood, R. M. *J. Phys. C* **1978**, *11*, 1523. (b) Sangster, M. J. L.; Atwood, R. M. *J. Phys. C* **1978**, *11*, 1541.

TABLE VI: Equilibrium Properties of Argon Crystal (Using Four Atoms per Cell)

			Ewald			direct summation		
	exper[a]	exact	0.00001[b]	0.001[b]	0.01[b]	9 Å[c]	15 Å[c]	30 Å[c]
A, Å	5.3109	5.3109	5.3109	5.3108	5.3090	5.3172	5.3176	5.3111
U, kcal/mol	−8.0975	−8.0976	−8.0970	−8.0981	−8.1171	−7.4202	−7.9756	−8.0830
B, GPa	2.67	3.0044	3.0044	3.0054	3.0164	3.0940	2.9482	3.0050
C_{11}, GPa	4.0	4.2031	4.2031	4.2048	4.2216	4.4123	4.1309	4.2052
C_{12}, GPa	2.0	2.4051	2.4051	2.4057	2.4138	2.4348	2.3569	2.4049
C_{44}, GPa	2.0	2.4051	2.4051	2.4057	2.4138	2.4348	2.3569	2.4049
σ	0.32	0.364	0.3640	0.3639	0.3638	0.3556	0.3633	0.3638
time,[d] s			0.171	0.143	0.084	0.045	0.124	0.866
pairs R space[d]			120	72	24	120	480	4320
pairs K space[d]			480	336	156			

[a] See ref 10 (A), 11 (U), and 12 (C_{11}, C_{12}, and C_{44}). [b] Accuracy parameters in kcal/mol. [c] Cutoff distances (R_{cut}). Using a cubic spline function to decrease the potential from full value at R_{cut} −1 Å to zero at R_{cut} −0.5 Å. [d] Only attractive terms are considered.

trostatic energy with respect to the strain components converge very slowly, requiring Ewald sums. By using (22), we have

$$\frac{\partial^2 S_1}{\partial e_1 \partial e_1} = \frac{1}{2\eta^5}\sum_{L,i,j} Q_{ij}\left\{\left[\frac{3\ \mathrm{erfc}\ (a)}{a^5} + \frac{6\pi^{-1/2}e^{-a^2}}{a^4} + \frac{4\pi^{-1/2}e^{-a^2}}{a^2}\right]\times (\mathbf{r}_i - \mathbf{r}_j - \mathbf{R}_L)_1^4 - 2\eta^2\left[\frac{\mathrm{erfc}\ (a)}{a^3} + \frac{2\pi^{-1/2}e^{-a^2}}{a^2}\right]\times (\mathbf{r}_i - \mathbf{r}_j - \mathbf{R}_L)_1^2\right\} + \frac{2\pi}{\Omega}\sum_{\mathbf{h}}{}' S(\mathbf{h})S(-\mathbf{h})\times \left[\frac{e^{-b^2}}{h^2}\left(1 - 8\frac{(1+b^2)}{h^2}\mathbf{h}_1^2\right) + \frac{4\mathbf{h}_1^4 e^{-b^2}}{h^6}\left(2 + \frac{h^2\eta^2}{2} + \frac{h^4\eta^4}{16}\right)\right] \tag{70}$$

$$\frac{\partial^2 S_1}{\partial e_1 \partial e_2} = \frac{1}{2\eta^5}\sum_{L,i,j} Q_{ij}\left[\frac{3\ \mathrm{erfc}\ (a)}{a^5} + \frac{6\pi^{-1/2}e^{-a^2}}{a^4} + \frac{4\pi^{-1/2}e^{-a^2}}{a^2}\right]\times (\mathbf{r}_i - \mathbf{r}_j - \mathbf{R}_L)_1^2(\mathbf{r}_i - \mathbf{r}_j - \mathbf{R}_L)_2^2 + \frac{2\pi}{\Omega}\sum_{\mathbf{h}}{}' S(\mathbf{h})S(-\mathbf{h})\left[\frac{e^{-b^2}}{h^2}\left(1 - 2\frac{(1+b^2)}{h^2}(\mathbf{h}_1^2 + \mathbf{h}_2^2)\right) + \frac{4\mathbf{h}_1^2\mathbf{h}_2^2 e^{-b^2}}{h^6}\left(2 + \frac{h^2\eta^2}{2} + \frac{h^4\eta^4}{16}\right)\right] \tag{71}$$

In this model, $C_{44} = C_{12}$. The calculations of these sums give

$$C_{11} = 51.4366 \text{ GPa}$$

$$C_{12} = C_{44} = 13.2598 \text{ GPa}$$

$$B = \frac{1}{3}(C_{11} + 2C_{12}) = 25.9854 \text{ GPa}$$

while the Poisson ratio (61) is

$$\sigma = 0.2050$$

D. Result. In Table VII, we show the results of optimizing the unit cell parameters of NaCl with three different accuracy parameters.

TABLE VII: Equilibrium Properties of NaCl Crystal (Using Four Molecules per Cell)

			Ewald		
	exper[a]	exact	0.1[b]	0.01[b]	0.001[b]
A, Å	5.578	5.5780	5.5776	5.5776	5.5780
U, kcal/mol	−740.0	−740.00	−739.9938	−740.0184	−739.9985
B, GPa	26.60	25.9858	25.97	25.963	25.9854
C_{11}, GPa	57.33		51.46	51.433	51.4366
C_{12}, GPa	11.23		13.23	13.228	13.2598
C_{44}, GPa	13.31		13.23	13.228	13.2598
σ	0.164		0.205	0.205	0.2050

[a] See ref 13. [b] Accuracy parameters in kcal/mol.

VII. Summary and Discussion

Using Ewald-inspired approximations for accelerated convergence of lattice sums, we developed and tested equations for the energies, forces, stresses, and second derivatives for both electrostatic ($1/R$) and dispersion ($1/R^6$) lattice sums. In addition, we developed an approach for estimating the convergence parameter η in order to minimize the computation time while retaining a fixed level of accuracy.

With these accuracy specification procedures, the costs of carrying out accurate lattice sums is less than that for normal direct sums (at the same level of accuracy) despite the more complicated formulas for accelerated convergence.

We suggest that these procedures may also prove equally valuable for biological systems. A molecule such as hemoglobin with ~6000 atoms would lead to 18 000 000 pairwise interactions, which are truncated to ~500 000 by using energy cutoffs of 9 Å. We suspect that such cutoffs lead to errors in the Coulomb interactions similar to those shown for NaCl. By considering the hemoglobin to be in a unit cell sufficiently large that interactions between cells is small, one could use the Ewald procedures to generate a given level of accuracy. This approach would be especially valuable for including explicit solvent (water) in the calculation. Water has large charges (0.4 e on each H and −0.8 e on O) so that use of a finite solvent shell leads to very large surface effects. With a periodic cell containing Hb and H_2O, one could eliminate surface effects while obtaining accurate energies.

Acknowledgment. This work was partially supported by a grant from Imperial Chemical Industries, Cleveland, England, and by a grant from the Air Force Office of Scientific Research (No. AFOSR-88-0051). We thank Molecular Simulation, Inc. (Biodesign, Inc.), Pasadena, CA for use of the PolyGraf polymer simulation program.

Registry No. NaCl, 7647-14-5.

Chapter II

Calculations of Crystal Properties in Molecular Mechanics

Abstract

Various equations used in the calculations of crystal properties are derived and summarized. Equations to calculate elastic constants and related properties in molecular mechanics are derived in (a). Equations for piezoelectric constants and dielectric constants are derived in (b). Equations for phonon frequencies and thermodynamic properties are summarized in (c). In (d), complete equations of the Ewald second derivatives including a dynamical matrix are shown. In this section, equations for elastic constants, piezoelectric constants, and dielectric constants derived in previous sections are compared with those obtained by the methods of long waves by Born and Huang, and equivalences are shown when force and stress are zero.

(a) Elastic Constants

Consider a crystal under external strain at zero macroscopic field. After atomic positions are equilibrated, all force components become zero, and the energy of the crystal per unit cell (E_t) can be expanded in terms of strain and stress up to the second order as

$$E_t = E_0 + \Omega\,(e_1 \ldots e_6) \begin{pmatrix} \sigma_1 \\ \vdots \\ \sigma_6 \end{pmatrix} + \frac{\Omega}{2}\,(e_1 \ldots e_6)\,c \begin{pmatrix} e_1 \\ \vdots \\ e_6 \end{pmatrix}, \qquad (a-1)$$

where Ω is volume of the cell, e_i is a strain component, σ_i is a stress component and c is an elastic stiffness matrix (6×6). E_0 is a constant.

The energy is determined by $3N-3$ components of atomic coordinates $r_{i\alpha}$ (N is a number of atoms) and 6 strain components e_i. This is because we can always fix one atom at an origin and eliminate three degrees of freedom by using translational symmetry ($i = 2 \ldots N$). By expanding the energy again about the equilibrium structure (zero force), using the derivatives of energy with respect to coordinates and strain, we have up to the second order,

$$E_t = E_0 + (e_1 \ldots e_6) \begin{pmatrix} \Pi_1 \\ \vdots \\ \Pi_6 \end{pmatrix} + \frac{1}{2}\,(e_1 \ldots e_6)\,Wee \begin{pmatrix} e_1 \\ \vdots \\ e_6 \end{pmatrix} + (e_1 \ldots e_6)\,Wer \begin{pmatrix} \delta r_{21} \\ \vdots \\ \delta r_{N3} \end{pmatrix}$$

$$+\frac{1}{2}\,(\delta r_{21} \ldots \delta r_{N3})\,Wrr \begin{pmatrix} \delta r_{21} \\ \vdots \\ \delta r_{N3} \end{pmatrix}. \qquad (a-2)$$

Here,

$$\Pi_i = \frac{\partial E_t}{\partial e_i} \qquad (a-3)$$

$$[Wee]_{i,j} = \frac{\partial^2 E_t}{\partial e_i \partial e_j} \qquad (a-4)$$

$$[\mathrm{Wer}]_{i,j\alpha} = \frac{\partial^2 E_t}{\partial e_i \partial r_{j\alpha}} \qquad (a-5)$$

$$[\mathrm{Wrr}]_{i\alpha,j\beta} = \frac{\partial^2 E_t}{\partial r_{i\alpha} \partial r_{j\beta}}. \qquad (a-6)$$

In molecular-mechanics calculations, the energy expression is given in terms of coordinates of atoms, and the total energy is usually the sum of 2-body, 3-body and 4-body terms. Given the energy expression, it is straightforward to evaluate these derivatives. The derivative of energy with respect to the strain component can be converted to those of coordinates by using the following relation[1],

$$\frac{\partial r_{k\alpha}}{\partial e_{ij}} = \frac{1}{2}\delta_{j\alpha} r_{ki} + \frac{1}{2}\delta_{i\alpha} r_{kj}, \qquad (a-7a)$$

where e_{ij} is a strain component expressed in terms of two indices and the correspondence is $1 \rightarrow 11$, $2 \rightarrow 22$, $3 \rightarrow 33$, $4 \rightarrow 23$, $5 \rightarrow 31$, and $6 \rightarrow 12$. By using this relation, we have, for example,

$$\frac{\partial E}{\partial e_{ij}} = \sum_{k,\alpha} \frac{\partial E}{\partial r_{k\alpha}} \left(\frac{1}{2}\delta_{j\alpha} r_{ki} + \frac{1}{2}\delta_{i\alpha} r_{kj} \right). \qquad (a-7b)$$

Although straightforward, the second derivatives of energy with respect to strain for 3-body and 4-body terms are quite lengthy. In an actual programming, symbolic derivative programs for these terms were written and FORTRAN source codes were generated directly to avoid typing errors.

In (a-2), $\delta r_{i\alpha}$ is a small deviation from an equilibrium geometry of coordinate of atom i in the α direction. Since force is zero, we take a partial derivative of the energy with respect to coordinates and equate this to be zero. Thus, we have

$$\frac{\partial E}{\partial r_{i\alpha}} = (e_1 \ldots e_6) \begin{pmatrix} \mathrm{Wer}_{1,i\alpha} \\ \vdots \\ \mathrm{Wer}_{6,i\alpha} \end{pmatrix} + (\mathrm{Wrr}_{i\alpha,21} \ldots \mathrm{Wrr}_{i\alpha,N3}) \begin{pmatrix} \delta r_{21} \\ \vdots \\ \delta r_{N3} \end{pmatrix} = 0. \qquad (a-8a)$$

This equation shows the balance of two forces; one arising from the strain, and the other arising from the displacement of atoms. By solving this equation, we have

$$\delta \mathbf{r} = -\mathrm{Wrr}^{-1}\mathrm{Wer}^{\dagger}\mathbf{e}, \qquad (\mathrm{a}-8\mathrm{b})$$

where

$$\mathbf{e} = \begin{pmatrix} e_1 \\ \vdots \\ e_6 \end{pmatrix}, \qquad (\mathrm{a}-8\mathrm{c})$$

$$\delta \mathbf{r} = \begin{pmatrix} \delta r_{21} \\ \vdots \\ \delta r_{N3} \end{pmatrix}. \qquad (\mathrm{a}-8\mathrm{d})$$

By inserting (a-8) in (a-2), we have

$$\begin{aligned} \mathrm{E_t} &= \mathrm{E_0} + \mathbf{e}^{\dagger}\mathbf{\Pi} + \frac{1}{2}\mathbf{e}^{\dagger}\mathrm{Wee}\ \mathbf{e} + \mathbf{e}^{\dagger}\mathrm{Wer}\delta\mathbf{r} + \frac{1}{2}\delta\mathbf{r}^{\dagger}\mathrm{Wrr}\delta\mathbf{r} \\ &= \mathrm{E_0} + \mathbf{e}^{\dagger}\mathbf{\Pi} + \frac{1}{2}\mathbf{e}^{\dagger}\left(\mathrm{Wee} - \mathrm{WerWrr}^{-1}\mathrm{Wer}^{\dagger}\right)\mathbf{e}. \end{aligned} \qquad (\mathrm{a}-9)$$

Comparing this equation with (a-1), we obtain stress and an elastic stiffness constant as,

$$\sigma_{\mathrm{i}} = \frac{1}{\Omega}\Pi_{\mathrm{i}} \qquad (\mathrm{a}-10)$$

$$\mathrm{c} = \frac{1}{\Omega}\left(\mathrm{Wee} - \mathrm{WerWrr}^{-1}\mathrm{Wer}^{\dagger}\right). \qquad (\mathrm{a}-11)$$

It is straightforward to show that this is equivalent to the result by Born and Huang[2] by using the method of long waves (see (d) in this chapter).

An elastic compliance matrix s is given by

$$\mathrm{s} = \mathrm{c}^{-1}. \qquad (\mathrm{a}-12)$$

The volume compressibility B can be obtained[3] by considering the hydrostatic pressure p. The stress is given by

$$\sigma_{kl} = -p\delta_{kl}. \qquad (a-13)$$

Here, δ is the Kronecker's delta function. The strain is given by

$$e_{ij} = -p\sum_{k,l} s_{ij,kl}\delta_{kl} = -p\sum_{k} s_{ij,kk}. \qquad (a-14)$$

Dilation Δ is given by

$$\Delta = \sum_{i} e_{ii} = -p\sum_{i,k} s_{ii,kk}. \qquad (a-15)$$

From these equations, we have

$$B = -\frac{\Delta}{p} = \sum_{i,k} s_{ii,kk}. \qquad (a-16)$$

Bulk modulus κ is given by

$$\kappa = \frac{1}{B}. \qquad (a-17)$$

The elastic wave velocities are calculated[3] by solving an equation of motion for small displacement u_i

$$\rho\frac{d^2u_i}{dt^2} = \sum_{j}\frac{\partial\sigma_{ij}}{\partial x_j} = \sum_{j,l,m} c_{ij,lm}\frac{\partial^2 u_m}{\partial x_j \partial x_l}, \qquad (a-18)$$

where ρ is density of the crystal. By assuming a solution of the form

$$u_i = u_{i0}e^{i(\mathbf{k}\cdot\mathbf{r}-\omega t)}, \qquad (a-19)$$

it can be shown that the frequency ω is given by solving the following equation,

$$\left| \sum_{j,l} c_{ij,lm} k_j k_l - \rho \omega^2 \delta_{im} \right| = 0. \qquad (a-20)$$

Here $\mathbf{k}$ is the wave vector. By writing $\omega = vk$, v is the speed of sound, the above equation becomes

$$\left| \sum_{j,l} c_{ij,lm} \hat{k}_j \hat{k}_l - \rho v^2 \delta_{im} \right| = 0, \qquad (a-21)$$

where $\hat{k}_l$ is a component of a unit vector in the direction of the wave vector. The solution of this equation gives three sound velocities for a given wave-vector direction $\hat{\mathbf{k}}$.

(b) Piezoelectric Constants and Dielectric Constants

We write small changes of stress (σ_{ij}) and polarization (P_i) as functions of strain (e_{kl}) and macroscopic electric field (E_m) as follows;

$$d\sigma_{ij} = \sum_{k,l} \left(\frac{\partial \sigma_{ij}}{\partial e_{kl}}\right)_{E_m} de_{kl} + \sum_{m} \left(\frac{\partial \sigma_{ij}}{\partial E_m}\right)_{e_{kl}} dE_m, \qquad (b-1)$$

$$dP_i = \sum_{k,l} \left(\frac{\partial P_i}{\partial e_{kl}}\right)_{E_m} de_{kl} + \sum_{m} \left(\frac{\partial P_i}{\partial E_m}\right)_{e_{kl}} dE_m. \qquad (b-2)$$

The change of internal energy per unit volume is given by

$$dU = \sum_{i,j} \sigma_{ij} de_{ij} + \frac{1}{4\pi} \sum_{k} E_k dD_k + TdS. \qquad (b-3)$$

Here, D_k is the electric displacement, T is the temperature and S is the entropy. By defining the Helmholtz free energy F

$$F = U - \frac{1}{4\pi} \sum_{k} E_k D_k - TS, \qquad (b-4)$$

we have

$$dF = \sum_{i,j} \sigma_{ij} de_{ij} - \frac{1}{4\pi} \sum_{k} D_k dE_k - SdT. \qquad (b-5)$$

At constant temperature,

$$dF = \sum_{i,j} \left(\frac{\partial F}{\partial e_{ij}}\right)_{E_k} de_{ij} + \sum_{k} \left(\frac{\partial F}{\partial E_k}\right)_{e_{ij}} dE_k. \qquad (b-6)$$

By comparing this equation with the above, we have

$$\sigma_{ij} = \left(\frac{\partial F}{\partial e_{ij}}\right)_{E_k}, \qquad (b-7)$$

$$-\frac{1}{4\pi} D_k = \left(\frac{\partial F}{\partial E_k}\right)_{e_{ij}}. \qquad (b-8)$$

From these equations, we have

$$\frac{\partial^2 F}{\partial e_{ij}\partial E_k} = \left(\frac{\partial \sigma_{ij}}{\partial E_k}\right)_{e_{ij}} = -\frac{1}{4\pi}\left(\frac{\partial D_k}{\partial e_{ij}}\right)_{E_k} = -\left(\frac{\partial P_k}{\partial e_{ij}}\right)_{E_k}. \qquad (b-9)$$

For small strain and field, we integrate (b-1) and (b-2):

$$\sigma = ce - g^{\dagger}\mathbf{E}, \qquad (b-10)$$

$$\mathbf{P} = ge + a\mathbf{E}, \qquad (b-11)$$

where c is an elastic stiffness matrix, g is a piezoelectric constant and a is a dielectric susceptibility constant. From (b-1),(b-2), and (b-9) we have

$$c_{ij,kl} = \left(\frac{\partial \sigma_{ij}}{\partial e_{kl}}\right)_{E_k}, \qquad (b-12)$$

$$g_{k,ij} = \left(\frac{\partial P_k}{\partial e_{ij}}\right)_{E_k} = -\left(\frac{\partial \sigma_{ij}}{\partial E_k}\right)_{e_{ij}}, \qquad (b-13)$$

$$a_{ij} = \left(\frac{\partial P_i}{\partial E_j}\right)_{e_{kl}}. \qquad (b-14)$$

Piezoelectric constants g can be obtained by considering the change of polarizability when the system is strained. Since displacement of atoms that is due to the strain is given by (a-8), we have the polarization as follows,

$$P_\beta = \frac{1}{\Omega}\sum_i q_i \delta r_{i\beta} = -\frac{1}{\Omega}\sum_i q_i \sum_{\alpha,\gamma}[Wrr^{-1}Wer^{\dagger}]_{i\beta,\alpha\gamma}e_{\alpha\gamma}. \qquad (b-15)$$

Therefore,

$$g_{\beta,\alpha\gamma} = -\frac{1}{\Omega}\sum_i q_i \sum_{\alpha,\gamma}[Wrr^{-1}Wer^{\dagger}]_{i\beta,\alpha\gamma}. \qquad (b-16)$$

Dielectric susceptibility constants are obtained by considering a change of the polarization when a macroscopic field is applied. After applying the macroscopic field, the force at each atom becomes zero, giving

$$\delta \mathbf{r_i} = \sum_j [\mathrm{Wrr}^{-1}]_{i,j} q_j \mathbf{E}. \qquad (b-17)$$

Polarization is given by

$$\mathbf{P} = \frac{1}{\Omega} \sum_i q_i \delta \mathbf{r_i} = \frac{1}{\Omega} \sum_{i,j} q_i q_j [\mathrm{Wrr}^{-1}]_{i,j} \mathbf{E}. \qquad (b-18)$$

Therefore the dielectric susceptibility matrix (3×3) is

$$a = \frac{1}{\Omega} \sum_{i,j} q_i q_j [\mathrm{Wrr}^{-1}]_{i,j}. \qquad (b-19)$$

Dielectric constants at constant strain ϵ_e are given by

$$\epsilon_e = 1 + 4\pi a. \qquad (b-20)$$

Instead of (b-1) and (b-2), we can choose the stress and the macroscopic field as independent variables as follows:

$$de_{ij} = \sum_{k,l} \left(\frac{\partial e_{ij}}{\partial \sigma_{kl}} \right)_{E_m} d\sigma_{kl} + \sum_m \left(\frac{\partial e_{ij}}{\partial E_m} \right)_{\sigma_{kl}} dE_m, \qquad (b-21)$$

$$dP_i = \sum_{k,l} \left(\frac{\partial P_i}{\partial \sigma_{kl}} \right)_{E_m} d\sigma_{kl} + \sum_j \left(\frac{\partial P_i}{\partial E_m} \right)_{\sigma_{kl}} dE_m. \qquad (b-22)$$

In this case, by defining the Gibbs free energy G,

$$G = U - \sum_{i,j} \sigma_{ij} e_{ij} - \frac{1}{4\pi} \sum_k E_k D_k - TS, \qquad (b-23)$$

we can show

$$\frac{\partial^2 G}{\partial\sigma_{ij}\partial E_k} = -\left(\frac{\partial e_{ij}}{\partial E_k}\right)_{\sigma_{ij}} = -\frac{1}{4\pi}\left(\frac{\partial D_k}{\partial\sigma_{ij}}\right)_{E_k} = -\left(\frac{\partial P_k}{\partial\sigma_{ij}}\right)_{E_k}. \qquad (b-24)$$

For small stress and field, we can write

$$\mathbf{e} = s\sigma + d^{\dagger}\mathbf{E}, \qquad (b-25)$$

$$\mathbf{P} = d\sigma + b\mathbf{E}, \qquad (b-26)$$

where

$$s_{ij,kl} = \left(\frac{\partial e_{ij}}{\partial\sigma_{kl}}\right)_{E_m}, \qquad (b-27)$$

$$d_{k,ij} = \left(\frac{\partial P_k}{\partial\sigma_{ij}}\right)_{E_k} = \left(\frac{\partial e_{ij}}{\partial E_k}\right)_{\sigma_{ij}}, \qquad (b-28)$$

$$b_{ij} = \left(\frac{\partial P_i}{\partial E_j}\right)_{\sigma_{kl}}. \qquad (b-29)$$

Here, s is an elastic compliance constant, d is the piezoelectric modulus, and b is a dielectric susceptibility constant at constant stress. By comparing the definitions of g and d, we can easily show that

$$d = gs. \qquad (b-30)$$

Also, from (b-25), (b-26), (b-30), and (b-11), we have

$$b = a + gsg^{\dagger} = a + dg^{\dagger}, \qquad (b-31)$$

and in this case, dielectric constants are given by

$$\epsilon_{\sigma} = 1 + 4\pi b. \qquad (b-32)$$

(c) Phonons and Thermodynamic Properties

According to Born and Huang[2], the phonon frequencies are given by diagonalizing a dynamical matrix C,

$$C_{\alpha\beta}\binom{y}{kk'} = \frac{e^{iy\cdot(r_{k'}-r_k)}}{(m_k m_{k'})^{1/2}} \sum_l \Phi_{\alpha\beta}\binom{0\ l}{kk'} e^{iy\cdot R_l}, \qquad (c-1)$$

where m_k is a mass and r_k is a position of an atom k in a unit cell, y is a wave vector, R_l is a lattice translation vector with an index l, and

$$\Phi_{\alpha\beta}\binom{0\ l}{kk'} = \frac{\partial^2\Phi}{\partial r_{0k\alpha}\partial r_{lk'\beta}} \qquad (c-2)$$

is a second derivative of the total potential energy Φ with respect to coordinates of atoms. In the above equation, $r_{lk} = r_k + R_l$.

In molecular-mechanics calculations, we have energy expression in terms of coordinates of atoms, and the total energy is usually the sum of 2-body, 3-body, and 4-body terms. It is straightforward to evaluate second derivatives of these terms. To obtain the dynamical matrix from these second derivatives, we multiply an appropriate phase factor and sum all terms. For an n-body term, we need to sum n^2 terms with different phase factors.

After obtaining the dynamical matrix C, all frequencies $\omega_s(y)$ ($s = 1, \ldots, 3N$, N is a total number of atoms) are given by solving the following equation,

$$\left|C_{\alpha\beta}\binom{y}{kk'} - [\omega_s(y)]^2\delta_{kk'}\delta_{\alpha\beta}\right| = 0. \qquad (c-3)$$

The thermodynamic properties are given by using the harmonic approximation,

$$F = \frac{1}{M}\sum_{y,s}\frac{1}{2}\hbar\omega_s(y) + \frac{1}{\beta M}\sum_{y,s}\ln\left(1 - e^{-\hbar\omega_s(y)\beta}\right), \qquad (c-4)$$

$$S = -\frac{k_B}{M}\sum_{y,s}\ln\left(1-e^{-\hbar\omega_s(y)\beta}\right)+\frac{1}{TM}\sum_{y,s}\frac{\hbar\omega_s(y)}{e^{\hbar\omega_s(y)\beta}-1}, \qquad (c-5)$$

$$U = \frac{1}{M}\sum_{y,s}\frac{1}{2}\hbar\omega_s(y)+\frac{1}{M}\sum_{y,s}\frac{\hbar\omega_s(y)}{e^{\hbar\omega_s(y)\beta}-1}, \qquad (c-6)$$

$$C_v = \frac{k_B}{M}\sum_{y,s}\frac{(\hbar\omega_s(y)\beta)^2 e^{\hbar\omega_s(y)\beta}}{\left(e^{\hbar\omega_s(y)\beta}-1\right)^2}. \qquad (c-7)$$

Here, F is the free energy, S is the entropy, U is the internal energy, and C_v is the specific heat per cell. $\beta = 1/k_BT$ and k_B is the Boltzmann constant. The sum is over all points in the Brillouin zone (M is the number of points in the Brillouin zone used in the calculation) and is over all modes(3N modes for each point in the Brillouin zone). In practice, we use a finite number of points in the Brillouin zone. Because of the inversion symmetry of the dispersion relation, we need to sample only half of the Brillouin zone in the general system. For a crystal with high space-group symmetry, the region in the Brillouin zone which we need to sample can be reduced further. For example, in the calculations of graphite (see Appendix I), only 1/24 of the Brillouin zone is used.

(d) Ewald Second Derivatives

In this section, equations for second derivatives of the Ewald lattice sums are shown in Section 1. Equations for phonon calculations are shown in Section 2. Finally in Section 3, it is shown that derived equations are equivalent to those given by Born and Huang[1], using the method of long waves for various properties.

1. Strain derivatives of Ewald Lattice Sums

The Coulomb lattice sum is given by[1]

$$S_1 = \frac{1}{2\eta}\sum_{L,i,j} Q_{ij}\frac{\mathrm{erfc}(a_{ijL})}{a_{ijL}} + \frac{2\pi}{\Omega}\sum_{\mathbf{h}}{}' S(\mathbf{h})S(-\mathbf{h})h^{-2}e^{-b^2} - \frac{1}{\pi^{1/2}\eta}\left(\sum_i Q_{ii}\right), \quad (d-1a)$$

where $Q_{ij} = (C_{unit}/\epsilon)q_i q_j$, Ω is volume of the unit cell and

$$S(\mathbf{h})S(-\mathbf{h}) = \sum_{i,j} Q_{ij}\cos(\mathbf{h}\cdot(\mathbf{r}_i - \mathbf{r}_j)). \quad (d-1b)$$

C_{unit}=332.0647, if the unit of charge q_i is one electron and that of length is Å. By taking a derivative with respect to strain $e_{\alpha\beta}$ we have

$$\frac{\partial S_1}{\partial e_{\alpha\beta}} = -\frac{1}{2\eta^3}\sum_{L,i,j} Q_{ij}F_1(a_{ijL})x_{ijL\alpha}x_{ijL\beta} - \frac{2\pi}{\Omega}\sum_{\mathbf{h}}{}' S(\mathbf{h})S(-\mathbf{h})\left[H_1(b^2)h_\alpha h_\beta + G_1(b^2)\delta_{\alpha\beta}\right], \quad (d-2a)$$

where

$$F_1(a) = (\mathrm{erfc}(a) + 2\pi^{-1/2}ae^{-a^2})/a^3, \quad (d-2b)$$

$$G_1(b^2) = \frac{\eta^2 e^{-b^2}}{4b^2}, \quad (d-2c)$$

$$H_1(b^2) = -\frac{\eta^4(1+b^2)e^{-b^2}}{8b^4}, \quad (d-2d)$$

$$\mathbf{x}_{ijL} = \mathbf{r}_i - \mathbf{r}_j - \mathbf{R}_L, \quad (d-2e)$$

$$a_{ijL} = |x_{ijL}|/\eta, \qquad (d-2f)$$

$$b = \frac{1}{2}h\eta. \qquad (d-2g)$$

Here $\mathbf{R}_L$ is a cell-translation vector (with an index L) in real space and $\mathbf{h}$ is a cell-translation vector in reciplocal space.

There are 21 second derivatives of energy with respect to strain components, but in the following, terms obtained by a simple permutation of indices are not shown;

$$\frac{\partial^2 S_1}{\partial e_1 \partial e_1} = -\frac{1}{2\eta^3}\sum_{L,i,j} Q_{ij}\left[F_1'\frac{1}{a_{ijL}\eta^2}x_{ijL1}^4 + 2F_1 x_{ijL1}^2\right] + \frac{2\pi}{\Omega}\sum_{\mathbf{h}}{}' S(\mathbf{h})S(-\mathbf{h})\left[\frac{1}{2}\eta^2 h_1^4 H_1' + 4H_1 h_1^2 + G_1\right], \qquad (d-3a)$$

$$\frac{\partial^2 S_1}{\partial e_1 \partial e_2} = -\frac{1}{2\eta^3}\sum_{L,i,j} Q_{ij}\left[F_1'\frac{1}{a_{ijL}\eta^2}x_{ijL1}^2 x_{ijL2}^2\right] + \frac{2\pi}{\Omega}\sum_{\mathbf{h}}{}' S(\mathbf{h})S(-\mathbf{h})\left[\frac{1}{2}\eta^2 h_1^2 h_2^2 H_1' + H_1(h_1^2+h_2^2) + G_1\right], \qquad (d-3b)$$

$$\frac{\partial^2 S_1}{\partial e_1 \partial e_4} = -\frac{1}{2\eta^3}\sum_{L,i,j} Q_{ij}\left[F_1'\frac{1}{a_{ijL}\eta^2}x_{ijL1}^2 x_{ijL2} x_{ijL3}\right] + \frac{2\pi}{\Omega}\sum_{\mathbf{h}}{}' S(\mathbf{h})S(-\mathbf{h})\left[\frac{1}{2}\eta^2 h_1^2 h_2 h_3 H_1' + H_1 h_2 h_3\right], \qquad (d-3c)$$

$$\frac{\partial^2 S_1}{\partial e_1 \partial e_5} = -\frac{1}{2\eta^3}\sum_{L,i,j} Q_{ij}\left[F_1'\frac{1}{a_{ijL}\eta^2}x_{ijL1}^3 x_{ijL3} + F_1 x_{ijL1} x_{ijL3}\right] + \frac{2\pi}{\Omega}\sum_{\mathbf{h}}{}' S(\mathbf{h})S(-\mathbf{h})\left[\frac{1}{2}\eta^2 h_1^3 h_3 H_1' + 2H_1 h_1 h_3\right], \qquad (d-3d)$$

$$\frac{\partial^2 S_1}{\partial e_4 \partial e_4} = -\frac{1}{2\eta^3}\sum_{L,i,j} Q_{ij}\left[F_1'\frac{1}{a_{ijL}\eta^2}x_{ijL2}^2 x_{ijL3}^2 + \frac{F_1}{2}(x_{ijL2}^2 + x_{ijL3}^2)\right]$$
$$+ \frac{2\pi}{\Omega}\sum_{\mathbf{h}}{}' S(\mathbf{h})S(-\mathbf{h})\left[\frac{1}{2}\eta^2 h_2^2 h_3^2 H_1' + \frac{1}{2}H_1(h_2^2 + h_3^2)\right], \qquad (d-3e)$$

$$\frac{\partial^2 S_1}{\partial e_4 \partial e_5} = -\frac{1}{2\eta^3}\sum_{L,i,j} Q_{ij}\left[F_1'\frac{1}{a_{ijL}\eta^2}x_{ijL1}x_{ijL2}x_{ijL3}^2 + \frac{1}{2}F_1 x_{ijL1}x_{ijL2}\right]$$
$$+ \frac{2\pi}{\Omega}\sum_{\mathbf{h}}{}' S(\mathbf{h})S(-\mathbf{h})\left[\frac{1}{2}\eta^2 h_1 h_2 h_3^2 H_1' + \frac{1}{2}H_1 h_1 h_2\right]. \qquad (d-3f)$$

In these equations,

$$F_1' = \frac{dF_1}{da} = -\left(\frac{3\mathrm{erfc}(a)}{a^4} + \frac{6\pi^{-1/2}e^{-a^2}}{a^3} + \frac{4\pi^{-1/2}e^{-a^2}}{a}\right), \qquad (d-3g)$$

$$H_1' = \frac{dH_1}{db^2} = \frac{\eta^4}{8b^6}(2 + 2b^2 + b^4)e^{-b^2}. \qquad (d-3h)$$

The second derivative of S_1 with respect to strain and coordinate is given by

$$\frac{\partial}{\partial r_{p\gamma}}\left(\frac{\partial S_1}{\partial e_{\alpha\beta}}\right) = -\frac{1}{\eta^3}\sum_{L,j} Q_{pj}\left[F_1'(a_{pjL})\frac{1}{a_{pjL}\eta^2}x_{pjL\alpha}x_{pjL\beta}x_{pjL\gamma}\right.$$
$$\left. + F_1(a_{pjL})(x_{pjL\beta}\delta_{\alpha\gamma} + x_{pjL\alpha}\delta_{\beta\gamma})\right]$$
$$+ \frac{4\pi}{\Omega}\sum_{\mathbf{h}}{}'\sum_{j} Q_{pj}h_\gamma \sin(\mathbf{h}\cdot(\mathbf{r}_p - \mathbf{r}_j))$$
$$\times [H_1 h_\alpha h_\beta + G_1\delta_{\alpha\beta}]. \qquad (d-4)$$

The second derivative of S_1 with respect to coordinates is given by

$$\frac{\partial^2 S_1}{\partial r_{p\alpha}\partial r_{q\beta}} = -\delta_{pq}\left\{\frac{1}{\eta^3}\sum_{L,j} Q_{pj}\left[F_1'(a_{pjL})\frac{1}{a_{pjL}\eta^2}x_{pjL\alpha}x_{pjL\beta} + F_1(a_{pjL})\delta_{\alpha\beta}\right]\right.$$

$$+\frac{4\pi}{\Omega}\sum_{\mathbf{h}}{}'\sum_{\mathrm{j}} Q_{\mathrm{pj}} G_1 h_\alpha h_\beta \cos(\mathbf{h}\cdot(\mathbf{r}_\mathrm{p}-\mathbf{r}_\mathrm{j}))\Bigg\}$$
$$+\frac{1}{\eta^3}\sum_{\mathrm{L}} Q_{\mathrm{pq}}\left[F_1'(a_{\mathrm{pqL}})\frac{1}{a_{\mathrm{pqL}}\eta^2}x_{\mathrm{pqL}\alpha}x_{\mathrm{pqL}\beta}+F_1(a_{\mathrm{pqL}})\delta_{\alpha\beta}\right]$$
$$+\frac{4\pi}{\Omega}\sum_{\mathbf{h}}{}' Q_{\mathrm{pq}} G_1 h_\alpha h_\beta \cos(\mathbf{h}\cdot(\mathbf{r}_\mathrm{p}-\mathbf{r}_\mathrm{q})). \qquad (\mathrm{d}-5)$$

The dispersion lattice sum is given by[1]

$$S_6 = \frac{1}{2\eta^6}\sum_{\mathrm{L,i,j}} B_{\mathrm{ij}}(a_{\mathrm{ijL}}^{-6}+a_{\mathrm{ijL}}^{-4}+\tfrac{1}{2}a_{\mathrm{ijL}}^{-2})e^{-a_{\mathrm{ijL}}^2}$$
$$+\frac{\pi^{3/2}}{24\Omega}\sum_{\mathbf{h}}{}'\sum_{\mathrm{i,j}} B_{\mathrm{ij}}\cos\left[\mathbf{h}\cdot(\mathbf{r}_\mathrm{i}-\mathbf{r}_\mathrm{j})\right]h^3\left[\pi^{1/2}\mathrm{erfc}(b)+\left(\frac{1}{2b^3}-\frac{1}{b}\right)e^{-b^2}\right]$$
$$+\frac{\pi^{3/2}}{6\eta^3\Omega}\sum_{\mathrm{i,j}} B_{\mathrm{ij}}-\frac{1}{12\eta^6}\sum_{\mathrm{i}} B_{\mathrm{ii}}. \qquad (\mathrm{d}-6)$$

By taking the derivative with respect to strain $e_{\alpha\beta}$, we have

$$\frac{\partial S_6}{\partial e_{\alpha\beta}} = -\frac{1}{2\eta^8}\sum_{\mathrm{L,i,j}} B_{\mathrm{ij}}F_6(a_{\mathrm{ijL}})x_{\mathrm{ijL}\alpha}x_{\mathrm{ijL}\beta}$$
$$-\frac{\pi^{3/2}}{24\Omega}\sum_{\mathbf{h}}{}'\sum_{\mathrm{i,j}} B_{\mathrm{ij}}\cos(\mathbf{h}\cdot(\mathbf{r}_\mathrm{i}-\mathbf{r}_\mathrm{j}))\left[H_6(b^2)h_\alpha h_\beta+G_6(b^2)\delta_{\alpha\beta}\right]$$
$$-\frac{\pi^{3/2}}{6\eta^3\Omega}\sum_{\mathrm{i,j}} B_{\mathrm{ij}}\delta_{\alpha\beta}. \qquad (\mathrm{d}-7\mathrm{a})$$

Here,

$$F_6(a) = (6a^{-8}+6a^{-6}+3a^{-4}+a^{-2})e^{-a^2}, \qquad (\mathrm{d}-7\mathrm{b})$$

$$G_6(b^2) = h^3\left\{\pi^{1/2}\mathrm{erfc}(b)+(\frac{1}{2b^3}-\frac{1}{b})e^{-b^2}\right\}, \qquad (\mathrm{d}-7\mathrm{c})$$

$$H_6(b^2) = 3h\left(\pi^{1/2}\mathrm{erfc}(b)-\frac{e^{-b^2}}{b}\right). \qquad (\mathrm{d}-7\mathrm{d})$$

Similarly to the Coulomb case, we have

$$\frac{\partial^2 S_6}{\partial e_1 \partial e_1} = -\frac{1}{2\eta^8} \sum_{L,i,j} B_{ij} \left[F_6' \frac{1}{a_{ijL}\eta^2} x_{ijL1}^4 + 2F_6 x_{ijL1}^2 \right] + \frac{\pi^{3/2}}{24\Omega} \sum_{\mathbf{h}}{}' \sum_{i,j} B_{ij} \cos(\mathbf{h}\cdot(\mathbf{r}_i - \mathbf{r}_j)) \left[\frac{1}{2}\eta^2 h_1^4 H_6' + 4H_6 h_1^2 + G_6 \right] + \frac{\pi^{3/2}}{6\eta^3\Omega} \sum_{i,j} B_{ij}, \qquad (d-8a)$$

$$\frac{\partial^2 S_6}{\partial e_1 \partial e_2} = -\frac{1}{2\eta^8} \sum_{L,i,j} B_{ij} \left[F_6' \frac{1}{a_{ijL}\eta^2} x_{ijL1}^2 x_{ijL2}^2 \right] + \frac{\pi^{3/2}}{24\Omega} \sum_{\mathbf{h}}{}' \sum_{i,j} B_{ij} \cos(\mathbf{h}\cdot(\mathbf{r}_i - \mathbf{r}_j)) \left[\frac{1}{2}\eta^2 h_1^2 h_2^2 H_6' + H_6(h_1^2 + h_2^2) + G_6 \right] + \frac{\pi^{3/2}}{6\eta^3\Omega} \sum_{i,j} B_{ij}, \qquad (d-8b)$$

$$\frac{\partial^2 S_6}{\partial e_1 \partial e_4} = -\frac{1}{2\eta^8} \sum_{L,i,j} B_{ij} \left[F_6' \frac{1}{a_{ijL}\eta^2} x_{ijL1}^2 x_{ijL2} x_{ijL3} \right] + \frac{\pi^{3/2}}{24\Omega} \sum_{\mathbf{h}}{}' \sum_{i,j} B_{ij} \cos(\mathbf{h}\cdot(\mathbf{r}_i - \mathbf{r}_j)) \times \left[\frac{1}{2}\eta^2 h_1^2 h_2 h_3 H_6' + H_6 h_2 h_3 \right], \qquad (d-8c)$$

$$\frac{\partial^2 S_6}{\partial e_1 \partial e_5} = -\frac{1}{2\eta^8} \sum_{L,i,j} B_{ij} \left[F_6' \frac{1}{a_{ijL}\eta^2} x_{ijL1}^3 x_{ijL3} + F_6 x_{ijL1} x_{ijL3} \right] + \frac{\pi^{3/2}}{24\Omega} \sum_{\mathbf{h}}{}' \sum_{i,j} B_{ij} \cos(\mathbf{h}\cdot(\mathbf{r}_i - \mathbf{r}_j)) \times \left[\frac{1}{2}\eta^2 h_1^3 h_3 H_6' + 2H_6 h_1 h_3 \right], \qquad (d-8d)$$

$$\frac{\partial^2 S_6}{\partial e_4 \partial e_4} = -\frac{1}{2\eta^8}\sum_{L,i,j} B_{ij}\left[F_6'\frac{1}{a_{ijL}\eta^2}x_{ijL2}^2 x_{ijL3}^2 + \frac{F_6}{2}(x_{ijL2}^2 + x_{ijL3}^2)\right]$$
$$+ \frac{\pi^{3/2}}{24\Omega}\sum_{\mathbf{h}}{}' \sum_{i,j} B_{ij}\cos(\mathbf{h}\cdot(\mathbf{r}_i - \mathbf{r}_j))$$
$$\times\left[\frac{1}{2}\eta^2 h_2^2 h_3^2 H_6' + \frac{1}{2}H_6(h_2^2 + h_3^2)\right], \qquad (d-8e)$$

$$\frac{\partial^2 S_6}{\partial e_4 \partial e_5} = -\frac{1}{2\eta^8}\sum_{L,i,j} B_{ij}\left[F_6'\frac{1}{a_{ijL}\eta^2}x_{ijL1}x_{ijL2}x_{ijL3}^2 + \frac{1}{2}F_6 x_{ijL1}x_{ijL2}\right]$$
$$+ \frac{\pi^{3/2}}{24\Omega}\sum_{\mathbf{h}}{}' \sum_{i,j} B_{ij}\cos(\mathbf{h}\cdot(\mathbf{r}_i - \mathbf{r}_j))$$
$$\times\left[\frac{1}{2}\eta^2 h_1 h_2 h_3^2 H_6' + \frac{1}{2}H_6 h_1 h_2\right], \qquad (d-8f)$$

where

$$F_6' = \frac{dF_6}{da} = -2(24a^{-9} + 24a^{-7} + 12a^{-5} + 4a^{-3} + a^{-1})e^{-a^2}, \qquad (d-8g)$$

$$H_6' = \frac{dH_6}{db^2} = \frac{3\pi^{1/2}}{b\eta}\mathrm{erfc}(b). \qquad (d-8h)$$

The second derivative of S_6 with respect to strain and coordinate is given by

$$\frac{\partial}{\partial r_{p\gamma}}\left(\frac{\partial S_6}{\partial e_{\alpha\beta}}\right) = -\frac{1}{\eta^8}\sum_{L,j} B_{pj}\left[F_6'(a_{pjL})\frac{1}{a_{pjL}\eta^2}x_{pjL\alpha}x_{pjL\beta}x_{pjL\gamma}\right.$$
$$\left. + F_6(a_{pjL})(x_{pjL\beta}\delta_{\alpha\gamma} + x_{pjL\alpha}\delta_{\beta\gamma})\right]$$
$$+ \frac{\pi^{3/2}}{12\Omega}\sum_{\mathbf{h}}{}' \sum_{j} B_{pj}h_\gamma \sin(\mathbf{h}\cdot(\mathbf{r}_p - \mathbf{r}_j))$$
$$\times\left[H_6 h_\alpha h_\beta + G_6\delta_{\alpha\beta}\right]. \qquad (d-9)$$

The second derivative of S_6 with respect to coordinates is given by

$$\frac{\partial^2 S_6}{\partial r_{p\alpha}\partial r_{q\beta}} = -\delta_{pq}\left\{\frac{1}{\eta^8}\sum_{L,j} B_{pj}\left[F_6'(a_{pjL})\frac{1}{a_{pjL}\eta^2}x_{pjL\alpha}x_{pjL\beta} + F_6(a_p)\delta_{\alpha\beta}\right]\right.$$
$$\left.\frac{\pi^{3/2}}{12\Omega}\sum_{\mathbf{h}}{}'\sum_{j} B_{pj}G_6 h_\alpha h_\beta \cos(\mathbf{h}\cdot(\mathbf{r}_p - \mathbf{r}_j))\right\}$$
$$+\frac{1}{\eta^8}\sum_{L} B_{pq}\left[F_6'(a_{pqL})\frac{1}{a_{pqL}\eta^2}x_{pqL\alpha}x_{pqL\beta} + F_6(a_{pqL})\delta_{\alpha\beta}\right]$$
$$+\frac{\pi^{3/2}}{12\Omega}\sum_{\mathbf{h}}{}' B_{pq}G_6 h_\alpha h_\beta \cos(\mathbf{h}\cdot(\mathbf{r}_p - \mathbf{r}_q)). \qquad (d-10)$$

2. Phonon Calculations of the Ewald Lattice Sums

To evaluate the dynamical matrix, we need to evaluate the sum of the type,

$$\sum_{l}\frac{e^{i\mathbf{y}\cdot\mathbf{x}\binom{l}{k}}}{|\mathbf{x}\binom{l}{k} - \mathbf{x}|^m}, \qquad (d-11)$$

where $\mathbf{x}\binom{l}{k} = \mathbf{r}_k + \mathbf{R}_l$, $\mathbf{y}$ is a wave vector, and $\mathbf{x}$ is an arbitrary position vector. Born and Huang[2] derived the formula for the Coulomb lattice sums ($m = 1$). Here, we show the general formula.

By using the integral representation,

$$\frac{1}{r^m} = \frac{2}{\Gamma(m/2)}\int_0^\infty \rho^{m-1}e^{-\rho^2 r^2}d\rho, \qquad (d-12)$$

we have

$$\sum_{l}\frac{e^{i\mathbf{y}\cdot\mathbf{x}\binom{l}{k}}}{|\mathbf{x}\binom{l}{k} - \mathbf{x}|^m} = \int_0^\infty f(\mathbf{x})e^{i\mathbf{y}\cdot\mathbf{x}}d\rho, \qquad (d-13)$$

where

$$f(\mathbf{x}) = \frac{2}{\Gamma(m/2)}\sum_{l}\rho^{m-1}e^{-|\mathbf{x}\binom{l}{k}-\mathbf{x}|^2\rho^2 + i\mathbf{y}\cdot(\mathbf{x}\binom{l}{k}-\mathbf{x})}. \qquad (d-14)$$

Since $f(\mathbf{x})$ is a periodic function of $\mathbf{x}$, we can Fourier-transform it in the reciprocal space as follows,

$$f(\mathbf{x}) = \sum_{\mathbf{h}} g(\mathbf{h}) e^{i\mathbf{h}\cdot\mathbf{x}}, \qquad (d-15a)$$

$$\begin{aligned} g(\mathbf{h}) &= \frac{1}{\Omega}\int_{\text{unit cell}} f(\mathbf{x}) e^{-i\mathbf{h}\cdot\mathbf{x}} d^3\mathbf{x} \\ &= \frac{2\pi^{3/2}}{\Gamma(m/2)\Omega}\rho^{m-4} e^{-\frac{1}{4\rho^2}|\mathbf{h}+\mathbf{y}|^2 - i\mathbf{h}\cdot\mathbf{r}_k}. \end{aligned} \qquad (d-15b)$$

By dividing the integral into two parts by introducing a parameter η, we have

$$\begin{aligned} \sum_{l} \frac{e^{i\mathbf{y}\cdot\mathbf{x}\binom{l}{k}}}{|\mathbf{x}\binom{l}{k} - \mathbf{x}|^m} &= \int_0^{1/\eta} \left(\sum_{\mathbf{h}} g(\mathbf{h}) e^{i\mathbf{h}\cdot\mathbf{x}}\right) e^{i\mathbf{y}\cdot\mathbf{x}} d\rho + \int_{1/\eta}^{\infty} f(\mathbf{x}) e^{i\mathbf{y}\cdot\mathbf{x}} d\rho \\ &= \frac{2\pi^{3/2}}{\Gamma(m/2)\Omega}\sum_{\mathbf{h}}\int_0^{1/\eta} \rho^{m-4} e^{-\frac{1}{4\rho^2}|\mathbf{h}+\mathbf{y}|^2} d\rho e^{i(\mathbf{h}+\mathbf{y})\cdot\mathbf{x} - i\mathbf{h}\cdot\mathbf{r}_k} \\ &+ \frac{2}{\Gamma(m/2)}\sum_{l}\int_{1/\eta}^{\infty} \rho^{m-1} e^{-|\mathbf{x}\binom{l}{k} - \mathbf{x}|\rho^2} d\rho e^{i\mathbf{y}\cdot\mathbf{x}\binom{l}{k}} \\ &= \frac{\pi^{3/2}}{\Gamma(m/2)\Omega}\sum_{\mathbf{h}}\left(\frac{|\mathbf{h}+\mathbf{y}|}{2}\right)^{m-3} I(-m+1, b') e^{i(\mathbf{h}+\mathbf{y})\cdot\mathbf{x} - i\mathbf{h}\cdot\mathbf{r}_k} \\ &+ \frac{1}{\Gamma(m/2)}\sum_{l}\frac{1}{|\mathbf{x}\binom{l}{k} - \mathbf{x}|^m} I(m-2, a') e^{i\mathbf{y}\cdot\mathbf{x}\binom{l}{k}}, \end{aligned} \qquad (d-16a)$$

where

$$a' = \frac{|\mathbf{x}\binom{l}{k} - \mathbf{x}|}{\eta}, \qquad (d-16b)$$

$$b' = \frac{\eta|\mathbf{h}+\mathbf{y}|}{2}, \qquad (d-16c)$$

and

$$I(n, c) = \int_{c^2}^{\infty} t^{n/2} e^{-t} dt, \qquad (d-17)$$

which has the recursion relation

$$I(n+1,c) = c^{n+1}e^{-c^2} + \frac{n+1}{2}I(n-1,c). \qquad (d-18)$$

The following terms are required for n = 1 and n = 6;

$$I(-1,c) = \pi^{1/2}\mathrm{erfc}(c), \qquad (d-19a)$$

$$I(0,c) = e^{-c^2}, \qquad (d-19b)$$

$$I(4,c) = (c^4 + 2c^2 + 2)e^{-c^2}, \qquad (d-19c)$$

$$I(-5,c) = \frac{4}{3}\left(\pi^{1/2}\mathrm{erfc}(c) + \left(\frac{1}{2c^3} - \frac{1}{c}\right)e^{-c^2}\right). \qquad (d-19d)$$

The dynamical matrix is given by

$$C^n_{\alpha\beta}\binom{y}{kk'} = \frac{e^{-iy\cdot r_k}}{(m_k m_{k'})^{1/2}} \sum_{l'} \Phi^n_{\alpha\beta}\binom{-l'}{kk'} e^{iy\cdot(r_{k'}+R_{l'})}, \qquad (d-20)$$

where m_k is a mass of an atom k and

$$\Phi^n_{\alpha\beta}\binom{-l'}{kk'} = -A_{kk'}\left\{\frac{\partial^2}{\partial x_\alpha \partial x_\beta}\frac{1}{|x|^n}\right\}_{x=r_k-r_{k'}+R_{l'}} + \delta_{l'0}\delta_{kk'}\sum_{l'',k''} A_{kk''}\left\{\frac{\partial^2}{\partial x_\alpha \partial x_\beta}\frac{1}{|x|^n}\right\}_{x=r_k-r_{k''}+R_{l''}}. \qquad (d-21)$$

Here $A_{kk'}$ is either $Q_{kk'}(n=1)$ or $B_{kk'}(n=6)$. The dynamical matrix can be obtained by taking the second derivatives of (d-16). We show the formula explicitly for n = 1 and n = 6 as follows;

$$C^1_{\alpha\beta}\binom{y}{kk'} = -\delta_{kk'}\frac{1}{m_k}\sum_{k''} Q_{kk''}\left\{\sum_{l'}\frac{1}{\eta^3} \times \left(F_1'(a_{k'k''(-l')})\frac{1}{a_{k'k''(-l')}\eta^2} x_{k'k''(-l')\alpha} x_{k'k''(-l')\beta} + F_1(a_{k'k''(-l')})\delta_{\alpha\beta}\right)\right.$$

$$+\frac{4\pi}{\Omega}\sum_{\mathbf{h}}{}' G_1(b^2)h_\alpha h_\beta e^{i\mathbf{h}\cdot(\mathbf{r}_k-\mathbf{r}_{k''})}\Bigg\}$$

$$+\frac{Q_{kk'}}{(m_k m_{k'})^{1/2}}\Bigg\{\sum_{l'}\frac{1}{\eta^3}\left(F_1'(a_{k'k(-l')})\frac{1}{a_{k'k(-l')}\eta^2}x_{k'k(-l')\alpha}x_{k'k(-l')\beta}\right.$$

$$\left.+F_1(a_{k'k(-l')})\delta_{\alpha\beta}\right)e^{iy\cdot x_{k'k(-l)}}$$

$$+\frac{4\pi}{\Omega}\sum_{\mathbf{h}}{}' G_1(\eta^2|\mathbf{h}+\mathbf{y}|^2/4)(\mathbf{h}+\mathbf{y})_\alpha(\mathbf{h}+\mathbf{y})_\beta e^{i\mathbf{h}\cdot(\mathbf{r}_k-\mathbf{r}_{k'})}$$

$$+\frac{4\pi}{\Omega}G_1(\eta^2 y^2/4)y_\alpha y_\beta\Bigg\}, \qquad (d-22)$$

$$C^6_{\alpha\beta}\binom{y}{kk'} = -\delta_{kk'}\frac{1}{m_k}\sum_{k''}B_{kk''}\Bigg\{\sum_{l'}\frac{1}{\eta^8}$$

$$\times\left(F_6'(a_{k'k''(-l')})\frac{1}{a_{k'k''(-l')}\eta^2}x_{k'k''(-l')\alpha}x_{k'k''(-l')\beta}+F_6(a_{k'k''(-l')})\delta_{\alpha\beta}\right)$$

$$+\frac{\pi^{3/2}}{12\Omega}\sum_{\mathbf{h}}{}' G_6(b^2)h_\alpha h_\beta e^{i\mathbf{h}\cdot(\mathbf{r}_k-\mathbf{r}_{k''})}\Bigg\}$$

$$+\frac{B_{kk'}}{(m_k m_{k'})^{1/2}}\Bigg\{\sum_{l'}\frac{1}{\eta^8}\left(F_6'(a_{k'k(-l')})\frac{1}{a_{k'k(-l')}\eta^2}x_{k'k(-l')\alpha}x_{k'k(-l')\beta}\right.$$

$$\left.+F_6(a_{k'k(-l')})\delta_{\alpha\beta}\right)e^{iy\cdot x_{k'k(-l')}}$$

$$+\frac{\pi^{3/2}}{12\Omega}\sum_{\mathbf{h}}{}' G_6(\eta^2|\mathbf{h}+\mathbf{y}|^2/4)(\mathbf{h}+\mathbf{y})_\alpha(\mathbf{h}+\mathbf{y})_\beta e^{i\mathbf{h}\cdot(\mathbf{r}_k-\mathbf{r}_{k'})}\Bigg\}. \qquad (d-23)$$

3. Correspondence to the Derivation by Born and Huang

Born and Huang[2] treat the dynamical matrix arising from the Coulomb interactions separately from other terms because it contains the term that is not defined at $\mathbf{y}=0$. They define a new dynamical matrix $\bar{C}$ by subtracting this term from the original matrix as follows:

$$\bar{C}_{\alpha\beta}\binom{y}{kk'} = C^{nc}_{\alpha\beta}\binom{y}{kk'} + C^{1}_{\alpha\beta}\binom{y}{kk'} - \frac{4\pi}{\Omega}\left(\frac{y_\alpha y_\beta}{y^2}\right)\frac{Q_{kk'}}{(m_k m_{k'})^{1/2}}, \qquad (d-24)$$

where C^{nc} is the non-Coulomb term and C^1 is the Coulomb term. The lattice-wave equation becomes

$$\omega^2 \begin{pmatrix} y \\ j \end{pmatrix} w_\alpha \left(k \middle|_j^y \right) = \sum_{k'\beta} \bar{C}_{\alpha\beta} \begin{pmatrix} y \\ kk' \end{pmatrix} w_\beta \left(k' \middle|_j^y \right) - \frac{C_{unit}}{\epsilon} \frac{q_k}{m_k^{1/2}} E_\alpha, \qquad (d-25)$$

where the displacement u in terms of an eigenvector $w\left(k|_j^y\right)$ (j is a mode index, $j = 1, \ldots, 3N$) is given by

$$u_\beta \begin{pmatrix} l' \\ k' \end{pmatrix} = m_{k'}^{-1/2} w_\beta \left(k' \middle|_j^y \right) e^{iy\cdot(r_{k'}+R_{l'})}, \qquad (d-26)$$

and the macroscopic field is given by

$$E_\alpha = -\frac{4\pi}{\Omega} \frac{y_\alpha}{y} \sum_\beta \frac{y_\beta}{y} \sum_{k'} q_{k'} m_{k'}^{-1/2} w_\beta \left(k' \middle|_j^y \right). \qquad (d-27)$$

By replacing y with δy and expanding $\bar{C}$ in terms of δ, we get the following equation,

$$\bar{C}_{\alpha\beta} \begin{pmatrix} \delta y \\ kk' \end{pmatrix} = \bar{C}^{(0)}_{\alpha\beta}(kk') + i\delta \sum_\gamma \bar{C}^{(1)}_{\alpha\beta,\gamma}(kk') y_\gamma / 2\pi + \frac{1}{2}\delta^2 \sum_{\gamma,\lambda} \bar{C}^{(2)}_{\alpha\beta,\gamma\lambda}(kk') y_\gamma y_\lambda / (4\pi^2) + \ldots, \qquad (d-28)$$

where[2]

$$\begin{aligned} \bar{C}^{(0)}_{\alpha\beta}(kk') = {} & \frac{1}{(m_k m_{k'})^{1/2}} \sum_l \Phi^{nc}_{\alpha\beta} \begin{pmatrix} l \\ kk' \end{pmatrix} \\ & - \delta_{kk'} \frac{1}{m_k} \left\{ \sum_{l,k''} \frac{Q_{kk''}}{\eta^3} \left(F_1' \frac{1}{a_{kk''(-l)}\eta^2} x_{kk''(-l)\alpha} x_{kk''(-l)\beta} + F_1 \delta_{\alpha\beta} \right) \right. \\ & \left. + \frac{4\pi}{\Omega} \sum_{\mathbf{h}}{}' \sum_{k''} Q_{kk''} G_1 h_\alpha h_\beta \cos(\mathbf{h}\cdot(\mathbf{r}_k - \mathbf{r}_{k''})) \right\} \\ & + \frac{Q_{kk'}}{(m_k m_{k'})^{1/2}} \left\{ \frac{1}{\eta^3} \sum_l \left(F_1' \frac{1}{a_{kk'(-l)}\eta^2} x_{kk'(-l)\alpha} x_{kk'(-l)\beta} + F_1 \delta_{\alpha\beta} \right) \right. \\ & \left. + \frac{4\pi}{\Omega} \sum_{\mathbf{h}}{}' G_1 h_\alpha h_\beta \cos(\mathbf{h}\cdot(\mathbf{r}_k - \mathbf{r}_{k'})) \right\}, \end{aligned} \qquad (d-29)$$

$$\bar{C}^{(1)}_{\alpha\beta,\gamma}(kk') = \frac{-2\pi}{(m_k m_{k'})^{1/2}} \sum_l \Phi^{nc}_{\alpha\beta}\binom{l}{kk'} x_{kk'(-l)\gamma}$$
$$+ \frac{2\pi Q_{kk'}}{(m_k m_{k'})^{1/2}} \sum_l \frac{1}{\eta^3}\left(F'_1 \frac{1}{a_{kk'(-l)}\eta^2} x_{kk'(-l)\alpha} x_{kk'(-l)\beta} x_{kk'(-l)\gamma} \right.$$
$$\left. + F_1 x_{kk'(-l)\gamma}\delta_{\alpha\beta}\right)$$
$$+ \frac{8\pi^2 Q_{kk'}}{\Omega(m_k m_{k'})^{1/2}} \sum_h{}' \sin(\mathbf{h}\cdot(\mathbf{r}_k - \mathbf{r}_{k'}))$$
$$\times [H_1 h_\alpha h_\beta h_\gamma + G_1(h_\alpha\delta_{\beta\gamma} + h_\beta\delta_{\alpha\gamma})], \qquad (d-30)$$

$$\bar{C}^{(2)}_{\alpha\beta,\gamma\lambda}(kk') = \frac{-4\pi^2}{(m_k m_{k'})^{1/2}} \sum_l \Phi^{nc}_{\alpha\beta}\binom{l}{kk'} x_{kk'(-l)\gamma} x_{kk'(-l)\lambda}$$
$$- \frac{4\pi^3\eta^2 Q_{kk'}}{\Omega(m_k m_{k'})^{1/2}}(\delta_{\alpha\gamma}\delta_{\beta\lambda} + \delta_{\alpha\lambda}\delta_{\beta\gamma})$$
$$- \frac{4\pi^2 Q_{kk'}}{\eta^3(m_k m_{k'})^{1/2}} \sum_l \left(F'_1 \frac{1}{a_{kk'(-l)}\eta^2} x_{kk'(-l)\alpha} x_{kk'(-l)\beta} x_{kk'(-l)\gamma} x_{kk'(-l)\lambda} \right.$$
$$\left. + F_1 x_{kk'(-l)\gamma} x_{kk'(-l)\lambda}\delta_{\alpha\beta}\right)$$
$$+ \frac{16\pi^3 Q_{kk'}}{\Omega(m_k m_{k'})^{1/2}} \sum_h{}' \cos(\mathbf{h}\cdot(\mathbf{r}_k - \mathbf{r}_{k'}))\{$$
$$(\delta_{\alpha\gamma}\delta_{\beta\lambda} + \delta_{\alpha\lambda}\delta_{\beta\gamma})G_1 + \frac{1}{2}\eta^2 h_\alpha h_\beta h_\gamma h_\lambda H'_1$$
$$+ H_1(h_\alpha h_\beta\delta_{\gamma\lambda} + h_\alpha h_\gamma\delta_{\beta\lambda} + h_\alpha h_\lambda\delta_{\beta\gamma}$$
$$+ h_\beta h_\gamma\delta_{\alpha\lambda} + h_\beta h_\lambda\delta_{\alpha\gamma})\}. \qquad (d-31)$$

The following terms are defined:

$$[\alpha\beta,\gamma\lambda] = \frac{1}{8\pi^2\Omega}\sum_{k,k'}(m_k m_{k'})^{1/2}\bar{C}^{(2)}_{\alpha\beta,\gamma\lambda}(kk'), \qquad (d-32)$$

$$(\alpha\gamma,\beta\lambda) = -\frac{1}{4\pi^2\Omega}\sum_{k,k'}\sum_{\mu,\nu}\Gamma_{\mu\nu}(kk')\sum_{k''}\bar{C}^{(1)}_{\mu\alpha,\gamma}(kk'')m^{1/2}_{k''}\sum_{k'''}\bar{C}^{(1)}_{\nu\beta,\lambda}(k'k''')m^{1/2}_{k'''}, \qquad (d-33)$$

$$[\beta,\alpha\gamma] = \frac{1}{2\pi\Omega}\sum_{k,k',\mu} m_k^{1/2}\bar{C}^{(1)}_{\alpha\mu,\gamma}(kk')\sum_{k''}\Gamma_{\mu\beta}(k'k'')q_{k''}m_{k''}^{-1/2}, \qquad (d-34)$$

where Γ is the inverse of $\bar{C}^{(0)}$. Because of the translational symmetry, we fix the first atom to invert the matrix and the degree of freedom becomes $3N-3$. So in the summation involving Γ, the sum must start from the second atom. By using these, it is shown[2] that at zero force and at zero stress, elastic constants(c), piezoelectric constants(g) and dielectric susceptibility constants(a) are given by

$$c_{\alpha\gamma,\beta\lambda} = [\alpha\beta,\gamma\lambda] + [\beta\gamma,\alpha\lambda] - [\beta\lambda,\alpha\gamma] + (\alpha\gamma,\beta\lambda), \qquad (d-35)$$

$$g_{\beta,\alpha\gamma} = [\beta,\alpha\gamma], \qquad (d-36)$$

$$a_{\alpha\beta} = \frac{1}{\Omega}\sum_{k,k'}\frac{Q_{kk'}}{(m_k m_{k'})^{1/2}}\Gamma_{\alpha\beta}(kk'). \qquad (d-37)$$

In the following, we show how each term corresponds to the equations obtained in the previous sections.

(a) Dielectric Susceptibility Constants

We write the total energy per cell(E_t) as a sum of non-Coulomb part (E_{nc}) and Coulomb part(S_1, (d-1)). Then $E_{nc} = (1/M)\Phi^{nc}$, where M is the total number of cells in the calculation. Then

$$\frac{\partial^2 E_t}{\partial r_{k\alpha}\partial r_{k'\beta}} = \sum_l \Phi^{nc}_{\alpha\beta}\binom{l}{kk'} + \frac{\partial^2 S_1}{\partial r_{k\alpha}\partial r_{k'\beta}}. \qquad (d-38)$$

By comparing (d-5) and (d-29), we have

$$\frac{\partial^2 E_t}{\partial r_{k\alpha}\partial r_{k'\beta}} = (m_k m_{k'})^{1/2}\bar{C}^{(0)}_{\alpha\beta}(kk'). \qquad (d-39)$$

Therefore,

$$(m_k m_{k'})^{-1/2}\Gamma_{\alpha\beta}(kk') = [Wrr^{-1}]_{k\alpha,k'\beta}, \qquad (d-40)$$

and from (b-19) and (d-37), it is clear that both equations are equivalent.

(b) Piezoelectric Constants

Second derivatives of the total energy with respect to the strain and the coordinate are given by

$$\begin{aligned}\frac{\partial}{\partial r_{k\gamma}}\left(\frac{\partial E_t}{\partial e_{\alpha\beta}}\right) &= \frac{1}{2}\sum_{l,k'}\Phi^{nc}_{\alpha\gamma}\binom{l}{k'k}r_{lk'\beta} + \frac{1}{2}\sum_{l,k'}\Phi^{nc}_{\beta\gamma}\binom{l}{k'k}r_{lk'\alpha} \\ &\quad - \frac{1}{2}\frac{\partial S_1}{\partial r_{k\alpha}}\delta_{\beta\gamma} - \frac{1}{2}\frac{\partial S_1}{\partial r_{k\beta}}\delta_{\alpha\gamma} \\ &\quad + \frac{\partial}{\partial r_{k\gamma}}\left(\frac{\partial S_1}{\partial e_{\alpha\beta}}\right), \qquad (d-41)\end{aligned}$$

where conditions of zero total force are used. By using the relation arising from the invariance of force with respect to rigid rotations of a crystal[2] and the conditions of zero total force

$$-\frac{\partial S_1}{\partial r_{k\nu}}\delta_{\alpha\mu} + \frac{\partial S_1}{\partial r_{k\mu}}\delta_{\alpha\nu} = \sum_{l,k'}\Phi^{nc}_{\mu\alpha}\binom{l}{k'k}r_{lk'\nu} - \sum_{l,k'}\Phi^{nc}_{\nu\alpha}\binom{l}{k'k}r_{lk'\mu}, \qquad (d-42)$$

we have

$$\begin{aligned}\frac{\partial}{\partial r_{k\gamma}}\left(\frac{\partial E_t}{\partial e_{\alpha\beta}}\right) &= \sum_{l,k'}\Phi^{nc}_{\alpha\gamma}\binom{l}{k'k}r_{lk'\beta} - \frac{\partial S_1}{\partial r_{k\alpha}}\delta_{\beta\gamma} + \frac{\partial}{\partial r_{k\gamma}}\left(\frac{\partial S_1}{\partial e_{\alpha\beta}}\right) \\ &= \sum_{l,k'}\Phi^{nc}_{\beta\gamma}\binom{l}{k'k}r_{lk'\alpha} - \frac{\partial S_1}{\partial r_{k\beta}}\delta_{\alpha\gamma} + \frac{\partial}{\partial r_{k\gamma}}\left(\frac{\partial S_1}{\partial e_{\alpha\beta}}\right). \qquad (d-43)\end{aligned}$$

By comparing the above equation with (d-30) and (d-4), we have

$$\frac{\partial}{\partial r_{k\gamma}}\left(\frac{\partial E_t}{\partial e_{\alpha\beta}}\right) = \frac{m_k^{1/2}}{2\pi}\sum_{k'} m_{k'}^{1/2}\bar{C}^{(1)}_{\gamma\alpha,\beta}(kk') = \frac{m_k^{1/2}}{2\pi}\sum_{k'} m_{k'}^{1/2}\bar{C}^{(1)}_{\gamma\beta,\alpha}(kk'). \qquad (d-44)$$

The piezoelectric constant is given previously as

$$g_{\alpha,\gamma\lambda} = -\frac{1}{\Omega}\sum_{k'',k,\beta} q_{k''}[Wrr^{-1}]_{k''\alpha,k\beta}[Wer]_{\gamma\lambda,k\beta} = -\frac{1}{\Omega}\sum_{k'',k,\beta} q_{k''}[Wrr^{-1}]_{k''\alpha,k\beta}\frac{m_k^{1/2}}{2\pi}\sum_{k'} m_{k'}^{1/2}\bar{C}^{(1)}_{\beta\gamma,\lambda}(kk') = \frac{1}{2\pi\Omega}\sum_{k,k',\beta} m_{k'}^{1/2}\bar{C}^{(1)}_{\gamma\beta,\lambda}(k'k)\sum_{k''}\Gamma_{\beta\alpha}(kk'')q_{k''}m_{k''}^{-1/2}, \qquad (d-45)$$

where antisymmetric property of $\bar{C}^{(1)}$ is used. By comparing this equation and (d-34), we have

$$g_{\alpha,\gamma\lambda} = [\alpha,\gamma\lambda]. \qquad (d-46)$$

(c) Elastic Stiffness Constants

At zero stress, we have

$$\frac{\partial^2 E_t}{\partial e_{\beta\lambda}\partial e_{\alpha\gamma}} = \frac{1}{2}\sum_{l,k,k'}\Phi^{nc}_{\beta\gamma}\binom{l}{k'k}r_{lk'\lambda}r_{0k\alpha} + \frac{1}{2}\sum_{l,k,k'}\Phi^{nc}_{\beta\alpha}\binom{l}{k'k}r_{lk'\lambda}r_{0k\gamma} - \frac{1}{2}\delta_{\gamma\lambda}\frac{\partial S_1}{\partial e_{\alpha\beta}} - \frac{1}{2}\delta_{\alpha\lambda}\frac{\partial S_1}{\partial e_{\gamma\beta}} + \frac{\partial^2 S_1}{\partial e_{\beta\lambda}\partial e_{\alpha\gamma}}, \qquad (d-47)$$

where (a-7) and (d-42) were used.

We separate $[\alpha\beta,\gamma\lambda]$ into non-Coulomb terms and Coulomb terms as follows:

$$[\alpha\beta,\gamma\lambda] = [\alpha\beta,\gamma\lambda]_{nc} + [\alpha\beta,\gamma\lambda]_1, \qquad (d-48)$$

where subscript nc specifies the term from the non-Coulomb part and 1 specifies the term from the Coulomb part. From (d-31) and (d-32), we have the non-Coulomb term as

$$\Omega[\alpha\beta,\gamma\lambda]_{\rm nc} = \frac{1}{2}\sum_{\rm l,k,k'} \Phi^{\rm nc}_{\alpha\beta}\left(^{\rm l}_{\rm k'k}\right) {\rm r}_{\rm lk'\gamma}{\rm r}_{\rm 0k\lambda} + \frac{1}{2}\sum_{\rm l,k,k'} \Phi^{\rm nc}_{\alpha\beta}\left(^{\rm l}_{\rm k'k}\right) {\rm r}_{\rm lk'\lambda}{\rm r}_{\rm 0k\gamma}. \qquad ({\rm d}-49)$$

From this equation, we have

$$\begin{aligned}
&\Omega\left([\alpha\beta,\gamma\lambda]+[\beta\gamma,\alpha\lambda]-[\beta\lambda,\alpha\gamma]\right) = \\
&\frac{1}{2}\sum_{\rm l,k,k'} \Phi^{\rm nc}_{\beta\alpha}\left(^{\rm l}_{\rm k'k}\right) {\rm r}_{\rm lk'\lambda}{\rm r}_{\rm 0k\gamma} + \frac{1}{2}\sum_{\rm l,k,k'} \Phi^{\rm nc}_{\beta\gamma}\left(^{\rm l}_{\rm k'k}\right) {\rm r}_{\rm lk'\lambda}{\rm r}_{\rm 0k\alpha} \\
&+\Omega\left([\alpha\beta,\gamma\lambda]_1+[\beta\gamma,\alpha\lambda]_1-[\beta\lambda,\alpha\gamma]_1\right) \\
&+\delta_{\beta\lambda}\frac{\partial {\rm S}_1}{\partial {\rm e}_{\alpha\gamma}} - \frac{1}{2}\delta_{\alpha\beta}\frac{\partial {\rm S}_1}{\partial {\rm e}_{\lambda\gamma}} - \frac{1}{2}\delta_{\gamma\beta}\frac{\partial {\rm S}_1}{\partial {\rm e}_{\lambda\alpha}}, \qquad ({\rm d}-50)
\end{aligned}$$

where we combined terms using (d-42). By comparing (d-47) and (d-50) we have

$$\begin{aligned}
\frac{\partial^2 {\rm E}_{\rm t}}{\partial {\rm e}_{\beta\lambda}\partial {\rm e}_{\alpha\gamma}} &= \Omega\left([\alpha\beta,\gamma\lambda]+[\beta\gamma,\alpha\lambda]-[\beta\lambda,\alpha\gamma]\right) \\
&\quad -\Omega\left([\alpha\beta,\gamma\lambda]_1+[\beta\gamma,\alpha\lambda]_1-[\beta\lambda,\alpha\gamma]_1\right) \\
&\quad -\delta_{\beta\lambda}\frac{\partial {\rm S}_1}{\partial {\rm e}_{\alpha\gamma}} + \frac{1}{2}\delta_{\alpha\beta}\frac{\partial {\rm S}_1}{\partial {\rm e}_{\lambda\gamma}} + \frac{1}{2}\delta_{\gamma\beta}\frac{\partial {\rm S}_1}{\partial {\rm e}_{\lambda\alpha}} \\
&\quad -\frac{1}{2}\delta_{\gamma\lambda}\frac{\partial {\rm S}_1}{\partial {\rm e}_{\alpha\beta}} - \frac{1}{2}\delta_{\alpha\lambda}\frac{\partial {\rm S}_1}{\partial {\rm e}_{\gamma\beta}} + \frac{\partial^2 {\rm S}_1}{\partial {\rm e}_{\beta\lambda}\partial {\rm e}_{\alpha\gamma}}. \qquad ({\rm d}-51)
\end{aligned}$$

From (d-31) and (d-32), we have

$$\begin{aligned}
\Omega[\alpha\beta,\gamma\lambda]_1 = &-\frac{1}{2\eta^3}\sum_{\rm L,i,j} {\rm Q}_{\rm ij}\left[{\rm F}_1'\frac{1}{{\rm a}_{\rm ijL}\eta^2}{\rm x}_{\rm ijL\alpha}{\rm x}_{\rm ijL\beta}{\rm x}_{\rm ijL\gamma}{\rm x}_{\rm ijL\lambda} + {\rm F}_1{\rm x}_{\rm ijL\gamma}{\rm x}_{\rm ijL\lambda}\delta_{\alpha\beta}\right] \\
&+\frac{2\pi}{\Omega}\sum_{\mathbf{h}}{}' {\rm S}(\mathbf{h}){\rm S}(-\mathbf{h})\Big[(\delta_{\alpha\gamma}\delta_{\beta\lambda}+\delta_{\alpha\lambda}\delta_{\beta\gamma}){\rm G}_1 + \frac{1}{2}\eta^2{\rm h}_\alpha{\rm h}_\beta{\rm h}_\gamma{\rm h}_\lambda{\rm H}_1' \\
&+{\rm H}_1({\rm h}_\alpha{\rm h}_\beta\delta_{\gamma\lambda}+{\rm h}_\alpha{\rm h}_\gamma\delta_{\beta\lambda}+{\rm h}_\alpha{\rm h}_\lambda\delta_{\beta\gamma} \\
&+{\rm h}_\beta{\rm h}_\gamma\delta_{\alpha\lambda}+{\rm h}_\beta{\rm h}_\lambda\delta_{\alpha\gamma})\Big]. \qquad ({\rm d}-52)
\end{aligned}$$

Therefore, we have

$$
\begin{aligned}
&-\Omega\left([\alpha\beta,\gamma\lambda]_1+[\beta\gamma,\alpha\lambda]_1-[\beta\lambda,\alpha\gamma]_1\right)\\
&-\delta_{\beta\lambda}\frac{\partial S_1}{\partial e_{\alpha\gamma}}+\frac{1}{2}\delta_{\alpha\beta}\frac{\partial S_1}{\partial e_{\lambda\gamma}}+\frac{1}{2}\delta_{\gamma\beta}\frac{\partial S_1}{\partial e_{\lambda\alpha}}\\
&-\frac{1}{2}\delta_{\gamma\lambda}\frac{\partial S_1}{\partial e_{\alpha\beta}}-\frac{1}{2}\delta_{\alpha\lambda}\frac{\partial S_1}{\partial e_{\gamma\beta}}\\
&=\frac{1}{2\eta^3}\sum_{L,i,j}Q_{ij}\left[F_1'\frac{1}{a_{ijL}\eta^2}x_{ijL\alpha}x_{ijL\beta}x_{ijL\gamma}x_{ijL\lambda}+\frac{1}{2}F_1x_{ijL\gamma}x_{ijL\lambda}\delta_{\alpha\beta}\right.\\
&+\frac{1}{2}F_1x_{ijL\alpha}x_{ijL\lambda}\delta_{\gamma\beta}+\frac{1}{2}F_1x_{ijL\alpha}x_{ijL\beta}\delta_{\gamma\lambda}+\frac{1}{2}F_1x_{ijL\beta}x_{ijL\gamma}\delta_{\alpha\lambda}\Big]\\
&-\frac{2\pi}{\Omega}\sum_{\mathbf{h}}{}'S(\mathbf{h})S(-\mathbf{h})\left[\delta_{\alpha\gamma}\delta_{\beta\lambda}G_1+\frac{1}{2}\eta^2h_\alpha h_\beta h_\gamma h_\lambda H_1'\right.\\
&+H_1\left(h_\alpha h_\gamma\delta_{\beta\lambda}+h_\beta h_\lambda\delta_{\alpha\gamma}+\frac{1}{2}h_\alpha h_\beta\delta_{\gamma\lambda}\right.\\
&\left.\left.+\frac{1}{2}h_\beta h_\gamma\delta_{\alpha\lambda}+\frac{1}{2}h_\lambda h_\gamma\delta_{\alpha\beta}+\frac{1}{2}h_\lambda h_\alpha\delta_{\gamma\beta}\right)\right]. \qquad (d-53)
\end{aligned}
$$

By comparing the above equation with (d-3), we find that the above equation is exactly minus of $\frac{\partial^2 S_1}{\partial e_{\alpha\gamma}\partial e_{\beta\lambda}}$. Therefore, we have

$$
\frac{\partial^2 E_t}{\partial e_{\beta\lambda}\partial e_{\alpha\gamma}}=\Omega\left([\alpha\beta,\gamma\lambda]+[\beta\gamma,\alpha\lambda]-[\beta\lambda,\alpha\gamma]\right). \qquad (d-54)
$$

From (d-40) and (d-44), it can be shown that

$$
\begin{aligned}
\Omega(\alpha\gamma,\beta\lambda)&=-\frac{1}{4\pi^2\Omega}\sum_{k,k'}\sum_{\mu,\nu}\Gamma_{\mu\nu}(kk')\sum_{k''}\bar{C}^{(1)}_{\mu\alpha,\gamma}(kk'')m^{1/2}_{k''}\sum_{k'''}\bar{C}^{(1)}_{\nu\beta,\lambda}(k'k''')m^{1/2}_{k'''}\\
&=-\sum_{k,k'}\sum_{\mu,\nu}[Wrr^{-1}]_{k\mu,k'\nu}[Wer]_{\alpha\gamma,k\mu}[Wer]_{\beta\lambda,k'\nu}\\
&=-[WerWrr^{-1}Wer^{\dagger}]_{\alpha\gamma,\beta\lambda}. \qquad (d-55)
\end{aligned}
$$

Therefore, we have

$$c_{\alpha\gamma,\beta\lambda} = \frac{1}{\Omega}\left[\mathrm{Wee} - \mathrm{Wer}\mathrm{Wrr}^{-1}\mathrm{Wer}^{\dagger}\right]_{\alpha\gamma,\beta\lambda}$$
$$= [\alpha\beta,\gamma\lambda] + [\beta\gamma,\alpha\lambda] - [\beta\lambda,\alpha\gamma] + (\alpha\gamma,\beta\lambda). \qquad (\mathrm{d}-56)$$

References

(1) Karasawa, N.; Goddard III, W. A. *J. Phys. Chem.*,**1989**, *93*, 7320. In this paper, stress is defined as $\sigma_i = -\frac{1}{\Omega}\frac{\partial E}{\partial e_i}$.

(2) Born, M.; Huang, K. *Dynamical Theory of Crystal Lattices* (Oxford Univ. Press, Oxford, 1954). In the Equation (31.23) in this book, $y_\gamma(h)y_\lambda(h)\delta_{\alpha\beta}$ must be deleted (see (d-31)).

(3) Nye, J. F. *Physical Properties of Crystals* (Oxford Univ. Press, Oxford, 1957).

(4) Landau, L. D.; Lifshitz, E. M. *Theory of Elasticity* (Pergamon Press, London, 1959).

Chapter III

Cell Multipole Methods and Nonbond Cutoffs

[This chapter is based on papers co-authored with Hong-Qiang Ding and William A. Goddard, and were submitted to *J. Chem. Phys.*(a) and *Phys. Rev. Lett.*(b)]

(a) Atomic-Level Simulations on a Million Particles: The Cell Multipole Method for Coulomb and London Interactions

Abstract

The N^2 computations implicit in the Coulomb and other long-range interactions remain the critical bottleneck in atomic-level simulations of the structure and dynamics of very large molecules and clusters. We report here the Cell Multipole Method (CMM), which involves no steps scaling a higher order than N, minimizes the effort of the remaining terms, and requires only modest memory. To demonstrate the feasibility of this approach, we report systematic calculations (using a laboratory workstation) on realistic polymers (polyvinylidene fluoride) with up to 1 million atoms and demonstrate that this method scales as N for a million atoms (where it is 1500 times faster than the exact method). CMM treats the reciprocal power-law class of interactions having the form $q_i q_j / r_{ij}^p$, which includes Coulomb ($p = 1$), London dispersion ($p = 6$), and shielded Coulomb ($p = 2$) interactions. This method is well suited for highly parallel and vector computers.

Introduction. In recent years, there has been a great deal of progress in simulating the atomic-level structure and dynamics of large molecules, with calculations reported on systems with thousands of atoms[1,2]. However, current methods are inadequate to simulate the million particles required to describe the interesting properties for many important systems. For example, amorphous polymers may have segments each with 100,000 atoms that associate to form partially crystalline lamellae, random coil regions, and interfaces between these regions, each of which may contribute special mechanical and chemical properties to the system. In order to carry out simulations for such systems, it is essential:

i. to eliminate computational steps or storage that depend quadratically (N^2) on system size, or worse;

ii. to minimize any calculation or storage procedures that are linear with N;

iii. to construct algorithms for the steps linear in N that allow the problem to be solved efficiently under parallel computer architectures.

In this paper we focus on the biggest bottleneck obstructing atomic-level simulations on superlarge systems, the long-range, nonbond interactions: the Coulomb interaction $q_i q_j / r_{ij}$, and the London dispersion $\lambda_i \lambda_j / r_{ij}^6$. [In addition, we consider the shielded Coulomb interaction $q_i q_j / r_{ij}^2$ which is used to replace the Coulomb interactions in an approximate treatment of solvent effects in calculations of large biological molecules.] The Cell Multipole Method (CMM) treats all these as special cases for the reciprocal power-law class of interactions

$$E = \sum_{i>j} q_i q_j / |\vec{r}_i - \vec{r}_j|^p, \qquad (a-1)$$

where the parameter p is an input to the algorithm, so that the identical program works for any interaction in this case. The CMM efficiently and rapidly calculates

the nonbond interactions for large (million-atom) systems, which we illustrate with calculations on polymers with up to a million atoms.

The Cell Multipole Method. The development of CMM builds upon ideas proposed by Appel[3], Barnes and Hut[4], and Greengard and Rokhlin[5]. The key steps are as follows:

a. Divide space into uniform cells. The box containing all the atoms is divided into M equal-sized cubic cells (Fig. a.1b). A single pass through all atoms generates a doublylinked list that stores grouping information (e.g., which atoms belong to a particular cell).

b. Compute multipole moments for each cell. The interactions of each cell with any other atom outside the cell are represented by the multipole series expansion:[6]

$$V_A^{pole}(\vec{r}) = \frac{Z}{R^p} + \sum_{\alpha} \frac{\mu_\alpha R_\alpha}{R^{p+2}} + \sum_{\alpha,\beta} \frac{Q_{\alpha\beta} R_\alpha R_\beta}{R^{p+4}} + \sum_{\alpha,\beta,\gamma} \frac{O_{\alpha\beta\gamma} R_\alpha R_\beta R_\gamma}{R^{p+6}} + \cdots, \quad (a-2)$$

where R_α are the components of the vector $\vec{R} = \vec{r} - \vec{r}_A$, $\vec{r}_A$ is the center of the cell A, and $\vec{r}$ is any observer position outside the cell. This series is essentially an expansion in terms of d/R, where d is the cell size. The lower-order moments are the charge

$$Z = \sum_i q_i, \quad (a-3)$$

dipoles

$$\mu_\alpha = \sum_i q_i p r_{i\alpha}, \quad (a-4)$$

quadrupoles

$$Q_{\alpha\beta} = \sum_i q_i p \left[(p+2) r_{i\alpha} r_{i\beta} - \delta_{\alpha\beta} r_i^2\right]/2, \quad (a-5)$$

octopoles

$$O_{\alpha\beta\gamma} = \sum_i q_i p(p+2) \left[(p+4) r_{i\alpha} r_{i\beta} r_{i\gamma} - (r_{i\alpha}\delta_{\beta\gamma} + r_{i\beta}\delta_{\gamma\alpha} + r_{i\gamma}\delta_{\alpha\beta}) r_i^2\right]/6 \quad (a-6)$$

etc.[6], where $r_{i\alpha}$ is the α component of the position vector for atom i measured with respect to the center of the cell A.

c. Partition the interactions for all atoms in terms of near fields and far fields. Consider all atoms i in cell C_0. The interaction with any atoms that are in either cell C_0 or one of the $3^3-1=26$ neighbor cells (C_n in Fig. a.1b) is calculated exactly. We refer to these 27 cells as the *near cells* for atom i and refer to all other cells as *far cells*. The potential is accordingly decomposed as $V(\vec{r}_i) = V_{far}(\vec{r}_i) + V_{near}(\vec{r}_i)$, or more explicitly,

$$V(\vec{r}_i) = \sum_{A \in far} V_A^{pole}(\vec{r}_i - \vec{r}_A) + \sum_{j \in near\ cells} \frac{q_j}{|\vec{r}_i - \vec{r}_j|^p}. \qquad (a-7)$$

The computational effort for the explicit evaluation of interactions with near cells is a fixed constant ($\sim 4 \times 27/2 = 54$ terms[7]).

d. Convert multipole fields to Taylor coefficients. To calculate $V_{far}(\vec{r}_i)$ efficiently, we avoid repeating the sum over all far cells for each atom i in cell C_0 by doing a local Taylor series expansion about the center of C_0,

$$\sum_A V_A^{pole}(\vec{r} - \vec{r}_A) = V^{(0)} + \sum_\alpha V_\alpha^{(1)} r_\alpha + \sum_{\alpha,\beta} V_{\alpha\beta}^{(2)} r_\alpha r_\beta + \sum_{\alpha,\beta,\gamma} V_{\alpha\beta\gamma}^{(3)} r_\alpha r_\beta r_\gamma \cdots \equiv V_{C_0}^T(\vec{r}). \qquad (a-8)$$

Here, both the atom position $\vec{r}$ and the the cell position $\vec{r}_A$ are with respect to the center of cell C_0. The Taylor coefficients are computed by expanding each multipole term in $\vec{r}$. Thus, the charge term is expanded as

$$\frac{Z}{|\vec{r} - \vec{r}_A|^p} = V_Z^{(0)} + \sum_\alpha V_{Z\alpha}^{(1)} r_\alpha + \sum_{\alpha,\beta} V_{Z\alpha\beta}^{(2)} r_\alpha r_\beta + \sum_{\alpha,\beta,\gamma} V_{Z\alpha\beta\gamma}^{(3)} r_\alpha r_\beta r_\gamma + \cdots \qquad (a-9a)$$

where

$$V_Z^{(0)} = \frac{Z}{r_A^p}, \qquad (a-9b)$$

$$V_{Z\alpha}^{(1)} = \frac{pZ r_{A\alpha}}{r_A^{p+2}}, \qquad (a-9c)$$

$$V^{(2)}_{Z\alpha\beta} = \frac{pZ}{2r_A^{p+4}}\left\{(p+2)r_{A\alpha}r_{A\beta} - \delta_{\alpha\beta}r_A^2\right\}, \qquad (a-9d)$$

$$V^{(3)}_{Z\alpha\beta\gamma} = \frac{p(p+2)Z}{6r_A^{p+6}}\left\{(p+4)r_{A\alpha}r_{A\beta}r_{A\gamma} - (r_{A\alpha}\delta_{\beta\gamma} + r_{A\beta}\delta_{\gamma\alpha} + r_{A\gamma}\delta_{\alpha\beta})r_A^2\right\}. \qquad (a-9e)$$

The dipole term is expanded as

$$\frac{\vec{\mu}\cdot(\vec{r}-\vec{r}_A)}{|\vec{r}-\vec{r}_A|^{p+2}} = V^{(0)}_{\mu} + \sum_{\alpha} V^{(1)}_{\mu\alpha}r_\alpha + \sum_{\alpha,\beta} V^{(2)}_{\mu\alpha\beta}r_\alpha r_\beta + \sum_{\alpha,\beta,\gamma} V^{(3)}_{\mu\alpha\beta\gamma}r_\alpha r_\beta r_\gamma + \cdots \qquad (a-10a)$$

where

$$V^{(0)}_{\mu} = \frac{-\vec{\mu}\cdot\vec{r}_A}{r_A^{p+2}}, \qquad (a-10b)$$

$$V^{(1)}_{\mu\alpha} = \frac{\mu_\alpha}{r_A^{p+2}} - \frac{(p+2)(\vec{\mu}\cdot\vec{r}_A)r_{A\alpha}}{r_A^{p+4}}, \qquad (a-10c)$$

$$V^{(2)}_{\mu\alpha\beta} = \frac{(p+2)}{2r_A^{p+4}}\left[(\vec{\mu}\cdot\vec{r}_A)\left\{\delta_{\alpha\beta} - \frac{(p+4)}{r_A^2}r_{A\alpha}r_{A\beta}\right\} + (\mu_\alpha r_{A\beta} + \mu_\beta r_{A\alpha})\right], \qquad (a-10d)$$

$$\begin{aligned} V^{(3)}_{\mu\alpha\beta\gamma} = \frac{(p+2)}{6r_A^{p+8}}\,[&(p+4)(\vec{\mu}\cdot\vec{r}_A)\{-(p+6)r_{A\alpha}r_{A\beta}r_{A\gamma} \\ &+(r_{A\alpha}\delta_{\beta\gamma} + r_{A\beta}\delta_{\gamma\alpha} + r_{A\gamma}\delta_{\alpha\beta})r_A^2\} \\ &+(p+4)(\mu_\alpha r_{A\beta}r_{A\gamma} + \mu_\beta r_{A\gamma}r_{A\alpha} + \mu_\gamma r_{A\alpha}r_{A\beta})r_A^2 \\ &-(\mu_\alpha\delta_{\beta\gamma} + \mu_\beta\delta_{\gamma\alpha} + \mu_\gamma\delta_{\alpha\beta})r_A^4]. \end{aligned} \qquad (a-10e)$$

The quadrupole term is expanded as

$$\begin{aligned} &\sum_{\alpha,\beta}\frac{Q_{\alpha\beta}(\vec{r}-\vec{r}_A)_\alpha(\vec{r}-\vec{r}_A)_\beta}{|\vec{r}-\vec{r}_A|^{p+4}} \\ &= V^{(0)}_{Q} + \sum_{\gamma} V^{(1)}_{Q\gamma}r_\gamma + \sum_{\gamma,\lambda} V^{(2)}_{Q\gamma\lambda}r_\gamma r_\lambda + \sum_{\gamma,\lambda,\eta} V^{(3)}_{Q\gamma\lambda\eta}r_\gamma r_\lambda r_\eta + \cdots \end{aligned} \qquad (a-11a)$$

where

$$V^{(0)}_{Q} = \frac{[QRR]}{r_A^{p+4}}, \qquad (a-11b)$$

$$V_{Q\gamma}^{(1)} = \frac{1}{r_A^{p+4}} \left[-2 \sum_\beta Q_{\gamma\beta} r_{A\beta} + (p+4) \frac{[QRR]}{r_A^2} r_{A\gamma} \right], \qquad (a-11c)$$

$$V_{Q\gamma\lambda}^{(2)} = \frac{Q_{\gamma\lambda}}{r_A^{p+4}} - \frac{(p+4)}{2r_A^{p+6}} \left[\delta_{\gamma\lambda}[QRR] + 2 \sum_\alpha Q_{\lambda\alpha} r_{A\alpha} r_{A\gamma} + 2 \sum_\alpha Q_{\gamma\alpha} r_{A\alpha} r_{A\lambda} \right] + \frac{(p+4)(p+6)[QRR]}{2r_A^{p+8}} r_{A\gamma} r_{A\lambda}, \qquad (a-11d)$$

$$V_{Q\gamma\lambda\eta}^{(3)} = \frac{(p+4)(p+6)[QRR]}{6r_A^{p+10}} \left[(p+8) r_{A\gamma} r_{A\lambda} r_{A\eta} - (r_{A\gamma}\delta_{\lambda\eta} + r_{A\lambda}\delta_{\eta\gamma} + r_{A\eta}\delta_{\gamma\lambda}) r_A^2 \right] - \frac{(p+4)(p+6)}{3r_A^{p+8}} \sum_\alpha r_{A\alpha} \left(Q_{\gamma\alpha} r_{A\lambda} r_{A\eta} + Q_{\lambda\alpha} r_{A\eta} r_{A\gamma} + Q_{\eta\alpha} r_{A\gamma} r_{A\lambda} \right) + \frac{(p+4)}{3r_A^{p+6}} (r_{A\gamma} Q_{\lambda\eta} + r_{A\lambda} Q_{\eta\gamma} + r_{A\eta} Q_{\gamma\lambda}) + \frac{(p+4)}{3r_A^{p+6}} \sum_\alpha r_{A\alpha} \left(Q_{\gamma\alpha}\delta_{\lambda\eta} + Q_{\lambda\alpha}\delta_{\eta\gamma} + Q_{\eta\alpha}\delta_{\gamma\lambda} \right), \qquad (a-11e)$$

$$[QRR] = \sum_{\alpha,\beta} Q_{\alpha\beta} r_{A\alpha} r_{A\beta}. \qquad (a-11f)$$

The octopole term is expanded as

$$\sum_{\alpha,\beta,\gamma} \frac{O_{\alpha\beta\gamma} (\vec{r} - \vec{r}_A)_\alpha (\vec{r} - \vec{r}_A)_\beta (\vec{r} - \vec{r}_A)_\gamma}{|\vec{r} - \vec{r}_A|^{p+6}} = V_O^{(0)} + \sum_\lambda V_{O\lambda}^{(1)} r_\lambda + \sum_{\lambda,\eta} V_{O\lambda\eta}^{(2)} r_\lambda r_\eta + \sum_{\lambda,\eta,\nu} V_{O\lambda\eta\nu}^{(3)} r_\lambda r_\eta r_\nu + \cdots \qquad (a-12a)$$

where

$$V_O^{(0)} = -\frac{[ORRR]}{r_A^{p+6}}, \qquad (a-12b)$$

$$V_{O\lambda}^{(1)} = \frac{1}{r_A^{p+8}} \left[-(p+6)[ORRR] r_{A\lambda} + 3r_A^2 \sum_{\alpha,\beta} O_{\lambda\alpha\beta} r_{A\alpha} r_{A\beta} \right], \qquad (a-12c)$$

$$V_{O\lambda\eta}^{(2)} = -\frac{(p+6)[ORRR]}{2r_A^{p+10}} \left[(p+8) r_{A\lambda} r_{A\eta} - r_A^2 \delta_{\lambda\eta} \right] + \frac{3(p+6)}{2r_A^{p+8}} \sum_{\alpha,\beta} r_{A\alpha} r_{A\beta} \left(O_{\eta\alpha\beta} r_{A\lambda} + O_{\lambda\alpha\beta} r_{A\eta} \right) - \frac{3\sum_\alpha O_{\lambda\eta\alpha} r_{A\alpha}}{r_A^{p+6}}, \qquad (a-12d)$$

$$V^{(3)}_{O\lambda\eta\nu} = \frac{(p+6)(p+8)[ORRR]}{6r_A^{p+12}}\left[-(p+10)r_{A\lambda}r_{A\eta}r_{A\nu}\right.$$
$$\left.+(r_{A\lambda}\delta_{\eta\nu}+r_{A\eta}\delta_{\nu\lambda}+r_{A\nu}\delta_{\lambda\eta})r_A^2\right]$$
$$+\frac{(p+6)(p+8)}{2r_A^{p+10}}\sum_{\alpha,\beta} r_{A\alpha}r_{A\beta}\left(O_{\lambda\alpha\beta}r_{A\eta}r_{A\nu}+O_{\eta\alpha\beta}r_{A\nu}r_{A\lambda}+O_{\nu\alpha\beta}r_{A\lambda}r_{A\eta}\right)$$
$$-\frac{(p+6)}{2r_A^{p+8}}\sum_{\alpha,\beta} r_{A\alpha}r_{A\beta}\left(O_{\lambda\alpha\beta}\delta_{\eta\nu}+O_{\eta\alpha\beta}\delta_{\nu\lambda}+O_{\nu\alpha\beta}\delta_{\lambda\eta}\right)$$
$$-\frac{(p+6)}{r_A^{p+8}}\sum_{\alpha} r_{A\alpha}\left(O_{\lambda\eta\alpha}r_{A\nu}+O_{\eta\nu\alpha}r_{A\lambda}+O_{\nu\lambda\alpha}r_{A\eta}\right)$$
$$+\frac{O_{\lambda\eta\nu}}{r_A^{p+6}}, \qquad (a-12e)$$

$$[ORRR] = \sum_{\alpha,\beta,\gamma} O_{\alpha\beta\gamma}r_{A\alpha}r_{A\beta}r_{A\gamma}. \qquad (a-12f)$$

$V^{(0)}$ is then the sum of all constant terms, $V^{(1)}$ is the sum of the linear coefficients of $\vec{r}$, $V^{(2)}$ is the sum of the quadratic coefficients of $\vec{r}$, and $V^{(3)}$ is the sum of the cubic coefficients of $\vec{r}$, as follows:

$$V^{(0)} = V_Z^{(0)} + V_\mu^{(0)} + V_Q^{(0)} + V_O^{(0)}, \qquad (a-13a)$$

$$V_\alpha^{(1)} = V_{Z\alpha}^{(1)} + V_{\mu\alpha}^{(1)} + V_{Q\alpha}^{(1)} + V_{O\alpha}^{(1)}, \qquad (a-13b)$$

$$V_{\alpha\beta}^{(2)} = V_{Z\alpha\beta}^{(2)} + V_{\mu\alpha\beta}^{(2)} + V_{Q\alpha\beta}^{(2)} + V_{O\alpha\beta}^{(2)}, \qquad (a-13c)$$

$$V_{\alpha\beta\gamma}^{(3)} = V_{Z\alpha\beta\gamma}^{(3)} + V_{\mu\alpha\beta\gamma}^{(3)} + V_{Q\alpha\beta\gamma}^{(3)} + V_{O\alpha\beta\gamma}^{(3)}. \qquad (a-13d)$$

This is repeated for all far cells. $V_{C_0}^T(\vec{r})$ thus contains interactions that are due to *all* atoms except those in the 27 near cells, which are evaluated as in (a-7). The derivatives of the Taylor series give the force, the Hessian, etc.

A particular advantage of this simple algorithm is that the far-field portion (represented by the Taylor series) changes very little during dynamics or minimization. Thus, one can use the same Taylor coefficients (without updating) for a number of dynamical time steps (say 100), reducing the computation essentially to

those of nearby atoms. We have tested this approach for calculations on polymers and find that updating at periods of 100 time steps, the force errors are no larger than 5% (compared to the force that would occur if the Taylor coefficients were computed anew each time step). To avoid ambiguities, the timings reported herein include all far-field interactions computed at each step and hence do *not* incorporate this advantage.

e. Group cells into progressively larger cells. For situations where the Taylor coefficients need to be computed anew at each time step, the calculation of $V_{C_0}^T(\vec{r})$, by summation over M–27 far cells (step d) is slow since it is an order-N operation. Such straightforward summation is very inefficient because the interactions from a very distant cell (with small d/R) are computed much more accurately than the interaction from a cell just two units away (with large d/R). An optimum arrangement is to use larger cell sizes for more distant regions such that d/R remains approximately constant.

To utilize larger cells automatically for more distant regions requires a simple scheme for grouping cells into progressively larger cells. This is achieved by introducing a family of cells[4,5], as shown in Fig. a.1c. Step a is modified slightly. The entire (cubic) space is considered a cell at level 0. This cell is divided into 8 children cells (level 1) each of which is further divided into 8 grandchildren cells (level 2), etc. Finally, at the deepest level L we have $M = 8^L$ cells; each contains only a few (say 4) atoms. Thus, a million atoms require $L \simeq log_8(10^6/4) \simeq 6$ levels. Fig. a.1c shows a four-level system. The level 2 cells are denoted as A, the level 3 cells are denoted as B, and level 4 cells as C. For C_0, the original $16^3 - 3^3$=4069 far cells are reduced to 415 cells ($37A$, $189B$, $189C_i$). [For the million-particle system, each level-6 cell interacts with 189 cells at levels 3 through 6 and 37 at level 2 for a total of 1171 cells instead of the original 262117 cells.]

Once multipoles of level l cells ($Z^{(l)}, \vec{\mu}^{(l)}, Q^{(l)}, O^{(l)}$, ...) are calculated, multipoles of level $l-1$ cells are obtained by translating and adding those of children cells, which are level l cells, as follows. Let $\vec{R}_l$ be a vector from the center of the level $l-1$ cell to the center of one of its children cells at level l. Also let $\vec{r}_{li}$ be a position vector of the ith atom in the lth child cell measured from the center of that cell. That atom has charge q_{li}. Then, from the definitions of multipoles, we have multipoles of level $l-1$ cells as follows:

$$Z^{(l-1)} = \sum_{l,i} q_{li} = \sum_{l} Z^{(l)}, \qquad (a-14a)$$

$$\begin{aligned} \mu_\alpha^{(l-1)} &= p \sum_{l,i} q_{li}(r_{li\alpha} + R_{l\alpha}) \\ &= \sum_l \mu_\alpha^{(l)} + p \sum_l Z^{(l)} R_{l\alpha}, \end{aligned} \qquad (a-14b)$$

$$\begin{aligned} Q_{\alpha\beta}^{(l-1)} &= p \sum_{l,i} q_{li} \left\{ (p+2)(r_{li\alpha} + R_{l\alpha})(r_{li\beta} + R_{l\beta}) - (\vec{r}_{li} + \vec{R}_l)^2 \delta_{\alpha\beta} \right\} /2 \\ &= \sum_l Q_{\alpha\beta}^{(l)} \\ &+ \sum_l \left\{ (p+2)(\mu_\alpha^{(l)} R_{l\beta} + \mu_\beta^{(l)} R_{l\alpha}) - 2(\vec{\mu}^{(l)} \cdot \vec{R}_l)\delta_{\alpha\beta} \right\} /2 \\ &+ p \sum_l Z^{(l)} \left\{ (p+2) R_{l\alpha} R_{l\beta} - R_l^2 \delta_{\alpha\beta} \right\} /2, \end{aligned} \qquad (a-14c)$$

$$\begin{aligned} O_{\alpha\beta\gamma}^{(l-1)} &= p(p+2) \sum_{l,i} q_{li} \left[(p+4)(r_{li\alpha} + R_{l\alpha})(r_{li\beta} + R_{l\beta})(r_{li\gamma} + R_{l\gamma}) \right. \\ &\left. - \{(r_{li\alpha} + R_{l\alpha})\delta_{\beta\gamma} + (r_{li\beta} + R_{l\beta})\delta_{\gamma\alpha} + (r_{li\gamma} + R_{l\gamma})\delta_{\alpha\beta}\} (\vec{r}_{li} + \vec{R}_l)^2 \right] /6 \\ &= \sum_l O_{\alpha\beta\gamma}^{(l)} \\ &+ \sum_l [QR]_{\alpha\beta\gamma}^{(l)} \\ &+ (p+2) \sum_l \left[(p+4)(\mu_\alpha^{(l)} R_{l\beta} R_{l\gamma} + \mu_\beta^{(l)} R_{l\gamma} R_{l\alpha} + \mu_\gamma^{(l)} R_{l\alpha} R_{l\beta}) \right. \end{aligned}$$

$$-2(\vec{\mu}^{(l)} \cdot \vec{R}_l)(R_{l\alpha}\delta_{\beta\gamma} + R_{l\beta}\delta_{\gamma\alpha} + R_{l\gamma}\delta_{\alpha\beta})$$
$$-R_l^2(\mu_\alpha^{(l)}\delta_{\beta\gamma} + \mu_\beta^{(l)}\delta_{\gamma\alpha} + \mu_\gamma^{(l)}\delta_{\alpha\beta})\Big]/6$$
$$+p(p+2)\sum_l Z^{(l)}[(p+4)R_{l\alpha}R_{l\beta}R_{l\gamma}$$
$$-(R_{l\alpha}\delta_{\beta\gamma} + R_{l\beta}\delta_{\gamma\alpha} + R_{l\gamma}\delta_{\alpha\beta})R_l^2]/6. \qquad (a-14d)$$

In the last equation,

$$[QR]^{(l)}_{xxx} = (p+2)Q^{(l)}_{xx}R_{lx} - 2Q^{(l)}_{xy}R_{ly} - 2Q^{(l)}_{xz}R_{lz}, \qquad (a-14e)$$

$$[QR]^{(l)}_{xxy} = \left(\frac{p+4}{3}Q^{(l)}_{xx} - \frac{2}{3}Q^{(l)}_{yy}\right)R_{ly} + \frac{2(p+3)}{3}Q^{(l)}_{xy}R_{lx} - \frac{2}{3}Q^{(l)}_{yz}R_{lz}, \qquad (a-14f)$$

$$[QR]^{(l)}_{xyz} = \frac{p+4}{3}(Q^{(l)}_{xy}R_{lz} + Q^{(l)}_{yz}R_{lx} + Q^{(l)}_{zx}R_{ly}), \qquad (a-14g)$$

and other components are obtained by permuting indices.

In these equations, the sum is over eight children cells. By using these equations from cells of the deepest level L successively, we can obtain multipoles of all cells in all levels. Thus, multipoles for B-level cells are obtained by translating and adding those of C-level cells, and those of A-level cells are obtained from B-level cells.

The sum over the 415 cells to obtain (a-8) is calculated using an approach analogous to the method of Greengard and Rokhlin[5]. (One can also directly compute (a-8) without shifting origin, similar to the method of Barnes and Hut[4].)

Consider a particular level 4 cell, C_0, and denote its parent and grandparent as B_0 and A_0, respectively. First we focus on A_0 (level 2). All cells labeled A in Fig. a.1c are far cells of A_0, and their contribution to the Taylor series of A_0 can be directly summed over the $4^3 - 3^3 = 37$ cells, by using (a-8): $V^T_{A_0}(\vec{r}) = \sum_A V^{pole}_A(\vec{r} - \vec{r}_A)$. Next we focus on the Taylor series of the level-3 cell B_0. It is computed as

$$V^T_{B_0}(\vec{r}) = V^T_{A_0}(\vec{r} + \vec{r}_0) + \sum_B V^{pole}_B(\vec{r} - \vec{r}_B), \qquad (a-15)$$

where $V_{A_0}(r)$ is the far field for A_0, shifted by r_0 to the center of B_0. The sum of Taylor coefficients is over $8 \times 27 - 27 = 189$ B cells, whose parents are nearest-neighbors of A_0 but themselves are not nearest-neighbors to B_0. $V_{B_0}^T$ represents the fields that are due to all atoms in cells labeled A or B in Fig. 1c. This procedure is then repeated at level 4 for C_0 to obtain the Taylor series for C_0. Excepting the level 2 cells A, all far cells to C_0 are computed in the series of sums (a-15), each over a 189-cell domain with cell-size (d), which reduces gradually as the distance to C_0 (R) becomes closer. During this process, d/R is approximately a constant ~ 0.5, an optimum condition when the multipole series (a-2) is used to sum over many groups of charges. This completes the algorithm.

The timing of the algorithm is estimated as follows[5]. For the assignment of atoms to the deepest-level cells and calculations of the multipole moments of these cells, a single loop over all atoms is used; hence the calculation time is proportional to N. The calculations of the multipoles of lower-level cells involve the manipulation of poles of 8 children cells. At level l, calculation time is proportional to $8 \times 8^l = 8^{l+1}$, since there are 8^l cells at this level. Total time of this operation is proportional to $\sum_{l=0}^{L} 8^{l+1} = 8(8^L - 1)/7 = 8(N/a - 1)/7$. Here, L is the maximum level and $a \simeq 4$ is the average number of atoms in the deepest level cell. Therefore, this operation is proportional to N. The calculations of Taylor expansion coefficients of each cell involve a maximum of 189 cells. The time is proportional to $\sum_{l=2}^{L} 189 n_T 8^l = 189 n_T \times 8(8^L - 8)/7 = 189 n_T \times 8(N/a - 8)/7$. Here, n_T is the number of Taylor coefficients used. Therefore, this is again proportional to N. We have to shift the Taylor coefficients 8 times for each parent cell; this shifting time is proportional to $\sum_{l=2}^{L-1} 8 n_T 8^l = n_T 8(8^L - 8)/7 = n_T 8(N/a - 8)/7$, and thus is proportional to N. Once the Taylor coefficients of the deepest level cells are obtained, the potential at the atomic position is evaluated by a single loop over all atoms, whose time is proportional to $n_T N$. Finally, for each atom we have to evaluate the exact potential

from atoms in 27 neighbor cells at the deepest level. An estimated number of interactions for each atom is $27a/2$; therefore, the total time for this operation is proportional to $27aN/2$. Since the calculation time of all operations is proportional to N, the total calculation time is proportional to N.

Discussion. Grouping objects into larger rectangular boxes as the distance increases was first implemented by Appel[3] as an important application of tree structures to the gravitation problem. It reduces the computations to order $Nlog(N)$. Barnes and Hut[4] devised an efficient algorithm of using cubic boxes and recursively opening up smaller boxes based on a geometric criterion that keeps the expansion parameter d/R at a fixed number close to 1. To further reduce the computation to order N, Greengard and Rokhlin[5],Greengard[8] introduced a local Taylor expansion and demonstrated it for a two-dimensional problem (using complex variables so that the expansion series is particularly simple).

These adoptive tree-structured methods have been applied mostly in gravitational problems, which typically lack intrinsic scales and often exhibit diverse structures and large density fluctuations. In contrast, molecular systems and crystals typically have clear length scales, and their structures are more stable and the density fairly uniform. These characteristics suggest that uniform cells should be adequate. We use the multipole expansions as in electrostatics[9], where the charge, dipole, and quadrupoles, etc., have clear physical content and are easy to manipulate. The CMM algorithm is a further development over the two-dimensional method of Greengard and Rokhlin, but with a simpler structure and capable of treating all interactions with a single program. The resulting algorithm is very efficient in execution and scales linearly with N with a very small proportional constant; thus, even for the 1792-atom case, CMM is already six times faster than the exact method. We find that terminating the expansions at quadrupole moments is

quite adequate. Independent developments for the three-dimensional problem have been reported[8,10], but the use of spherical harmonics[8] or partial derivatives[10] makes these algorithms rather complex.

Although the relation between a cell and the eight subcells leads to a tree structure, we find it more useful and efficient to use a Cartesian integer system to index cells at each level. This index system alleviates the use of recursive subroutine calls in the computer program (which is written in FORTRAN), and the calculation easily proceeds cell after cell at each level, and then, level after level. The Cartesian indexing also greatly facilitates algorithm improvements and verification.

This structure of the CMM algorithm allows most parts to be easily vectorized. In addition, CMM is particularly simple to adapt to parallel computers, when the processors are connected as a 4×4×4 (8×8×8 or 16×16×16, etc.) grid. In this case, the three-dimensional space is naturally mapped into the processors and the deeper levels work independently. Because the computations are dominated by the deeper-level cells and by pairwise interactions that are well localized in near-neighbor processors, we expect high efficiency.

Application to a Million-Atom Polymer. The speed and accuracy for CMM were assessed by calculations of a realistic polymer system, poly(vinylidene fluoride), denoted PVDF. PVDF has chains of $(-CH_2-CF_2-CH_2-CF_2-)$ packed together and exhibits at least four stable crystalline forms of which three are piezoelectric. We started with form I (which has a net dipole per unit cell) and constructed clusters as multiples of the crystallographic unit cell [2.56 × 8.58 × 4.91 Å with 12 atoms (2 chains)]. Thus, combining 9×4×4 = 144 cells leads to 1728 atoms in 32 chains. We add an H or F at the end of the chain to make ($-CH_3$ or $-CF_3$), leading to a total of 1792 atoms and a size of 24.2 by 34.2 by 21.4 Å. We constructed progressively larger systems with 15360 atoms, 122880 atoms, and 1013760 atoms.

The last system with one million atoms has 66×32×40 cells and a size of 168 × 272 × 196 Å.

The total computation time divided by N is shown in Fig. a.2. The CPU time of the CMM algorithm is linear with N, whereas the exact algorithm computes $N(N-1)/2$ pairs[7]. For the 1013760-atom case, CMM is a factor of 1500 faster than the exact method (even for the 1792 atom, CMM is already six times faster). All tests were carried out using a single *scalar* processor on the Silicon Graphics 4D/380 workstation, where the million-atom system required 51 minutes for CMM versus 1280 hours for the exact calculation (estimated from the 1792 atom case).

A typical dynamical simulation involves calculations of the force on each atom (and the total energy). The accuracy is controlled by the orders in the multipoles (a-2) and the Taylor series (a-8), which we implemented through third order (the octopole level). Our estimates and explicit tests indicate that it is best that these two orders be equal. At the second order (third order) for the Coulomb interaction, the error in total energy is 0.014% (0.006%) while the rms error in force is 0.36% (0.17%). For the London dispersion, errors in both energy and force are extremely small (2×10^{-6} and 6×10^{-7}) at second order and a factor of two smaller at third order. This decrease in errors by a factor of two is expected since the multipole series is essentially an expansion in term of $d/R \sim 0.5$. The accuracy at the second order is already a factor of 5 to 10 times more accurate than standard approximations (spline cutoffs, *vide infra*). Thus, we consider the quadrupole order to be adequate and report all results in this paper at this level (unless stated otherwise).

The memory usage of the CMM is $140M+8N$ bytes, for storing multipoles, Taylor coefficients, and cell indices, where M is the total number of cells. Including $28N$ for coordinates, charges and force, and assuming $M \simeq N/4$ (optimum choice), the total memory is $\sim 43N$ bytes [keeping all quantities in fast memory, our program

requires 45 MBytes for $N = 1$ million].

The Cutoff Method. The most common approach for treating the Coulomb interactions of large molecules is the cutoff method[11,12], which evaluates exactly all contributions that are due to the nearby atoms (up to r_{in}), while those atoms beyond r_{out} are ignored completely. Between r_{in} and r_{out}, typically[11,12] $r_{out} - r_{in} \sim$ 1Å, a cubic spline function $S(r^2)$ is used to take the potential smoothly to zero, where

$$S(r^2) = 1, \; r \leq r_{in} \qquad (a-16a)$$

$$S(r^2) = \frac{(r_{out}^2 - r^2)^2 (r_{out}^2 + 2r^2 - 3r_{in}^2)}{(r_{out}^2 - r_{in}^2)^3}, \; r_{in} < r < r_{out} \qquad (a-16b)$$

$$S(r^2) = 0, \; r \geq r_{out}. \qquad (a-16c)$$

This method requires an order N^2 search to establish a near-neighbor list. Although the time for setting up this list could be ignored (the list is refreshed infrequently), the list requires a substantial memory to store (several gigabytes for one million atoms). Given r_{out}, the average number of atoms with which each atom interacts is roughly independent of the total number N. Thus, the computation time and storage are linear in N. However, as r_{out} increases, the proportional constants of these linear relations increase very quickly (as r_{out}^3), whereas, the errors decrease[14] as $r_{out}^{-1/2}$. In Figure a.3, calculation time and memory for 1792-atom PVDF are shown as a function of r_{out}, with those of CMM. If the size of the system is much larger than r_{out}, time and memory would be proportional to r_{out}^3, but in this case, the size of the system is not very large ($\simeq$ 30 Å) so that the relations are almost linear in the range of r_{out} shown in the figure. The time of CMM is 1.4 times faster than that of the cutoff method even at a small cutoff distance $r_{out} = 10.5$ Å (2.7 seconds vs. 3.8 seconds). Also CMM requires only 10 % of memory compared with the cutoff method at $r_{out} = 10.5$ Å (0.146 MB vs. 1.43 MB).

The cutoff method leads to large errors. Using the common choice[11] in the spline cutoff method [(r_{in}, r_{out})= (9.5Å, 10.5Å)] for the 1792-atom PVDF, the rms force error is 43.8 [units are (kcal/mol)/Å for force and kcal/mol for energy], while the corresponding error in CMM is 0.411 (0.218 at third order), two orders of magnitude lower. The error in total energy is also large −4666.31 for cutoff versus −18.6 for CMM (−4.7 at third order). Although use of larger cutoffs can decrease the error, we find that the errors remain at least five times larger than the CMM. Thus the cutoff method is incapable of providing the accurate results of CMM. (In addition, more accurate cutoff requires $\sim$ 15 times more storage and 10 times the computer time than CMM.) In Figure a.4, rms force errors as a function of r_{out} are shown. Here, given r_{out}, the rms force errors are calculated for three different values of $\Delta = r_{out} - r_{in}$. For a given r_{out}, the rms force error decreases as Δ increases. Also for a given Δ, the rms error decreases[14] according to $r_{out}^{-1/2}$. CMM gives a 5.7 times smaller error compared with the best case in the figure (r_{out} = 25 Å,Δ = 5 Å).

Perhaps more significant than the errors in force, the long-range tails in the interactions ignored in the cutoff methods can have profound effects on thermodynamical properties[12] and can lead to large errors in structures. Thus, in Fig. a.5, we compare the minimized structures for the 1792-atom cluster of PVDF. We see here that CMM produces a structure almost identical to the exact calculation (rms deviation 0.061 Å). For the spline cutoff method, two different calculations using different spline functions (Δ = 2 Å and 5 Å) are shown. Both spline functions give visibly distorted structures, although a structure obtained by larger Δ is less distorted (rms deviation 0.812 Å for Δ=1 Å and 0.639 Å for Δ = 5 Å). [In all cases the minimization started with the exact structure.]

Summary. The Cell Multipole Method is an efficient and practical approach to

handle long-range interactions, as demonstrated with calculations (on a laboratory workstation) of systems having up to a million atoms. This method should be applicable for a wide range of materials simulations. The computer used here (Silicon Graphics 4D/380, one processor, 5 Mflops[13]) is well short of the state of the art (Cray YMP,one processor, 160 Mflops[13]). The vectorization and parallelization capability intrinsic to CMM should allow further gains of 10–20 in speed to be achieved on existing super computers (Cray YMP, 8 processor, 2Gflops[13] or Intel Delta 512 nodes, 3Gflops). Thus, we believe that CMM will allow atomic-level simulations on million-atom systems to become quite practical.

References

(1) Hockney, R. W.; Eastwood, J. W. *Computer Simulation Using Particles* (Mc-Graw-Hill, New York, 1981). Allen, M. P.; Tildesley, D. J. *Computer Simulation of Liquids* (Oxford University Press, Oxford, 1987).

(2) Sharp, K.; Fine, R.; Honig, B. *Science,* **1987,** *236,* 1461. Tomalia, D. A.; Naylor, A. M.; Goddard III, W. A. *Angew. Chem. Int. Ed. Engl.,* **1990,** *29,* 138.

(3) Appel, A. W. *SIAM J. Sci. Stat. Comput.,* **1985,** *6,* 85.

(4) Barnes, J. E.; Hut, P. *Nature,* **1986,** *324,* 446.

(5) Greengard, L.; Rokhlin, V. I. *J. Comput. Phys.,* **1987,** *73,* 325.

(6) The series is derived by writing $|\vec{R}-\vec{r}|^{-p} = R^{-p}[1+(-2\vec{r}\cdot\vec{R}/R^2+r^2/R^2)]^{-p/2}$ and treating the terms in the parentheses as a small quantity. The multipoles are obtained by writing quantities such as $(\vec{r}\cdot\vec{R})^2$ as scalar products of tensors and then symmetrizing the tensors with respect to x, y, z components.

(7) The pairwise evaluation of energy and force is arranged such that each pair is computed only once, leading to the factor 1/2.

(8) Greengard, L. *The Rapid Evaluation of Potential Fields in Particle Systems* (MIT Press, Cambridge, Mass., 1988).

(9) Jackson, J. D. *Classical Electrodynamics* (Wiley and Sons, New York, 1962).

(10) Zhao, F. Master thesis, MIT Artificial Intelligence Lab Report 995 ,1987.

(11) Weiner, P.; Kollman, P. *J. Comp. Chem.,* **1981,** *2,* 287.

(12) Brooks, C. L.; Pettitt, B. M.; Karplus, M. *J. Chem. Phys.,* **1985,** *83,* 5897. Brooks, C. L. *J. Chem. Phys.,* **1987,** *86,* 5156.

(13) Based on LINPACK numbers of J.J. Dongarra.

(14) Ding, H.; Karasawa, N.; Goddard III, W. A. "Optimal Spline Cutoffs for Coulomb and van der Waals Interactions", *J. Chem. Phys.,* submitted for publication.

Figure Captions

Fig. a.1. Cell hierarchy for CMM. All cells are 3D cubes.

Fig. a.2. Computational costs for calculation of the Coulomb nonbond interactions for a series of poly(vinylidene fluoride) polymers (N = 1792, 15360, 122880, and 1013760 atoms).

Fig. a.3. Computational time and memory usage of cutoff method as functions of r_{out} compared with CMM.

Fig. a.4. RMS force error of cutoff method as functions of r_{out} with different $\Delta = r_{out} - r_{in}$ compared with CMM.

Fig. a.5. Optimized structures for the 1792-atom PVDF polymer with exact (a), CMM (b) and spline (r_{out},r_{in}) cutoff methods (c and d). This shows 8 layers of chains, most of which are in the shadow of the top layer (for accurate calculations). Optimizations for CMM and spline cutoff methods started with the exact structure.

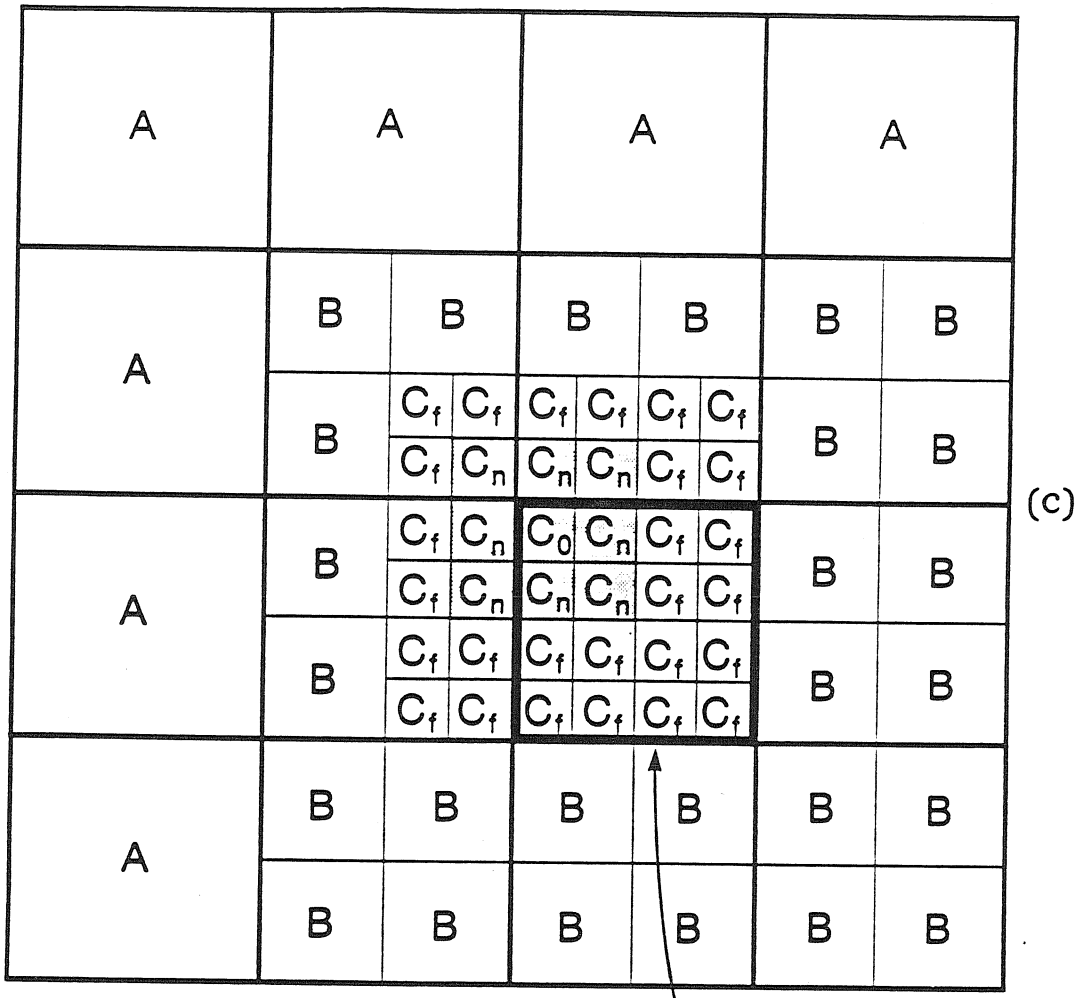

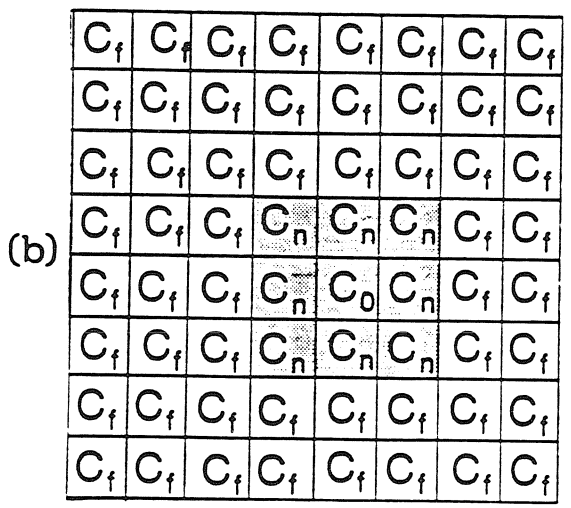

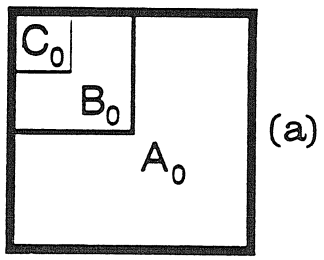

Figure a.1

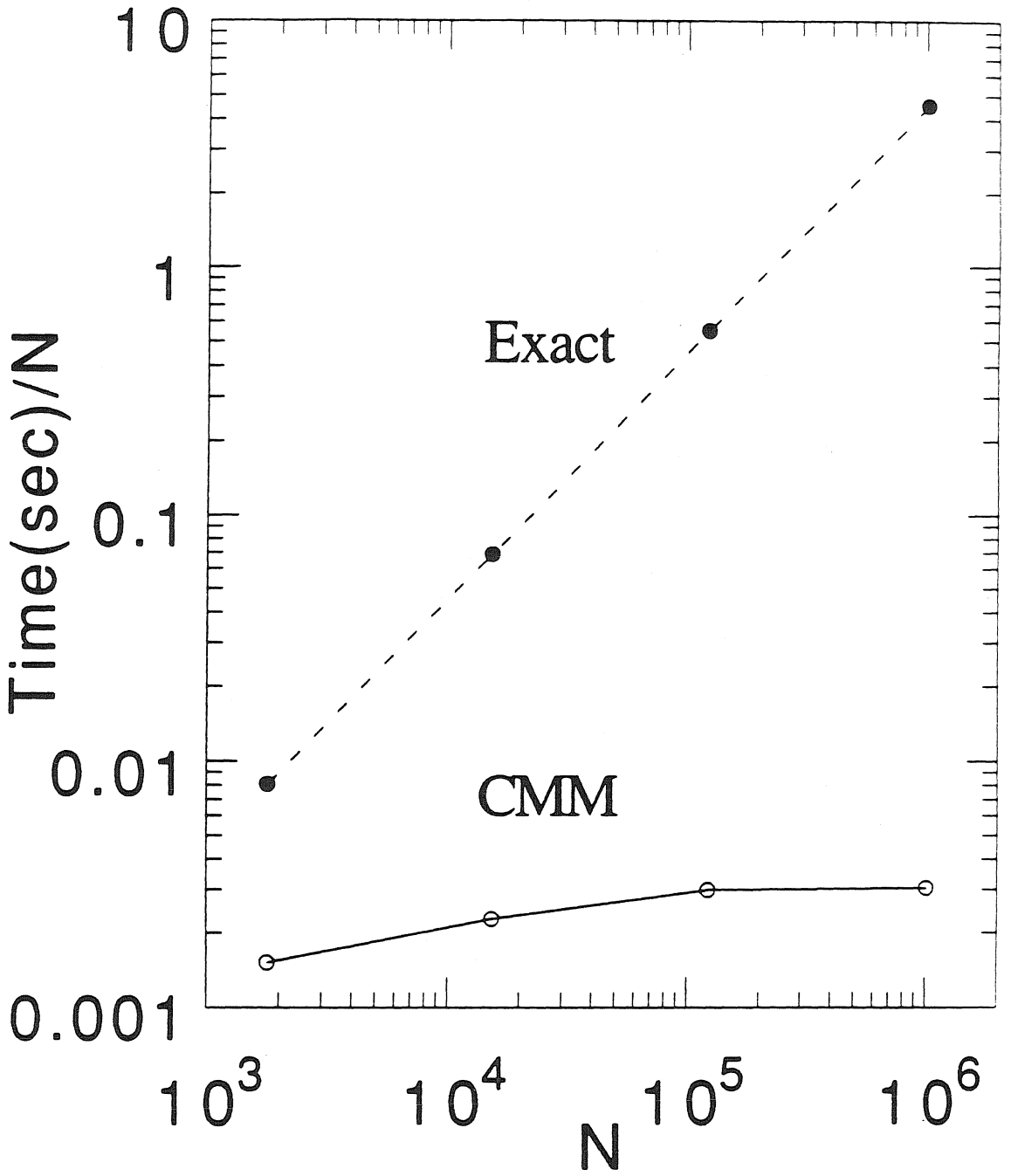

Figure a.2

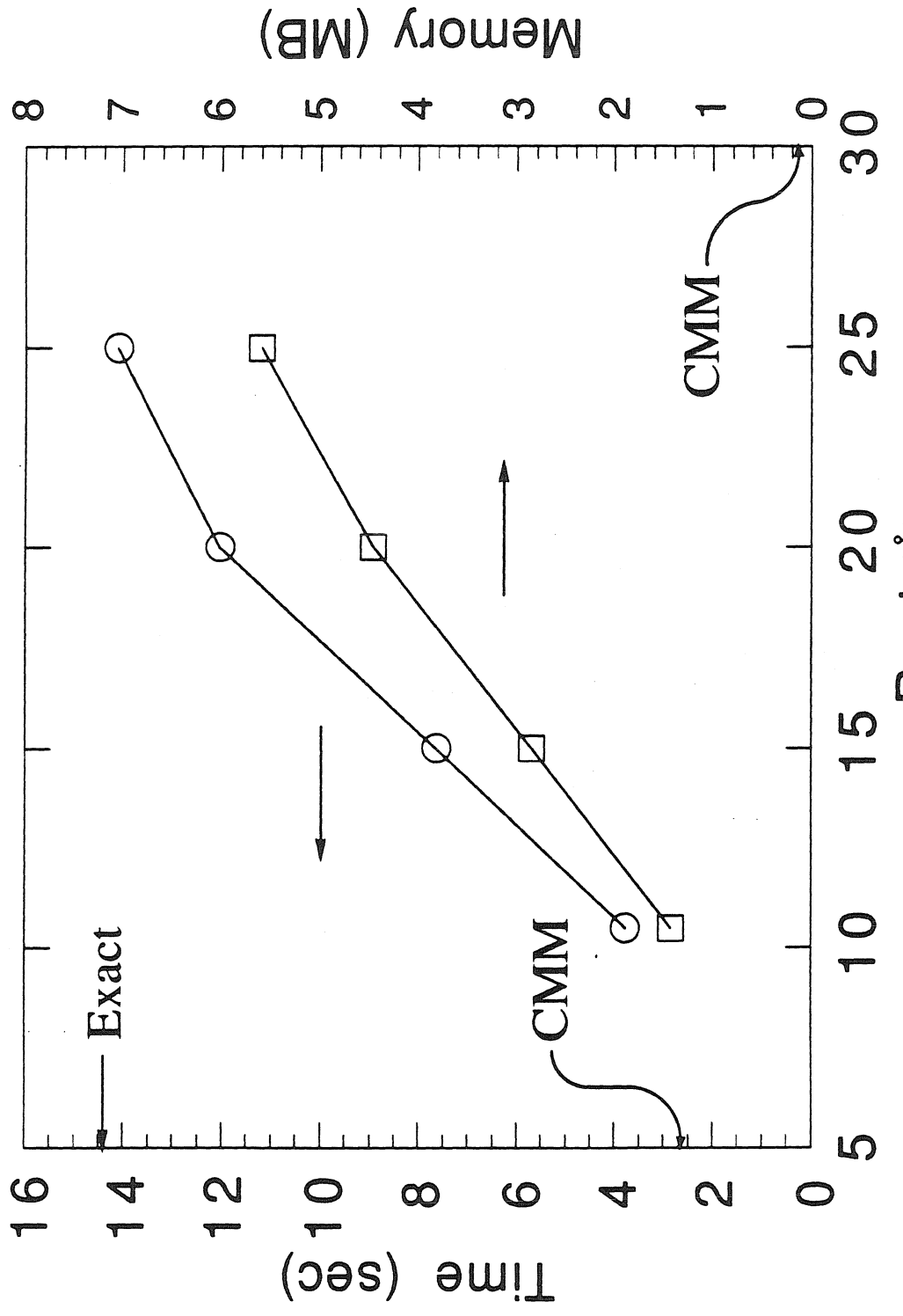
Time (sec)
Memory (MB)
Rout (Å)
Exact
CMM
CMM
0
2
4
6
8
10
12
14
16
0
1
2
3
4
5
6
7
8
5
10
15
20
25
30

Figure a.3

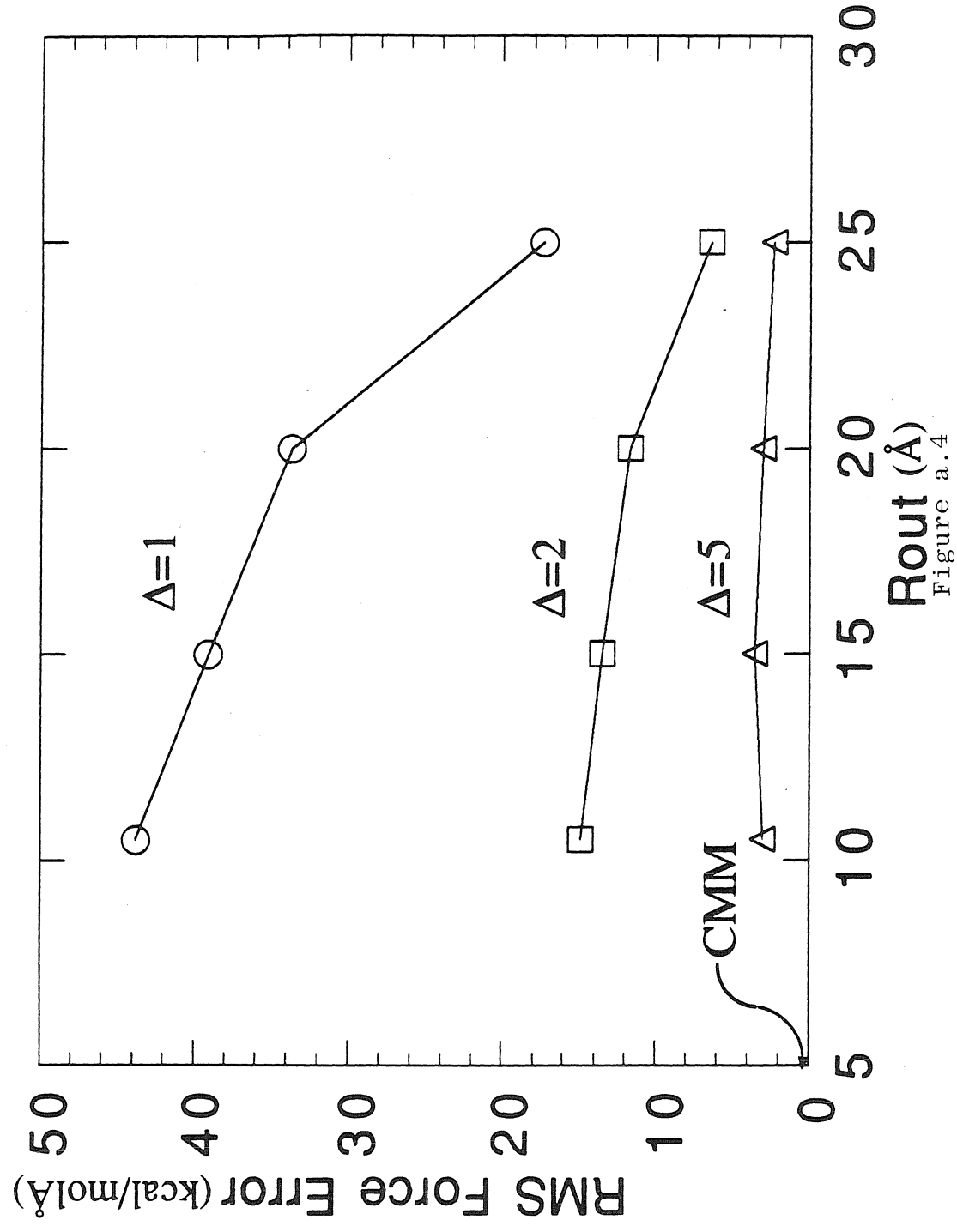
RMS Force Error (kcal/molÅ)
0
10
20
30
40
50
5
10
15
20
25
30
Rout (Å)
Δ=1
Δ=2
Δ=5
CMM

Figure a.4

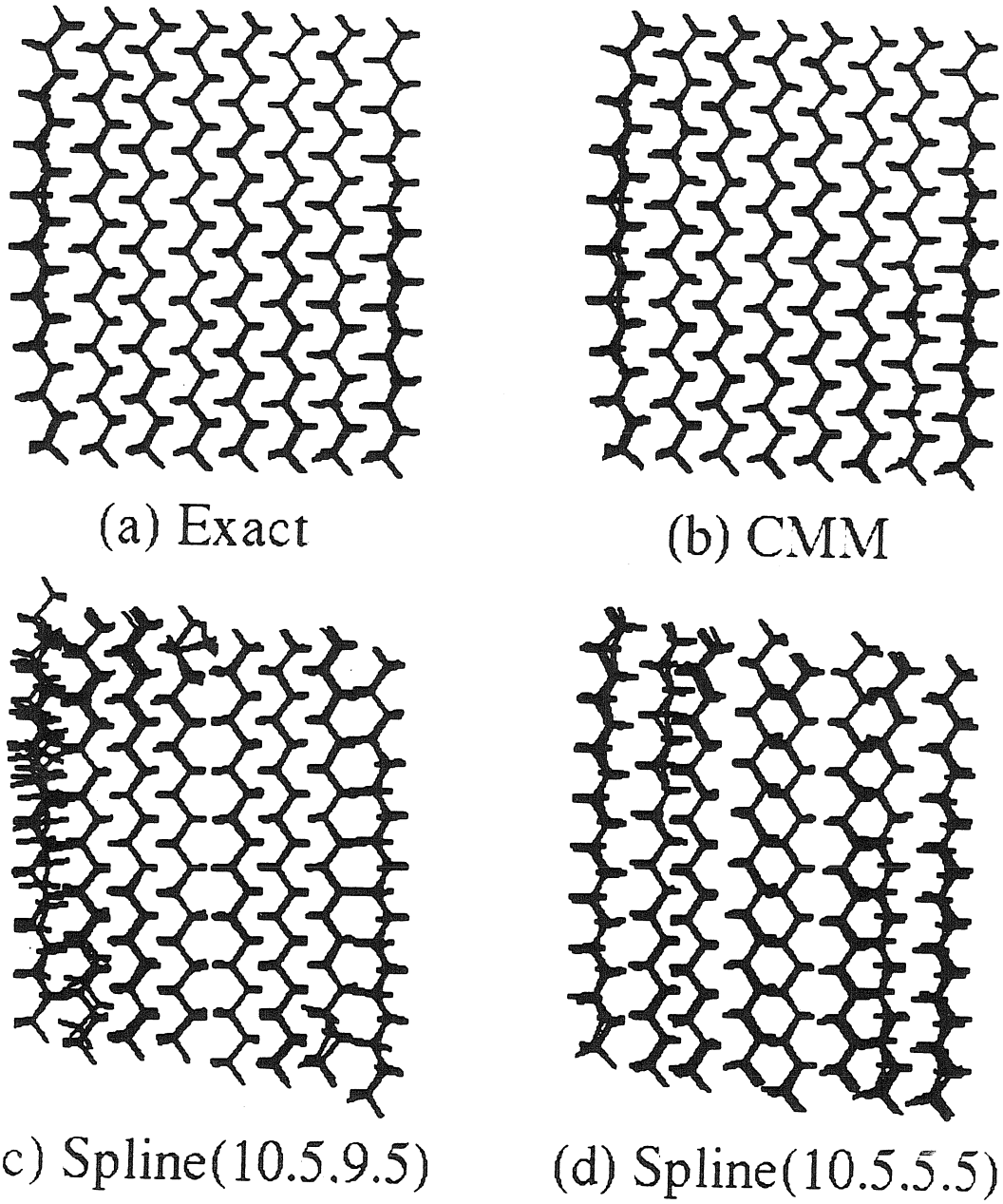

Figure a.5

(b) The Cell Multipole Method for Coulomb Interactions in Periodic Systems with Million-Atom Unit Cells

Abstract

Standard methods for calculating Coulomb interactions of periodic systems use Ewald-type formulations or Minimum Image approximations, neither of which is practical for megacrystals (million atoms per unit cell). Here we describe the Cell Multipole Method for Periodic Systems, which for a polymer with one million atoms per cell is more than 700 times faster than either the Ewald or Minimum Image methods, making megacrystal calculations practical. The method is well suited for massively parallel and vector computers.

Introduction. Atomic-level simulations of *periodic* materials are typically limited to hundreds or thousands of atoms, whereas studies of such problems as partially amorphous polymers might require 10^5 or 10^6 atoms per unit cell. The most difficult problem with infinite crystals is computing the Coulomb interactions $V_i = \sum_j' q_j/R_{ij}$, which are conditionally convergent. The most general approach is the Ewald method[1,2], which separates the Coulomb sum into two parts, one of which converges rapidly in the real space, and the other which converges rapidly in the reciprocal space (Fourier transforms). The potential calculated by the Ewald method corresponds to the limiting value inside the crystal made of a charge-repeating unit whose charge, dipoles, quadrupoles, and second moments all vanish[7]; therefore, the potential is shape and surface character-independent. Moreover, the potential is periodic and its average inside the unit cell is zero[1]. The Ewald potential is called the intrinsic potential[8]. However, the calculation time for Ewald is $T = C_{real}R_{cut}^3N + C_{reci}k_{cut}^3N^2$, where N is the number of atoms in the unit cell, R_{cut} and k_{cut} are cutoffs for the sums in the real and the reciprocal space, and C_{real} and C_{reci} are constants (see Appendix A.). The presence of the quadratic terms renders the Ewald impractical for megacrystals (million atoms per unit cell).

Because the Ewald calculation is so time-consuming, many simulations use the Minimum Image Approximation[3,4]. In Minimum Image, any given atom A interacts with only $N-1$ atoms, each of which is either the atom in the central cell or one of its 26 images in neighboring cells, depending on which is closest to A. This method gives approximate potential of the crystal whose shape (of the infinite crystal) is cubic. Since dipoles and quadrupoles are not zero in general in the unit cell, it gives a different potential and force from those of the Ewald method (see Table I). It requires $N(N-1)/2$ pairwise calculations, so that it is also impractical for megacrystals.

In this paper, we propose a new and efficient approach, the Cell Multipole

Method for Crystals (CMMX), to compute the Coulomb and van der Waals interactions (in fact, it handles all interactions of the type $E = \sum_{ij} q_i q_j / |\mathbf{r}_i - \mathbf{r}_j|^p$, where, $p \geq 1$). The main elements of CMMX are that it:

i. use the Reduced Set of $P = 35$ atoms to replace all distant unit cells;

ii. represent the interactions from all distant cells by a Taylor series;

iii. compute the interactions from neighboring cells through the Cell Multipole Method recently developed for finite systems[5].

The standard Ewald procedure is applied only to the Reduced Set so that the calculation time becomes a fixed constant independent of the system (2 seconds on a SGI 380 workstation for 1 million atoms).

Reduced Set. The central unit cell plus its 26 neighbor cells are referred to as *neighbor* cells (see Fig. b.1). The remaining $\infty - 27$ cells are referred to as *distant* cells. In each distant cell, we replace the original N atoms with a Reduced Set of P virtual charges, which have the same dipoles, quadrupoles,$\cdots$, up to Kth-order multipoles (with $K \geq 2$) as the original cell.

The principle behind this Reduced Set approach is that the difference between the Reduced Set system and the original system involves only high-order multipole and is both small and absolutely convergent. All subtleties associated with the conditional convergence of Coulomb sums are taken care of by the P charges in the reduced set, which is evaluated with the standard Ewald method. The remaining interactions fall off very quickly ($1/r^{K+1}$) and can be well approximated by including only the interactions from neighbor cells. Therefore, we have

$$V^N_{\rm EW}(r_i) \approx V^N_{\rm nbr}(r_i) + V^P_{\rm dist}(r_i), \qquad (b-1a)$$

where

$$V^P_{\rm dist}(r_i) = V^P_{\rm EW}(r_i) - V^P_{\rm nbr}(r_i). \qquad (b-1b)$$

Here, V^N is the potential that is due to original N atoms, V^P is due to the reduced set of P charges. The subscript "EW" denotes that the potential is calculated through the Ewald procedure and "nbr" indicates the 27 neighbor cells. For details, see Appendix B. The subtraction of $V^P_{\rm nbr}(r_i)$ in (b-1b) is conveniently included in the real space sum inside the Ewald calculation of $V^P_{\rm EW}(r_i)$. We are left with calculations of a *finite* system composed of the 27 neighbor cells. This formula provides a practical way to calculate accurately the energy and the force for megacrystals.

The construction of the Reduced Set of atoms proceeds by generating a set of $P=(K+1)(K+2)(K+3)/6$ random points in the unit cell. Assuming that each point has a charge q_j, we calculate up to Kth Cartesian moments of this Reduced Set and set them equal to those of the original set (this guarantees that the multipole moments are the same since the multipole moments are linear combinations of the Cartesian moments). We then solve the resulting P linear equations to obtain q_j $(j=1,\cdots,P)$. For up to 1 million atoms per cell, we find that $K=4$ $(P=35)$ is sufficient (the neglected 5th and higher-order terms fall off as $1/r^6$).

The accuracy of the Reduced Set method can be assessed from calculations of amorphous polyethylene periodic systems listed in Table I. We calculated the total energy E_{tot} and the force on each atom $\mathbf{F}_i$. The error in total energy was about 0.02kcal/mol, or 0.001%. The rms error in force was about 0.003kcal/mol/Å, or 0.02%. As expected, these calculations showed no increase in error as the system size increased. Thus, the Reduced Set of 35 atoms was sufficient for most applications.

In CMMX we express $V^P_{\rm dist}(r)$ as a polynomial (Taylor) series about the center,

$$V^P_{\rm dist}(r)=V^{(0)}+\sum_\alpha V^{(1)}_\alpha r_\alpha+\sum_{\alpha,\beta}V^{(2)}_{\alpha\beta}r_\alpha r_\beta+\cdots, \qquad (b-2)$$

where the coefficients are either derivatives of $V^P_{\rm dist}(r)$ or interpolation coefficients from a set of $V^P_{\rm dist}(r_k)$. These coefficients need only be updated infrequently during

dynamics or minimization.

Cell Multipole Method. By using only $P = 35$ atoms to represent the $\infty - 27$ distant cells of megacrystals , we effectively eliminate the CPU time spent on the Ewald calculation (a fixed 2 seconds on SGI). However, the interaction of the center cell with its 27 neighbor cells would still require $27N^2/2$ pairwise calculations, prohibitively slow for a megacrystal. To reduce these N^2 calculations to N calculations, we extend the Cell Multipole Method (CMM)[5], previously developed for a finite system, to the crystal case.

The Cell Multipole Method is a natural approach for calculating long-range interactions of the type $q_i q_j/|\vec{r}_i - \vec{r}_j|^p$, $p \geq 1$. We divide the crystal unit cell into eight equal-sized cubic boxes (level 1 boxes; the original unit cells are level 0 boxes), each of which is further divided into eight level-2 boxes, and so on, until at level L ($L = 6$ for million atoms), each micro box contains ~ 4 atoms (Fig. b.1). The multipole moments are computed for each box. For each box at any level, the 26 neighbor boxes plus itself are called *nearby* boxes, while the remaining are called *faraway* boxes. The potential energy of an atom i is computed as

$$V(\vec{r}_i) = \sum_{j \in nearby} \frac{q_j}{|\vec{r}_i - \vec{r}_j|} + V_{far}(\vec{r}_i) + V^P_{dist}(\vec{r}_i). \qquad (b-3)$$

Thus the interactions of nearby atoms are calculated exactly, whereas those from faraway boxes is computed from $V_{far}(r)$ using a Taylor series similar to (b-2). The calculation is illustrated for a level-2 box in Fig. b.1. The essential idea is to use larger boxes as the distance increases, so that use of the multipole expansion is optimal[5,6].

Application to million-atom systems. The CMMX was used to compute the energy and force on periodic systems with a unit cell containing up to 1 million atoms. For periodic systems with up to 5000 atoms in the unit cells, a model

for amorphous polyethylene was constructed by a Monte Carlo procedure, which considers the torsional potential plus Coulomb and van der Waals interactions of the growing polymer with itself and with its image in all other unit cells. The resulting polymer strand traverses a number of unit cells. The results are listed in Table I. For larger crystals we started with the 2003-atom amorphous polyethylene strand (667 monomers) and formed a new unit cell consisting of D^3 such 2003-atom strands. Using $D = 2, 3, \cdots, 8$, leads to crystals with 16024, 54081, $\cdots$, 1025536 atoms in the crystal unit cell.

The total computational time per atom, T/N, is plotted in Fig. b.2. The total time of CMMX is linear in N ($T \approx 3.3N$msec on a single processor SGI 380 workstation) and the overhead is rather small. For 400 atoms in the unit cell, the CMMX is already 4 times faster than the standard Ewald method (see Table I). The gradual decrease from $T/N \approx 8$ for 398 atoms to $T/N \approx 3.3$ for 3184 atoms reflects the constant overhead of 2 sec for the Ewald calculation on the 35-atom Reduced Set. With the Ewald method, the real-space cutoff R_{cut} and the reciprocal-space cutoff k_{cut} can be optimized for any specified accuracy (see Appendix A.). Using an accuracy of $\delta E_{tot}/N = 0.001$kcal/mol, we find that $T \approx 53.3(N/1000)^{1.54}$sec, as shown in Fig.2. For the Minimum Image, we find that $T \approx 10.9(N/1000)^2$sec. For the 1025536 atom/unit cell polymer, CMMX uses a total of 0.90 hours, whereas Ewald would require 642 hours and Minimum Image would require 3368 hours.

The memory requirements for CMMX are modest. Storing multipoles, Taylor coefficients, and cell indices requires $140M+8N$ bytes, where M is the total number of boxes in a unit cell. Including $28N$ for coordinates, charges, and force, and assuming $M \simeq N/4$ (optimum choice), the total memory is $\sim 43N$ bytes. Keeping all quantities in memory, our program requires 45 MBytes for $N = 1$ million.

The accuracy of CMMX is specified by the number of terms retained in the multipole series and in the Taylor series $V_{far}(r)$ (b-2,b-3). At second order (up

to the quadrupole in multipole series and up to second-order terms in the Taylor series), the total energy error is about 0.07%, and the rms force error is about 0.2kcal/mol/Å, or 1%. At third order (up to the octopole in multipole series and up to third-order terms in the Taylor series), the error in total energy is further reduced to about 0.02%, and the rms force error is further reduced to about 0.4%. Since the accuracy at second order is already adequate for most applications, all results reported in this paper are obtained at this order, CMMX/2.

Discussion. In order to assess the significance of the errors in CMMX and Minimum Image, we have used these methods for predicting the minimum-energy structure. Using the Ewald structure as reference, we find that the 602-atom polyethylene crystal has an rms coordinate deviation of 0.022Å for CMMX/2, which is quite adequate. Minimum Image gives a structure with an rms deviation of 0.26Å, which is too large for some applications.

In addition to energy and force, simulations of crystals generally require calculations of the internal stress. To calculate the six independent stress components with CMMX, we first use the Ewald method[2] to compute the stress from the $\infty - 27$ distant cells (Reduced Set). Within the 27 neighbor cells, the contribution from the atoms in *nearby* boxes is computed as atom-atom (charge-charge) interactions, while those from the *faraway* boxes is computed as box-box interactions (which includes charge-charge, charge-dipole, dipole-dipole, etc.). For details, see Appendix C. For the 398-atom/cell polyethylene, CMMX gives an rms stress error of 0.0008kcal/mol/Å^3 = 0.0056 GPa. This leads to an error in the cell parameter of 0.0034Å out of 18Å (estimated by assuming that the bulk modulus of polyethylene is 10 GPa).

CMMX can handle any cell shape. Expressing the coordinates of the atoms in terms of the (nonorthogonal) unit-cell vectors $\mathbf{a}, \mathbf{b}, \mathbf{c}$, the algorithm remains un-

changed. By defining a 3 by 3 matrix $H = [\mathbf{a}, \mathbf{b}, \mathbf{c}]$, we calculate a scaled coordinate of atom i as $\mathbf{s_i} = H^{-1}\mathbf{r_i}$. Then each component of a scaled coordinate is in a range [0,1). By treating this unit cube as a level 0 cell, exactly the same algorithm used in the cubic cell can be used. During the calculation, the real coordinates can be recovered by calculating $\mathbf{r_i} = H\mathbf{s_i}$. For example, shearing a polyethylene crystal (398 atoms per cell) from a cell angle $\gamma = 90°$ to $\gamma = 80°$ leads to an rms force error 0.18kcal/mol/Å compared with the Ewald method.

An additional advantage of CMMX is that the Taylor series (cf. Eqs. b-2,b-3) used to represent the interactions from distant cells and the faraway boxes change only very slightly from step to step during dynamics and minimizations, and need not be recomputed at every step. Typically updating them every 100 steps leads to negligible errors in the force and stress. Since over half the computational time is spent in calculating this series, the total computation is reduced substantially.

The CMMX is well suited to parallel and vector computers. The $V^P_{dist}(r)$ that is due to the $\infty - 27$ cells of the reduced set is an insignificant computation (2 seconds on a workstation) and can be computed on a single processor of the parallel computer or on the scalar mode of a vector computer. The remaining 27 cells containing the original set of atoms is computed using the CMM[5]. The CMM is dominated by the deeper-level calculations and is highly localized and is therefore well suited to parallel computers. The loop structure using the Cartesian coordinates in the CMM makes it easily vectorized on a vector computer.

In conclusion, the CMMX method for calculating the long-range interactions in the periodic systems is accurate, substantially faster than the standard methods, and allows practical simulations of megacrystals with current computers. Moreover, the method is ideal for massive parallelism suitable for future computer architectures.

Appendix A. Calculation Time of the Ewald Method

In the Ewald method, we use the accuracy specified cutoffs for both real and reciprocal space sums[2]. In this approach, the error in the total energy is specified, and cutoff distances for the real space (R_{cut}) and the reciprocal space (k_{cut}) are calculated. The total calculation time is given by

$$time = C_{real} N R_{cut}^3 + C_{reci} N^2 k_{cut}^3, \qquad (b-4)$$

where C_{real} and C_{reci} are constants and N is the number of atoms in the unit cell. In the Ewald procedure, there is one parameter η, which determines how much of the real-space sum is converted to the reciprocal space sum. For a given energy error per atom (ϵ_{real} and ϵ_{reci}), R_{cut} and k_{cut} are functions of η as follows (C_R and C_k are constants):

$$\epsilon_{real} = C_R \eta^2 erfc(R_{cut}/\eta), \qquad (b-5a)$$

$$\epsilon_{reci} = C_k \frac{N}{\eta} erfc(\pi \eta k_{cut}). \qquad (b-5b)$$

η is chosen such that the total estimated time is minimized[2]. Since k_{cut} is a function of N, η and R_{cut} depend on N also. Because of the dependence, time increases more slowly than N^2, as expected from the above equation. The actual increase of time with respect to N is about $N^{1.54}$(see Fig. b.1). We calculated the estimated time by using the same procedures for N up to 10^6 atom systems and found that this relation still held. Of course, we could choose η, R_{cut} and k_{cut} such that the calculation time increases as N (set R_{cut} and η constants and change k_{cut} proportional to $N^{-1/3}$). But in this case, the error per atom increases with N in the reciprocal space sums as N becomes large. Perram et al.[10] showed that if the maximum term neglected is fixed and the boxing algorithm is implemented in the real space sum, the total

time scales as $N^{3/2}$ if the number of boxes is optimized.

Appendix B. Reduced Set Approach

For any atom i in the central cell, the potential is written as

$$V_{\rm EW}^{N}(r_i) = V_{\rm EW}^{N-P}(r_i) + V_{\rm EW}^{P}(r_i) = V^{N-P}(r_i) + V_{\rm EW}^{P}(r_i), \qquad (b-6)$$

where V^N is the potential that is due to original N atoms, V^P is due to the reduced set of P charges, and V^{N-P} is due to the combined $N+P$ charge system where the P charges of the Reduced Set have their signs reversed. The subscript "EW" denotes that the potential is calculated through the Ewald procedure. V^{N-P} is absolutely convergent because its charge, dipoles, quadrupoles, $\cdots$, up to Kth-order multipoles, are zero by construction. Also the second moments of the combined atom system are zero (since the Cartesian moments are fitted), ensuring that the potential calculated using the combined charge set converges to the Ewald potential. The remaining interactions fall off very quickly ($1/r^{K+1}$). Thus, we need not use the Ewald procedure in computing V^{N-P}, and indeed, V^{N-P} can be well approximated by including only the interactions from neighbor cells. Therefore, we have

$$V_{\rm EW}^{N}(r_i) \approx V_{\rm nbr}^{N-P}(r_i) + V_{\rm EW}^{P}(r_i) = V_{\rm nbr}^{N}(r_i) + V_{\rm dist}^{P}(r_i), \qquad (b-7a)$$

where

$$V_{\rm dist}^{P}(r_i) = V_{\rm EW}^{P}(r_i) - V_{\rm nbr}^{P}(r_i), \qquad (b-7b)$$

and "nbr" indicates the 27 neighbor cells. The subtraction of $V_{\rm nbr}^{P}(r_i)$ in (b-7b) is conveniently included in the real space sum inside the Ewald calculation of $V_{\rm EW}^{P}(r_i)$.

Appendix C. Stress Calculations in CMMX

Six independent stress components (strain derivatives of the total energy divided by cell volume) are calculated in CMMX without any major modifications.

For the contributions of $\infty - 27$ (distant) cells, the Ewald method is used for the reduced charge set to calculate stress components[2]. The stress components arising from 27 neighbor cells are subtracted inside the real-space sums in these calculations. 27 neighbor cells are handled by CMM, in which the exact calculations are used for stress components for near-cell calculations in the deepest level. Here, stress components $\Pi_{\alpha\beta}$ arising from the charge-charge interaction, $\frac{q_i q_j}{r}$, is given by

$$\Omega\Pi_{\alpha\beta} = -\frac{q_i q_j}{r^3} r_\alpha r_\beta, \qquad (b-8)$$

where Ω is a volume of the unit cell and $r = |\vec{r}_i - \vec{r}_j|$. In the downward process of CMM, local expansions around box i arising from the multipoles of box j are calculated. The interaction energy between various multipoles of boxes i and j can be calculated at the same time, and these are used to calculate stress components. Up to the dipole-dipole interactions, the interaction energy is given by

$$E = \frac{Z_i Z_j}{R} + \frac{Z_i(\vec{\mu}_j \cdot \vec{R})}{R^3} - \frac{Z_j(\vec{\mu}_i \cdot \vec{R})}{R^3} + \frac{(\vec{\mu}_i \cdot \vec{\mu}_j)R^2 - 3(\vec{\mu}_i \cdot \vec{R})(\vec{\mu}_j \cdot \vec{R})}{R^5}. \qquad (b-9)$$

Here, $\vec{R}$ is a position vector of a center of box i measured from a center of box j. From this energy, stress components are calculated by

$$\begin{aligned}
\Omega\Pi_{\alpha\beta} = & -\frac{Z_i Z_j R_\alpha R_\beta}{R^3} \\
& - 3Z_i \frac{(\vec{\mu}_j \cdot \vec{R})R_\alpha R_\beta}{R^5} + Z_i \frac{\mu_{j\alpha} R_\beta + \mu_{j\beta} R_\alpha}{R^3} \\
& + 3Z_j \frac{(\vec{\mu}_i \cdot \vec{R})R_\alpha R_\beta}{R^5} - Z_j \frac{\mu_{i\alpha} R_\beta + \mu_{i\beta} R_\alpha}{R^3} \\
& - 3(\vec{\mu}_i \cdot \vec{\mu}_j)\frac{R_\alpha R_\beta}{R^5} + \frac{\mu_{i\alpha}\mu_{j\beta} + \mu_{i\beta}\mu_{j\alpha}}{R^3} \\
& + 15(\vec{\mu}_i \cdot \vec{R})(\vec{\mu}_j \cdot \vec{R})\frac{R_\alpha R_\beta}{R^7} \\
& - 3(\vec{\mu}_i \cdot \vec{R})\frac{\mu_{j\alpha} R_\beta + \mu_{j\beta} R_\alpha}{R^5} - 3(\vec{\mu}_j \cdot \vec{R})\frac{\mu_{i\alpha} R_\beta + \mu_{i\beta} R_\alpha}{R^5}. \qquad (b-10)
\end{aligned}$$

It is straightforward to derive terms arising from higher-order interactions.

References

(1) Ewald, P. P. *Ann. Phys.*, **1921**, *64*, 253. Tosi, M. P. in *Solid State Physics*, ed. Seitz, F. and Turnbull, D. (Academic Press, New York, 1964).

(2) Karasawa, N.; Goddard III, W. A. *J. Phys. Chem.*, **1989**, *93*, 7320.

(3) Allen, M. P.; Tildesley, D. J. *Computer Simulations of Liquids* (Oxford University Press, Oxford, 1987).

(4) For another approximate method, the Particle-Particle/Particle-Mesh method, see Hockney, R. W. ; Eastwood, J. W. *Computer Simulation Using Particles* (McGraw-Hill, New York, 1981).

(5) See (a) in this chapter. Ding, H-Q.; Karasawa, N.; Goddard III, W. A. submitted to *J. Chem. Phys.*

(6) Appel, A. W. *SIAM J. Sci. Stat. Comput.*, **1985**, *6*, 85. Barnes, J. E; Hut, P. *Nature*, **1986**, *324*, 446. Greengard, L.; Rokhlin, V. I. *J. Comput. Phys.*, **1987**, *73*, 325.

(7) Harris, F. E. in *Theoretical Chemistry Advances and Perspectives* eds. Eyring, H. and Henderson, D. (Academic Press, New York, 1975). Euwema, R. N.; Surratt, G. T. *J. Phys. Chem. Solids*, **1975**, *36*, 67.

(8) Stuart, S. N. *J. Comput. Phys.*, **1978**, *29*, 127.

(9) See Introduction of this thesis.

(10) Perram, J. W.; Petersen, H. G.; de Leeuw, S. W. *Molec. Phys.*, **1988**, *65*, 875.

TABLE I. Accuracy and timing for CMMX (2nd and 3rd order) compared with the Ewald and Minimum Image methods[a].

Method	Energy kcal/mol	Force kcal/mol Å	Time sec
$N = 398$			
Ewald	(−2395.58)	(16.25)	12.4
Reduced Set	−0.013	0.003	-
CMMX/3	0.427	0.094	4.2
CMMX/2	−2.53	0.190	3.2
Minimum Image	3.22	0.76	1.7
$N = 602$			
Ewald	(−3600.40)	(16.29)	24.6
Reduced Set	0.022	0.008	-
CMMX/3	0.578	0.107	4.9
CMMX/2	−1.70	0.203	4.0
Minimum Image	−8.77	0.74	3.9
$N = 1001$			
Ewald	(−5954.68)	(16.32)	53.3
Reduced Set	−0.035	0.003	-
CMMX/3	−1.71	0.070	6.3
CMMX/2	−1.80	0.138	5.1
Minimum Image	−2.67	0.60	12.8
$N = 2003$			
Ewald	(−11878.13)	(16.30)	150.5
Reduced Set	−0.012	0.004	-
CMMX/3	1.89	0.132	13.4
CMMX/2	−6.17	0.232	7.8
Minimum Image	−8.05	0.47	43.6
$N = 3184$			
Ewald	(−19164.64)	(16.25)	311.0
CMMX/3	1.58	0.095	17.3
CMMX/2	−21.41	0.192	10.5
Minimum Image	−221.58	0.86	109.8
$N = 4816$			
Ewald	(−28803.19)	(16.29)	600.2
CMMX/3	1.85	0.106	23.6
CMMX/2	−11.00	0.208	16.3
Minimum Image	−274.63	0.72	254.1

[a] The total energy and rms force values are given for Ewald in parentheses. Only the errors are given for other methods. In CMMX/2, up to the quadrupole in multipole series and up to second-order terms in the Taylor series are retained. In CMMX/3, up to the octopole in multipole series and up to third-order terms in the Taylor series are retained.

Figure Captions

Fig. b.1. The central unit cell and its 26 neighbor cells (only 8 are shown). Also shown are level-1 boxes (A) and level-2 boxes (B) used in the CMMX algorithm. Interactions from the infinite distant cells (shaded) are expressed in a Taylor series $V^T_{dist}(r)$ about the center of the central cell. Consider a box B_0 and its parent A_0. Interactions from all A's are expressed in a Taylor series $V^T_{A_0}(r)$ about the center of A_0. Similarly for B_0, the interactions from all B_f's are contained in $V^T_{B_0}(r)$. $V_{far}(r)$ for B_0 is obtained by shifting the centers of expansion for $V^T_{dist}(r)$ and $V^T_{A_0}(r)$ and adding to $V^T_{B_0}(r)$. Atoms in the 26 nearby boxes, B_n, are computed exactly (this occurs at the 6th level for the million-atom calculation).

Fig. b.2. Computation time per atom of CMMX compared with the Ewald and the Minimum Image methods (on a single processor SGI 4D/380 workstation). The increase in CMMX for small N is due to the fixed time for the Ewald calculation on the Reduced Set.

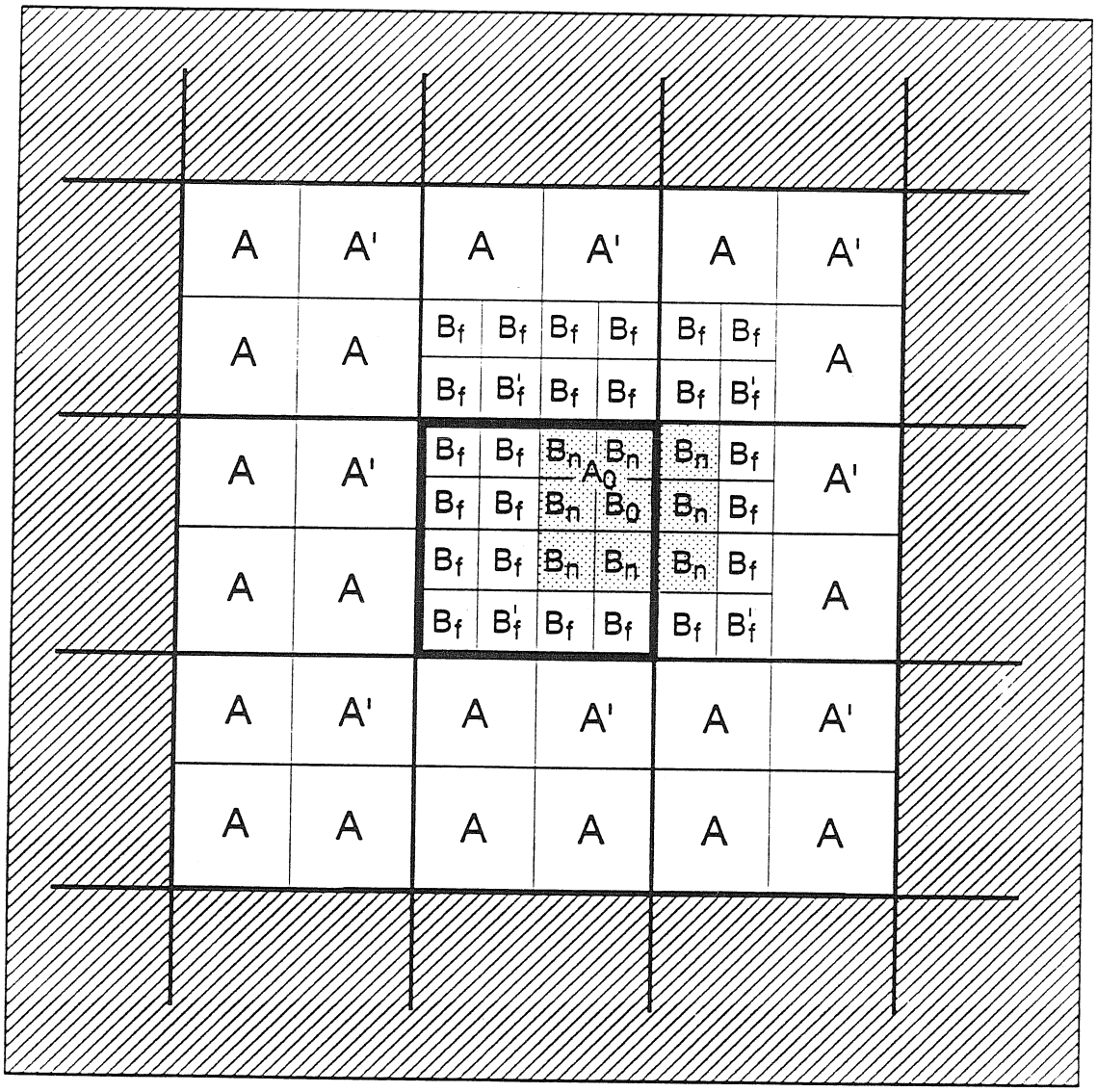
A
A'
A
A'
A
A'
A
A
B_f B_f B_f B_f
B_f B_f' B_f B_f
B_f B_f
B_f B_f'
A
A
A'
B_f B_f B_n B_n
B_f B_f B_n B_Q
A_Q
B_n B_f
B_n B_f
A'
A
A
B_f B_f B_n B_n
B_f B_f' B_f B_f
B_n B_f
B_f B_f'
A
A
A'
A
A'
A
A'
A
A
A
A
A
A

Figure b.1

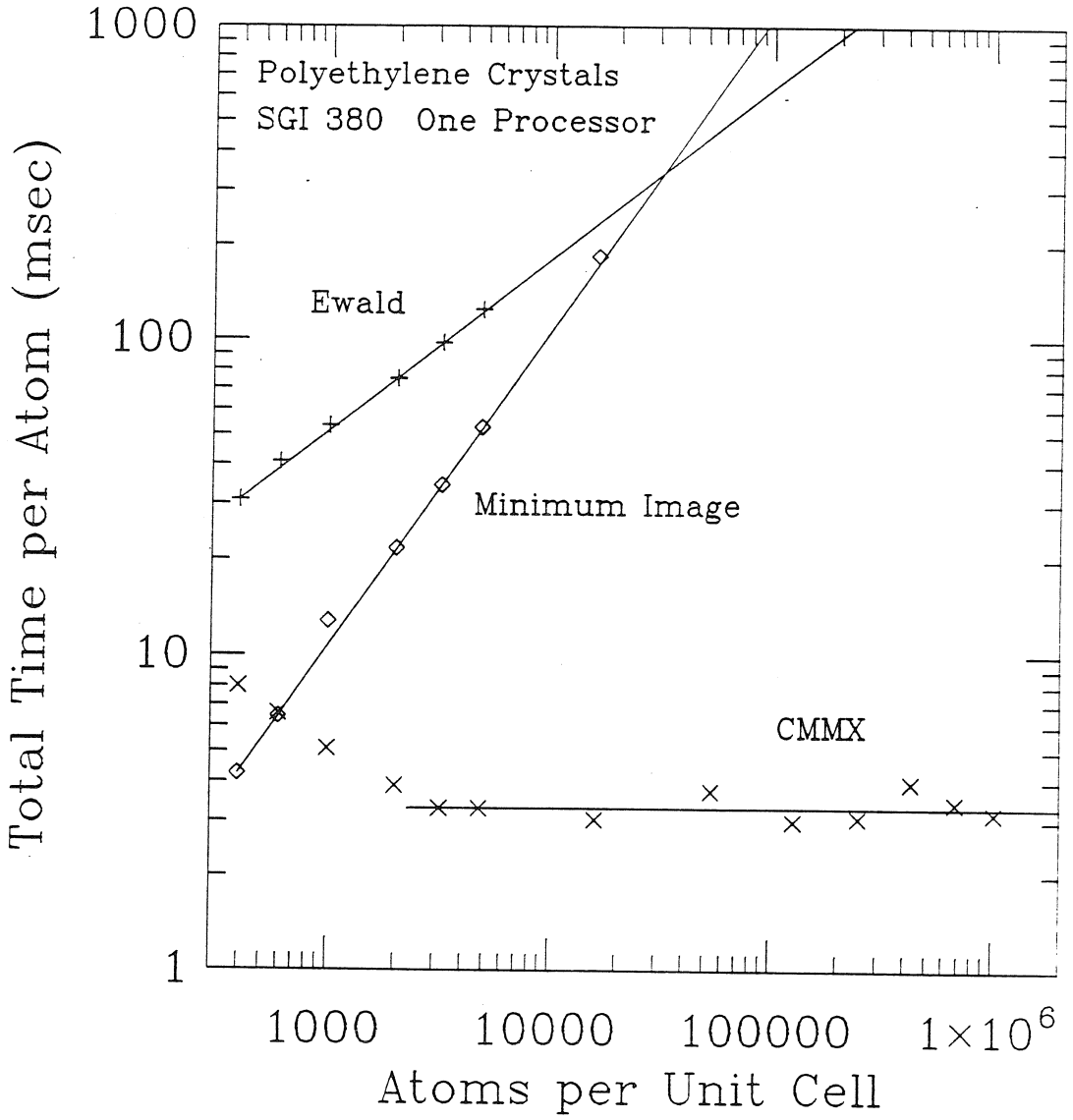
1000
100
10
1
Total Time per Atom (msec)
Polyethylene Crystals
SGI 380 One Processor
Ewald
Minimum Image
CMMX
1000
10000
100000
1×10^6
Atoms per Unit Cell

Figure b.2

Part II

Force-Field Parameters and Properties of Polymer Crystals

Chapter IV

Mechanical Properties and Force-Field Parameters for Polyethylene Crystals

Reprinted from The Journal of Physical Chemistry, 1991, 95.

Mechanical Properties and Force Field Parameters for Polyethylene Crystal

Naoki Karasawa, Siddharth Dasgupta, and William A. Goddard III*

Materials and Molecular Simulation Center, Beckman Institute (139.74),† California Institute of Technology, Pasadena, California 91125 *(Received: December 7, 1989; In Final Form: September 7, 1990)*

Crystal structures, phonon dispersion relations, and elastic constants of polyethylene crystal are calculated by using a new force field where the van der Waals parameters are selected on the basis of comparing these properties with experiment. The cell parameters and atomic coordinates are optimized simultaneously, and elastic constants and phonon bands are calculated by using analytic second derivatives at the optimized structure. Yield stresses and surface energies are obtained from calculations of the stress–strain relations in directions perpendicular to polymer chains.

I. Introduction

Given a force field (the analytical description of forces on all atoms in terms of the distances and angles in a structure), one can calculate a number of important properties of crystalline polymers—structure, elastic constants, yield stresses, vibrational (phonon) states, specific heat, free energy, etc. However, suitable force fields do not exist for most polymers of interest. Herein, we report a new force field suitable for polyethylene (PE) and other hydrocarbons using a systematic approach to developing force fields that should be applicable to other polymers of interest.

† Contribution No. 7903.

0022-3654/91/2095-2260$02.50/0

With the new force field we calculate the structure by optimizing the six unit-cell parameters simultaneously with the atomic coordinates for all atoms within the unit cell. Allowing all atomic coordinates to readjust, the elastic constants and phonon dispersion relations (lattice modes and intramolecular modes) are obtained at the optimized structure (from analytical second derivatives). The phonon states are then used to obtain thermodynamic properties. These calculated properties of polyethylene are compared with experimental values.

For the directions perpendicular to the polyethylene chains, we calculate the stress–strain relations for finite strains until the crystal fractures. This is used to obtain the yield stresses and ultimate stresses for PE crystals and to obtain the surface energies.

II. The Force Field

The energy expression involves valence (E_{val}) and nonbond (E_{nb}) interactions

$$E = E_{val} + E_{nb} \tag{1}$$

where E_{val} includes the terms arising from covalent bond formation and E_{nb} includes the long-range noncovalent interactions. Here we take the covalent terms

$$E_{val} = E_b + E_a + E_t + E_x \tag{2}$$

to include bond stretch (E_b), angle bend (E_a), dihedral angle torsion (E_t), and cross (E_x) terms, while the nonbond terms

$$E_{nb} = E_{vdW} + E_Q \tag{3}$$

consist of van der Waals (E_{vdW}) and electrostatic (E_Q) terms. Consistent with common practice, we exclude 1-2 (bond) and 1-3 (angle) nonbond interactions.

A. Valence Interactions. The valence interactions (2) are described by using the following expressions:

(i) Morse terms

$$E_{IJ} = D_b[e^{-\alpha_b(R-R_b)} - 1]^2 \tag{4}$$

where R is the length of bond IJ, R_b and D_b are the position and depth of the well, and $k_b = 2D_b\alpha_b^2$ is the force constant.

(ii) Cosine angle-bond terms

$$E_a = \tfrac{1}{2}C[\cos\theta - \cos\theta_a]^2 \tag{5}$$

where θ is the angle between bonds IJ and JK, θ_a is the equilibrium angle, and $k_\theta = C\sin^2\theta_a$ is the diagonal force constant.

(iii) Threefold torsion terms

$$E_t = \tfrac{1}{2}V_t(1 + \cos 3\phi) \tag{6}$$

where ϕ is the torsional angle for bonds IJ, JK, and KL ($\phi = 0$ corresponds to cis) and V_t is the barrier.

(iv) Bond–angle and bond–bond cross terms of the form

$$E_{ax} = D_1(\cos\theta - \cos\theta_a)(R_1 - R_{b1}) + D_2(\cos\theta - \cos\theta_a)(R_2 - R_{b2}) + k_{rr}(R_1 - R_{b1})(R_2 - R_{b2}) \tag{7}$$

associated with each angle term (5), where R_1 and R_2 are the lengths of the IJ and JK bonds, $k_{r\theta} = -D\sin\theta_a$ is the angle-stretch force constant, and k_{rr} is the stretch–stretch force constant.

(v) One-center angle–angle cross terms of the form

$$E_{1aa} = G(\cos\theta_{IJK} - \cos\theta_{aIJK})(\cos\theta_{IJL} - \cos\theta_{aIJL}) \tag{8}$$

where $k_{1\theta\theta} = G\sin\theta_{aIJK}\sin\theta_{aIJL}$ is the force constant for two angle terms (IJK and IJL) sharing a common central bond (IJ) and a common central atom (J).

(vi) Two-center angle–angle terms

$$E_{2aa} = F\cos\phi(\cos\theta_{IJK} - \cos\theta_{aIJK})(\cos\theta_{JKL} - \cos\theta_{aJKL}) \tag{9}$$

where $k_{2\theta\theta} = F\cos\phi\sin\theta_{aIJK}\sin\theta_{aJKL}$ is the force constant for angle terms (IJK and JKL) in which the central atoms (J and K) are bonded to each other.

These cross terms are considered collectively as

$$E_x = E_{ax} + E_{1aa} + E_{2aa} \tag{10}$$

B. Nonbond Interactions. The electrostatic part (E_Q) of the nonbond interaction (3) is described by using the Coulomb expression

$$E_Q = \frac{Q_I Q_J}{\epsilon_0 \epsilon R_{IJ}} \tag{11}$$

where Q_I is the charge on center I (electron units), $\epsilon = 1$, and the constant $1/\epsilon_0 = 332.0637$ gives E in kcal/mol when R_{IJ} is the distance in Å.

Experimental and theoretical studies on alkanes suggest that all hydrogens have about the same charge. Thus, Hartree–Fock (HF) calculations[1] [all with the same valence double zeta basis with polarization functions on C and H] lead to Mulliken populations of $Q_H = 0.118$ for CH_4, $Q_H = 0.111$ for C_2H_6, $Q_H = 0.109$ and 0.108 for the terminal and central groups of propane, and $Q_H = 0.108$ and 0.106 for the terminal and central groups of *n*-butane. In comparison, fitting point charges to match electrostatic potentials from HF calculations (with similar basis sets) for CH_4 leads to Q_H of 0.124[2b] and 0.139,[2a] while the calculated octupole moment of methane using a high-quality CI wave function[3] yields $Q_H = 0.150$. On the basis of these results, we used

$$Q_H = 0.144|e|$$

in all calculations for polyethylene and *n*-butane. (The charges of carbon atoms are taken as $-0.144|e|$ times the number of bonded hydrogen atoms.)

The vdW part of the nonbond interaction (3) for atoms I and J is described by using the exponential-6 potential

$$E_{vdW_{IJ}} = Ae^{-BR_{IJ}} - \frac{C}{R_{IJ}^6} = \frac{D_v}{(\zeta - 6)}[6e^{\zeta(1-\rho)} - \zeta\rho^{-6}] \tag{12}$$

where $\rho = R_{IJ}/R_v$. These parameters are obtained empirically as described below.

C. The Hessian-Biased Force Field. The valence force field parameters for polyethylene (PE) are obtained by using the Hessian-biased method[4] for the valence force field of *n*-butane

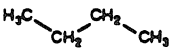

(13)

where the parameters associated with the central CH_2 units apply to PE. In the Hessian-biased approach, we input two quantities: (a) the experimental frequencies ν_i^{exp} of the $3N - 6$ normal modes of *n*-butane,[5] and (b) the analytical second derivative matrix or Hessian,

$$B_{\alpha I,\beta J}^{HF} = \frac{\partial^2 E^{HF}}{\partial X_{\alpha I}\,\partial X_{\beta J}} \tag{14}$$

(where $\alpha, \beta = x, y, z$ and $I, J = 1, 2, \ldots, N$, for an N-atom system), from the HF wave function of *n*-butane.

Defining the mass-weighted Hessian from the HF wave functions

$$\bar{B}_{\alpha I,\beta J}^{HF} = B_{\alpha I,\beta J}^{HF}/[M_I M_J]^{1/2} \tag{15}$$

the vibrational eigenfunctions are obtained from the eigenvalue equation

$$\bar{\mathbf{B}}^{HF}\mathbf{U}_i^{HF} = \mathbf{U}_i^{HF}\lambda_i^{HF}, \qquad i = 1, \ldots, 3N \tag{16}$$

The eigenvalues λ_i^{HF} are related to the vibrational frequencies ν_i^{HF}

$$\lambda_i = \kappa(\nu_i^{HF})^2 \tag{17}$$

(where $\kappa = 8.480\,27 \times 10^{-5}$ if masses are in atomic mass units, energies are in kcal/mol, distances are in Å, and ν_i are in cm^{-1}). However, the ν_i^{HF} differ by up to 20% from experiment, ν_i^{exp}

(1) Dasgupta, S.; Goddard III, W. A. "Hessian-Biased Force Fields for Alkanes". To be submitted for publication.

(2) (a) Cox, S. R.; Williams, D. E. *J. Comput. Chem.* **1981**, *2*, 304. (b) Chirlian, L. E.; Francl, M. M. *J. Comput. Chem.* **1987**, *8*, 894.

(3) Amos, R. D. *Mol. Phys.* **1979**, *38*, 33. The charge was calculated by using a C–H bond length of 1.093 54 Å.

(4) Dasgupta, S.; Goddard III, W. A. *J. Chem. Phys.* **1989**, *90*, 7207.

(5) Cangeloni, M. L.; Schettino, V. *Mol. Cryst. Liq. Cryst.* **1975**, *31*, 219.

The B^{HF}_{ij} are used to specify the vibrational eigen*functions* and the ν_i^{exp} are used to determine the vibrational eigen*values*. Combining these leads to a new Hessian determined partly from experiment and partly from theory.

The Hessian-biased $\mathbf{B}^{BH}$ is defined as

$$B^{BH}_{\alpha I,\beta J} = [M_I M_J]^{1/2} \tilde{B}^{BH}_{\alpha I,\beta J} \tag{18}$$

where

$$\tilde{\mathbf{B}}^{BH} = \mathbf{U}^{HF} \lambda^{exp} \tilde{\mathbf{U}}^{HF} \tag{19}$$

λ^{exp} is the diagonal matrix with elements $\lambda_i^{exp} = \kappa(\nu_i^{exp})^2$, and $\tilde{\mathbf{U}}$ is the transpose of $\mathbf{U}$. Thus, by construction $\mathbf{B}^{BH}$ leads to the experimental vibrational frequencies and the theoretical vibrational eigenfunctions. We then determine the force field parameters for the terms (4)–(9) so that the force-field Hessian matches the biased Hessian

$$\frac{\partial^2 E^{FF}}{\partial X_{\alpha I}\, \partial X_{\beta J}} \approx B^{BH}_{\alpha I,\beta J} \tag{20}$$

[In these calculations (11) and (12) are included but the parameters Q_I, ζ, D_v, and R_v are kept fixed.] We also require that this force field lead to zero forces at the experimental geometry

$$\frac{\partial E^{FF}}{\partial X_{\alpha I}} \approx 0 \tag{21}$$

The result for *n*-butane is a total of

$$(3N-6)(3N-5)/2 + (3N-6) = 3(3N-6)(N-1)/2 = 702 \tag{22}$$

conditions, sufficient to determine the 76 parameters of even the most elaborate (MCXX) force field. To extract the force field parameters, we use a least-squares procedure in which the errors in satisfying (20) and (21) are simultaneously minimized.[1,4]

The HF calculations (including analytic second derivatives) were carried out with the GAUSSIAN-86 program.[6] The 6-31G** basis was used, which is valence double zeta on both C and H with d polarization functions on the C and p polarization functions on the H. These calculations were carried out at the experimental structure.[7]

D. Procedures for the Valence Force Field. We optimized the valence force field of *n*-butane using three levels of force field [all with electrostatic (11) and vdW (12) interactions]: (a) MC, Morse (4), cosine angle bend (5), torsion (6), electrostatic (11), vdW (12) but not cross terms; (b) MCX, MC plus bond-angle and bond–bond cross terms (7); (c) MCXX, MCX plus angle–angle cross terms (8), (9). These valence force fields (along with the force fields of methane, ethane, and propane) are discussed in more detail elsewhere.[1] The bond energy parameter (D_b) for the Morse potentials was fixed at a typical experimental value for the bond of interest and not optimized [the normal modes are not sensitive to D_b].

The notation on cross terms is illustrated as follows.

The angle cross terms (7) for the H–C–C angle involve two $k_{r\theta}$ terms denoted as $k_{H\theta}$ and $k_{C\theta}$ and one stretch–stretch term denoted k_{HC}.

For the tetrahedral center

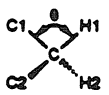

(23)

(6) Frisch, M. J.; Binkley, J. S.; Schlegel, H. B.; Raghavachari, K.; Melius, C. F.; Martin, R. L.; Stewart, J. J. P.; Bobrowicz, F. W.; Rohlfing, C. M.; Kahn, L. R.; Defrees, D. J.; Seeger, R.; Whiteside, R. A.; Fox, D. J.; Fleuder, E. M.; Pople, J. A. Carnegie-Mellon Quantum Chemistry Publishing Unit, Pittsburg, PA, 1984.

(7) No reliable μ-wave experimental structure is available for *n*-butane. The available electron diffraction studies [Bonham, R. A.; Bartell, L. S. *J. Am. Chem. Soc.* **1959**, *81*, 3491. Kuchitsu, K. *Bull. Chem. Soc. Jpn.* **1959**, *32*, 748] report average length and angle values for a 60:40 mixture of trans and gauche conformers. Consequently, for our ab initio calculations, we based the structure for *n*-butane on the microwave structure of propane (Lide, Jr., D. *J. Chem. Phys.* **1960**, *33*, 1514).

TABLE I: Valence Force Field Parameters Used in the Calculations for Polyethylene[a]

		n-butane		
		MCXX	MCX	MC
		Bond Stretch (Eq 4)		
C–C	R_b	1.4841	1.4720	1.5221
	k_b	884.9940	960.7682	570.0549
	D_b	(85.80)	(85.80)	(85.80)
C–H	R_b	1.0765	1.0702	1.0908
	k_b	741.3720	774.0032	672.4147
	D_b	(95.10)	(95.10)	(95.10)
		Angle Bend (Eq 5)		
H–C–H	k_θ	55.6076	46.0545	29.8261
	θ_a	119.3933	124.5427	134.0770
C–C–H	k_θ	65.7301	72.5454	67.8248
	θ_a	117.7291	119.7212	122.6576
C–C–C	k_θ	84.1810	76.0945	89.4018
	θ_a	121.2400	124.6770	123.5544
		Torsion (Eq 6)		
H–C–C–H	V_t	5.1686	3.5854	4.6266
C–C–C–H	V_t	6.1626	6.4680	6.8816
C–C–C–C	V_t	5.7070	6.3298	11.5449
		Angle Cross Terms (Eq 7)		
H–C–H	$D_{H\theta}$	−22.6583	−26.8877	
	k_{HH}	3.1321	3.2767	
C–C–H	$D_{C\theta}$	−34.3195	−36.9016	
	$D_{H\theta}$	−25.9234	−28.3688	
	k_{HC}	1.3684	1.4648	
C–C–C	$D_{C\theta}$	−54.0185	−55.0881	
	k_{CC}	26.2187	26.1288	
		One-Center Angle–Angle Cross Terms (Eqs 8 and 24)		
$G_{CC:HC}$		−7.6083		
$G_{CC:HH}$		−5.3356		
$G_{CH:CC}$		−5.0824		
$G_{CH:CH}$		−5.3356		
		Two-Center Angle–Angle Cross Terms (Eqs 9 and 26)		
$F_{H:CC:H}$		−17.7274		
$F_{C:CC:H}$		−16.4004		
$F_{C:CC:C}$		−21.5910		

[a] Units are kcal/mol for energies, Å for length, and degrees for angles. Values in parentheses were not optimized.

there are 12 one-center angle–angle terms of the form (8), each of which involves four atoms

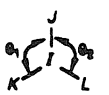

(24)

We denote the angle–angle force constant for (24) as $k_{IJ:KL}$ (where $k_{IJ:KL} = k_{IJ:LK}$). Thus, for PE there are four cases:

$$k_{CC:CH},\quad k_{CC:HH},\quad k_{CH:CC},\quad k_{CH:CH}$$

For a pair of adjacent centers, say, two carbons,

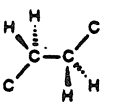

(25)

there is a total of $3^2 = 9$ two-center angle-angle terms, each of which involves four atoms

(26)

Here we denote the force constant as $k_{IJ:KL}$ (where $k_{LKJ:I} = k_{IJ:KL}$) Thus, for PE there are three cases: $k_{C:CC:C}$, $k_{C:CC:H}$, and $k_{H:CC:H}$

The valence FF parameters were optimized for *n*-butane (with the vdW parameter fixed) and then used (without readjustment) for polyethylene, whereas the vdW parameters were optimized for PE with fixed valence parameters (vide infra). As a result, we carried out a cycle of such optimizations. The final valence

TABLE II: van der Waals Parameters for C and H[a]

	LJ12-6[f]	exponential-6								exptl	Williams[h]
vdW parameters (eq 12)					OPT[i]			OPT[i]			
ζ_C		11.0	11.0	12.0	12.0	12.0	13.0	13.0	13.0		14.0340
R_{vC}, Å	3.8050	3.9425	3.9425	3.8837	3.8837	3.8837	3.8410	3.8410	3.8410		3.8983
D_{vC}, kcal/mol	0.06921	0.09115	0.09115	0.08444	0.08444	0.08444	0.07918	0.07918	0.07918		0.0951
ζ_H		12.0	13.0	11.0	11.8	12.0	11.0	11.2	12.0		12.3822
R_{vH}, Å	2.9267	3.3400	3.2212	3.2705	3.1975	3.1840	3.1810	3.1665	3.1132		3.3107
D_{vH}, kcal/mol	0.0335	0.00830	0.01144	0.0145	0.0160	0.01613	0.0199	0.0200	0.0210		0.0128
cohesive energy,[j] kcal/mol	1.838	1.849	1.860	1.849	1.857	1.852	1.863	1.851	1.829	1.838 ± 0.032[b]	1.686
zero-point energy cor,[j] kcal/mol	0.291	0.161	0.191	0.171	0.189	0.191	0.189	0.192	0.205		0.270
stress, GPa											
σ_{xx}	0.0033	−0.0940	−0.0670	−0.0853	−0.0655	−0.0619	−0.0689	−0.0649	−0.0501	0	−0.1473
σ_{yy}	−0.0029	0.0950	0.0679	0.0835	0.0672	0.0630	0.0646	0.0638	0.0512	0	−0.0587
setting angle, deg	41.7	42.4	42.3	42.4	42.3	42.4	42.4	42.4	42.3	41 ± 1[g]	43.4
lattice modes, cm^{-1}											
A_u	67	43	49	45	48	49	47	48	51		44
B_{3g}	87	67	74	73	74	75	78	78	78	(108[d])	104
B_{1u}	94	79	84	83	84	85	86	86	86	80[c]	97
E_{2u}	142	112	122	114	119	120	117	118	122	109[c]	125
A_g	198	126	147	129	141	144	137	140	150	137[d]	144
av error,[e] cm^{-1}	36.0	5.0	9.0	5.3	6.0	7.7	4.7	6.0	10.7		13.3
rms error,[e] cm^{-1}	40.8	6.6	9.7	5.7	6.6	8.1	5.8	6.5	11.2		14.1

[a] The calculations were carried out for the experimental structure at 4 K.[g] The optimum values are for $\zeta_H = 11.8$ with $\zeta_C = 12.0$ and $\zeta_H = 11.2$ with $\zeta_C = 13.0$. [b] Reference 14. [c] Reference 15. [d] Reference 16. See discussion in section VI.A about the B_{3g} mode. [e] Using B_{1u}, B_{2u}, and A_g modes. [f] $E_{LJ} = D_v[(R_v/R)^{12} - 2(R_v/R)^6]$. [g] Reference 13. [h] Reference 10. [i] These are the two sets of optimum parameters. We have selected $\zeta_C = 13.0$ for the other studies in this paper. [j] The calculated cohesive energy was corrected by subtracting the calculated zero-point-energy correction from using 1, 1, and 2 points in k_a, k_b, and k_c directions in the Brillouin zone.

FF parameters reported in Table I were optimized by using the $\zeta_H = 11.2$ and $\zeta_C = 13.0$ vdW parameters of Table II.

The final parameters are listed in Table I. The presence of cross terms leads to changes in the diagonal parameters as cross terms are added.

E. Procedure for the Nonbond Interactions. In a study of the elastic properties of graphite,[8] a force field for carbon was developed by requiring that the experimental parameters, elastic constants, and vibrational frequencies be reproduced. For the nonbond interactions, the available experimental data (c lattice parameter and C_{33} elastic constant) allowed two vdW parameters (R_{vC} and D_{vC}) to be specified for an exponential-6 potential (12) but not the third (ζ_C). As a result, a family of parameters were reported where $\xi_C = 11$, 12, and 13 (see Table II). In the current paper we use the exponential-6 form (12) and optimize the vdW parameters for hydrogen (ξ_H, R_{vH}, D_{vH}) for each choice of ξ_C, as described below. For hydrogen–carbon interactions we assume the combination rules,

$$A_{HC} = (A_{HH}A_{CC})^{1/2}$$

$$B_{HC} = \tfrac{1}{2}(B_{HH} + B_{CC})$$

$$C_{HC} = (C_{HH}C_{CC})^{1/2}$$

These rules allow the accuracy-bounded convergence acceleration (ABCA) calculations to be optimized[9] and have been found adequate in previous studies.[10]

The most complete previous studies of vdW parameters for H and C is due to Williams and co-workers.[10] Considering the X-ray crystal structures of a number of hydrocarbons, Williams[10] estimated the charges, fixed the internal structure of each molecule (based on the X-ray studies), and optimized the C and H exponential-6 parameters to obtain the most accurate unit cell parameters and sublimation energies. For two molecules (n-hexane and benzene), there are accurate sublimation energies for 0 K and hence these molecules were emphasized. Since these data fixed only two parameters, Williams selected $\zeta_C = 14.034$ based on theoretical estimates.

Using our new vdW parameters for C, we initially optimized the H vdW parameters by fitting to n-hexane and benzene. However, a better procedure is to fit to the properties of PE. A major reason for this is that the crystal structure data for n-hexane[11] are available only at 160 K and for benzene[12] only at 77 K, whereas for optimization we need to compare with the crystal parameters near 0 K. On the other hand, there are structural parameters for PE down to 4 K.[13] In PE there are accurate experimental data[14] for the sublimation energies near 0 K. Data for the lattice-mode (vibrational) spectra in the crystal are available for all three systems, but for PE[15,16] these modes are accurately known near 0 K, whereas for n-hexane[17] and benzene[18] the experimental values are at higher temperatures (20 and 77 K, respectively).

At this point we would like to make a plea for accurate experimental studies of cell parameters, thermodynamics, elastic constants, and phonon dispersions of crystals at the lowest possible temperatures, (say 4 K). Such data are essential for determining the accurate vdW parameters needed for quantitative simulations of the properties of polymers, ceramics, and biological systems. With better data we could develop representations of the vdW potentials more accurately than exponential-6 and we could consider inclusion of the three-body terms that could be important at short range. Our perspective is that the technology has been available for such studies for over 20 years but that in the United States and many other countries, funding for such fundamental studies has lagged.

To determine the vdW parameters for H, we considered the polyethylene crystal and varied the vdW parameters (12) to obtain accurate cell parameters, lattice frequencies, and sublimation energies. These are the only experimental quantities sensitive to vdW interactions that are known near 0 K. Of the internal coordinates, the most relevant quantity is the setting angle, θ, which

(8) Goddard III, W. A.; Karasawa, N. "Elastic Constants and Phonon States for Graphite; van der Waals Parameters for Carbon". *J. Phys. Chem.*, submitted for publication.
(9) Karasawa, N.; Goddard III, W. A. *J. Phys. Chem.* **1989**, *93*, 7320.
(10) Williams, D. E.; Cox, S. R. *Acta Crystallogr.* **1984**, *90*, 404.
(11) Norman, N.; Mathisen, H. *Acta Chem. Scand.* **1961**, *15*, 1755.
(12) Bacon, G. E.; Curry, N. A.; Wilson, S. A. *Proc. R. Soc. London, Ser. A* **1964**, *279*, 98.
(13) Avitabile, G.; Napolitano, R.; Pirozzi, B.; Rouse, K. D.; Thomas, H. W.; Wills, B. T. M. *J. Polym. Sci., Polym. Lett. Ed.* **1975**, *13*, 351.
(14) Billmeyer, Jr., F. W. *J. Appl. Phys.* **1957**, *28*, 1114.
(15) Dean, G. D.; Martin, D. H. *Chem. Phys. Lett.* **1967**, *1*, 415.
(16) Harley, R. T.; Hayes, W.; Twisleton, J. F. *J. Phys. C* **1973**, *6*, L167.
(17) Brunel, L-C; Dows, D. A. *Spectrochim. Acta, Part A* **1974**, *30*, 929.
(18) (a) Sataty, Y. A.; Ron, A.; Brith, M. *Chem. Phys. Lett.* **1973**, *23*, 500. (b) Sataty, Y. A.; Ron, A. *J. Chem. Phys.* **1976**, *65*, 1578.

TABLE III: Comparison of Electrostatic Energy (E_Q) and van der Waals energy (E_v) of Polyethylene from (a) Accuracy-Bounded Convergence Acceleration (ABCA) Procedures and (b) Direct Summations[a]

(a) ABCA

ϵ_Q, kcal/mol	E_Q, kcal/mol	R_Q, Å	H_Q, Å^{-1}	η_Q, Å	ϵ_v, kcal/mol	E_v, kcal/mol	R_d, Å	H_d, Å^{-1}	η_d, Å	R_r, Å	N_{real}	N_{rec}
0.05	0.1351	4.1	4.3	1.7	0.01	−5.5729	5.1	4.2	1.8	5.6	560	189
0.005	0.1299	4.7	4.7	1.6	0.001	−5.5749	5.7	4.6	1.8	6.4	832	231
0.0005	0.1313	5.4	5.0	1.6	0.0001	−5.5747	6.1	5.1	1.7	7.2	1244	585

(b) Direct Sum

R_{cut},[b] Å	E_Q, kcal/mol	E_v, kcal/mol	N_{real}
9	−69.4635	−4.6865	2388
15	26.7702	−5.4015	11308
25	−31.8484	−5.5386	52743
35	12.8783	−5.5618	144895

[a] Here ϵ is the specified accuracy parameter. Cutoff distances in real space (R) and reciprocal space (H), convergence parameters (η), number of cells in reciprocal space (N_{rec}), and number of atom pairs used in real space (N_{real}) are shown for each ϵ. Subscripts are Q for electrostatic, d for dispersion, r for repulsive, and v for van der Waals (sum of dispersion and repulsion terms). [b] Using a cubic spline function to decrease the potential from full value at R_{cut} − 1 Å to zero at R_{cut}.

is the angle between the *ac* lattice plane and the CC plane of either chain. As indicated in Table II, the setting angle is independent of the vdW parameters, and we did not use the setting angle in fitting parameters. In these studies, we considered a range of values for ζ_H and used the experimental cell parameter and cohesive energies to determine the optimum R_{vH} and D_{vH} for each ζ_H. [We required that the residual stress in the *a* and *b* directions add to zero for the experimental cell parameters.]

We optimized all $3N = 36$ internal coordinates simultaneously with the six cell coordinates. This leads to the results in Table II where we see that better fits of cell parameters are obtained for larger ζ_H. On the other hand, lattice frequencies are too large for large ζ_H. To obtain an exact fit we need a form of the vdW potential with a less repulsive inner wall than exponential-6. However, we do not believe there is enough data to test a more flexible function. We chose two sets, $\zeta_C = 13.0$, $\zeta_H = 11.2$ and $\zeta_C = 12$, $\zeta_H = 11.8$, as the best compromises. These values lead to a good description of the lattice frequencies and less than 1.5% error in the *a* and *b* lattice parameters. As shown in the table, these two sets give very similar results. In this paper, we use $\zeta_C = 13$ and $\zeta_H = 11.2$ for all the calculations (including optimization of valence parameters) for polyethylene. In addition to the properties of PE reported here, these vdW parameters were used to calculate various properties for a number of hydrocarbon crystals, leading to excellent results.[19]

In Table II we have also included the results using the van der Waals parameters of Williams.[10] These calculations use $\zeta_C = 14.0340$, $R_{vC} = 3.8983$, and $D_{vC} = 0.0951$; $\zeta_H = 12.3822$, $R_{vH} = 3.3107$, and $D_{vH} = 0.0128$. In the Williams approach the nonbond interactions are calculated with each CH bond shortened by 0.07 Å from the experimental value (from 1.096 to 1.026 Å for PE). In PE the charges are 0.102 on each H and −0.204 on each C.

We see that the cohesive energy is about 8% smaller than experiment. Also σ_{xx} and σ_{yy} are both negative, indicating that the optimum cell parameters would be too large for these parameters. This would be expected because Williams' parameters are fitted to room temperature lattice parameters. The average error for the lattice frequencies is 13.3 cm^{-1}, which is about twice as large as the errors for the parameters developed here.

III. Calculational Details

A. Nonbond Summations. For all calculations on crystals, we use the ABCA procedure[9] to optimize convergence of the Coulomb ($1/R$) and dispersion ($1/R^6$) energies. In ABCA the input data are the required accuracy in the energy (we generally use $\epsilon_Q = 0.005$ kcal/mol for electrostatic sums and $\epsilon_v = 0.001$ kcal/mol for vdW sums) rather than cutoff distances. The program then chooses Ewald parameters[9] η_Q and η_v for the electrostatic and dispersion sums and chooses cutoff distances R_{cut} and H_{cut} for the real space sums and reciprocal space sums so that the terms beyond the cutoffs sum to less than ϵ. This estimate of the error is obtained by converting the sum of terms past the cutoff (R_{cut} or H_{cut}) to an integral, leading to an analytic approximation to the total error.[9] For a wide range of Ewald parameters η one can find values of R_{cut} and H_{cut} that yield the desired accuracy ϵ; however, the number of terms required in the real space sum relative to the number for the reciprocal space sum increases with η. Since the computational costs for real space terms are a factor of 5 or 10 larger than for the reciprocal space sums, ABCA selects η so as to minimize computation cost while ensuring a given accuracy ϵ. Similarly for the repulsive (exponential) part of the vdW interactions, ABCA estimates the R_{cut} to achieve the specified accuracy ϵ_v. For the calculations of energies, forces, stresses, and second derivatives in this paper, we use $\epsilon_Q = 0.005$ kcal/mol and $\epsilon_v = 0.001$ kcal/mol. For purposes of predicting structure and unit cell parameters accuracies of 0.1 kcal/mol would be satisfactory.

The ABCA procedure is illustrated in Table III for PE. Here we see that changing the accuracy parameter for Coulomb sums from $\epsilon_Q = 0.05$ to 0.005 to 0.0005 kcal/mol leads to $E_Q = 0.1351$, 0.1299, 0.1313 kcal/mol, consistent with the specified accuracies. This requires real space sums out to 4.1, 4.7, and 5.4 Å, respectively, and 560, 832, and 1244 pairwise interactions. [Actually fewer terms are required; the N_{real} in Table III is determined by the largest R_{cut} (which is R_r in each case) and the program evaluates E_Q using the smaller set satisfying R_Q.] In contrast, the direct sum approach using cutoffs of 9, 15, 25, and 35 Å leads to energies of −69.46, 26.77, −31.85, and +12.88 kcal/mol, respectively, with 2388, 11308, 52743, and 144895 pairwise interactions. Thus it would be far more accurate to ignore charges than to evaluate E_Q with the direct summation approach! For the dispersion energy the errors in the direct approach are smaller but still too large (16% error for 9 Å cutoff, 3% error for 15 Å cutoff) for accurate properties.

B. Optimization. All calculations were carried out using POLYGRAF,[20] an interactive molecular simulations package for molecular mechanics and molecular dynamics of polymer crystals. During the calculations, the $3N = 36$ atomic coordinates and the six cell coordinates were simultaneously optimized and displayed on an Evans & Sutherland PS330 graphics system at each optimization cycle. The atomic coordinates were optimized by using conjugate gradient techniques until the rms force per degree of freedom became less than 0.02 (kcal/mol)/Å. All six cell parameters were also optimized by using conjugate gradient techniques (where the internal coordinates were optimized for each

(19) Karasawa, N.; Goddard, W. A. "Lattice Properties and van der Waals Parameters for Hydrocarbons". To be submitted for publication.

(20) POLYGRAF is an interactive molecular simulation/three-dimensional graphics program from Molecular Simulations Incorporated, Pasadena, CA 91101.

TABLE IV: Optimized Cell Parameters and Setting Angle (θ) of Polyethylene Crystal Using *n*-Butane Parameter Sets[a]

	a	b	c	α	β	γ	θ
n-butane MC	7.202	4.795	2.542	90.0	90.0	90.0	41.9
n-butane MCX	7.203	4.797	2.545	90.0	90.0	90.0	41.9
n-butane-MCXX	7.202	4.795	2.546	90.0	90.0	90.0	41.9
expt at 4 K[b]	7.121	4.851	2.548	90.0	90.0	90.0	41 (1)

[a] a, b, and c are in Å, and α, β, γ, and θ are in degrees (using ζ_C = 13.0 and ζ_H = 11.2). The setting angle is the angle between the ac plane and the plane containing the C–C bonds of a chain. [b] Reference 13.

choice of cell parameters) until the rms strain derivatives became less than 0.002 kcal/mol. At the optimized structure, all stress components are less than 0.0005 GPa.

C. Phonon States, Moduli, and Thermodynamics. Using the predicted equilibrium structure, we calculated the elastic constants and phonon frequencies from analytic first and second derivatives of the energy. These elastic constants were used to calculate the Young's moduli (E_i) and compressibility (β).

Phonon frequencies for all 36 vibrational bands were calculated as a function of wavevector. We report the phonon dispersion in the [0 0 1], [1 0 0], and [1 1 0] directions for PE crystal. In order to compare with neutron scattering data,[21] we also report the lattice modes in the [1 0 0] and [1 1 0] directions for deuteriopolyethylene crystal.

To obtain thermodynamic properties we calculated all 36 phonon states for the 1000 equally spaced points in the Brillouin zone obtained by using 10 points along each reciprocal lattice vector. The quantum partition function of the crystal was then described in terms of the sum (properly weighted) of 36 000 Einstein oscillators (using the harmonic oscillator quantum partition function).

D. Finite Strains. The above properties relate to the equilibrium configuration of the PE crystal. In addition, we examined the response of this crystal to large strain (tension and compression) in the directions perpendicular to the chain axis. Sufficiently large strain in these directions fractures the crystal and creates a new surface. To simulate this behavior, we considered the calculational unit cell to contain four crystallographic unit cells in either the a or b directions and deformed the cell in the a or b directions, respectively. The procedure was first to strain the cell coordinates *without* changing the internal atomic coordinates (within each cell) and then reoptimize the internal coordinates while keeping the strain fixed. These studies used ABCA accuracy parameters of ϵ_q = 0.005 kcal/mol and ϵ_v = 0.001 kcal/mol. Optimization of atomic coordinates continued until rms forces were less than 0.05 (kcal/mol)/Å.

These calculations were carried out with two boundary conditions for the cell coordinates perpendicular to the strain direction:

(a) zero stress—the cell coordinates perpendicular to the strain are optimized along with the atomic coordinates to obtain zero stress;

(b) fixed strain—the cell coordinates perpendicular to the strain are kept fixed at the unstrained values. Case a simulates the conditions of a real experiment where the crystal would relax to obtain zero stress perpendicular to the applied stress.

IV. Structure and Cohesive Energy

A. Crystal Structures. The optimized structures of PE are shown in Table IV along with the experimental values.[13] With full optimization of cell parameters and atomic coordinates, the cell angles are all 90 ± 0.1°. For the chain direction (c) the calculated cell parameter (*n*-butane MCXX) is 0.08% smaller than experiment (at 4 K). The differences in c for various force fields seem to arise from very small shifts in the equilibrium C–C bond distance. For the directions (a, b) perpendicular to the chains the errors are 1.1% for a and −1.1% for b (*n*-butane MCXX). These parameters depend mainly on the vdW parameters, which are unchanged. Perhaps the changes in b are due to small changes in the equilibrium C–C–C angle. The calculated setting angle is θ = 41.9°, which agrees quite well with the experimental value of 41 ± 1° at 4 K.

TABLE V: Geometries and Properties of Isolated Chain and Chain of Optimum Crystal

	isolated chain	chain of optimum crystal
lattice parameters, Å		
c	2.5459	2.5457
bond distances, Å		
C–C	1.533	1.532
C–H	1.096	1.095
bond angles, deg		
C–C–C	112.30	112.42
H–C–H	108.81	108.64
C–C–H	108.92	108.93
velocity of sound		
v_c, km/s	17.8	17.9
Young's modulus		
E_c, GPa	335.7	337.1

TABLE VI: Theoretical and Experimental Lattice Energy of Polyethylene Crystal[a]

	total energy	zero-point energy	lattice energy[c]
isolated chain	3.9035	17.4199	
crystal	1.8549	17.5984	
difference	2.0486	−0.1785	1.8701
experiment			1.838 ± 0.032[b]

[a] All energies in kcal/mol per CH_2. [b] Reference 14. [c] Total energy corrected for zero-point energy.

B. Lattice Energy. Using all available thermodynamic data (heats of fusion, heats of vaporization, and heat capacities) on *n*-alkanes, Billmeyer[14] estimated the cohesive energy of crystalline PE at 0 K as

$$\Delta H^{sub}_{0K} = 1.838 \pm 0.032 \text{ kcal/mol}$$

per CH_2 group. This is the energy to separate the PE crystal into isolated all-trans PE chains.

To calculate the energy and zero-point energy of the isolated chain, we used a single chain in the three-dimensional tetragonal cell with $a = b = 100$ Å and optimized the atomic coordinates and cell parameters. a and b do not change during the optimization, indicating that the chains can be regarded as isolated. In Table V we see that there are small changes in the structural parameters when the lateral forces of the crystal are absent. Thus the C–C–C bond angle increases by 0.12°, while the H–C–H angle decreases by 0.17°. Also the CH and CC bond distances decrease by 0.001 Å.

At the optimized structure, the zero-point energy is calculated by using 1000 points in Brillouin zone. As indicated in Table VI, the lattice energy per CH_2 group is calculated as 2.0486 kcal/mol (*n*-butane force field). After the zero-point energy is corrected, this value becomes 1.8701 kcal/mol, which can be compared with the experimental value[14] of 1.838 ± 0.032 kcal/mol at 0 K.

V. Moduli and Elastic Constants

A. Young's Modulus. Although it is not yet possible to obtain single crystals of PE, it is possible (by successive drawing along the chain axis) to obtain fibers in which the crystalline regions are highly oriented, with the chain axis along the fiber axis. Thus there are a number of experimental measurements for the Young's modulus *along* the chain direction, E_c. Unfortunately, careful experimental results span the range from 210 to 340 GPa!

1. Review of Experiments on Young's Modulus. Using X-ray diffraction to observe directly the changes in cell coordinates for various crystallites as stress is applied leads to a Young's modulus (at room temperature) of 235 GPa[22] or 213–229 GPa.[23] Since

(21) Twisleton, J. F.; White, J. W.; Reynolds, P. A. *Polymer* **1982**, *23*, 578.

(22) Sakurada, I.; Nukushina, Y.; Ito, T. *J. Polym. Sci.* **1962**, *57*, 651

(23) Matsuo, M.; Sawatari, C. *Macromolecules* **1986**, *19*, 2036.

TABLE VII: (a) Comparison between Elastic Constants Using Various Force Fields at Optimized Cell Parameters. (b) Elastic Constants from Various Experimental Cell Parameters Using *n*-Butane MCXX Force Field Parameters[a]

(a)

	n-butane		
	MCXX	MCX	MC
C_{11}	14.0	14.0	13.9
C_{22}	13.5	13.6	13.5
C_{33}	338.9	287.1	237.9
C_{12}	7.9	7.9	7.9
C_{13}	2.1	2.8	2.3
C_{23}	4.8	5.4	4.8
C_{44}	5.3	5.4	5.4
C_{55}	3.0	3.0	3.0
C_{66}	5.9	6.0	5.9
E_a	9.4	9.4	9.3
E_b	9.0	9.1	9.0
E_c	337.1	284.9	236.1
β, GPa^{-1}	0.0937	0.0936	0.0943
E_c (isolated chain)	335.7	283.2	234.4

(b)

	4 K[b]	77 K[c]	213 K[c]	303 K[c]	411 K[c]
C_{11}	14.9	13.3	10.6	8.3	3.9
C_{22}	12.9	11.2	9.6	8.2	5.4
C_{33}	338.2	333.2	325.7	318.4	306.5
C_{12}	7.8	6.9	5.4	4.3	3.7
C_{13}	2.2	1.8	1.2	0.7	0.09
C_{23}	4.2	3.5	3.0	2.5	1.9
C_{44}	4.8	4.0	3.5	3.0	2.5
C_{55}	2.9	2.5	2.1	1.7	1.4
C_{66}	6.7	6.1	4.7	3.6	2.3
E_a	10.2	9.1	7.5	6.1	1.3
E_b	8.8	7.6	6.8	6.0	1.8
E_c	336.8	332.1	324.7	317.6	304.6
β, GPa^{-1}	0.0945	0.107	0.130	0.161	0.258
a, Å	7.121	7.155	7.287	7.413	7.706
b, Å	4.851	4.899	4.918	4.942	4.936
c, Å	2.548	2.5473	2.5473	2.5473	2.5473
θ, deg	42.4	42.5	42.3	42.2	40.4

[a] All quantities in GPa unless otherwise indicated. [b] Cell parameters (a, b, and c) from ref 13. [c] Cell parameters (a, b, and c) from ref 31.

the crystallites are separated by amorphous regions, Matsuo and Sawatari[23] used samples with various draw ratios to determine the effects of amorphous regions in the crystal upon the measured Young's moduli and found no significant changes in E_c, indicating that $E_c \approx 225$ GPa is the intrinsic value (at 300 K) for the embedded crystallites.

An alternative strategy to oriented crystals is to grow PE fibers at 120 °C from solutions of high molecular weight PE in xylene.[24] With such fibers, Barham and Keller[25] used a dynamic tester to measure the tensile modulus and loss factor (tan δ) as a function of temperature. The direct measurement leads to a maximum modulus of $E_c = 262$ GPa (at 77 K), which they consider a lower bound. Correcting for finite strain rate and other factors, they estimate a true modulus at 77 K of $E_c = 288 \pm 10$ GPa, and they suggest that the modulus should increase to $E_c \approx 324$ GPa at 0 K.

This value of 288 GPa is the largest directly measured modulus for PE. Other estimates of the modulus come from spectroscopic studies or theory. Thus, using inelastic neutron scattering to measure the dispersion in the longitudinal acoustical phonon band of PE leads to $E_c = 329$ GPa[26] (from the slope of the dispersion curve) at 300 K.

An alternative estimate can be made by extrapolating the vibrational frequencies of accordion-like motions (from Raman spectroscopy) for the series of linear hydrocarbon molecules (C_{18} to C_{94}) to the value for an infinite chain.[27] One such extrapolation leads to a Young's modulus of 358 ± 25 GPa at 300 K for the infinite chain.[27] Another extrapolation includes corrections for the effect of interlamellar forces in the crystal and leads to an estimate fo 290 ± 5 GPa at 300 K for the infinite chain.[28]

(24) Zwitnewberg, A.; Pennings, A. J. *Colloid Polym.* **1976**, *252*, 868.
(25) Barham, P. J.; Keller, A. *J. Polym. Sci., Polym. Lett. Ed.* **1979**, *17*, 591.
(26) Holliday, L.; White, J. W. *Pure Applied Chem.* **1971**, *26*, 545, and references therein.

TABLE VIII: Young's Moduli (in GPa) of Polyethylene[a]

	0 K	77 K	300 K
(a) E_c (chain axis)			
theory (MCXX, *n*-butane)	337	332	318
experimental			
direct			
X-ray			235[b]
X-ray			213–229[c]
dynamic tester	(324 ± 30)[g]	288 ± 10[f]	
spectroscopic			
neutron scattering			329[e]
Raman			358 ± 25[h]
Raman			290 ± 5[d]
(b) E_a (⊥ chain, long axis)			
theory (MCXX, *n*-butane)	9.4	9.1	6.1
experiment			
X-ray			3.2[i]
X-ray			2.5[i]
X-ray			5.0[i]
(c) E_b (⊥ chain, short axis)			
theory (MCXX, *n*-butane)	9.0	7.6	6.0
experiment			
X-ray			3.9[i]
X-ray			1.9[i]

[a] The theoretical values are calculated from $E_a = (S_{11})^{-1}$, $E_b = (S_{22})^{-1}$, $E_c = (S_{33})^{-1}$, where $S = C^{-1}$ is the compliance matrix. [b] Reference 22. [c] Reference 23. [d] Reference 28. Extrapolation from isolated *n*-alkane chains corrected for interlamellar interactions. [e] Reference 26. [f] Reference 25. [g] Estimated in ref 25. [h] Reference 27, extrapolation from isolated *n*-alkane chains. [i] Reference 29.

2. Calculations. The theoretical value of E_c depends strongly on the valence parameters of PE, most notably the angle–angle cross terms. Thus, with better fits to the force field of *n*-butane, we find more accurate values of E_c with $E_c = 236$ GPa for MC, 285 GPa for MCX, and 337 GPa for MCXX (see Table VII). Thus we take $E_c = 337$ GPa as the theoretical value, which is in agreement with the estimated value ($E_c \approx 324$ GPa at 0 K) from studies of high modulus PE on a dynamic tester. Various experimental results are tabulated in Table VIII.

Using the experimental cell parameters for 300 K, we calculate $E_c = 318$ GPa, which is in good agreement with the neutron scattering results of $E_c = 329$ GPa.

For the isolated chain (with the density at 300 K, 0.998 g/cm^3), we calculate $E_c = 316$ GPa, which is close to the average for the two extrapolations of Raman data (358 ± 25 GPa[27] and 290 ± 5 GPa[28]). Thus the interaction between chains leads to a 1.4 GPa increase (0.5%) in E_c (the correction is sensitive to the quality of the force field; see Table VIIa).

We carried out calculations of the vibrational frequencies for normal alkanes up to $C_{16}H_{34}$ using the MCXX force fields. The accordion modes from these calculations are compared with experiment in Table XIII where we see excellent agreement (about 0.7% lower than the least-squares fit[27] to data with higher N). In this table, we show the experimental frequencies observed in the liquid and solid phases[42] together with a least-squares fit to these frequencies.[27] This agreement suggests that our calculated elastic constants (318 GPa at 300 K and 337 GPa at 0 K) are about 1.4% lower than the true experimental values (suggested as 322 and 341 GPa, respectively).

Summarizing, the extrapolated modulus for the dynamic tester and the results from neutron scattering and Raman spectroscopy are all consistent with the theoretical values of Young's modulus, $E_c = 337$ GPa at 0 K and $E_c = 318$ GPa at 303 K. On the basis

(27) Shaufele, R. F.; Shimanouchi, T. *J. Chem. Phys.* **1967**, *47*, 3605.
(28) Strobl, G. R.; Eckel, R. *J. Polym. Sci., Polym. Phys. Ed.* **1976**, *14*, 913.

TABLE IX: Comparison of Theoretical and Experimental Elastic Constants at 213 and 77 K[a]

	T = 213 K		T = 77 K	
	theory	exptl[b]	theory	exptl[c]
C_{11}	10.6	8.4	13.3	11.5
C_{22}	9.6		11.2	
C_{33}	325.7	102	333.2	
C_{12}	5.4	4.2	6.9	
C_{13}	1.2	5.5	1.8	
C_{23}	3.0		3.5	
C_{44}	3.5	1.81	4.0	
C_{55}	2.1		2.5	
C_{66}	4.7	2.02	6.1	
a	7.287		7.155	
b	4.918		4.899	
c	2.5473		2.5473	

[a] Cell parameters from ref 31 are used in the calculation. [b] Reference 30. The values for HDPE (draw ratio = 27) at −60 °C. [c] Reference 21.

of comparison to Raman data for linear alkanes, we estimate the exact results to be

$$E_c = 341 \pm 9 \text{ GPa} \quad \text{at 0 K}$$

$$E_c = 322 \pm 9 \text{ GPa} \quad \text{at 300 K}$$

In contrast, the Young's moduli in the a and b directions (perpendicular to the chain) depend most sensitively upon the vdW parameters and the temperature. We find E_a = 9.4 GPa and E_b = 9.0 GPa for the theoretical cell parameters and

$$E_a = 10.2 \text{ GPa} \quad \text{at 4 K}$$

$$E_b = 8.8 \text{ GPa} \quad \text{at 4 K}$$

for the experimental cell parameters at 4 K. This indicates that the interactions between the chains at the corner and center of the unit cell are stronger than those along the short (b) axis.

Experimental results for the moduli perpendicular to the chains (E_a and E_b) are expected to be far less reliable than for E_c because crystalline imperfections should greatly decrease the net bonding. In addition, thermal expansion leads to large decreases in those moduli as temperature is increased from 0 K to room temperature. Thus, using the experimental cell parameters at room temperature, we find

$$E_a = 6.1 \text{ GPa} \quad \text{at 300 K}$$

$$E_b = 6.0 \text{ GPa} \quad \text{at 300 K}$$

(decreases of 4.1 and 2.8 GPa, respectively). Three sets of experimental moduli perpendicular to the chain direction of PE have been reported:[29] (1) E_a = 3.2 GPa, E_b = 3.9 GPa, (2) E_a = 2.5 GPa, E_b = 1.9 GPa, and (3) E_a = 4.0 GPa. All are much smaller than the calculated moduli.

B. Elastic Constants. The calculated elastic constant values for various force fields are listed in Table VII. Only the chain–chain constant C_{33} changes appreciably, suggesting that for PE crystal the elastic constants involving distortions parallel to the chain are largely determined by the valence force field, while the perpendicular and shear elastic constants are largely determined by the nonbond force field.

Choy and Leung[30] measured the elastic constants of PE at 213 K using high-density polyethylene with a draw ratio of 27. This should orient the chains toward the axis, but incompletely. The result is a value of C_{33} = 102 GPa, which is less than one-third of the limiting value (326 GPa at 213 K). In Table IX we compare the experimental results with calculated values using the experimental unit cell at 213 K. The other experimental values are smaller than values obtained here except for C_{13} (see Table IX).

(29) Odajima, A.; Maeda, T. *J. Polym. Sci. C.* **1966**, *15*, 55.
(30) Choy, C. L.; Leung, W. P. *J. Polym. Sci., Polym. Phys. Ed.* **1985**, *23*, 1759.

TABLE X: Comparisons of Theoretical (MCXX) and Experimental Vibrational Frequencies (cm^{-1}) of Polyethylene Crystal at the Γ Point (Zone Center)

		calculations		
mode[b]	symmetry	optimum cell	(300 K)	expt[a] (300 K)
lattice	A_u	50	39	
	B_{3g}	82	65	(108)[d]
	B_{1u}	84	66	80[c]
	B_{2u}	115	88	109[c]
	A_g	132	105	137[d]
CH_2 rock	B_{2u}	784	783	720
	B_{1u}	798	791	731
	A_g	1164	1163	1168
	B_{3g}	1165	1164	1168
CH_2 twist	A_u	1031	1032	
	B_{3u}	1033	1033	1050
	B_{2g}	1306	1305	1295
	B_{1g}	1311	1308	1295
skeletal	B_{1g}	1046	1042	1061
	B_{2g}	1052	1046	1061
	B_{3g}	1101	1097	1131
	A_g	1101	1097	1131
CH_2 wag	A_u	1220	1219	
	B_{3u}	1216	1216	1175
	B_{1g}	1438	1435	1415
	B_{2g}	1441	1437	1415
CH_2 sciss	A_g	1461	1462	1440
	B_{3g}	1490	1485	1464
	B_{2u}	1484	1482	1463
	B_{1u}	1485	1481	1473
CH_2 sym str	B_{2u}	2873	2865	2851
	B_{1u}	2873	2868	2851
	B_{3g}	2890	2880	2848
	A_g	2892	2882	2848
CH_2 asym str	A_g	2924	2913	2883
	B_{3g}	2934	2922	2883
	B_{1u}	2937	2929	2919
	B_{2u}	2937	2929	2919
$\lvert\Delta\nu\rvert_{avg}$		24	24[e]	

[a] Reference 32 unless indicated otherwise. T = 300 K. [b] The modes are grouped by type and the label placed with the first mode of a type. [c] Reference 15. T = 2 K. [d] Reference 16. T = 4 K. [e] Excluding lattice modes.

There is also an experimental value of C_{11} = 11.5 GPa (at 77 K) from Twisleton et al.,[21] which can be compared with the calculated elastic constant of C_{11} = 13.3 GPa using cell parameters for 77 K[31] (see Table IX).

VI. Phonons and Thermodynamics

A. Vibrational Frequencies. The MCXX force field from *n*-butane leads to the vibrational levels of polyethylenes as reported in Table X (all at the Γ point or zone center). In these calculations, we did *not* change any parameters for *n*-butane; we used the predicted cell parameters and the experimental cell parameters at 300 K. The experimental vibrational frequencies of PE from infrared and Raman spectra are also listed in Table X (the lattice modes are for 2 and 4 K, but the higher modes are at 300 K). The average error for PE at room temperature is 24 cm^{-1}. In comparison, this force field leads to an average error of 7.9 cm^{-1} for the free molecule *n*-butane. Although we could have readjusted the valence force field to obtain a better fit to the vibrations, we have not done so here. The reason is that we consider this procedure of calculating the phonons and other properties of crystals using the valence force field for a finite molecule to be a prototype for similar calculations for many other polymers where experimental data are not available.

Overall agreement between calculated and experimental intramolecular frequencies is good. The exception occurs for the CH_2 rocking modes observed in PE at 720 and 731 cm^{-1} but

(31) Swan, P. R. *J. Polym. Sci.* **1962**, *56*, 403.
(32) Tasumi, M.; Shimanouchi, T. *J. Chem. Phys.* **1965**, *43*, 1245.

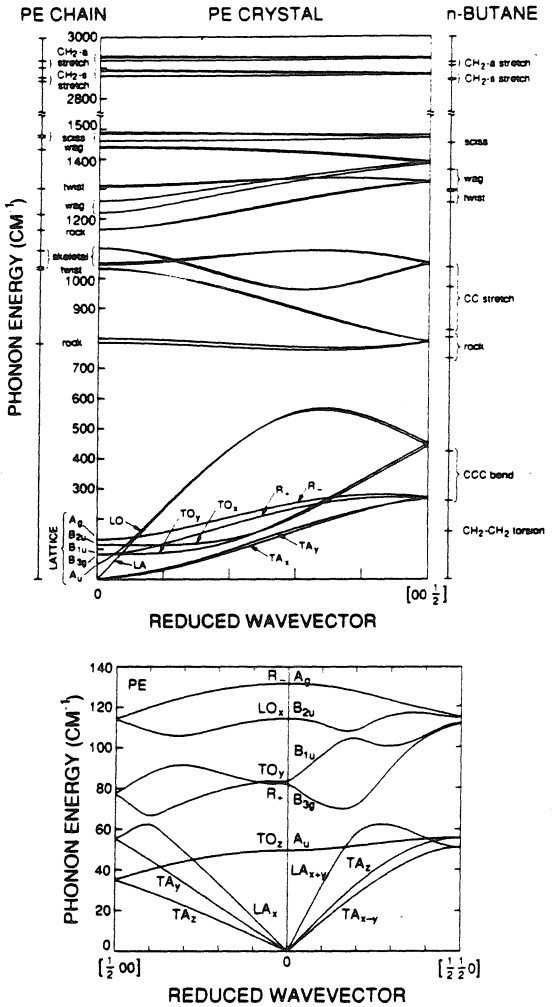

Figure 1. Phonon dispersion curves of polyethylene crystal (MCXX *n*-butane force field) (a, top) in the chain direction (*c* axis) and (b, bottom) in the [1 0 0] and [1 1 0] directions. In (a), frequencies of the isolated infinite chain at $k = 0$ and those of *n*-butane are also shown.

calculated at 789 and 798 cm^{-1}, respectively. The analogous mode for *n*-butane is well described (0.5 cm^{-1} error, observed at 733 cm^{-1}) where it involves a mixture of CH_3 rock and CH_2–CH_3 torsion modes. In contrast for PE, this mode corresponds to nearly pure CH_2 rock motion. Probably fitting to the modes of *n*-pentane or *n*-hexane (which have purer rock character) would have improved the comparison for PE. The temperature dependence of the splitting in the 720 and 731 cm^{-1} modes indicates that intermolecular interactions may also play some role in these modes.

In the case of B_u modes, we find that the frequency of the internal mode depends on the direction of the wave vector near the Γ point. In such modes, nonzero polarization is produced in the unit cell and a depolarization field is created. This field depends on the direction of the wave vector and affects the lattice distortion differently;[33] hence, the frequency depends on the direction of the wave vector. For example, the calculated frequency for the B_{2u} rocking mode is 784, 784, and 797 cm^{-1} for wave vectors in the *z*, *x*, and *y* directions, respectively. However, in this case, the allowed transition occurs only for the *z* and *x* directions, so that 784 cm^{-1} is quoted. Similarly for all other B_u

(33) Brüesch, P. *Phonons: Theory and Experiments I*; Springer-Verlag: Berlin, 1982.

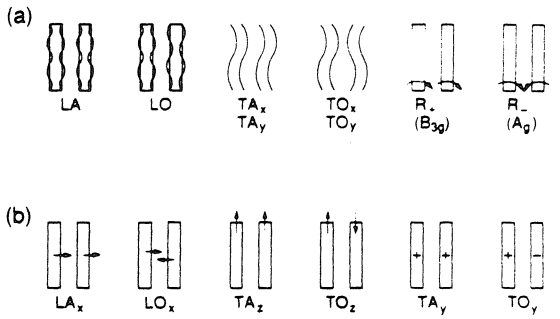

Figure 2. Schematic diagram for lattice modes of PE: (a) wave vector along chain axis; (b) wave vector perpendicular to chain axis.

modes, the allowed directions for the wave vector lead to equivalent results and only such values are quoted in Table X.

The various Raman and infrared (IR) experiments provide data for four of the five possible lattice modes. Three modes (B_{1u}, B_{2u}, and A_g) are strong and well resolved experimentally;[15,16] however, one mode, B_{3g}, is rather weak and observed at a value nearly concident with the B_{2u} mode.[16] Consequently, we used the three former states to select the optimum scale parameter ζ_H.

B. Phonon Bands. The phonon frequencies of the lattice bands calculated along the [0 0 1], [1 0 0], and [1 1 0] directions are shown in Figure 1.

Also indicated at the left in Figure 1 are the modes for the isolated chain (for the Γ point). Thus, the packing of PE fibers leads to only small changes in the positions of these levels. Also indicated at the left in Figure 1 are the positions of the vibrations in *n*-butane associated with the central CH_2 groups. From these comparisons we see that the modes associated with CH_2 motion in *n*-butane correspond closely to the modes in PE. In addition, the C–C stretch modes of *n*-butane correspond to the skeletal modes of PE. However, the C–C–C angle-bend and torsion modes of *n*-butane become lattice modes in PE.

The lattice modes can be understood by considering the crystal of PE fiber to be a collection of round rods packed together. This is indicated in Figure 2 for vibrations parallel and perpendicular to the chain direction. The energies of these lattice modes are sensitively dependent upon the vdW interactions. Indeed, we used the comparison with experiment to help determine the ζ_H vdW parameter. For the [0 0 $^1/_2$] point we see that the eight lattice modes have coalesced into four, at 268, 272, 442, and 451 cm^{-1}. These values correspond roughly to the g and u modes for C–C–C bend in *n*-butane (425 and 267 cm^{-1}, respectively). The torsion mode for the central bond in *n*-butane is at 155 cm^{-1}.

For wave vectors perpendicular to the chain (Figure 1b), the highest energy lattice mode is at 130 cm^{-1}. Thus, for temperatures above ~200 K, all such lattice modes are activated, allowing the spacing and orientations of the rods freedom to change rapidly. It is interesting that the glass transition temperature of PE is ~213 K, which corresponds reasonably well to the highest lattice mode perpendicular to the chain. This is reasonable since multiple energy loss processes for macroscopic deformation of the polymer become possible when all lattice modes are active. It will be interesting to see if the lattice modes of other polymers correlate with the glass temperature.

Inelastic neutron scattering experiments have been reported for deuteriopolyethylene in the direction [1 0 0] and [1 1 0],[21] and hence we calculated (Figure 3) the phonon bands of deuteriopolyethylene (using the experimental cell parameters at 77 K). For the [$^1/_2$ $^1/_2$ 0] direction there is excellent agreement in the dispersion for the lowest three observed transitions. The highest observed case lies in between the two calculated curves (LA_{x+y} and TO_z). Similarly for [$^1/_2$ 0 0], the lower energy transition corresponds well to LA_z, but the highest observed transition is between LA_x and TA_y.

Low-frequency Raman-active vibrations of *n*-paraffins have been studied by Wu and Nicol,[41] Olf and Fanconi,[39] and Vergoten

TABLE XI: Calculated Thermodynamic Properties of Polyethylene Crystal[a]

T, K	C_p, cal/(mol K)	C_v, cal/(mol K)	S, cal/(mol K)	U, kcal/mol	F, kcal/mol	$10^4\alpha$, K^{-1}	V, Å^3	β, GPa^{-1}
20	0.1769	0.1756	0.0689	0.0010	−0.0004	0.433	22.006	0.0946
40	0.6583	0.6473	0.3286	0.0091	−0.0041	0.907	22.036	0.0956
60	1.1836	1.1495	0.6869	0.0270	−0.0142	1.32	22.086	0.0975
80	1.6701	1.5990	1.0809	0.0546	−0.0318	1.67	22.151	0.1000
100	2.0944	1.9764	1.4795	0.0905	−0.0574	1.95	22.230	0.1031
120	2.4629	2.2931	1.8686	0.1333	−0.0909	2.17	22.324	0.1069
140	2.7875	2.5692	2.2432	0.1820	−0.1321	2.32	22.426	0.1114
160	3.0838	2.8240	2.6030	0.2360	−0.1805	2.41	22.530	0.1160
180	3.3583	3.0727	2.9500	0.2949	−0.2361	2.43	22.643	0.1213
200	3.6158	3.3258	3.2868	0.3589	−0.2985	2.37	22.749	0.1267
220	3.9075	3.5898	3.6160	0.4280	−0.3675	2.41	22.859	0.1325
240	4.2043	3.8677	3.9402	0.5025	−0.4431	2.43	22.970	0.1387
260	4.5141	4.1597	4.2612	0.5828	−0.5251	2.44	23.082	0.1450
280	4.8410	4.4646	4.5806	0.6691	−0.6135	2.48	23.195	0.1524
300	5.1937	4.7798	4.8993	0.7615	−0.7083	2.57	23.312	0.1601
320	5.5796	5.1022	5.2180	0.8603	−0.8095	2.73	23.436	0.1686
340	6.0067	5.4287	5.5372	0.9656	−0.9171	3.00	23.570	0.1790
360	6.4897	5.7565	5.8567	1.0774	−1.0310	3.38	23.720	0.1916
380	7.0399	6.0829	6.1767	1.1958	−1.1513	3.91	23.893	0.2086
400	7.6699	6.4059	6.4970	1.3207	−1.2780	4.59	24.096	0.2316

[a] The vibrational specific heat (C_p, C_v), entropy (S), energy (U), and free energy (F) are each per CH_2 of polyethylene crystal (using *n*-butane MCXX force parameters). Thermal expansion coefficient (α), volume (V), and compressibility (β), used to convert C_v to C_p, are also shown.

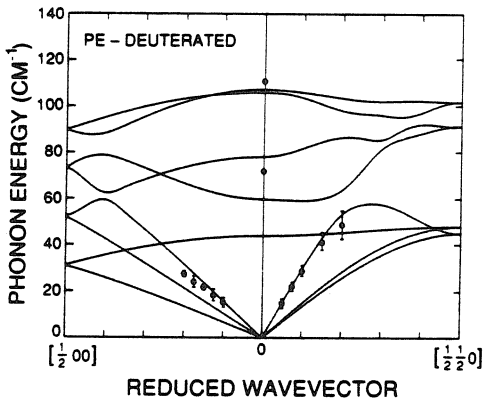

Figure 3. Phonon dispersion curves of deuteriopolyethylene crystal (MCXX *n*-butane force field) in the [1 0 0] and [1 1 0] directions. Experimental points are from ref 21.

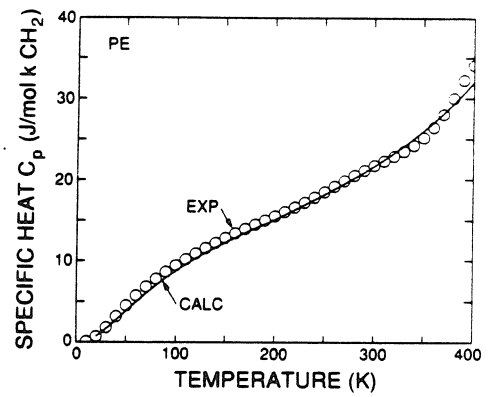

Figure 4. Calculated C_p and experimental[34] C_p versus temperature.

et al.[40] Olf and Fanconi[39] and Vergoten et al.[40] find that low-frequency modes of orthorhombic *n*-paraffins correspond to the transverse acoustical branches of polyethylene (TA_x and TA_y in Figure 1a). In Figure 8 we show these phonon bands calculated using the experimental cell parameters at 77 and 168 K (atomic coordinates and setting angles were optimized). As indicated in Figure 8, the modes assigned by Vergoten et al.[40] agree quite well with our calculations. However, the assignments by Olf and Fanconi do not agree with our calculations or with the results by Vergoten. Since our calculated bands perpendicular to the chain direction also agree well with the neutron-scattering experiments (which provide a more direct test), we suggest that the assignments for the experiments by Olf and Fanconi be reconsidered.

C. Thermodynamic Properties. Thermodynamic properties were calculated by using the phonon states at 0 K (see section III.C for details) and are reported in Table XI as a function of temperature.

The calculated values of specific heat at constant volume C_v were converted to constant pressure, C_p, using the thermodynamic relation $C_p = C_v + V\alpha^2T/\beta$, where V is the volume, α is the thermal expansion coefficient, and β is the compressibility [$\beta = \sum_{ij=1}^{3}(C^{-1})_{ij}$]. Temperature variations of cell parameters were measured by Swan[31] between 203 and 403 K. Experimental results are also available at 4 and 90 K.[13] Using spline fits to these data yields the $V(T)$ and $\alpha(T)$ in Table XI. With these cell parameters we calculated $\beta(T)$ as in Table XI. This leads to the $C_p(T)$ given in Table XI, and these are compared with experimental[34] $C_p(T)$ in Figure 4.

These calculations of the thermodynamic properties assume each normal mode (phonon) is harmonic, an approximation that becomes poorer at higher temperatures. This should underestimate C_v at high temperature. We see that the theoretical and experimental C_p are in excellent agreement below 300 K but diverge increasingly as the melting temperature (414.6 ± 0.5 K[34]) is approached.

VII. Finite Stress–Strain Relations

A. Stress and Ultimate Yield Stress. In Figure 5a, stresses are plotted as functions of deformation of the cell in the *a* and *b* directions. Here the cell parameters perpendicular to the deformation direction and the atomic coordinates are optimized starting from the structures optimized at fixed cell parameters. In both directions, there is a near singularity at a value (σ_{ult}) beyond which two new surfaces are created. Below this distance, the polymer rods are uniformly spaced. As the crystal is stretched, the rods separate further until a distance is reached at which it is better to create a surface and let all other chains relax to their normal distance. For the *a* direction, the yield point is $\sigma_y = 0.097$ GPa at 1.0% strain and the ultimate stress is $\sigma_{ult} = 0.20$ GPa at 3.5% strain. For the *b* direction we find $\epsilon_y = 0.23$ GPa at 3.1% strain and $\sigma_{ult} = 0.44$ GPa at 8.3% strain.

In Figure 5 we see that the stress–strain relation is approximately linear (elastic) up to the yield point (σ_y), and it bends over

(34) Gaur, U.; Wunderlich, B. *J. Phys. Chem. Ref. Data* **1981**, *10*, 119.

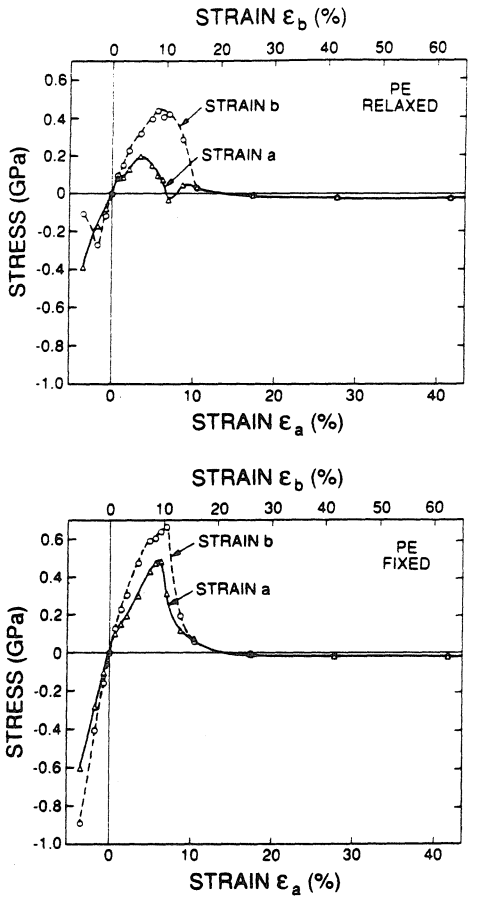

Figure 5. Stress versus strain for finite deformation in the *a* and *b* directions of polyethylene crystal (MCXX *n*-butane force field). Cell parameters perpendicular to the deformation direction are optimized in (a, top) and fixed in (b, bottom).

as the system enters a nonlinear regime. This is reminiscent of the properties of any ductile material, where Young's modulus is constant up to the yield stress σ_y. At this point, plastic deformation begins and the modulus decreases with further strain until the ultimate stress (σ_{ult}) is reached where the sample fractures.

Because we fix the cell dimension along the strain direction, there are small negative stresses at large distances. Optimization of all cell parameters at such distances gives zero stresses without changing the energy significantly.

In Figure 6, strains in the direction perpendicular to the deformation are shown at each finite strain in the *a* (a) and *b* (b) directions. In Figure 6a, when the cell is compressed along a direction (negative strain), the cell is stretched in the *b* direction (positive strain). Conversely, when the cell is stretched in the *a* direction, the cell is compressed in the *b* direction. After the surface is created, the strain in the *b* direction approaches zero as strain in the *a* direction is increased. Similar behavior is observed in Figure 6b except that *a* and *b* are interchanged. In both cases, we find that the strain in the *c* direction is very small (less than 0.05%).

We also carried out calculations in which the cell parameters perpendicular to the deformation direction are fixed. The result is shown in Figure 5b. The stress at each point changes significantly and the position of the peak is also changed. The ultimate stresses are not calculated as 0.48 GPa at 6.2% strain in the *a* direction and 0.66 GPa at 10.4% strain in the *b* direction. The yield stresses are 0.10 and 0.23 GPa.

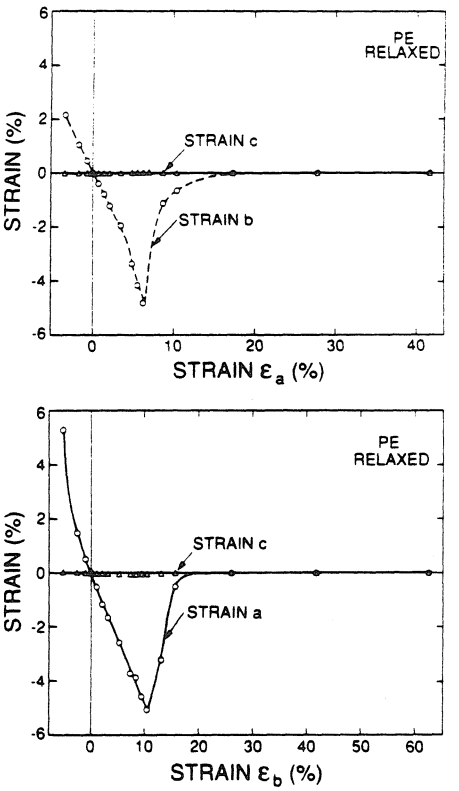

Figure 6. Strain in the perpendicular direction versus strain in the deformation direction. Here cell parameters perpendicular to the deformation direction are optimized. (a, top) Deformation along *a* direction; (b, bottom) deformation along *b* direction.

A particularly interesting behavior is found in the deformation along the *a* direction at a distance of 1.8–2.0 Å. At these distances, stresses become small, but a surface is not created, indicating that the energy is near a stationary point. Starting with the structure at 7.3% strain and using conjugate gradients to optimize all cell parameters and atomic coordinates, we obtain a new extended structure at which forces and stresses vanish! It has an orthorhombic unit cell with $a = 7.727$ Å, $b = 4.483$ Å, and $c = 2.547$ Å. The energy is 0.0931 kcal/mol higher than the optimized structure in Table IV per unit cell (four CH_2 groups). The elastic constant matrix calculated at this structure is

$$\mathbf{C} = \begin{bmatrix} 8.1 & 13.0 & 4.0 & 0 & 0 & 0 \\ 13.0 & 8.0 & 4.4 & 0 & 0 & 0 \\ 4.0 & 4.4 & 338.2 & 0 & 0 & 0 \\ 0 & 0 & 0 & 6.1 & 0 & 0 \\ 0 & 0 & 0 & 0 & 5.6 & 0 \\ 0 & 0 & 0 & 0 & 0 & 6.3 \end{bmatrix} \text{GPa} \qquad (27)$$

The matrix is not positive-definite [$(C_{12})^2 \sim 2C_{11}C_{22}$ leads to a negative eigenvalue], showing that the structure is mechanically unstable.

B. Surface Energy. In Figure 7, the energies are plotted as functions of distance with (a) and without (b) relaxing cell parameters perpendicular to the deformation direction. In Figure 7, the energy varies quadratically near zero and rises monotonically to a constant value for large distances. Since the slabs do not interact for large deformations, the surface energy E_s was calculated by

$$E_s = \frac{E_{def} - E_{eq}}{2S} \qquad (28)$$

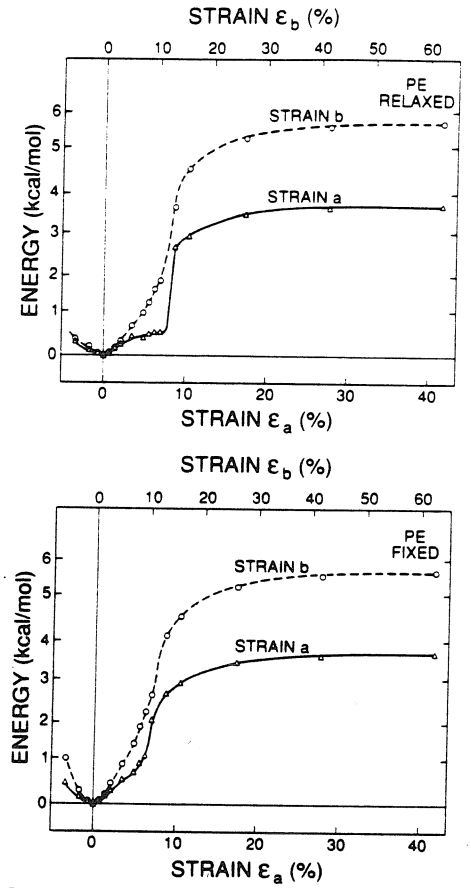

Figure 7. Energy versus strain for finite deformation in the *a* and *b* directions of polyethylene crystal (MCXX *n*-butane force field). Cell parameters perpendicular to the deformation direction are optimized in (a, top) and fixed in (b, bottom).

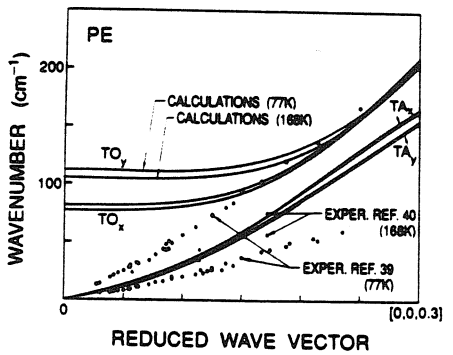

Figure 8. Transverse acoustic and optical bands of PE [using cell parameters at 77 K and 168 K. The circles indicate experimental data of Olf and Fanconi (ref 39) at 77 K, and triangles indicate experimental data of Vergoten et al. (ref 40) at 168 K.

where E_{def} is the energy of the fully deformed cell and E_{eq} is that of the equilibrium cell. Here S is the original area of the unit cell perpendicular to the strain direction, and we take into account that two surface are created.

This leads to a surface energy of 106.8 dyn/cm for the *a* direction [creating the (100) surface] and 109.2 dyn/cm for the *b* direction [creating the (010) surface]. When the (100) surface is created (deformation along the *a* axis), there are two CH_2 groups per unit cell in the new surface cell. Thus the surface energy per CH_2 is $^1/_4$ of the total energy increase or 0.938 kcal/mol. On the other hand, when the (010) surface is created (deformation along the *b* axis), there are four CH_2 groups per new surface cell. Thus the surface energy per CH_2 is $^1/_8$ of the energy change or 0.720 kcal/mol.

If the interactions were nearest-neighbor fiber–fiber only, one would expect the surface energy to be $^1/_3$ the bulk cohesive energy (or 0.683 kcal/mol) for both (100) and (010). This is reasonably close to the calculated values, indicating that such simple models may give useful first estimates.

The calculated surface energies neglect zero-point-energy effects, but this correction should be much smaller than that of lattice energy calculation. Since the calculated cohesive energy for bulk PE is within 2% of the experimental value, we expect our calculated surface energy to have similar accuracy.

An experimental surface energy for low-density PE has been obtained by using the contact angle measurements.[35] The experimental value of 33.1 dyn/cm is about one-third of our calculated values. This suggests that the surface of low-density PE is quite disordered.

TABLE XII: Cell Parameters and Elastic Constants (in GPa) of Polyethylene from Various Calculations

parameter	expt[f] (4 K)	current calcns[e]	other calculations SLB[a]	WB[b]	OM[c]	TKT[d]
a	7.121	7.202	7.05	7.156		
b	4.851	4.795	4.94	4.894		
c	2.546	2.548	2.544			
θ, deg	41 ± 1	41.9	43.1	43.68		
C_{11}		14.0	14.3	13.8	9.27	7.99
C_{22}		13.5	12.2	12.5	10.93	9.92
C_{33}		338.9	341	325	257.4	316
C_{12}		7.9	7.2	7.34	3.68	3.28
C_{13}		2.1	1.92	2.46	3.36	1.13
C_{23}		4.8	3.30	3.96	6.67	2.14
C_{44}		5.3	3.64	3.19	3.46	3.19
C_{55}		3.0	2.27	1.98	1.27	1.62
C_{66}		5.9	7.3	6.24	4.99	3.62

[a] Reference 36. [b] Reference 3. [c] Reference 29. [d] Reference 38. [e] MCXX from *n*-butane. [f] Reference 13.

TABLE XIII: Comparison of Theoretical and Experimental Frequencies (cm^{-1}) for the Accordion (Raman) Mode for *n*-Alkanes (C_nH_{2n+2})

n	theory (MCXX)	experiment least squares[a]	liquid[b]	solid[b]
4	424	473	429 (5)	425 (4)
5	402	411	400 (7)	406 (3)
6	372	358	370 (4)	373 (3)
7	305	313	310 (6)	311 (5)
8	278	278	279 (5)	283 (3)
9	243	249	248 (3)	249 (2)
10	225	225	230 (3)	231 (3)
11	198	206		
12	189	189	195 (1)	194 (2)
13	177	175		
14	163	163		
15	153	153		
16	143	144		140 (3)

[a] Based on the analytic least-squares fit to the observed frequencies (m = 1) as reported in ref 27. [b] Reference 42.

VIII. Comparison with Other Calculations

The cell parameters and elastic constants are compared with other calculated values in Table XII.

Recently, Sorensen et al.[36] (SLB) have obtained the optimized structures and properties of polymer crystals utilizing simultaneous inter- and intramolecular energy minimization. They have used parameters optimized for the polyethylene and poly(oxymethylene)

(35) Owens, D. K.; Wendt, R. C. *J. Appl. Polym. Sci.* **1969**, *13*, 1741.
(36) Sorensen, R. A.; Liau, W. B.; Boyd, R. H. *Macromolecules* **1988**, *21*, 194–199, 200–208.

and calculated properties at the optimized structure of these crystals.

As can be seen from Table XII, there is good agreement between our elastic constants and those of SLB.

The elastic constants of PE have also been obtained theoretically by Odajima and Maeda (OM),[29] Wobser and Blasenbrey (WB),[37] and Tashiro et al. (TKT),[38] as listed in Table XII. The values from WB are in reasonable agreement with our values and those of SLB. However, the elastic constants obtained by OM and by TKT do not agree well with other calculated elastic constants, especially for components perpendicular to the chain directions (C_{11}, C_{22}, C_{12}, C_{66}). This is probably because they used an unreasonably small cutoff distance (4 Å) for the intermolecular interactions.

The vdW parameters of SLB are slightly modified from those of Williams, while the vdW parameters of WB were adjusted to fit the energy and cell parameters of PE. The setting angles of these calculations are 1.2° and 1.8° larger than ours, which is in turn 0.9° larger than experiment.

IX. Summary

Force field parameters adequate for molecular mechanics calculations for PE crystal are developed and tested. Valence force field parameters are obtained by using a theoretical Hessian as well as experimental data for *n*-butane. Nonbond parameters are determined empirically from graphite and PE crystals. The cell and atomic coordinate optimizations were carried out on PE crystal, and elastic constants and phonon bands were calculated by using analytical second derivatives. To examine the behavior of the crystal under large strain in the directions perpendicular to the chain, stress and energy are plotted as functions of deformation distances. Yield stresses and surface energies are calculated from these relations.

Acknowledgment. This work was partially supported by grants from the Air Force Office of Scientific Research (No. AFOSR-88-0051), the Caltech Consortium in Chemistry and Chemical Engineering, and Imperial Chemical Industries, Wilton Materials Research Centre, Cleveland, England.

Registry No. Polyethylene (homopolymer), 9002-88-4.

(37) Wobser, G.; Blasenbrey, S. *Kolloid Z. Z. Polym.* **1970**, *241*, 985.
(38) Tashiro, K.; Kobayashi, M.; Tadokoro, H. *Macromolecules* **1978**, *11*, 914.
(39) Olf, H. G.; Fanconi, B. J. *Chem. Phys.* **1973**, *59*, 534.
(40) Vergoten, G.; Fleury, G.; Tasumi, M.; Shimanouchi, T. *Chem. Phys. Lett.* **1973**, *19*, 191.
(41) Wu, C-K.; Nicol, M. *J. Chem. Phys.* **1973**, *58*, 5150.
(42) Mizushima, S.; Shimanouchi, T. *J. Am. Chem. Soc.* **1948**, *71*, 1320.

Chapter V

Molecular Simulations of Structure and Properties of Poly (vinylidene fluoride) Crystals

Abstract

Structure and properties of four different experimentally observed forms of poly (vinylidene fluoride) crystals are studied by using the molecular-mechanics method. Force-field parameters are obtained by experimental frequencies of form I crystal as well as the Hartree-Fock calculations of 1,1,1,3,3-pentafluorobutane. To take into account atomic polarizabilities, a shell model is used and their effects on the properties are examined. By using the force field thus developed, cell parameters, elastic constants, dielectric constants, and piezoelectric constants are calculated. Various properties of the fifth crystal form suggested by Lovinger are calculated and are found to be mechanically stable with comparable energy with other forms. Also two different packings of chains (up-up and up-down) in the unit cell are examined for all forms except form I.

I. Introduction

Poly (vinylidene fluoride) (PVDF) is a technologically important polymer because of its piezoelectric properties. Four crystal forms (I, II, III and IV) are known for this polymer, of which piezoelectric properties are observed in two forms (I and IV).

Form I (β form) has a planar-zigzag type of conformation, and cell parameters are determined[1] as a=8.58 Å, b=4.91 Å, and c (chain axis)=2.56 Å, and the space group is Cm2m (C_{2v}^{14}). There are two chains in the unit cell, and the polarities of these chains are aligned in the direction parallel to b axis.

Form II (α form) has a molecular conformation of TGT$\bar{\text{G}}$ and a space group reported[2] is $P2_1/c$ (C_{2h}^{5}). There are two chains in the unit cell, and these are aligned in the nonpolar fashion in a direction perpendicular to the chains. There are four molecules in the unit cell, and orientations of these molecules are determined statistically in the experiment[2]. The cell parameters are a=4.96 Å, b=9.64 Å, c (chain axis) = 4.62 Å, and $\beta = 90.0°$.

Form III (γ form) has a molecular conformation of $T_3GT_3\bar{G}$, and the unit cell is monoclinic with a=4.96Å, b=9.67Å, c (chain axis)=9.20Å, and $\beta = 93.0°$[3]. The space group reported[4] is Cc (C_s^4). Two chains are packed in the unit cell such that the polarities of these chains in the direction perpendicular to the chains are aligned in the same direction. The existence of an antipolar analogue of this form is suggested by Lovinger[3].

Form IV (δ or IIp form) has the same molecular conformation as form II but two chains in the cell are aligned in a polar fashion in a direction perpendicular to the chains. The unit cell[5] is orthorhombic with lattice constants a=4.96Å, b=9.64Å and c (chain axis)=4.62Å. The chains are packed with a statistical up-down packing[5], and the space group is $P2_1cn$ (C_{2v}^{9}).

Theoretically, elastic and piezoelectric constants of form I crystal were cal-

culated previously by Tashiro et al.[6] by considering the short-range Coulomb interactions and without considering the atomic-polarization effects.

In this study, force-field parameters are determined by experimental vibrational frequencies of form I crystal as well as the Hartree-Fock calculations of 1,1,1,3,3-pentafluorobutane ($C_4H_5F_5$) and we apply this force field for all crystal forms to examine the relative stability of these forms.

Also, we developed a shell model to examine the effects of atomic polarizabilities to the properties of the system. The atomic charges are determined consistently with the shell model using the charges obtained from the Hartree-Fock wave function of the $C_4H_5F_5$ molecule[7].

For treating the long-range, nonbonding interactions (Coulomb and van der Waals) accurately and efficiently, the ABCA method[8] (based on the Ewald method) is used. Elastic, dielectric and piezoelectric properties are calculated from analytic second derivatives of energy at optimized structure[9].

Derived force-field parameters are used to study the stabilities of all forms and also new forms. Particularly, it is used to study the antipolar form III suggested by Lovinger[3].

II. The Force Field

We have developed two independent sets of force-field parameters for this polymer. The first set (set I) does not have parameters for a shell model. It has Coulomb and van der Waals terms for nonbonding interactions. Valence interactions include bond, angle, torsion, and cross (angle-stretch, stretch-stretch, 1-center and 2-center angle-angle) terms. The second set (set II) includes parameters for a shell model in addition to parameters of the first set, but actual values of these parameters are different. Here we first show the method of developing the force field for set I and then explain the shell model used for representing the polarizabilities of atoms.

Finally, we show the method of obtaining parameters for the shell model.

A. Parameters without the shell model (set I)

In the previous study[10], we have developed force-field parameters of polyethylene crystal by using a biased Hessian approach. In that study, experimental data as well as Hartree-Fock calculations of n-butane are used to develop the force-field parameters, since experimental geometry and frequencies of n-butane are known.

In the case of PVDF, not enough experimental data for oligomers suitable for fitting parameters are known except for 2,2-difluoropropane. On the other hand, experimental frequencies of form I crystal are reported[11]. Therefore, we use these frequencies to obtain valence force-field parameters.

For the geometry, we optimized the structure of $C_4H_5F_5$ by using the Hartree-Fock calculations with a 6-31G** basis set[12] and determined the atomic positions inside the crystal by using the force-field parameters to reproduce the geometry of this molecule.

The van der Waals parameters are previously determined for carbon[13] and hydrogen[10]. For the fluorine parameters, we use the parameters derived previously for CF_4 and polytetrafluoroethylene crystals[14], because of the lack of experimental crystal structure of fluorinated hydrocarbons. These fluorine vdW parameters are used in this study since cell parameters of all crystal forms are reproduced reasonably well.

Atomic charges used are based on the electrostatic-potential derived charges[7] of the Hartree-Fock wave function of $C_4H_5F_5$ molecule. In this method, several thousand points around the molecule are chosen and the electrostatic potential is calculated from the Hartree-Fock wave function, and atomic charges are assigned at each atomic position to fit the potential around the molecule. We calculated charges

at both trans and gauche conformations, but calculated charges are quite similar (RMS difference of 0.015e). Given these results, 0.18e and -0.26e are assigned for the charges of hydrogen and fluorine and -0.54e and 0.70e are assigned for the charges of carbons in CH_2 and CF_2 groups, respectively.

The experimental frequencies of form I crystal[11] are used to determine the valence parameters. Valence terms used are the Morse bond, cosine angle, torsion and cross (angle-stretch, stretch-stretch, 1-center angle-angle, and 2-center angle-angle) terms. In the parameter optimization[15], van der Waals parameters and charges are fixed. During the optimization, force and stress in the chain direction are also minimized.

Since we are interested in crystal forms with gauche conformation, it is necessary to reproduce the torsional potential of the chain, including both the trans and the gauche conformations. To describe this potential adequately, we used the torsional potential curve of the CH_3-CF_2-CH_2-CF_3 molecule obtained by the Hartree-Fock calculations with a 6-31G** basis set[12]. In these calculations, the central C-C bond is rigidly rotated from the optimized structure at the trans and the energy is calculated at each point. In the molecular-mechanics calculations, six terms with different periods are used in the C-C-C-C torsion, and these terms are fitted to the values of the Hartree-Fock calculations, using the Fourier transformation.

In Table I, the force-field parameters are shown. In Table II, the experimental and calculated vibrational frequencies of the form I crystal are shown. The line group of the all-trans chain is C_{2v}. In the crystal, the Raman and infrared frequencies are split (correlation splitting) because of the nonbond interactions between the chains. The RMS difference between calculated and experimental frequencies is 5.4 cm^{-1}. In Figure 1, the torsional potential curves of $C_4H_5F_5$ molecule calculated by molecular mechanics and the Hartree-Fock method are shown.

B. The Shell Model

In the usual molecular-mechanics calculations, fixed atomic charges are used to represent the electrostatic properties of the molecule. But it is clear that the polarizability of a molecule is not adequately represented by this model, since most of the polarizability effects come from the displacement of electronic clouds and a fixed charge model cannot describe these. It is well known that the polarizability has significant effects on vibrational frequencies, but its effects on piezoelectric and elastic properties are not well known.

Here we use the shell model originally used to model ionic crystals[16] to incorporate the atomic polarizability in the molecular-mechanics calculations.

Previously, polarizable points are introduced in the molecular-mechanics calculations to take into account the atomic polarizability. Applequist developed an atom dipole interaction model[17] to calculate the optical properties of the molecules and Boyd and Kesner introduced a polarization-mutual induction model[18] to represent inductive effects of the molecules.

In the shell model, atomic polarizabilities are represented by using two charged points (shell and core) for each atom, and these points are connected by the harmonic spring of a force constant k. Then the atomic polarizability ($Å^3$) is determined by

$$\alpha_{\text{atom}} = \text{Cunit}\frac{q_{\text{shell}}^2}{k}, \tag{1}$$

where q_{shell} is the shell charge (in e) and Cunit=332.0637, if a unit of energy is kcal/mol and that of a distance is Å. The net atomic charge is the sum of shell and core charges. Molecular polarizability is determined by including all dipole-dipole interactions of atomic polarizability centers and is given by

$$\alpha_{\text{molecule a,b}} = \text{Cunit} \sum_{i,j} q_i q_j D_{ia,jb}, \tag{2}$$

where $D_{ia,jb}$ is the inverse of the second-derivative matrix (Hessian), and a sum is over all charged centers (shells and cores) as follows:

$$D_{ia,jb} = \Phi^{-1}_{ia,jb}, \qquad \Phi_{ia,jb} = \frac{\partial^2 V}{\partial r_{ia} \partial r_{jb}}. \tag{3}$$

Here, V is the total potential energy of the system and r_{ia} is the a direction (a = x, y, or z) of a position vector of the center i. For the derivation of these equations, see Appendix I. This model gives the same molecular polarizability as the atom dipole interaction model by Applequist[17], if no net atomic charges exist. The shell model can be incorporated in molecular-mechanics calculation more naturally than models with polarizability centers, since shells are treated as extrarigid ions so that no special treatment for shells is necessary during energy-minimization procedures or calculations of mechanical properties. In vibrational-frequency calculations, we assign small masses (0.001u) to shells to obtain vibrational modes of cores as first 3N-6 (or 3N-3 for a crystal) modes where N is a number of atoms.

According to the usual convention, the charge-charge interactions between bonded atoms or atoms involved in angle-bending terms are excluded. In addition, the charge-dipole interactions of these terms are excluded, but all dipole-dipole interactions are included.

The atomic polarizabilities for hydrogen, carbon, and fluorine are determined by the Hartree-Fock calculations[12] of 2,2-difluoropropane by using the basis set based on DZ95**, but adding extra polarization functions (2d for carbon and fluorine and 1p for hydrogen). The exponents of extrapolarization functions are the same as those of p orbitals for carbon and fluorine and an s orbital for hydrogen. For fluoromethane, various basis sets are tested, and this basis set gives reasonably good polarizabilities. The results are shown in Table III. It is shown that the values of

polarizability depend strongly on the basis set but not strongly on the effects of the electron correlation.

In the case of 2,2-difluoropropane, we obtained $\alpha_{11} = 4.63\text{Å}^3$, $\alpha_{22} = 5.01\text{Å}^3$, $\alpha_{33} = 4.71\text{Å}^3$ from the Hartree-Fock calculations[12] with a DZ95** basis set ([4s2p1d/2s1p]), and $\alpha_{11} = 5.30\text{Å}^3$, $\alpha_{22} = 5.98\text{Å}^3$, $\alpha_{33} = 5.45\text{Å}^3$ with the extended basis set ([4s2p3d/2s2p]). Here all carbon atoms are in the yz plane and the z axis is the C_2 axis, and calculations are done at the experimental geometry[19]. We assign -1e as shell charges, since only atomic polarizabilities (the ratio of the atomic charge squared and the shell-core force constant) are important in determining the molecular polarizability. In the parameter fitting, shell charges are fixed, and only shell-core force constants are optimized. From this, we obtain atomic polarizabilities as $\alpha_C = 0.632\text{Å}^3$, $\alpha_F = 0.409\text{Å}^3$, $\alpha_H = 0.163\text{Å}^3$. The calculated molecular polarizability of 2,2-difluoropropane is $\alpha_{11} = 5.33\text{Å}^3$,$\alpha_{22} = 5.64\text{Å}^3$, $\alpha_{33} = 5.39\text{Å}^3$. Without a shell model, all polarizability components become about 10 % of these values.

C. Parameters with the Shell Model (set II)

Except for charges, the parameter optimization procedure is quite similar in this case. In set I, atomic charges are determined by using the Hartree-Fock calculation of $C_4H_5F_5$. In this procedure, atomic charges are fitted to reproduce the electrostatic potential around the molecule. In the shell model, net atomic charges displace shells and create an atomic dipole at each atomic position. Therefore, if the same net atomic charges as in the set I are used in the calculations, the electrostatic potential around the molecule will be quite different from those obtained by the Hartree-Fock calculations. To describe the electrostatic potential adequately, net atomic charges are determined iteratively to fit the electrostatic potential by the Hartree-Fock calculation. Initially, net atomic charges of set I are used, and

the shell positions are optimized with fixed core positions. Then the electrostatic potential arising from the induced dipoles is subtracted from the Hartree-Fock potential at all points used in the fitting. New atomic charges are obtained by fitting the electrostatic potential that is due to charges with the resultant Hartree-Fock potential, and these charges are used to obtain the new shell positions. This iteration is stopped when the change of charges becomes small. In the case of $C_4H_5F_5$, three iterations are sufficient to determine charges with accuracies better than 0.01e. In Figure 2, the net atomic charges of $C_4H_5F_5$ before and after the fitting are shown. On the basis of this, 0.16e and -0.32e are assigned for the net atomic charges of hydrogen and fluorine and -0.45e and 0.77e are assigned for the net atomic charges of carbon in CH_2 and CF_2 groups, respectively, in the calculations of PVDF for this parameter set.

The same van der Waals parameters as in set I are used in this set. Valence parameters (except for the C-C-C-C torsion parameters) are determined for the form I structure as in set I; in this case, experimental vibrational frequencies of form I crystal are fitted with the vibrational frequencies of the cores in the calculation. Torsion parameters are similarly determined by using the Hartree-Fock calculations of $C_4H_5F_5$, but in the calculations of the energy, shell positions are optimized at each conformation.

The final force-field parameters are shown in Table I. The vibrational frequencies for form I are shown in Table II. In this case, the RMS difference between calculated and experimental values is 5.0 cm^{-1}, which is about 10 % better than that of set I. The torsional potential curve of this set and the Hartree-Fock potential curve are shown in Figure 1.

III. Calculational Procedures

After obtaining the force-field parameters, atomic coordinates are

optimized[25] with the fixed experimental cell parameters for all forms I-IV. After the optimization, energy, elastic constants, dielectric constants and piezoelectric constants are calculated from the analytic second derivatives[9]. Also, the optimizations that allow cell deformations are performed. In all the calculations (including parameter fitting), nonbond interactions are calculated using the ABCA method[8], with an accuracy of 0.1kcal/mol for both Coulomb and van der Waals terms.

IV. Energy and Cell Parameters

The energy and optimized cell parameters for all four forms are shown in Tables IV and V. A single polymer chain in the forms II,III and IV has a net dipole in the chain direction as well as in the direction perpendicular to the chain. In these forms, dipoles along the chain direction are assumed to be orienting statistically[2,4,5] in the experiment. For the calculation, perfectly aligned chains allowed by the space group symmetry are used. For the forms II and IV, two chains are aligned in the opposite direction (up-down). For form III, two chains are aligned in the same direction (up-up). Calculations assuming different chain alignment in the unit cell are performed, and results are shown in Section VII.

It is noted that differences of total energy of these four forms are quite small (within 1 kcal/mol for a monomer unit) with or without shell parameters. In particular, electrostatic energy in forms II and IV are almost the same, although the alignment of chains is different. Optimized cell parameters are shown in Table V. The RMS difference between the calculations and the experiment is 0.14Å for cell lengths for set I and 0.17Å for set II. The cell angles are all 90 degrees except for β in forms II and III. The differences between the calculations and the experiment of this angle are about 2 degrees for form II and about 4 degrees for form III. One reason for differences is that the calculations correspond to the values at 0 K, but the experiment is performed usually at room temperature.

V. New Crystal Form

Lovinger suggested[3] that there are possibilities for the occurrence of the antipolar analogue of the form III crystal. We have examined this possibilities by optimizing the structure starting from form III, but one chain is rotated by 180 degrees so that these chains are aligned in the antipolar fashion. The energy of this form is comparable to other forms (see Table IV).

The elastic-stiffness tensor is calculated and found to be a stable form. These calculations support the possibility of the new form suggested by Lovinger. The optimized cell parameters and atomic coordinates of new forms using set II parameters are listed in Table VI. The cell is orthorhombic and the space group is $Pca2_1$ (C^5_{2v}). In Figure 3, the end view and the side view of the structure are shown.

VI. Elastic, Dielectric and Piezoelectric Properties

In Table VII, calculated elastic stiffness constants, Young's modulus in the chain direction and bulk modulus of five forms are shown. Young's modulus in the chain direction shows that the strength of the crystal is in the order I > IV > II > III > V.

The effects of including the shell parameters in the model are that the elastic constants are decreased by about 10%. These changes come mainly from the change of valence parameters, which are modified by the inclusion of the shells.

The experimental Young's modulus of form I crystal in the chain direction quoted in Ref. 6 is 177 GPa. This value is much smaller than the calculated value. We believe that the discrepancy is caused mainly by the difficulty in measuring the properties of a crystal by using the sample, which is a mixture of the crystal and amorphous regions. We are now investigating methods to calculate the properties of such a sample by actually including both crystal and amorphous regions in the calculational cell.

In Table VIII, dielectric constants at constant strain as well as constant stress are shown for all the forms with and without shell parameters. The difference between a dielectric constant at constant stress and that at constant strain is given by $4\pi dg^{\dagger}$, where d is the piezoelectric modulus and g is the piezoelectric constant[9]. For form I, the axes are transformed such that the orientation is the same one used in the experiments (1 axis is parallel to chain direction c, 2 axis is parallel to a, and 3 axis is parallel to b and the polarization direction). Here, the effect of the shell model is clear, as expected. The experiment of the crystal form is quite difficult since the dielectric constant of the amorphous region is quite large and also depends strongly on temperature and frequency. Measurements using the oriented films of form I crystal[20] gave $\epsilon_3 = 3.6$ (-106° C, 0.065MHz), 3.7 (-100° C,0.049MHz), and 3.1 (-102° C, 0.059MHz). The calculated values with the shell model are 1.95 at constant strain and 2.44 at constant stress. Constant stress value should be compared with experimental values, but it is still smaller than experimental values presumably because of the existence of amorphous regions in the sample used in the experiment.

In Table IX, piezoelectric moduli and piezoelectric constants calculated at experimental cell parameters for all forms are shown. In form I, the axes are transformed as in the dielectric constants for comparison with the experiment. In form IV, a and c axes are interchanged such that these values are compared directly with form I (1 axis is parallel to the chain direction c, 2 axis is parallel to a, and 3 axis is parallel to b and the polarization direction). In form II, calculated values of these constants are zero as expected by space group symmetry and are not shown in the table. The comparison of calculated values with and without the shell model shows that values generally increase by including the shells, but the effect is not as large as in the case of the dielectric constants.

The experimental value of d_{33} of form I crystal is quoted in Ref. 6 and

is -20pC/N, which is quite close to the calculated value with the shell model of -18.8pC/N. Also, the experimental value of d_{31} is reported to be much smaller than d_{33}, and it is consistent with the calculated values.

Although the new form has no net polarization in the direction perpendicular to the chain, piezoelectric constants are nonzero, and these are shown in Table IX (space-group symmetry allows this to be nonzero). The calculated values are similar to those of form III except that there is no large value for the shear piezoelectric modulus in this case.

VII. Calculations with Different Chain Alignment

For forms II, III, IV and V, dipoles along two chains in the unit cell can be aligned in the same direction (up-up) or in the opposite direction (up-down). Optimizations of structure with a different chain alignment for each form are performed by using the parameter set I; results are shown in Table X. After optimizations, elastic constants are calculated for each structure and it is found that the structure is mechanically stable.

For a form II crystal, the optimized cell of up-up structure is orthorhombic, and the energy is almost the same as the up-down structure. The difference between optimized cell parameters of up-down structure and up-up structure is small except for an angle β. This supports the interpretation of x-ray results, that in the form II crystal, up chains and down chains are packed statistically[2]. Also, it suggests that the form II crystal with up-up packing can be observable. In fact, Newman and Scheinbeim[26] suggested this structure from the sample obtained by poling the unoriented form II films. Since there is a net dipole moment in the chain direction in the up-up structure, piezoelectric constants are nonzero in this crystal. These constants are calculated at the experimental cell parameters by using the shell model. Calculated nonzero elements of piezoelectric modulus (in pC/N) are

d_{15}=1.15, d_{24}=3.85, d_{31}=3.28, d_{32}=-2.54, and d_{33}=0.71.

For a form III crystal, the energy of the up-down structure is 1.6 kcal/mol higher than that of the up-up structure, and the agreement between experimental and calculated cell parameters of the orthorhombic up-down structure is worse than that of the monoclinic up-up structure.

For a form IV crystal, the energy of the up-up structure is about the same as that of the up-down structure, but the optimized unit cell of the up-up structure is monoclinic and a cell angle β, which corresponds to a shift of one chain in the chain direction with respect to another, is 104 degrees. Considering the small energy difference between these two structures, it seems to be reasonable to assume the statistical packing of up and down chains in the unit cell in this form as suggested by Bachmann et al.[5]

For a form V crystal, the optimized up-down unit cell is monoclinic with $\beta = 120$ degrees, and the energy is about 0.7 kcal/mol higher than that of the up-up structure. Since the up-down crystal has inversion symmetry, all piezoelectric constants vanish for this structure.

VIII. Comparison with Other Calculations

Tashiro et al.[6] have calculated the elastic and the piezoelectric constants of a form I crystal by using the point-charge model. In their calculations, valence parameters and nonbonding parameters are used in the calculations, and these are determined to fit the experimental vibrational frequencies. The main differences between this study and theirs are the following: (1) In their calculations, long-range Coulomb interactions are ignored, but here, these are included by using the Ewald method; (2) in their calculations, atomic polarizabilities are not considered, but here, these are included by using the shell model, and (3) in our calculation, all crystal forms are considered (including a new form).

In Table XI, calculated values of the elastic constants and the piezoelectric

constants of a form I crystal are compared. The elastic-stiffness constants of both calculations are quite similar except that C_{11} is about 10% smaller in their calculation. For the piezoelectric modulus, discrepancy is more noticeable; especially the sign of d_{31} is different, and d_{24} of our calculated value is much greater than theirs (-4.28 pC/N). The recent measurement of the shear piezoelectric constants[21] gives d_{24} of -38.3 pC/N, which is much greater than our calculated value of -16.8 pC/N.

IX. Summary

Force-field parameters including shell parameters are developed for all forms of poly (vinylidene fluoride) polymer crystals. Structure, elastic, dielectric, and piezoelectric properties are calculated for all the crystal forms. Also, structure and energy of a new form (antipolar form III) are calculated, and the results show that it is mechanically stable with comparable energy with other forms.

Acknowledgments

We thank Jean-Marc Langlois and Dr. Murco N. Ringnalda for helping charge calculations. We also thank Dr. Siddharth Dasgupta for helpful discussions.

Appendix I. Derivation of Polarizabilities

Atomic polarizability is calculated by applying the constant external-electric field $\mathbf{E}$ to an atom. After a shell is displaced by the field, the force at the shell becomes 0 as follows:

$$\mathbf{F} = C_{\text{unit}} q_{\text{shell}} \mathbf{E} - k\delta\mathbf{r} = 0. \tag{4}$$

Since the dipole moment μ is given by

$$\mu = q_{\text{shell}} \delta\mathbf{r} = \alpha_{\text{atom}} \mathbf{E}, \tag{5}$$

where α_{atom} is the atomic polarizability, we have, by eliminating $\delta\mathbf{r}$,

$$\alpha_{atom} = C_{unit} \frac{q_{shell}^2}{k}. \tag{6}$$

For the molecule, we replace the force constant k by the Hessian at the equilibrium geometry. After applying the constant field $\mathbf{E}$ to the system of N particles, the force in a direction at charge center i given below (including both shells and cores) becomes 0,

$$F_{ia} = C_{unit} q_i E_a - (\Phi_{ia,11} \Phi_{ia,12} \ldots \Phi_{ia,N3})\, \delta\mathbf{r}. \tag{7}$$

Here,

$$\Phi_{ia,jb} = \frac{\partial^2 V}{\partial r_{ia} \partial r_{jb}} \tag{8}$$

is the element of the Hessian matrix (V is the total potential energy of the system), q_i is the charge of a center i, and $\delta\mathbf{r}$ is a displacement vector,

$$\delta\mathbf{r} = \begin{pmatrix} \delta\mathbf{r}_1 \\ \delta\mathbf{r}_2 \\ \vdots \\ \delta\mathbf{r}_N \end{pmatrix}. \tag{9}$$

The above equation leads to

$$\Phi \delta\mathbf{r} = C_{unit}\, q\mathbf{E}, \tag{10}$$

where $q\mathbf{E}$ is a $3N \times 1$ vector and is given by

$$q\mathbf{E} = \begin{pmatrix} q_1\mathbf{E} \\ q_2\mathbf{E} \\ \vdots \\ q_N\mathbf{E} \end{pmatrix}. \tag{11}$$

By solving (10), we have

$$\delta \mathbf{r_i} = C_{unit} \sum_{j}^{N} D_{i,j} q_j \mathbf{E}, \tag{12}$$

where $D = \Phi^{-1}$ (In the calculation of this inverse, we need to eliminate translational and rotational degrees of freedom.)

The induced dipole moment of the molecule is given by

$$\mu_{mol} = \sum_{i}^{N} q_i \delta \mathbf{r_i} = \alpha_{mol} \mathbf{E}. \tag{13}$$

By eliminating $\delta \mathbf{r_i}$ from the last equation, we have

$$\alpha_{mol} = C_{unit} \sum_{i,j}^{N} q_i q_j D_{i,j}. \tag{14}$$

References

(1) Hasegawa, R.; Takahashi, Y.; Chatani, Y.; Tadokoro, H. *Polymer J.* **1972,** *3,* 600.

(2) Takahashi, Y.; Matsubara, Y.; Tadokoro, H. *Macromolecules* **1983,** *16,* 1588.

(3) Lovinger, A. J. *Macromolecules* **1981,** *14,* 322.

(4) Takahashi, Y.; Tadokoro, H. *Macromolecules* **1980,** *13,* 1317.

(5) Bachmann, M.; Gordon, W. L.; Weinhold, S.; Lando, J. B. *J. Appl. Phys.* **1980,** *51,* 5095.

(6) (a) Tashiro, K.; Kobayashi, M.; Tadokoro, H.; Fukada, E. *Macromolecules* **1980,** *13,* 691. (b) Tashiro, K.; Tadokoro, H.; Kobayashi, M. *Ferroelectrics* **1981,** *32,* 167.

(7) Woods, R. J.; Khalil,M.; Pell, W.; Moffat, S. H.; Smith, Jr., V. H. *J. Comp. Chem.* **1990,** *11,* 297. Calculations are done by using the charge-fitting program written by Langlois, J. M. and Ringnalda, M., using the pseudospectral Hartree-Fock method.

(8) Karasawa, N.; Goddard III, W. A. *J. Phys. Chem.* **1989,** *93,* 7320.

(9) See Chapter II of this thesis.

(10) Karasawa, N.; Dasgupta, S.; Goddard III, W. A. *J. Phys. Chem.* **1991,** *95,* 2260.

(11) Kobayashi, M.; Tashiro, K.; Tadokoro, H. *Macromolecules* **1975,** *8,* 158.

(12) Calculations done by (a) Gaussian 88, Frisch, M. J. ; Head-Gordon, M.; Schlegel, H. B.; Raghavachari, K.; Binkley, J. S.; Gonzalez, C.; Defrees, D. J.; Fox, D. J.; Whiteside, R. A.; Seeger, R.; Melius, C. F.; Baker, J.; Martin, R. L.; Kahn, L. R.; Stewart, J. J. P.; Fluder, E. M.; Topiol, S.; Pople, J. A., Gaussian, Inc., Pittsburgh PA.,1988. and (b) Gaussian 90, Frisch, M. J.; Head-Gordon, M.; Trucks, G. W.; Foresman, J. B.; Schlegel, H. B.; Raghavachari, K.; Robb, M. A.; Binkley, J. S.; Gonzalez, C.; Defrees, D. J.;

Fox, D. J.; Whiteside, R. A.; Seeger, R.; Melius, C. F.; Baker, J.; Martin, R. L.; Kahn, L. R.; Stewart, J. J. P.; Topiol, S.; Pople, J. A., Gaussian, Inc., Pittsburgh PA, 1990.

(13) Goddard III, W. A.; Karasawa, N. "Elastic Constants and Phonon States for Graphite; van der Waals Parameters for Carbon," *J. Phys. Chem.*, submitted.

(14) Maekawa, T.; Goddard III, W. A. , unpublished

(15) Calculations are done by using the parameter-optimization program originally developed by Dasgupta, S. and Goddard III, W. A.

(16) Brüesch, P. *Phonons: Theory and Experiments I* (Springer-Verlag, Berlin, 1982).

(17) Applequist, J. *Acc. Chem. Res.* **1977,** *10,* 79.

(18) Boyd, R. H.; Kesner, L. *J. Chem. Phys.* **1980,** *72,* 2179.

(19) Durig, J. R.; Guirgis, G. A.; Li, Y. S. *J. Chem. Phys.* **1981,** *74,* 5946.

(20) Ohigashi, H. *J. Appl. Phys.* **1976,** *47,* 949.

(21) Nix, E. L.; Ward, I. M. *Ferroelectrics* **1986,** *67,* 137.

(22) Liu, S.; Dykstra, C. E. *J. Phys. Chem.* **1987,** *91,* 1749.

(23) Applequist, J.; Carl, J. R.; Fung, K. *J. Amer. Chem. Soc.* **1972,** *94,* 2952.

(24) Anderson, F. A.; Bak, B.; Brodersen, S. *J. Chem. Phys.* **1956,** *24,* 989.

(25) Calculations are done by POLYGRAF™, an interactive molecular simulation/three-dimensional graphics program from Biodesign Inc., Pasadena, California 91101.

(26) Newman, B. A.; Scheinbeim, J. I. *Macromolecules* **1983,** *16,* 60.

Table I. Force-field parameters used in the calculations for PVDF. Units are kcal/mol for energies, Å for length, and degrees for angles. van der Waals parameters and values in parentheses were not optimized.

		Set I(no shell)	Set II(with shell)
van der Waals[b]			
C	R_v	3.8837	3.8837
	ϵ_v	0.0844	0.0844
	γ_v	12.0	12.0
H	R_v	3.1975	3.1975
	ϵ_v	0.016	0.016
	γ_v	11.8	11.8
F	R_v	3.5380	3.5380
	ϵ_v	0.0211	0.0211
	γ_v	16.0	16.0
Bond Stretch[c]			
C-C	R_b	1.5242	1.5269
	k_b	682.1823	665.4933
	D_b	(101.2)	(101.2)
C-H	R_b	1.0789	1.0820
	k_b	729.3088	715.6092
	D_b	(106.7)	(106.7)
C-F	R_b	1.3457	1.3394
	k_b	832.0755	876.8641
	D_b	(108.0)	(108.0)
Shell C	k_b	-	525.8132
Shell H	k_b	-	2033.3751
Shell F	k_b	-	811.5098
Angle Bend[d]			
H-C-H	k_θ	52.7607	55.8315
	θ_a	116.4161	115.5015
C-C-H	k_θ	64.7621	62.7458
	θ_a	116.0913	116.5150
C_F-C-C_F[a]	k_θ	178.4806	137.3946
	θ_a	116.3318	119.6434
C-C_F-C[a]	k_θ	155.5421	138.6187
	θ_a	119.3277	119.7954
F-C-C	k_θ	139.2072	136.0475
	θ_a	114.8591	116.6151
F-C-F	k_θ	184.7170	178.9011
	θ_a	109.5665	111.3060
Torsion[e]			
C-C-C-H	V_3	4.4115	4.4057
C-C-C-C	V_1	−8.2966	21.7670
C-C-C-C	V_2	−7.8439	4.4309
C-C-C-C	V_3	13.7195	18.6795
C-C-C-C	V_4	−0.6973	1.2270
C-C-C-C	V_5	−2.2890	1.3265
C-C-C-C	V_6	−2.9580	−0.0531
F-C-C-H	V_3	1.0690	1.0936
F-C-C-C	V_3	−5.3835	−5.2046

Table I. (Continued.)

		Set I(no shell)	Set II(with shell)
Angle Cross Terms[f]			
H-C-H	$D_{H\theta}$	−20.5879	−17.2328
	k_{rr}	5.3363	2.3686
C-C-H	$D_{C\theta}$	−26.0949	−27.8737
	$D_{H\theta}$	−22.0763	−15.3201
	k_{rr}	0.9924	0.9978
C_F-C-C_F[a]	$D_{C\theta}$	−20.1366	−16.3585
	k_{rr}	18.6314	17.9468
C-C_F-C[a]	$D_{C\theta}$	−27.1200	−17.3844
	k_{rr}	12.0600	11.8674
F-C-C	$D_{F\theta}$	−62.9535	−69.8823
	$D_{C\theta}$	−48.9831	−42.5101
	k_{rr}	111.1305	109.2529
F-C-F	$D_{F\theta}$	−75.9852	−74.3431
	k_{rr}	145.3960	127.2188
One-Center Angle-Angle Cross Terms[g]			
$G_{CC:HC}$		2.4693	2.2899
$G_{CC:HH}$		−1.6436	−1.5733
$G_{CH:CC}$		20.7375	18.6381
$G_{CH:CH}$		0.8571	0.8027
$G_{CC:FC}$		2.4667	2.4677
$G_{CC:FF}$		27.3593	25.4020
$G_{CF:CC}$		2.5382	2.6365
$G_{CF:CF}$		−5.8372	−5.7643
Two-Center Angle-Angle Cross Terms[h]			
$F_{C:CC:H}$		28.5400	18.2612
$F_{C:CC:C}$		−10.6192	−9.6901
$F_{F:CC:H}$		0.2414	0.2430
$F_{F:CC:C}$		29.2978	25.0190

[a] C_F is used to specify the carbon in the CF_2 group to distinguish two kinds of C-C-C terms. [b] $E_{vdWIJ} = \frac{\epsilon_v}{\gamma_v - 6}(6e^{\gamma_v(1-R/R_v)} - \gamma_v(R_v/R)^6)$. [c] $E_{IJ} = D_b(e^{-\alpha_b(R-R_b)} - 1)^2, k_b = 2D_b\alpha_b^2$. [d] $E_a = (1/2)C(\cos\theta - \cos\theta_a)^2, k_\theta = C\sin^2\theta_a$. [e] $E_t = (1/2)\sum_n V_n(1 + \cos n\phi)$. [f] $E_{ax} = D_{1\theta}(\cos\theta - \cos\theta_a)(R_1 - R_{b1}) + D_{2\theta}(\cos\theta - \cos\theta_a)(R_2 - R_{b2}) + k_{rr}(R_1 - R_{b1})(R_2 - R_{b2}), k_{r\theta} = -D\sin\theta_a$. [g] $E_{1aa} = G_{IJ:KL}(\cos\theta_{IJK} - \cos\theta_{aIJK})(\cos\theta_{IJL} - \cos\theta_{aIJL})$. [h] $E_{2aa} = F_{I:JK:L}\cos\phi(\cos\theta_{IJK} - \cos\theta_{aIJK})(\cos\theta_{JKL} - \cos\theta_{aJKL})$.

Table II. Vibrational frequencies of Form I Crystal.

Mode	Symmetry	Calc. w.o. shell	Calc. with shell	Exp.[a]	
Lattice	B_1	40	41		
	B_2	35	28		
	A_1	35	36		
	B_2	87	87	70	Ir
	B_2	101	96	77	Raman
CF_2 twist	A_2	267	267	268	Raman
	A_2	267	268	268	Raman
CF_2 rock	B_2	436	440	445	Raman
	B_2	447	448	442	Ir
CF_2 wag	B_1	478	470	475	Raman
	B_1	480	472	468	Ir
CF_2 bend	A_1	511	508	508	Ir
	A_1	512	509	514	Raman
CH_2 rock	B_2	840	843	840	Ir
	B_2	839	842	845	Raman
CF_2 s-str	A_1	887	882	884	Ir
	A_1	888	883	886	Raman
CH_2 twist	A_2	980	980	980	Raman
	A_2	981	980	980	Raman
CC a-str	B_1	1073	1075	1071	Ir
	B_1	1073	1075	1078	Raman
CF_2 a-str	B_2	1165	1164	1176	Ir
	B_2	1190	1187	1175	Raman
CF_2 s-str	A_1	1276	1272	1273	Ir
	A_1	1279	1275	1283	Raman
CH_2 wag	B_1	1397	1399	1400	Raman
	B_1	1397	1399	1398	Ir
CH_2 bend	A_1	1429	1426	1428	Ir
	A_1	1431	1427	1436	Raman
CH_2 s-str	A_1	2982	2975	2980	Ir
	A_1	2985	2978	2984	Raman
CH_2 a-str	B_2	3016	3020	3022	Ir
	B_2	3023	3025	3020	Raman
RMS error[b]		5.4	5.0		

[a] Ref. 11, [b] without lattice modes.

Table III. Molecular polarizabilities (Å^3) of fluoromethane calculated by *ab initio* methods[a]. Experimental geometry[b] is used. N_b is the number of the basis function.

Basis set	N_b	method	$\alpha_1 = \alpha_2$	α_3
DZ95** [4s2p1d/2s1p]	47	HF	1.8612	1.8405
DZ95+3d,2p [4s2p3d/2s2p]	80	HF	2.3055	2.4151
ELP[c] [6s5p3d/4s2p]	108	HF	2.3378	2.4666
DZ95+3d,2p	80	MP2	2.4115	2.5606
Exp.[d]			2.34	3.18

[a] Ref. 12, [b] Ref. 24, [c] Ref. 22, [d] Ref. 23.

Table IV. Energies (in kcal/mol) per CH_2CF_2 for all forms of PVDF at experimental (exp) and optimized (opt) cell parameters. Energy components are also shown (Angle includes all cross terms. El is the electrostatic energy, Pol is the polarization energy, respectively).

(a) set I

Form	I		II		III		IV		V	
	exp	opt	exp	opt	exp	opt	exp	opt	exp	opt
Total	-123.93	-124.06	-123.17	-123.28	-123.71	-123.76	-123.23	-123.37	-	-123.60
Bond	0.18	0.18	0.19	0.18	0.17	0.18	0.19	0.18	-	0.19
Angle	7.62	6.65	8.15	7.27	7.81	6.89	8.15	7.29	-	6.89
Torsion	3.09	3.06	2.18	2.17	2.76	2.78	2.17	2.15	-	2.76
vdW	0.28	0.29	0.98	1.22	0.42	0.58	0.91	1.13	-	0.66
El	-135.10	-135.25	-134.67	-135.06	-134.87	-135.17	-134.66	-135.07	-	-135.07

(b) set II

Form	I		II		III		IV		V	
	exp	opt	exp	opt	exp	opt	exp	opt	exp	opt
Total	-131.87	-132.04	-131.15	-131.32	-131.48	-131.58	-131.15	-131.37	-	-131.40
Bond	0.37	0.36	0.35	0.39	0.35	0.38	0.36	0.39	-	0.38
Angle	10.67	10.73	11.14	11.24	10.79	10.85	11.15	11.31	-	10.86
Torsion	2.26	2.23	2.64	2.62	2.56	2.58	2.63	2.60	-	2.58
vdW	0.25	0.29	1.00	1.38	0.36	0.62	0.86	1.25	-	0.69
El	-146.83	-146.94	-150.63	-151.68	-147.84	-148.43	-150.48	-151.66	-	-148.25
Pol	1.41	1.30	4.36	4.73	2.31	2.42	4.32	4.76	-	2.35
El + Pol	-145.42	-145.64	-146.27	-146.95	-145.53	-146.01	-146.16	-146.90	-	-145.90

Table V. Optimized cell parameters (Å, degree) of all forms of PVDF crystals. In all forms, the c axis corresponds to the chain direction.

(a) set I

Form	I		II		III		IV		V	
	calc	exp	calc	exp	calc	exp	calc	exp	calc	exp
a	8.61	8.58	5.07	4.96	5.02	4.96	5.08	4.96	9.68	-
b	4.72	4.91	9.47	9.64	9.53	9.67	9.32	9.64	4.98	-
c	2.56	2.56	4.59	4.62	9.14	9.20	4.58	4.62	9.13	-
α	90.0	90.0	90.1	90.0	90.0	90.0	90.1	90.0	90.0	-
β	90.0	90.0	92.0	90.0	97.7	93.0	90.0	90.0	90.0	-
γ	90.0	90.0	90.0	90.0	90.0	90.0	90.0	90.0	90.0	-

(b) set II

Form	I		II		III		IV		V	
	calc	exp	calc	exp	calc	exp	calc	exp	calc	exp
a	8.55	8.58	5.05	4.96	4.98	4.96	5.05	4.96	9.65	-
b	4.71	4.91	9.37	9.64	9.45	9.67	9.23	9.64	4.93	-
c	2.56	2.56	4.58	4.62	9.13	9.20	4.58	4.62	9.12	-
α	90.0	90.0	90.1	90.0	90.0	90.0	89.8	90.0	90.0	-
β	90.0	90.0	92.2	90.0	96.8	93.0	89.9	90.0	90.0	-
γ	90.0	90.0	90.0	90.0	90.0	90.0	90.0	90.0	90.0	-

Table VI. Fractional coordinates of the antipolar form III obtained by optimization, using the parameter set I. The cell is orthorhombic with a= 9.68 Å, b= 4.98Å, and c=9.13 Å. The space group is $Pca2_1(C_{2v}^5)$.

Atom	X	Y	Z
C_1	0.248	0.730	0.917
C_2	0.370	0.818	0.825
C_3	0.368	0.718	0.667
C_4	0.242	0.802	0.579
F_1	0.491	0.732	0.886
F_2	0.382	0.090	0.827
F_3	0.128	0.681	0.637
F_4	0.218	0.069	0.596
H_1	0.155	0.824	0.877
H_2	0.236	0.515	0.908
H_3	0.461	0.796	0.616
H_4	0.375	0.502	0.666

Table VII

(a). Elastic stiffness constants(GPa) of PVDF calculated at experimental structures (except for form V, where the optimized structure is used).

Form I

set I						set II					
25.5	3.0	4.0	0.0	0.0	0.0	23.7	2.4	4.7	0.0	0.0	0.0
3.0	12.4	2.4	0.0	0.0	0.0	2.4	11.8	3.1	0.0	0.0	0.0
4.0	2.4	283.4	0.0	0.0	0.0	4.7	3.1	266.8	0.0	0.0	0.0
0.0	0.0	0.0	3.5	0.0	0.0	0.0	0.0	0.0	3.7	0.0	0.0
0.0	0.0	0.0	0.0	5.1	0.0	0.0	0.0	0.0	0.0	5.2	0.0
0.0	0.0	0.0	0.0	0.0	4.0	0.0	0.0	0.0	0.0	0.0	4.0

Form II

23.5	7.1	-5.5	0.0	-3.1	0.0	22.4	6.3	-7.4	0.0	-3.1	0.0
7.1	13.8	9.1	0.0	0.5	0.0	6.3	13.1	7.9	0.0	0.0	0.0
-5.5	9.1	162.8	0.0	0.4	0.0	-7.4	7.9	148.4	0.0	0.3	0.0
0.0	0.0	0.0	2.6	0.0	0.5	0.0	0.0	0.0	3.8	0.0	0.2
-3.1	0.5	0.4	0.0	6.8	0.0	-3.1	0.0	0.3	0.0	7.6	0.0
0.0	0.0	0.0	0.5	0.0	6.1	0.0	0.0	0.0	0.2	0.0	5.3

Form III

19.9	7.3	-1.8	0.0	-0.8	0.0	19.2	6.3	-2.7	0.0	-0.6	0.0
7.3	15.0	10.6	0.0	-0.4	0.0	6.3	14.4	9.8	0.0	-0.6	0.0
-1.8	10.6	118.5	0.0	-0.9	0.0	-2.7	9.8	106.9	0.0	-1.0	0.0
0.0	0.0	0.0	2.7	0.0	-0.4	0.0	0.0	0.0	2.7	0.0	-0.4
-0.8	-0.4	-0.9	0.0	2.5	0.0	-0.6	-0.6	-1.0	0.0	2.8	0.0
0.0	0.0	0.0	-0.4	0.0	8.2	0.0	0.0	0.0	-0.4	0.0	7.7

Form IV

24.2	5.8	-4.7	0.0	0.0	0.0	22.7	4.6	-7.2	0.0	0.0	0.0
5.8	11.2	6.3	0.0	0.0	0.0	4.6	10.2	5.5	0.0	0.0	0.0
-4.7	6.3	162.6	0.0	0.0	0.0	-7.2	5.5	146.8	0.0	0.0	0.0
0.0	0.0	0.0	2.8	0.0	0.0	0.0	0.0	0.0	3.9	0.0	0.0
0.0	0.0	0.0	0.0	6.8	0.0	0.0	0.0	0.0	0.0	7.6	0.0
0.0	0.0	0.0	0.0	0.0	6.3	0.0	0.0	0.0	0.0	0.0	5.1

Form V

20.2	7.4	14.6	0.0	0.0	0.0	22.3	8.1	15.9	0.0	0.0	0.0
7.4	17.5	-1.8	0.0	0.0	0.0	8.1	19.0	-2.6	0.0	0.0	0.0
14.6	-1.8	115.9	0.0	0.0	0.0	15.9	-2.6	108.1	0.0	0.0	0.0
0.0	0.0	0.0	3.4	0.0	0.0	0.0	0.0	0.0	4.1	0.0	0.0
0.0	0.0	0.0	0.0	2.3	0.0	0.0	0.0	0.0	0.0	2.6	0.0
0.0	0.0	0.0	0.0	0.0	7.2	0.0	0.0	0.0	0.0	0.0	7.5

Table VII (b). Young's modulus in the chain direction (E) and bulk modulus (B) for all forms of PVDF in GPa. Calculations are done at experimental cell parameters (exp) and at optimized cell parameters (opt).

(i) Set I

Form	I		II		III		IV		V	
	exp	opt	exp	opt	exp	opt	exp	opt	exp	opt
E	282.5	292.7	151.2	152.9	107.7	113.4	156.0	162.8	-	101.7
B	9.5	14.8	11.7	12.4	11.7	13.3	9.8	12.1	-	12.5

(ii) Set II

Form	I		II		III		IV		V	
	exp	opt	exp	opt	exp	opt	exp	opt	exp	opt
E	265.2	277.2	136.8	140.9	97.2	107.2	139.3	150.2	-	92.3
B	8.8	15.2	10.5	13.6	10.8	14.7	8.6	13.6	-	13.5

Table VIII

(a). Dielectric Constants of PVDF at constant strain calculated at experimental structure (except for form V, where the optimized structure is used).

Set I			Set II		
Form I					
1.1210	0.0000	0.0000	2.1475	0.0000	0.0000
0.0000	1.4480	0.0000	0.0000	2.7324	0.0000
0.0000	0.0000	1.0687	0.0000	0.0000	1.9549
Form II					
1.2242	0.0000	-0.0706	2.2338	0.0000	-0.1434
0.0000	1.1943	0.0000	0.0000	2.1385	0.0000
-0.0706	0.0000	1.1377	-0.1434	0.0000	2.1603
Form III					
1.2521	0.0000	-0.0692	2.2892	0.0000	-0.1364
0.0000	1.1481	0.0000	0.0000	2.0994	0.0000
-0.0692	0.0000	1.1455	-0.1364	0.0000	2.1653
Form IV					
1.2159	0.0000	0.0000	2.2422	0.0000	0.0000
0.0000	1.1733	0.0000	0.0000	2.1282	0.0000
0.0000	0.0000	1.1372	0.0000	0.0000	2.1518
Form V					
1.1802	0.0000	0.0000	2.1302	0.0000	0.0000
0.0000	1.2918	0.0000	0.0000	2.2968	0.0000
0.0000	0.0000	1.1466	0.0000	0.0000	2.1833

(b). Dielectric Constants of PVDF at constant stress calculated at experimental structure (except for form V, where the optimized structure is used).

	Set I			Set II	
Form I					
1.8012	0.0000	0.0000	2.8716	0.0000	0.0000
0.0000	1.4638	0.0000	0.0000	2.8599	0.0000
0.0000	0.0000	1.2848	0.0000	0.0000	2.4405
Form II					
1.2242	0.0000	-0.0706	2.2338	0.0000	-0.1434
0.0000	1.1943	0.0000	0.0000	2.1385	0.0000
-0.0706	0.0000	1.1377	-0.1434	0.0000	2.1603
Form III					
1.3343	0.0000	-0.1284	2.4571	0.0000	-0.1860
0.0000	1.1839	0.0000	0.0000	2.1608	0.0000
-0.1284	0.0000	1.4326	-0.1860	0.0000	2.4544
Form IV					
1.2597	0.0000	0.0000	2.3340	0.0000	0.0000
0.0000	1.2105	0.0000	0.0000	2.1501	0.0000
0.0000	0.0000	1.2127	0.0000	0.0000	2.2228
Form V					
1.1802	0.0000	0.0000	2.1545	0.0000	0.0000
0.0000	1.2948	0.0000	0.0000	2.3010	0.0000
0.0000	0.0000	1.2115	0.0000	0.0000	2.2507

Table IX

(a). Piezoelectric moduli (pC/N) calculated at experimental structures (except for form V, where the optimized structure is used).

	Set I						Set II					
Form I												
0.0	0.0	0.0	0.0	-41.3	0.0		0.0	0.0	0.0	0.0	-41.9	0.0
0.0	0.0	0.0	-5.9	0.0	0.0		0.0	0.0	0.0	-16.8	0.0	0.0
0.07	1.1	-12.7	0.0	0.0	0.0		0.57	-1.3	-18.8	0.0	0.0	0.0
Form III												
0.80	4.9	-2.0	0.0	-1.3	0.0		4.4	4.2	-2.7	0.0	-1.2	0.0
0.0	0.0	0.0	3.7	0.0	6.1		0.0	0.0	0.0	12.0	0.0	5.1
3.5	-3.5	2.1	0.0	29.1	0.0		3.3	-1.6	2.2	0.0	27.6	0.0
Form IV												
0.0	0.0	0.0	0.0	-9.9	0.0		0.0	0.0	0.0	0.0	-9.1	0.0
0.0	0.0	0.0	-7.3	0.0	0.0		0.0	0.0	0.0	-6.1	0.0	0.0
1.4	-3.5	0.15	0.0	0.0	0.0		1.8	-2.4	-2.9	0.0	0.0	0.0
Form V												
0.0	0.0	0.0	0.0	-0.08	0.0		0.0	0.0	0.0	0.0	9.1	0.0
0.0	0.0	0.0	2.8	0.0	0.0		0.0	0.0	0.0	3.0	0.0	0.0
-4.0	3.3	2.1	0.0	0.0	0.0		-3.5	4.0	2.2	0.0	0.0	0.0

(b). Piezoelectric constants (C/m**2) calculated at experimental structures (except for form V, where the optimized structure is used).

	Set I						Set II					
Form I												
0.0	0.0	0.0	0.0	-0.15	0.0		0.0	0.0	0.0	0.0	-0.15	0.0
0.0	0.0	0.0	-0.024	0.0	0.0		0.0	0.0	0.0	-0.067	0.0	0.0
-0.007	-0.01	-0.15	0.0	0.0	0.0		0.087	-0.073	-0.22	0.0	0.0	0.0
Form III												
0.057	0.059	-0.19	0.0	-0.004	0.0		0.12	0.062	-0.26	0.0	-0.006	0.0
0.0	0.0	0.0	0.007	0.0	0.048		0.0	0.0	0.0	0.031	0.0	0.034
0.017	-0.017	0.18	0.0	0.071	0.0		0.032	0.0036	0.19	0.0	0.074	0.0
Form IV												
0.0	0.0	0.0	0.0	0.067	0.0		0.0	0.0	0.0	0.0	0.069	0.0
0.0	0.0	0.0	0.045	0.0	0.0		0.0	0.0	0.0	0.032	0.0	0.0
-0.21	0.030	0.023	0.0	0.0	0.0		-0.27	0.028	0.089	0.0	0.0	0.0
Form V												
0.0	0.0	0.0	0.0	-0.0002	0.0		0.0	0.0	0.0	0.0	0.024	0.0
0.0	0.0	0.0	0.0096	0.0	0.0		0.0	0.0	0.0	0.012	0.0	0.0
-0.026	0.024	0.18	0.0	0.0	0.0		-0.011	0.042	0.18	0.0	0.0	0.0

Table X. Optimized energy (kcal/mol per CH_2CF_2) and cell parameters (Å, degree) of various forms of PVDF with parallel (up-up) and antiparallel (up-down) alignment of chains in the unit cell by using the parameter set I. In all forms, the c axis corresponds to the chain direction. Experimental cell parameters are shown in parentheses where available.

Form	II		III		IV		V	
	up-down	up-up	up-up	up-down	up-down	up-up	up-up	up-down
Space group	$P2_1/c$	$Pca2_1$	Cc	$Pna2_1$	$P2_1cn$	Cc	$Pca2_1$	$P2_1/c$
Energy	-123.28	-123.21	-123.76	-122.16	-123.37	-123.38	-123.60	-122.86
a	5.07 (4.96)	5.09	5.02 (4.96)	5.24	5.08 (4.96)	5.20	9.68	6.04
b	9.47 (9.64)	9.50	9.53 (9.67)	9.27	9.32 (9.64)	9.36	4.98	9.01
c	4.59 (4.62)	4.59	9.14 (9.20)	9.28	4.58 (4.62)	4.58	9.13	9.26
α	90.1 (90.0)	90.0	90.0 (90.0)	90.0	90.1 (90.0)	90.0	90.0	90.0
β	92.0 (90.0)	90.0	97.7 (93.0)	90.0	90.0 (90.0)	104.0	90.0	120.0
γ	90.0 (90.0)	90.0	90.0 (90.0)	90.0	90.0 (90.0)	90.0	90.0	90.0

Table XI. Comparison of elastic constants(C, in GPa) and piezoelectric modulus(d, in pC/N) of PVDF form I between the present calculations with set II and those by Tashiro et al.[a].

	calc.	Tashiro et al.[a]
C_{11}	23.7	23.60
C_{22}	11.8	10.64
C_{33}	266.8	238.24
C_{12}	2.4	1.92
C_{13}	4.7	3.98
C_{23}	3.1	2.19
C_{44}	3.7	4.40
C_{55}	5.2	6.43
C_{66}	4.0	2.15
d_{15}	-41.9	-30.70
d_{24}	-16.8	-4.28
d_{31}	0.57	-0.25
d_{32}	-1.3	-4.05
d_{33}	-18.8	-25.19

[a] Ref. 6.

Figure 1. Torsional potential curves of CH_3CF_2-CH_2CF_3 obtained by the Hartree-Fock calculations with the 631G** basis set and the molecular mechanics calculations (set I and set II). 0 degree corresponds to cis conformation.

Figure 2. Net atomic charges (in a unit of electron charge) obtained by fitting the electrostatic potential from the Hartree-Fock calculations of $C_4H_5F_5$ with and without shell parameters.

Figure 3. The end view (a) and the side view (b) of antipolar form III crystal of PVDF.

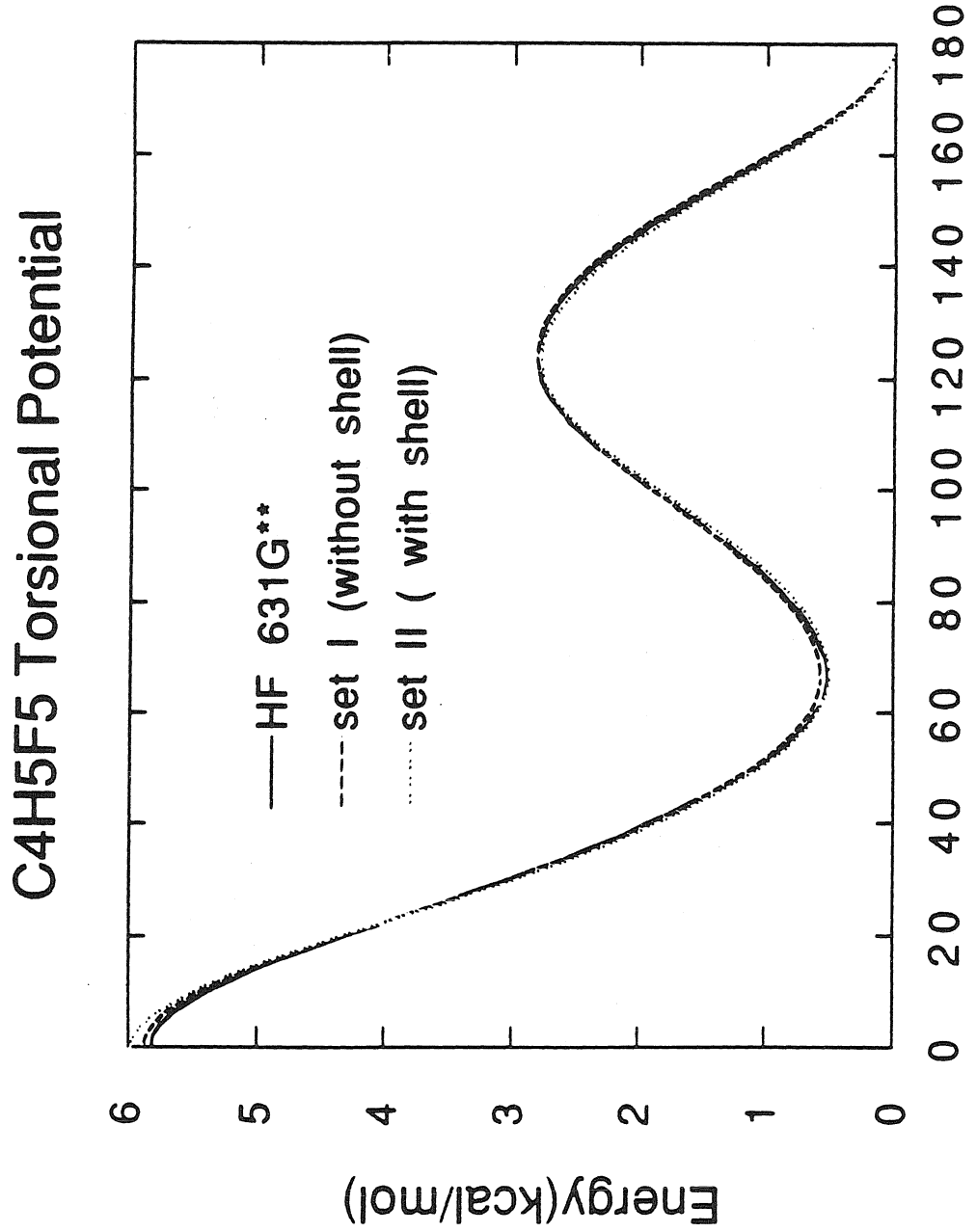
C4H5F5 Torsional Potential
HF 631G**
set I (without shell)
set II (with shell)
Energy(kcal/mol)
0
1
2
3
4
5
6
0 20 40 60 80 100 120 140 160 180
Torsional angle(degree)

Figure 1.

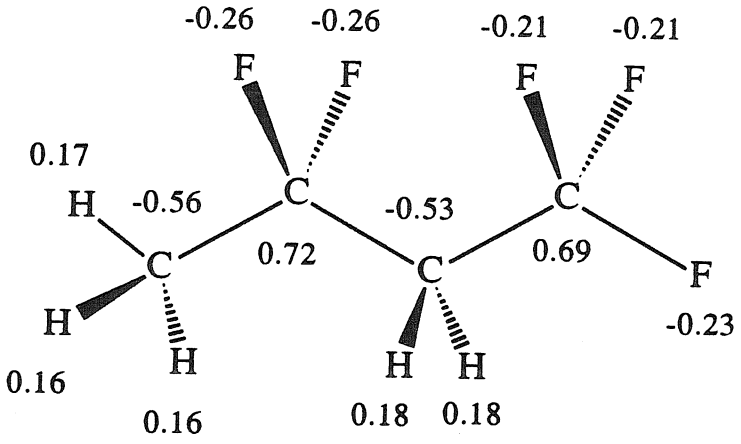

(a) Set I (without shell)

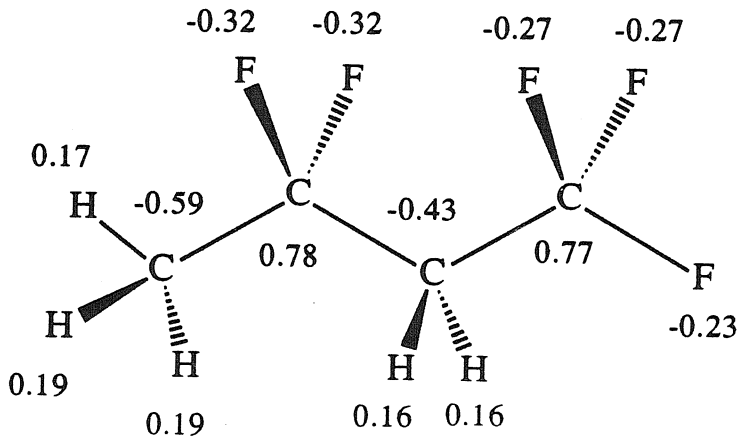

(b) Set II (with shell)

Figure 2.

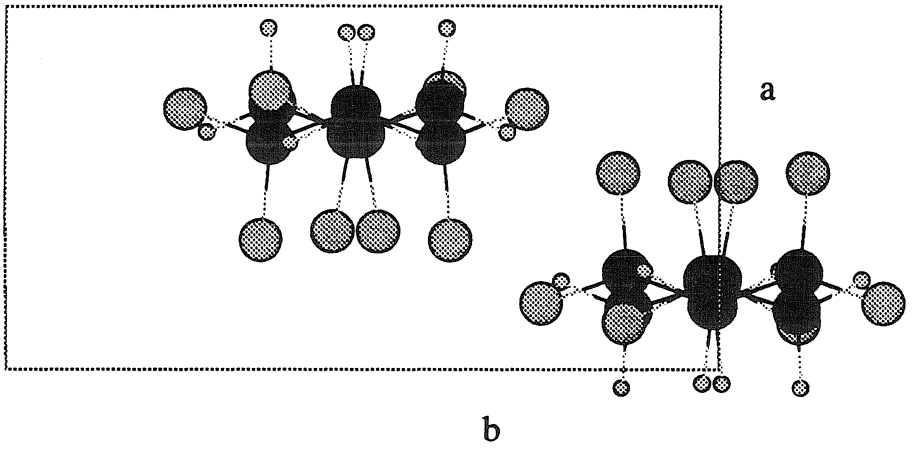

(a) Top view

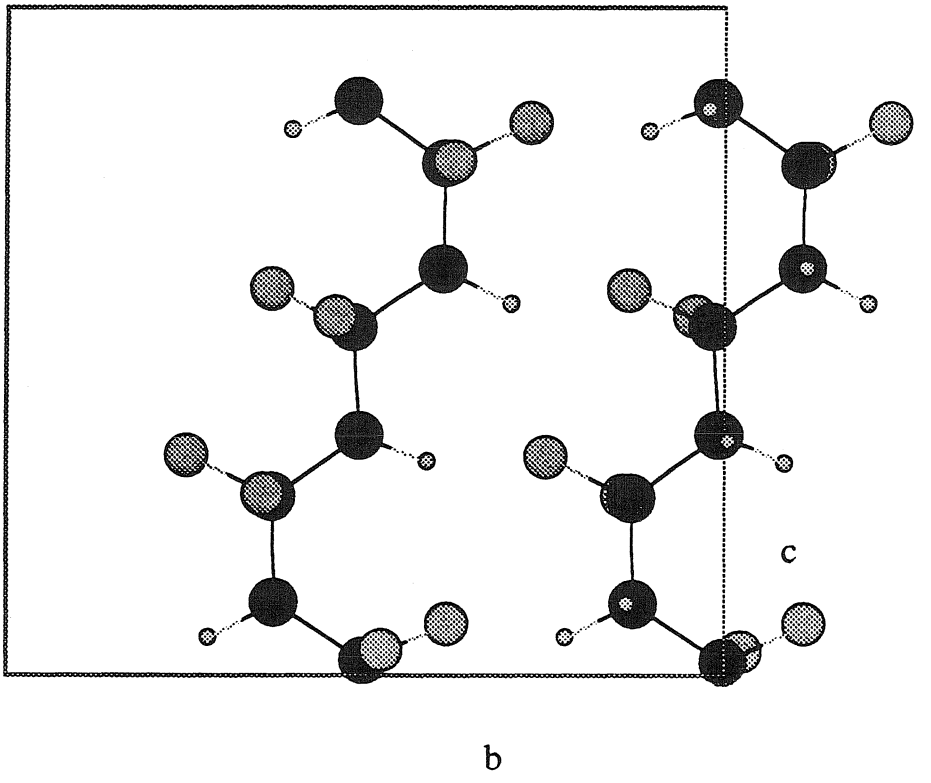

(b) Side view

Figure 3.

Appendix I

Elastic Constants and Phonon States for Graphite; van der Waals Parameters for Carbon

[This appendix is based on a paper co-authored with William A. Goddard III, and was submitted to *J. Phys. Chem.*]

Abstract

Using available experimental data for the properties of graphite at 0 K, we derive a force field (including the van der Waals parameters) useful for predicting the mechanical properties of graphite (elastic constants, Poisson ratios, lattice modes). This is used to predict the phonon dispersion curves, specific heat, and other properties of graphite.

I. Introduction

As a first step in atomic-level simulations for the surface and bulk properties of graphite and of interfaces between graphite and polymers, we report here a force field for describing interatomic interactions in graphite and use it to examine the elastic properties and related properties.

All calculations are for the low-temperature structure, and in Section II we outline the selection of experimental values and corrections to 0 K. Section III describes the process used in obtaining the force field for graphite. In Section IV we discuss the predictions of the less well-characterized properties (e.g., C_{44}, C_{13}). In Section V we report a more detailed analysis of properties for graphite on the basis of the predicted force field. This includes phonon dispersion curves and prediction of thermodynamic properties. In Section VI we consider the discrepancy between experimental values of C_{44} (which differ by a factor of 15) and we compare it [i.e., the discrepancy] with theory.

II. Experimental Data for Graphite

A. Crystal Structure

The space group of graphite was taken as $P6_3/mmc$ (D_{6h}^{14}), which assumes flat layers.[1] The lattice parameters at 25°C are[1] $a = 2.4612$ Å, $c = 6.7090$ Å. To convert the lattice parameters at low temperature, we used the thermal expansion data from Bailey and Yates[2] (20-270 K), extrapolated and interpolated to obtain

$$\delta a = -0.0072 \text{ Å}$$

$$\delta c = +0.0369 \text{ Å}$$

for 0 K to 298 K. This leads to

$$a(0 \text{ K}) = 2.4684 \text{ Å}$$

$$c(0\ \mathrm{K}) = 6.6721\ \text{Å}.$$

B. Elastic Constants

A complete study of the elastic constants of compression-annealed pyrolytic graphite (at room temperature) was carried out by Blakslee et al.[3], who find elastic constants (stiffness), Young's moduli, and Poisson ratios as listed in Table I. The elastic constants C_{11} and C_{12} relate to in-plane deformations, C_{33} is a direct measure of the force constant for the C··C van der Waals interactions, and C_{44} relates to shear of one plane with respect to the next. The quantities C_{11}, C_{12}, C_{33}, and C_{44} are derived from direct experiments; however, C_{13} (which involves coupling of stress in the plane to the spacing between the planes) is indirect and rather uncertain (33% quoted uncertainty).

The biggest variations in the literature on graphite occur for C_{44}, where values from 0.18 to 0.35 GPa[4] are obtained[3] from mechanical studies on compression-annealed samples (the values were independent of external compression), while neutron scattering studies[5,6] lead to values of [5] $C_{44} = 4.2 \pm 0.2$ and[6] 4.6 ± 0.2, or 15 times larger! The neutron-irradiated samples are referred to as "dislocation-free graphite," since it is believed that neutron damage (or impregnation with boron) impedes dislocation motion.[5,7,8] Our calculations agree with the low values from the mechanical studies and suggest that the neutron damage leads to larger shear values than the intrinsic material (see discussion in Sections IV.B and VI).

The temperature dependence of the elastic constants was measured by Ganster and Fritz[9] on compression-annealed graphite from 4 to 300 K, yielding changes as listed in Table I. The values for δC_{11}, δC_{12}, δC_{33}, and δC_{44} are obtained from independent experiments; however, δC_{13} is obtained from a complex mode after subtracting the contributions from the other quantities (see Section IV.C). As a result, δC_{13} has an uncertainty comparable to its magnitude. Combining the

above results leads to the total values in Table I.

C. Lattice Vibrations

With four atoms per unit cell, graphite has 12 vibrational bands. For the Γ point of the Brillouin zone (k = 0), this leads to the following 12 modes[10]:

E_{1u}, A_{2u}: transverse (TA) and longitudinal (LA) acoustic (at 0 cm^{-1})

E_{2g}, B_{2g}: transverse (TO) and longitudinal (LO) modes for sheet-sheet interactions (at ~10 cm^{-1} and ~ 140 cm^{-1})

A_{2u}, B_{2g}: out-of-plane crinkling of graphite (at ~868 cm^{-1})

E_{1u}, E_{2g}: in-plane ring modes (at ~1588 cm^{-1}).

The 868 cm^{-1} mode (A_{2u}) was used to determine the torsional parameters for our force field. The 1588 cm^{-1} mode (E_{1u}) was used to help determine the in-plane force constants.

The sheet-sheet modes (E_{2g}, B_{2g} or TO, LO) have been obtained from neutron-scattering studies on "dislocation-free" graphite at room temperature, yielding[5] 45 cm^{-1} and 126 cm^{-1} for the TO (E_{2g}) and LO (B_{2g}) transition at the Γ point. These neutron-scattering studies lead to elastic constants of $C_{33} = 37.1 \pm 0.5$ GPa, $C_{44} = 4.6 \pm 0.2$ GPa, and $C_{11} = 1440 \pm 200$ GPa. The value for C_{33} is consistent with the mechanical studies (36.5), but the other values are significantly higher than mechanical results ($C_{44} = 0.27$ and $C_{11} = 1060$). We believe that this may be due to the neutron damage, and we have not used the neutron-scattering values for the TO and LO modes in our fits.

III. Calculations

A. The Force Field

van der Waals Terms. The van der Waals interactions were described

with an exponential-six potential,

$$E = Ae^{-CR} - B/R^6 = \frac{D_v}{(\zeta - 6)} \left\{ 6e^{\zeta(1-\rho)} - \zeta\rho^{-6} \right\}, \tag{1}$$

where D_v is the well depth,

$$\rho = \frac{R}{R_v} \tag{2}$$

is the scaled distance, R_v is the well radius (distance between the carbons at the well minimum), and ζ is a dimensionless parameter. Equation (1) leads to a force constant at the minimum of the form

$$k_v = \left(\frac{\partial^2 E}{\partial R^2} \right)_{R_v} = \frac{6\zeta(\zeta - 7)D_v}{(\zeta - 6)R_v^2}, \tag{3}$$

so that ζ is directly related to the dimensionless force constant,

$$\bar{\kappa} = k_v R_v^2 / D_v = \frac{6\zeta(\zeta - 7)}{\zeta - 6}. \tag{4}$$

We also considered the Lennard-Jones potential

$$E = D_v \left[\rho^{-12} - 2\rho^{-6} \right] \tag{5}$$

for describing the van der Waals interactions, where ρ is given by (2). This leads to $\bar{\kappa} = 72$.

All calculations used the Accuracy-Bounded Convergence Acceleration (ABCA) method,[11] with an accuracy parameter of 0.001 kcal/mol. For $\zeta = 12$, this leads to an Ewald parameter of $\eta = 1.59$ Å and to cutoffs of $R_{cut} = 5.2$ Å and $H_{cut} = 5.2$ Å^{-1}.

Valence Terms. The valence interactions were described using:

(i) A Morse bond stretch

$$E_b = D_b \left[e^{-\alpha_b(R - R_b)} - 1 \right]^2 \tag{6}$$

for the C-C interaction, where R_b and D_b are the position and depth of the well and $k_b = 2D_b\alpha_b^2$ is the force constant.

(ii) A cosine angle bend with angle-stretch ($k_{r\theta}$) and stretch-stretch (k_{rr}) coupling

$$E_a = \tfrac{1}{2}\ C[\cos\theta - \cos\theta_a]^2 + k_{rr}(R_1 - R_b)(R_2 - R_b)$$

$$+D(\cos\theta - \cos\theta_a)[(R_1 - R_b) + (R_2 - R_b)] \qquad (7)$$

for the C-C-C interaction, where θ_a is the equilibrium angle, $k_{\theta\theta} = C\sin^2\theta_a$ is the diagonal angle-force constant, and $k_{r\theta} = -D\sin\theta_a$ is the angle-stretch force constant.

(iii) A two-fold torsion

$$E_t = \tfrac{1}{2}V_t(1 - \cos 2\phi), \qquad (8)$$

where ϕ is the torsional angle, V_t is the barrier, and the minimum is for ϕ = 0 or 180 degrees (planar).

B. Fitting Parameters

The sequence in fitting parameters was

(a) choose R_v so that there is zero stress along the z axis for the experimental *c* lattice parameter;

(b) choose D_v so that the C_{33} elastic constant is matched to experiment;

(c) adjust V_t to describe the 868 cm^{-1} lattice mode;

(d) adjust R_b, k_b, $k_{\theta\theta}$, $k_{r\theta}$, and k_{rr} to obtain zero stress in the plane for the experimental *a* lattice parameter, while obtaining the experimental C_{11} and C_{12} elastic constants, and the 1588 cm^{-1} lattice mode.

(e) The C_{13} elastic constant and the sheet-sheet lattice modes ($\sim$10 cm^{-1} and $\sim$140 cm^{-1}) are insensitive to all of these parameters and were not used in any fits.

(f) The scale parameter ζ for the van der Waals interaction was considered as an independent variable. The total interaction energy between the planes (E_{coh}) is a sensitive function of ζ and the quantities in (e) all change smoothly with ζ.

In these fits we required that the lattice constants be accurate to 0.0001 Å, that the elastic constants be within 0.04 GPa for C_{33}, within 1 GPa for C_{11}, and within 6 GPa for C_{12}, and that the lattice modes be within 1.5 cm^{-1} for the 868 cm^{-1} mode and 2 cm^{-1} for the 1588 cm^{-1} mode. These uncertainties are well within experimental error bounds. The number of parameters in the force field exceeds the experimental data, and further optimization could have reproduced the experimental quantities exactly. Because of this redundancy, we did not optimize θ_a, D_b, or k_{rr}.

The final parameters are listed in Table II, and the calculated properties are in Table III.

C. Comparison with Other van der Waals Parameters

It is possible that the optimum van der Waals parameters for an atom would depend upon its hydridization; however, current experimental data have not been sufficient for such subtleties. As a result, most force fields have one set of parameters for C. In Table IV we include the predicted properties for graphite from other sets of van der Waals parameters[12–17] (none of which was derived for graphite). The van der Waals interactions within a sheet lead to a tension that is balanced by the bond-stretch force. Consequently, for each case we used the valence parameters for the Lennard-Jones force field in Table II and readjusted the bond radius R_b to obtain zero stress for the experimental a lattice parameter. Then we optimized the unit cell (and internal atoms) and calculated the properties.

The most important quantity to compare is the c lattice constant. The errors

are: MM2 (−0.08 Å), Dreiding (+0.11 Å), Williams (+0.13 Å), CHARMM/EF3 (−0.15 Å), AMBER (−0.15 Å), CHARMM/EF2 (−0.36 Å), and Jorgensen (+0.70 Å). The errors for the first five are not large and could be considered adequate. The Jorgensen potential[16] leads to large errors, partially because it was optimized for the case where an implicit hydrogen was used (we used the Jorgensen value for the sp^2 carbon of phenylalanine bonded to three carbons, but the parameters are the same as for the carbons having hydrogen).

The next most relevant comparison is the C_{33} elastic constant, where the errors (out of 40.7) are: CHARMM/EF3 (+15%), Williams (+38%), MM2 (−41%), Dreiding (+48%), AMBER (+53%), Jorgensen (+83%), and CHARMM/EF2 (+168%). The first case is reasonably good, and the next four are marginally acceptable.

More relevant to test the parameters would be the cohesive energy, but it is not well known. Assuming that the value of $E_{coh} \approx 1.3$ kcal/mol (see Section IV.A), the errors are: MM2 (−21%), Williams (+27%), Dreiding (+27%), CHARMM/EF3 (+33%), AMBER (+77%), Jorgensen (+80%), and CHARMM/EF2 (+156%).

Combining all three criteria, the most accurate, previous van der Waals parameters for carbon are CHARMM/EF3, Dreiding, Williams, and MM2. We consider none of these to be adequate for accurate calculations on graphite and find that the new van der Waals parameters in Table II are useful in examining polymers[21] or proteins [of course, because of the coupling of experimentally derived van der Waals parameters, the van der Waals parameters for other atoms (H, N, O, etc.) have to be rederived].

IV. Comparison with Experiment

A. Cohesive Energy

The cohesive energy is a dramatic function of ζ, changing from 1.2 to 2.0

kcal/mol as ζ goes from 15 to 11. Unfortunately there are no reliable experimental data on this quantity for graphite. However, there are recent experimental heats of sublimation [23] for polycrystalline mixtures of C_{60} and C_{70}. We used LJ parameters and calculated heats of sublimations of these crystals and found excellent agreements between calculated and experimental values[24] (ΔH_{707K} = 40.9 kcal/mol for C_{60} and ΔH_{739K} = 46.4 kcal/mol for C_{70} from calculations versus $\Delta H_{707K} = 40.1 \pm 1.3$ kcal/mol for C_{60} and $\Delta H_{739K} = 43.0 \pm 2.2$ kcal/mol for C_{70} from experiments). This suggests that the cohesive energy calculated by LJ parameters (1.3 kcal/mol) is a good estimate for a graphite crystal. In comparison, the experimental cohesive energy (at 0 K) of polyethylene[18] is 1.838 $\pm$ 0.032 kcal/mol (per carbon), and the experimental heat of sublimation (per carbon) for benzene is 2.1 kcal/mol[13] and for n-hexane is 2.1 kcal/mol.[13] Correcting these values for zero-point energy leads to 2.01, 2.3, and 2.3 kcal/mol, respectively. In Table II, we show exponential-six parameters, which yield the same cohesive energy as LJ parameters (ζ = 14.255). In Table III, various properties calculated using these parameter sets are shown.

Given the cohesive energy of 1.3 kcal/mol C, the smallest energy to create a new surface would be $0.65/(\sqrt{3}\ a^2/4) = 0.25$ (kcal/mol)/Å^2 = 1.0 (kJ/mol)/Å^2 = 0.17 J/m^2 = 170 erg/cm^2. This should be a lower bound on the surface energy.

B. C_{44} Shear Stiffness

In mechanical studies of graphite,[3] the observed, shear elastic constant C_{44} ranged from 0.18 to 0.33 GPa, whereas the neutron-irradiated samples[5] led to 4.2 to 4.6 GPa. It is widely believed that neutron irradiation pins dislocations, leading to parameters appropriate for the intrinsic system; hence the name "dislocation-free graphite" for these materials.[7,8] Boron implantation also leads to the larger values of C_{44}.[7,8]

There is evidence against this belief. Thus, in studying C_{44} down to 2 K,

Ganster and Fritz[9] observed a nearly constant low value, whereas if the low value were due to dislocations, one would have expected an increase for temperatures too low to activate the dislocations. Similarly, Ayasse et al.[8] measured C_{44} down to 0.1 K and found no evidence of the hardening expected if the low C_{44} were due to dislocations.

Our calculations lead to small values of C_{44} (0.23 to 0.33) for a wide range of such parameters ($\zeta = 11$ to $\zeta = 15$). Thus, these calculations provide evidence that the low C_{44} value ($\sim$0.27 GPa) from neutron-free samples is intrinsic, suggesting that the neutron irradiation (and boron implantation) cause a dramatic increase in shear resistance. Our speculation is that neutron-induced defects might disrupt the resonance system in graphite, leading to lower symmetry regions that might cause the planes to be "stickier." This is illustrated in Figure 1 for saturated carbon atoms at sheet edges. The result is a "pinned" resonance structure, where bond charges in adjacent planes might couple the sheets, leading to larger C_{44} (and C_{13}). In addition, such structures could have single-bond torsions smaller than in normal resonant graphite, allowing crinkling that would couple the layers. Alternatively, the increased values of C_{44} for neutron-irradiated graphite could be due to increased charge carriers and electronic coupling between the planes. However, experiments on neutron-irradiated samples at high magnetic fields[8] found no change in C_{44}, suggesting that such electronic effects are not responsible for the large C_{44}.

Assuming that impurities and imperfections increase what would be a small value of C_{44}, we believe that the intrinsic value for graphite should be in the lower half of the observed values (0.19 to 0.29 GPa).

As the temperature is increased, the instantaneous structure should have increasing crinkling of the planes. This could increase C_{44} markedly while affecting C_{33} only a small amount. However, the observed small change in C_{44} with

temperature[9] indicates that this is not an important effect. These issues about C_{44} are discussed in more detail in Section VI.

C. C_{13} Stiffness

The calculated values for C_{13} are small and track the values for C_{44} (in all cases C_{13} is within 2% of C_{44}). Experimental values are much larger, but the measurements are indirect. Thus, in the mechanical studies of Blakslee et al.[3] it was not possible to measure C_{13} directly, nor was it possible to measure the related compliance S_{13} in ultrasonic experiments. Instead, S_{13} was obtained by measuring the Poisson ratio in static experiments, and C_{13} was calculated using

$$C_{13} = -S_{13}/[S_{33}(S_{11} + S_{12}) - 2S_{13}^2], \tag{9}$$

leading to $C_{13} = 15 \pm 5$ GPa at room temperature.

In the temperature-dependence studies of Ganster and Fritz,[9] C_{13} could be obtained only from crosscut samples (45° from the c axis), leading to a velocity of sound v given by

$$\rho v^2 = \tfrac{1}{4}\left\{C_{11} + C_{33} + 2C_{44} - \sqrt{(C_{11} - C_{33})^2 + 4(C_{13} + C_{44})^2}\right\} \tag{10}$$

(where ρ is the density). Since C_{11} is much larger than C_{13}, this leads to considerable uncertainty in C_{13} (the uncertainty is comparable to the magnitude). Interestingly, the values for C_{13} deduced from these experiments are independent of temperature from 0 to 250 K and then change rapidly for higher temperatures.

Our calculated (small) values of C_{13} are consistent with flat, graphite planes. For higher temperatures the mean fluctuations in crinkling of the sheets should increase, leading to an increased c lattice constant (as observed). Applying tension parallel to the sheets might decrease these fluctuations, thereby decreasing the c axis. Thus, it is plausible that C_{13} might be small and constant for low temperatures and large for high temperatures (as observed[9]).

Consistent with the small, calculated value of C_{13}, we obtain small values for the Poisson ratios that couple strain in the a and c directions. Thus, for strain in the x direction we find $\mu_y = 0.175$ (observed values at room temperature = 0.16 ± 0.06), but $\mu_z = 0.005 \pm 0.001$ (observed values at room temperature = 0.34 ± 0.08). For stress in the z direction, we find almost no effect in the x and y directions, $\mu_x = 0.0002$ (the estimate from observations at room temperature is = 0.012 ± 0.003). Experiments at low temperature on these Poisson ratios would be most valuable in resolving these issues.

D. Lattice Modes

The mean value of the out-of-plane crinkling modes (868 cm^{-1}) was adjusted to fit the experiment. This leads to a rotational barrier of 21 kcal, about 1/3 the value for ethylene (65 kcal), as might be expected (since the resonance structures have one π bond for each three CC bonds). There are two modes at 868 cm^{-1} (one infrared-allowed), and we calculate the splitting to be 0.6 to 1.4 cm^{-1} for X6 potentials ($\zeta = 11$ to 15) and 1.8 cm^{-1} for LJ. Similarly, the splitting of the in-plane modes (1588 cm^{-1}) is predicted to be 0.1 to 0.2 cm^{-1}. Since the splitting of the 868 cm^{-1} mode is sensitive to the form of the nonbond potential, a direct spectroscopic observation of this splitting might help determine the scale for the van der Waals parameters.

The LO mode (B_{2g}) is predicted to be at 139 to 142 cm^{-1} and is observed (room temperature) by neutron scattering at 126 cm^{-1}. Expansion of the *c* lattice parameter from the value at 0 K to the value at 300 K (see Section V.A) leads to a prediction value of $\nu = 132$ cm^{-1} at 300K, explaining most of the discrepancy. The frequency of this mode is directly related to C_{33}, which we calculate to be 0.2%.

The TO mode (E_{2g}) is directly related to the C_{44} elastic constant. Thus, neutron-irradiated samples that yield $C_{44} = 4.4$ lead to a much higher frequency (45

cm^{-1}) than the calculations (which yield ~11 cm^{-1} and $C_{44} \sim 0.28$). As discussed above, we believe that the discrepancy is due to neutron damage. Experimental studies of the TO mode for low temperature and low irradiation would be most valuable to help resolve these uncertainties.

V. Properties of Graphite

We have used graphite parameters thus derived to calculate phonon-dispersion curves and thermodynamic properties of a graphite crystal (we used exponential-6 potential with $\zeta = 12$, since vibrational properties are not sensitive to ζ).

A. Phonon Dispersion Curves

In Figure 2 we show the calculated phonon dispersion curves for the lattice modes of graphite at 0 K. The vibrational frequencies are plotted in THz and cm^{-1} (to convert THz to cm^{-1}, multiply by 33.35641). The left half is for waves along the *c* axis, while the right half is for waves along the *a* axis. The acoustical modes are denoted TA and LA (transverse and longitudinal), while the sheet-sheet optical modes are denoted TO and LO.

The velocity of sound from these calculations is

$$v_T = \sqrt{C_{44}/\rho} = 0.34 \text{ km/sec}$$

$$v_L = \sqrt{C_{33}/\rho} = 4.24 \text{ km/sec}$$

for modes along the *c* axis and

$$v_{T_1} = \sqrt{C_{44}/\rho} = 0.34 \text{ km/sec}$$

$$v_{T_2} = \sqrt{C_{66}/\rho} = \sqrt{(C_{11} - C_{12})/2\rho} = 14.33 \text{ km/sec}$$

$$v_L = \sqrt{C_{11}/\rho} = 22.29 \text{ km/sec}$$

for modes along the *a* axis.

In Figure 3 we show all phonon modes. For vibrations within the sheets, there is little dispersion for waves in the c direction.

The full set of elastic constants (stiffness C_{ij} and compliance S_{ij}) are given in Table V.

There are direct experimental data on the lattice modes from neutron scattering;[5,6] however, these data are for room temperature. To better compare our results with these data, we recalculated the lattice modes using the lattice parameters for room temperature. To do this we modified the valence and van der Waals parameters to fit the room-temperature lattice constants (a and c), elastic constants (C_{11}, C_{12}, C_{33}), and sheet vibrational modes (868 and 1588 cm^{-1}) as in Section III.B for 0 K. The modified force field is in the last column of Table II, and the various properties are summarized in Table VI. The room-temperature lattice modes are plotted in Figure 4 along with the experimental data. For waves in the *a* direction, there is good agreement with the $TO_{\perp}$ and $TA_{\perp}$ modes (with amplitudes perpendicular to the sheets). The data for longitudinal modes lie slightly higher than the calculated LO and LA modes. This is expected since the experimental dispersion curve leads to an elastic constant of C_{11} = 1440 GPa, whereas the calculated dispersion leads to C_{11} = 1061 GPa, in agreement with the experimental value from mechanical studies (C_{11} = 1060 ± 20 GPa). The $TA_{||}$ and $TO_{||}$ modes are apparently not observed in the neutron-scattering experiments.

For waves along the *c* direction, the predicted LA and LO modes are in good agreement with the experiment. As discussed earlier, the TA modes for neutron-irradiated samples lead to a C_{44} that is 15 times larger than the C_{44} from mechanical experiments on irradiated samples. Our calculations support the low values for C_{44} and lead to TA and TO modes much lower in energy than for neutron experiments.

B. Thermodynamic Properties

In Figure 5 we show the specific heat calculated using the phonon states of Figure 3 and compare with experimental results.[19] To convert the calculated values

of C_v to C_p, we used the thermal expansion data of Bailey and Yates.[2] The entropy (S), energy (V), and free energy (F) are plotted in Figure 6 and tabulated in Table VII.

In addition to the calculations for the optimum parameters (leading to C_{44} = 0.25 GPa), we developed a second set of parameters to yield C_{44} = 4.0 GPa (the value observed with neutron scattering). The modified parameters include three-body angle interactions of the form $\frac{1}{2}k(\theta - \theta_0)^2$, where k = 3.1650 kcal/mol rad^2 and $\theta_0 = 90°$. Here the angle is between C-C bond in one sheet and the line parallel to the c axis, connecting two carbon atoms in adjacent sheets. The introduction of this term changes C_{44} without changing other properties.

We see that all three experiments and both theoretical cases agree above 20K. However, below 10K the experimental results for pile graphite and Canadian natural graphite lead to specific heats significantly below that of graphitized lampblack. Also, it is clear that the calculated optimum parameters for graphite (C_{44} = 0.25 GPa) lead to a C_p in excellent agreement with experiment for graphitized lampblack down to 1K. On the other hand, calculations using the modified parameters (C_{44} = 4.0 GPa) lead to a C_p, in good agreement with experiment for pile graphite and Canadian natural graphite.

a. Calculations, Uniform Grid

Our standard approach for calculating the thermodynamic properties is to use a uniform grid (N_g = 20 and 100) along all three directions in reciprocal space (a total of N_g^3 points). The vibrational states for each such point were considered as independent harmonic oscillators in calculating the quantum-partition function and thermodynamic properties. In these calculations we used 1/24 of the Brillouin zone with proper weights to obtain the sum over the full Brillouin zone. The three zero-frequency modes for the central cell are ignored in all calculations.

From Figure 6 we see that the results from the 20×20×20 grid (dotted lines) differ from the 100×100×100 grid (solid lines above T = 10K, dashed lines below) for T < 40K. This sensitivity to grid size is primarily due to the low-frequency modes in the z direction (see Figures 2 and 3). In particular, neglecting the contribution of the three acoustical modes for the central point leads to a low C_p. However, the calculated C_p for $N_g = 20$ is too *high* for T < 10K. This occurs because only modes with $k_x = k_y = 0$ contribute to C_p, and the weights of these modes are too large because of the small number of points in the k_x-k_y plane.

At T = 10K we tested these $N_g = 100$ results by using $N_g = 120$ (1728000 total points). Here we find that C_v increases by 3×10^{-6} cal/mol K or 0.08%. On the basis of comparisons to the calculations described below, it appears that the C_p from $N_g = 100$ is accurate down to about 2K.

b. Calculations, Thin Plate Approximation

To test the accuracy of the calculated thermodynamic properties at lower temperature (T < 10K), we used the frequency-distribution functions derived by Komatsu.[22] These functions were derived from the equations for vibrations of thin plates with coupling terms between the plates. This approximation describes only the acoustic modes and is accurate for frequencies below about 130 cm^{-1}. Thus, for low temperatures (where contributions from high frequencies are small), it is adequate to use these functions for thermodynamic properties. The frequency-distribution functions are[22]

$$f(\nu) = \frac{4V}{c'}\left(\frac{1}{v_l^2} + \frac{1}{v_t^2}\right)\nu \sin^{-1}\left(\frac{\nu}{\nu_z}\right), \quad \text{for } \nu \le \nu_z = \sqrt{\zeta}/\pi c' \qquad (11a)$$

and

$$f(\nu) = \frac{4V}{c'}\left(\frac{1}{v_l^2} + \frac{1}{v_t^2}\right)\nu\frac{\pi}{2}, \quad \text{for } \nu \ge \nu_z \qquad (11b)$$

for waves with the polarization vectors in the plate and

$$f(\nu) = \frac{V}{\pi c' \kappa} x \int_0^{\sin^{-1}(1/\sqrt{1+(x_o/x)^2})} \frac{d\varphi}{\sqrt{1 - x^2(1+(x_o/x)^2)\sin^2\varphi}}, \quad \text{for } \nu \le \nu_z' = \frac{\mu}{\pi}$$

$$= \frac{V}{\pi c' \kappa} \left[1 + \left(\frac{x_o}{x}\right)^2\right]^{-1/2} \int_0^{\pi/2} \frac{d\varphi}{\sqrt{1 - x^{-2}(1+(x_o/x)^2)^{-1}\sin^2\varphi}}, \quad \text{for } \nu \ge \nu_z' \tag{11c}$$

for waves with the polarization vector out of the plate, where $x = \nu/\nu_z'$ and $x_o = \zeta/4\pi\kappa\nu_z'$. Our force field leads to the following parameters in these calculations:

$c' = c/2 = 3.33605 \times 10^{-8}$ cm

$V =$ volume per mole $= 5.3004$ cm^3/mol

$v_l =$ longitudinal wave velocity in the plate

$= \sqrt{C_{11}/\rho} = 2.229 \times 10^6$ cm/s

$v_t =$ transverse wave velocity in the plate

$= \sqrt{C_{66}/\rho} = 1.433 \times 10^6$ cm/s

$\kappa =$ bending modulus of the plate $= 5.616 \times 10^{-3}$ cm^2/s

$\mu = (1/c')\sqrt{C_{33}/\rho} = 1.2704 \times 10^{13}$ s^{-1}

$\zeta = C_{44}/\rho = 1.1562 \times 10^9$ cm^2/s^2.

Here, the bending modulus κ was obtained by fitting the equation $\nu = \kappa k_x^2/2\pi$ to the frequencies calculated for the out-of-the-plane modes at $k_x = 0.1\ k_a$. In this calculation, we used a single, isolated, infinite layer of graphite.

These thin plate results for $T \le 10$K are shown in Figure 6 by the solid lines (for both $C_{44} = 0.25$ GPa and 4.0 GPa). For $T \le 2$K we see that the thin-plate approximation is clearly superior to using the $N_g = 100$ uniform grid.

C. Rhombohedral Graphite

The planes in graphite stack in the sequence ABABAB..., leading to hexagonal symmetry. A second structure has been observed with the stacking ABCABC..., leading to rhombohedral symmetry.[1] From experiment, the hexag-

onal form is clearly the more stable, but an estimate of the difference in energy is not available. Using the force fields, we calculated these forms to have energies within 0.0001 kcal/mol. [These calculations use an accuracy parameter of 0.0001 kcal/mol in the convergence acceleration,[11] leading to $\eta = 1.55$ Å, $R_{cut} = 5.55$ Å, and $H_{cut} = 5.72$ Å^{-1} for the hexagonal form with $\zeta = 12$.] The phonon modes for rhombohedral graphite are shown in Figure 8. The thermodynamic properties of rhombohedral graphite are calculated and compared with hexagonal graphite in Figures 5 and 6, but the differences are too small to see. Since high-quality graphite is hexagonal with but few stacking faults, we believe that the calculated energy difference is too small.

VI. Discussion

The experiments and calculations on graphite leave some important discrepancies unresolved. The major issue is the value of C_{44}. Ultrasonic measurements on compression-annealed graphite lead to $C_{44} = 0.28 \pm .08$. Our theoretical force field yields $C_{44} = 0.23$ to 0.30, in excellent agreement with the above results. This force field predicts a specific heat, Cp, in agreement with experiments on graphitized lampblack.

On the other hand, neutron scattering leads to $C_{44} \sim 4.0$ GPa and using force-field parameters adjusted for $C_{44} = 4.0$ GPa leads to a Cp in agreement with high-quality graphite down to 1K.

A second troubling result from the theory is that the energy of Rhombohedral graphite is less than 0.0001 kcal/mol above hexagonal graphite. The observed strong preference for hexagonal graphite suggests a larger energy separation.

We should emphasize here that the assumption (1) that the graphite sheets are flat and (2) that the van der Waals interactions are described in terms of X6 or LJ-type, two-body functions combined with (3) the requirement of fitting the

experimental values of c = 6.6721 Å and C_{33} = 40.7 GPa, leads directly to values of C_{44} = 0.2 to 0.3 and necessarily leads to (a) $C_{13} \approx C_{44}$, (b) the high values of Cp near 1K and (c) a small energy separation between hexagonal and rhombohedral graphite.

[Al-Jishi and Dresselhaus[20] have reported a set of parameters that lead to C_{44} = 4.2 and C_{33} = 36.9; however, the model used considers only interactions of atoms on the same or adjacent layers (and only up to 4th neighbors) and involves individually adjusted radial and tangential pairwise force constants. These pairwise force constants are not derivable from a smooth, two-body potential.]

If the high value of C_{44} from neutron experiments is the correct value for perfect graphite, then we believe that either (or both) of the above assumptions (flat sheets or two-body, long-range attractions) must be false. That is, either the graphite planes are ruffled (as suggested by Pauling[1] but not confirmed by any experiments), or the van der Waals interactions are *not* described in terms of smooth, pairwise, additive terms.

The latter hypothesis is possible. Graphite is a semimetal; that is the valence-band maximum (highest-occupied, molecular orbital) is degenerate with the conduction band minimum (lowest-unoccupied, molecular orbital). In this circumstance there should be extralarge contributions to the dispersion interactions that are due to the states near the band edges (small energy denominators). This might well have a major effect on C_{44} (and C_{13}). We are not in a position to test this hypothesis (it would require many-body, electron-correlation calculations on crystals of graphite). However, even if true, we believe that the van der Waals parameters derived here for carbon are the appropriate parameters for other systems.

VII. Summary

We report van der Waals properties for C, given the fitting experimental data

for graphite, and we use these parameters to examine other mechanical properties of graphite. These studies support the low value for the shear elastic constant from mechanical experiments ($C_{44} \sim 0.27$ rather than $C_{44} \sim 4.2$) and suggest that neutron irradiation may increase the shear resistance. In addition, the simulations lead to a much smaller coupling of in-plane stress to layer spacing (e.g., C_{13}) than is observed indirectly from experiment.

The specific heat and other thermodynamic properties are in good agreement with experiment for $T > 20K$. At temperatures lower than 10K, the low value of $C_{44} \approx 0.3$ GPa consistent with ultrasonic measurements gives a specific heat in agreement with graphitized lampblack but larger than that of natural graphite. The larger value of $C_{44} \approx 4.0$ GPa from neutron-irradiated samples leads to a specific heat in agreement with natural graphite. This larger C_{44} is inconsistent with a standard, two-body description of the long-range van der Waals interaction of planar graphite sheets. This could indicate the need for more complicated potentials.

We believe that these carbon potentials will be useful for examining surface properties and adsorbates on graphite. In addition, they should be useful in considering the intercalation of various molecules in graphite and in examining adhesion to polymers and other molecules.

Acknowledgements.

This research was supported by grants from the Air Force Office of Scientific Research (No. AFOSR-88-0051) and the Caltech Consortium in Chemistry and Chemical Engineering. Preliminary studies were carried out earlier with funding from Hughes Aircraft Company (Mike Gardos). We thank BioDesign, Inc. for the use of POLYGRAF, which was used for all calculations in the paper.

References

(1) Donohue, J. *The Structures of the Elements* (Robert E. Krieger Publishing Co., Malabar, Florida, 1974).

(2) Bailey, A. C.; Yates, B. *J. Appl. Phys.* **1970,** *41,* 5088.

(3) Blakslee, O. L.; Proctor, D. G.; Soldin, E. J.; Spence, G. B.; Weng, T. *J. Appl. Phys.* **1970,** *41,* 3373.

(4) 1 GPa = 10^{10} dynes/cm^2 = 10 kbar = 0.14393 (kcal/mol)/Å^3.

(5) Dolling, G.; Brockhouse, B. N. *Phys. Rev.* **1962,** *128,* 1120.

(6) Nicklow, R.; Wakabayashi, N.; Smith, H. G.*Phys. Rev. B* **1972,** *5,* 4951.

(7) Baker, C.; Kelly, A. *Phil. Mag.* **1964,** *9,* 927.

(8) Ayasse, J. B.; Ayache, C.; Jager, B.; Bonjour, E.; Spain, I. L. *Solid State Commun.* **1979,** *29,* 659.

(9) Ganster, W. G.; Fritz, I. J. *J. Appl. Phys.* **1974,** *45,* 3309.

(10) Nemanich, R. J.; Lucovsky, G.; Solin, S. A. *Solid State Commun.* **1977,** *23,* 117.

(11) Karasawa, N.; Goddard III, W. A. *J. Phys. Chem.* **1989,** *93,* 7320.

(12) Allinger, N. L. *J. Am. Chem. Soc.* **1977,** *99,* 8127. Sprague, J. T.; Tai, J. C.; Yuh, Y.; Allinger, N. L. *J. Comput. Chem.* **1987,** *8,* 581.

(13) Williams, D. E.; Cox, S. R. *Acta Crystallogr., Sect. B* **1984,** *40,* 404.

(14) Brooks, B. R.; Bruccoleri, R. E.; Olafson, B. D.; States, D. J.; Swaminathan, S.; Karplus, M. *J. Comput. Chem.* **1983,** *4,* 187. Nillson, L.; Karplus, M. *ibid.* **1986,** *7,* 591.

(15) Weiner, S. J.; Kollman, P. A.; Case, D. A.; Singh, U. C.; Ghio, G.; Algona, G.; Profeta, Jr., S.; Weiner, P. *J. Am. Chem. Soc.* **1984,** *106,* 765. Weiner, S. J.; Kollman, P. A.; Nguyen, D. T.; Case, D. A. *J. Comput. Chem.* **1986,**

7, 230.

(16) Jorgensen, W. J.; Tirado-Rives, J. *J. Am. Chem. Soc.* **1988,** *110,* 1657.

(17) Mayo, S. L.; Olafson, B. D.; Goddard III, W. A. *J. Phys. Chem.*, **1990,** *94,* 8897.

(18) Billmeyer, F. W., Jr. *J. Appl. Phys.* **1957,** *28,* 1114.

(19) DeSorbo, W.; Tyler, W. W. *J. Chem. Phys.* **1953,** *21,* 1660.

(20) Al-Jishi, R.; Dresselhaus, G. *Phys. Rev.* **1982**, *B26*, 4514.

(21) Karasawa, N.; Dasgupta, S.; Goddard III, W. A. *J. Phys. Chem.* **1991,** *95,* 2260.

(22) Komatsu, K. *J. Phys. Soc. Japan* **1955**, *10*, 346.

(23) Pan, C.; Sampson, M. P.; Chai, Y.; Hauge, R. H.; Margrave, J. L. *J. Phys. Chem.* **1991,** *95,* 2944.

(24) Guo, Y.; Karasawa, N.; Goddard III, W. A. *Nature* **1991,** *351,* 464.

TABLE I. Experimental Parameters for Graphite.

	300K[a]	300K → 0K[b]	0K
Lattice Parameters (Å)[c]			
a	2.4612	0.0072	2.4684
c	6.7090	−0.0369	6.6721
Elastic Constants (GPa)			
C_{11}	1060 ± 20	66 ± 8	1126 ± 22
C_{12}	180 ± 20	20 ± 2.5	200 ± 20
C_{33}	36.5 ± 1.0	4.2 ± 0.5	40.7 ± 1.1
C_{44}	0.28 ± 0.08	0.0088 ± 0.001	0.289 ± 0.08
C_{13}	15 ± 5	23.8 ± 40	39.5 ± 40.
Young's Moduli (GPa)			
E_1	1020 ± 30		
E_3	36.5 ± 1.0		
Poisson Ratios			
μ_{21}	0.16 ± 0.06		
μ_{31}	0.34 ± 0.08		
μ_{13}	0.012 ± 0.003		

[a] References 1 and 3.

[b] References 2 and 9.

[c] 298 K was used in place of 300 K.

TABLE II. Force Field Parameters. Values in Parentheses Were Not Optimized.

	Exponential-6 [Eq (1)]						Lennard-Jones [Eq (5)]	exp-6, ζ=12 Room Temperature
Parameters	ζ = 11	ζ = 12	ζ = 13	ζ = 14	ζ = 14.255	ζ = 15		
Van der Waals								
R_v (Å)	3.9425	3.8837	3.8410	3.8086	3.8013	3.78191	3.8050	3.9048
D_v (kcal/mol)	0.09115	0.08444	0.07918	0.07474	0.07372	0.07094	0.06921	0.07443
ζ	(11.0)	(12.0)	(13.0)	(14.0)	14.255	(15.0)	—	(12.0)
Bond Stretch [Eq (6)]								
R_b (Å)	1.42142	1.41988	1.41836	1.416754	1.416311	1.414933	1.41144	1.41548
k_b [(kcal/mol)/Å^2]	802	792	782	775.9406	773.8580	762.8735	720	732.5
D_b (kcal/mol)	(133.0)	(133.0)	(133.0)	(133.0)	(133.0)	(133.0)	(133.0)	(133.0)
Angle Bend [Eq (7)]								
θ_a (deg)	(120.0)	(120.0)	(120.0)	(120.0)	(120.0)	(120.0)	(120.0)	(120.0)
$k_{\theta\theta}$ [(kcal/mol)/rad^2]	178.36	181.0	182.54	181.4709	181.9882	183.8277	196.13	186.1
D [(kcal/mol)/ Å]	−79.24	−78.0	−76.76	−74.1293	−73.7091	−72.5216	−72.41	−68.7
k_{rr} [(kcal/mol)/Å^2]	(68.0)	(68.0)	(68.0)	(68.0)	(68.0)	(68.0)	(68.0)	(68.0)
Torsion [Eq (8)]								
V_t (kcal/mol)	21.38	21.37	21.35	21.2884	21.2789	21.2507	21.28	21.24

TABLE III. Predicted Properties for Graphite[c].

	Experiment[a] (0 K)	Fitted	Exponential 6 (X6) ζ=11	ζ=12	ζ=13	ζ=14	ζ=14.255	ζ = 15	LJ12-6
Lattice Parmeters									
a	2.4684 ± 0.001	yes	2.4684	2.4684	2.4684	2.4684	2.4684	2.4684	2.4684
c	6.6721 ± 0.001	yes	6.6721	6.6721	6.6721	6.6721	6.6721	6.6721	6.6721
Elastic constant									
C_{11}	1126 ± 22	yes	1126.0	1126.3	1126.0	1126.0	1126.0	1126.0	1127.0
C_{12}	200 ± 20	yes	199.1	195.8	194.7	200.0	200.0	200.0	194.2
C_{33}	40.7 ± 1.1	yes	40.70	40.70	40.66	40.70	40.70	40.70	40.74
C_{44}	0.289 ± 0.08	no	0.229	0.262	0.289	0.310	0.315	0.330	0.304
C_{13}	39.5 ± 40	no	0.227	0.260	0.288	0.309	0.315	0.330	0.310
Young's Moduli									
E_1	(1020 ± 30)	no	1090.8	1092.2	1092.3	1090.5	1090.5	1090.5	1093.6
E_3	(36.5 ± 1.0)	no	40.70	40.70	40.66	40.70	40.70	40.70	40.74
Poisson Ratios									
μ_{21}	(0.16 ± 0.06)	no	0.177	0.174	0.173	0.178	0.178	0.178	0.172
μ_{31}	(0.34 ± 0.08)	no	0.0046	0.0053	0.0059	0.0063	0.0064	0.0067	0.0063
μ_{13}	(0.012 ± 0.003)	no	0.0002	0.0002	0.0002	0.0002	0.0002	0.0002	0.0002
Compressibility									
β	0.026	no	0.02606	0.02606	0.02609	0.02606	0.02606	0.02605	0.02604
Lattice Modes									
E_{2g}	(45)[b]	no	10.1	11.1	11.4	11.8	11.9	12.1	11.7
B_{2g}	(134)[b]	no	142.3	140.7	139.6	138.9	138.8	138.4	139.0
A_{2u}	868	yes	867.4	868.1	868.2	867.4	867.7	867.7	867.8
B_{2g}	868	no	868.0	868.9	869.2	868.6	869.1	869.1	869.6
E_{2g}	1588	no	1588.1	1589.7	1588.1	1588.0	1588.7	1588.7	1586.0
E_{1u}	1588	yes	1588.2	1589.8	1588.2	1588.1	1588.8	1588.8	1586.2
Cohesive energy									
E_{coh}			2.048	1.723	1.500	1.338	1.303	1.211	1.303
E_{rhom}-E_{hex}			0.000	0.000	0.000	0.000	0.000	0.000	0.000

[a] Parentheses indicate values at room temperature.

[b] See discussion in Section II.C. 8 cm^{-1} were added to correct from 300K to 0K (see Section II.d).

[c] Units are Å for lattice parameters, GPa for elastic constants and Young's moduli, 1/GPa for compressibility, 1 cm for lattice modes, and kcal/mol per carbon for cohesive energy.

TABLE IV. Comparison with Published van der Waals Parameters for Carbon.

Parameters	MM2[a]	Williams[b]	Amber [c]	CHARMM[d]		Jorgensen[e]	DREIDING[f]	Exact[g]
				EF2	EF3			
Force-Field Parameters								
van der Waals								
R_v (Å)	3.8005	3.8983	3.70	3.60	3.7008	4.209	3.88	—
D_v (kcal/mol)	0.0515	0.09512	0.12	0.1972	0.090	0.110	0.095	—
ζ	12.5	14.034	—	—	—	—	—	
Bond								
R_b (Å)	1.4219	1.40952	1.40998	1.40975	1.41380	1.31663	1.39925	—
Properties								
Cell Parameters (Å)								
c	6.5923	6.8014	6.5256	6.3102	6.5264	7.3678	6.7773	6.6721
Elastic Constants (GPa)								
C_{33}	24.12	56.09	62.31	109.14	46.84	74.39	60.13	40.7 ± 1.0
C_{44}	0.168	0.385	0.500	0.936	0.376	0.400	0.422	0.29 ± 0.08
C_{13}	0.167	0.387	0.499	0.936	0.376	0.402	0.423	0.29 ± 0.08
Cohesive Energy								
E_{coh} (kcal/mol C)	1.021	1.656	2.300	3.332	1.725	2.344	1.731	(1.3)
Compressibility (GPa^{-1})								
β	0.04306	0.01938	0.01747	0.01051	0.02282	0.01459	0.01810	0.0261
Lattice Modes (cm^{-1})								
E_{2g}	8.8	13.1	15.4	13.5	13.3	12.8	13.7	(10.5 ± 1)
B_{2g}	109.3	161.0	176.9	141.9	153.2	178.2	167.2	(141 ± 1)

[a] Reference 12.

[b] Reference 13.

[c] Reference 15.

[d] Reference 14.

[e] Reference 16.

[f] Reference 17.

[g] Values in parentheses estimated from calculations; see Table III.

TABLE V. Properties at 0K for Graphite Using the $\zeta = 12$ Exponential-6 Potential.

C_{ij} Elastic Constant Matrix (Stiffness) (GPa).

$$\begin{pmatrix} 1126.4 & 195.8 & 0.260 & 0 & 0 & 0 \\ & 1126.4 & 0.260 & 0 & 0 & 0 \\ & & 40.70 & 0 & 0 & 0 \\ & & & 0.262 & 0 & 0 \\ & & & & 0.262 & 0 \\ & & & & & 465.45 \end{pmatrix}$$

S_{ij} Compliance Matrix (GPa^{-1}).

$$\begin{pmatrix} 9.1545E-4 & -1.5913E-4 & -4.8315E-6 & 0 & 0 & 0 \\ & 9.1545E-4 & -4.8315E-6 & 0 & 0 & 0 \\ & & 2.4570E-2 & 0 & 0 & 0 \\ & & & 3.8168 & 0 & 0 \\ & & & & 3.8168 & 0 \\ & & & & & 2.1485E-3 \end{pmatrix}$$

TABLE VI. Predicted Properties for Graphite at Room Temperature.

	Experiment	Exponential 6 (X6)[b] $\zeta = 12$
Lattice Parameters (Å)		
a	2.4612 ± 0.001	(2.4612)
c	6.7090 ± 0.001	(6.7090)
Elastic Constant (GPa)		
C_{11}	1060 ± 20	(1061.3)
C_{12}	180 ± 20	(181.0)
C_{33}	36.5 ± 1.0	(36.50)
C_{44}	0.28 ± 0.08	0.224
C_{13}	15 ± 5	0.224
Young's Moduli (GPa)		
E_1	1020 ± 30	1030.6
E_3	36.5 ± 1.0	36.50
Poisson Ratios		
μ_{21}	0.16 ± 0.06	0.171
μ_{31}	0.34 ± 0.08	0.0051
μ_{13}	0.012 ± 0.003	0.0002
Compressibility (GPa^{-1})		
β	0.0268 ± 0.0013[c] 0.0286[d]	0.02899
Lattice Modes (cm^{-1})		
E_{2g}	45[a]	10.0
B_{2g}	126[a]	132.0
A_{2u}	868	(867.7)
B_{2g}	868	868.4
E_{2g}	1588	1587.0
E_{1u}	1588	(1587.1)
Cohesive Energy (kcal/mol C)		
E_{coh}		1.540

[a] See discussion in Section II.C.

[b] Quantities in parentheses used in the fit.

[c] Reference 3.

[d] Kabalkina, S. S.; Vereshchagin, L. F. *Sov. Phys. Dokl.* **1960,** *5,* 373.

TABLE VII. Calculated Thermodynamic Properties (per Carbon Atom).

Temp	C_v (cal/mol K)	S (cal/mol K)	V (kcal/mol)	F (kcal/mol)
1	3.209×10^{-5}	1.311×10^{-5}	9.226×10^{-9}	-3.885×10^{-9}
2	1.389×10^{-4}	6.267×10^{-5}	8.682×10^{-8}	-3.851×10^{-8}
3	3.349×10^{-4}	1.530×10^{-4}	3.162×10^{-7}	-1.428×10^{-7}
4	6.215×10^{-4}	2.864×10^{-4}	7.868×10^{-7}	-3.589×10^{-7}
6	1.465×10^{-3}	6.859×10^{-4}	2.814×10^{-6}	-1.302×10^{-6}
8	2.667×10^{-3}	1.263×10^{-3}	6.886×10^{-6}	-3.221×10^{-6}
10	3.871×10^{-3}	1.850×10^{-3}	1.128×10^{-5}	-6.696×10^{-6}
15	9.014×10^{-3}	4.414×10^{-3}	4.405×10^{-5}	-2.216×10^{-5}
20	0.01665	7.989×10^{-3}	1.071×10^{-4}	-5.269×10^{-5}
40	0.07516	0.03505	9.543×10^{-4}	-4.479×10^{-4}
60	0.1656	0.08186	3.324×10^{-3}	-1.588×10^{-3}
80	0.2749	0.1441	7.701×10^{-3}	-3.824×10^{-3}
100	0.3992	0.2185	0.01442	-7.432×10^{-3}
200	1.168	0.7204	0.09122	-0.05285
300	2.000	1.352	0.2497	-0.1558
400	2.768	2.035	0.4890	-0.3249
500	3.411	2.724	0.7991	-0.5629
600	3.918	3.393	1.167	-0.8690
700	4.309	4.027	1.579	-1.240
800	4.608	4.623	2.025	-1.673
900	4.839	5.180	2.498	-2.164
1000	5.019	5.699	2.992	-2.708
1500	5.503	7.843	5.643	-6.121
2000	5.695	9.456	8.449	-10.463
2500	5.788	10.738	11.322	-15.523
3000	5.840	11.798	14.231	-21.165
4000	5.893	13.487	20.101	-33.847

Figure Captions

Figure 1. Illustration of pinning of resonance structures by saturation of bonds at edges of graphite.

Figure 2. Phonon-dispersion curves for low-frequency modes of (hexagonal) graphite at 0K (using the X6 potential with $\zeta = 12$).

Figure 3. Phonon-dispersion curves for all vibrational modes of (hexagonal) graphite at 0 K.

Figure 4. Phonon-dispersion curves for low-frequency modes of (hexagonal) graphite at 300K.

Figure 5. Specific heat of graphite. Experimental results indicated with circles.

Figure 6. Thermodynamic properties of graphite. Theoretical values for hexagonal and rhombohedral structures are plotted, but the lines are essentially superimposed. (a) Vibrational entropy (S) of graphite. (b) Vibrational energy (V) and free energy (F) of graphite.

Figure 7. Phonon-dispersion curves for low-frequency modes of rhombohedral graphite at 0 K (using the X6 potential with $\zeta = 12$).

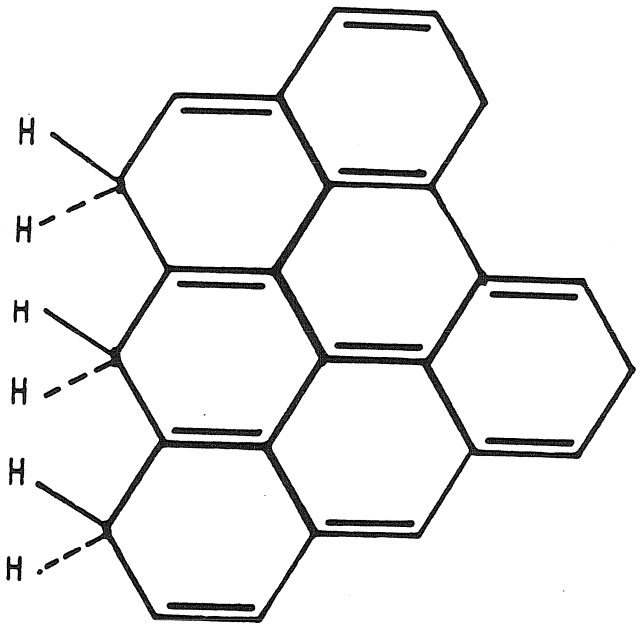

Figure 1

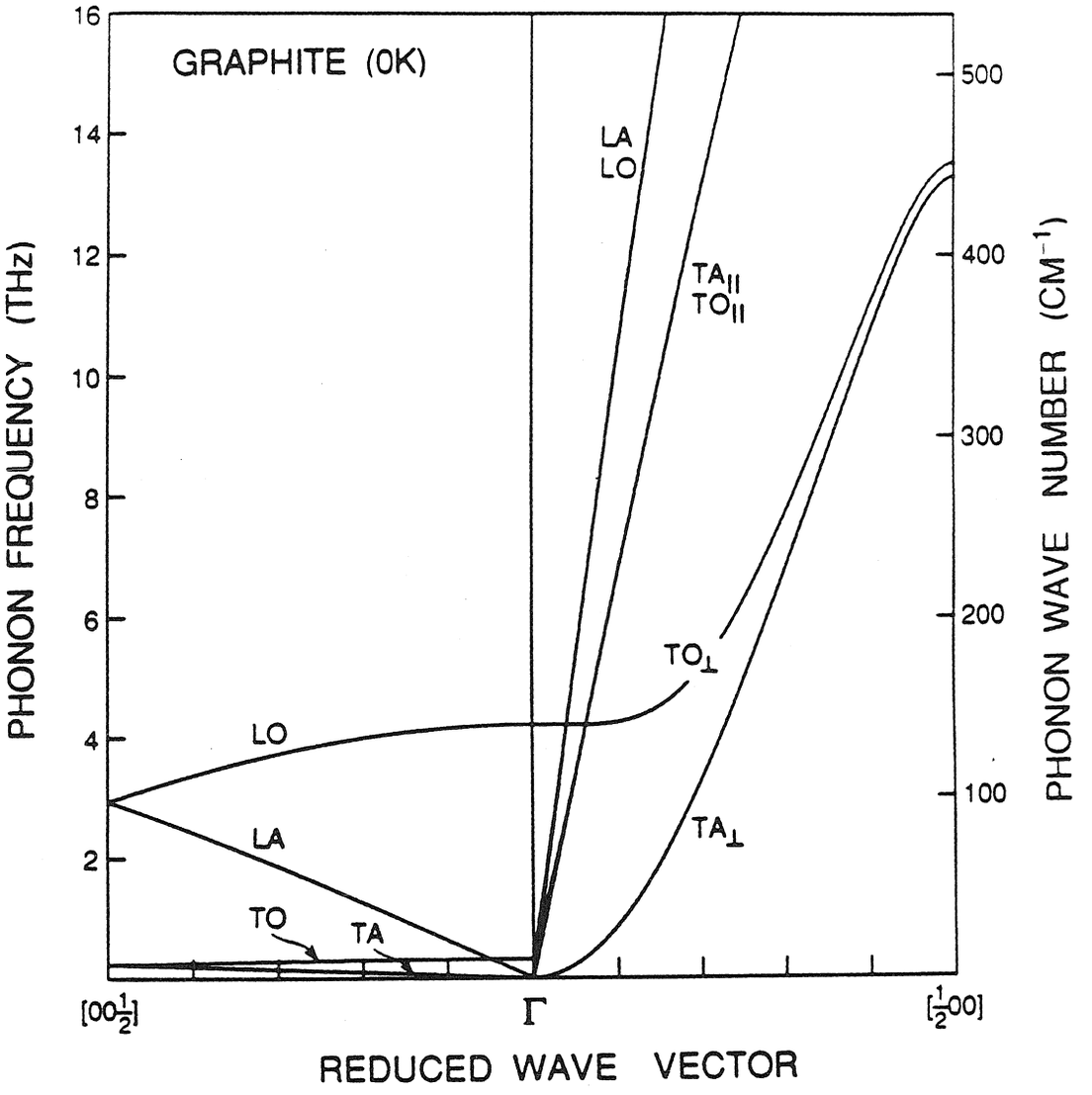
GRAPHITE (0K)
PHONON FREQUENCY (THz)
PHONON WAVE NUMBER (CM^{-1})
REDUCED WAVE VECTOR
16
14
12
10
8
6
4
2
500
400
300
200
100
LA
LO
TA$_{II}$
TO$_{II}$
TO$_{\perp}$
TA$_{\perp}$
LO
LA
TO
TA
[00$\frac{1}{2}$]
Γ
[$\frac{1}{2}$00]

Figure 2

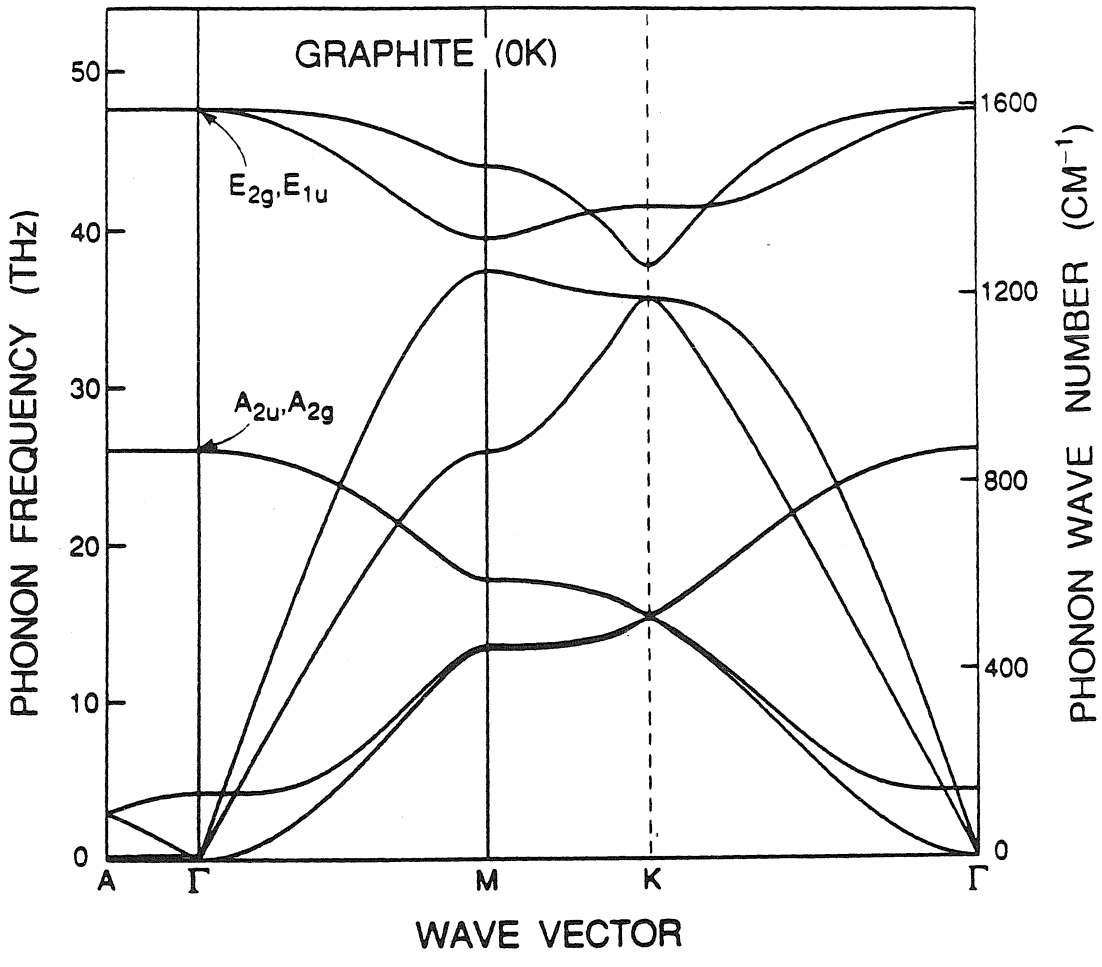
GRAPHITE (0K)
PHONON FREQUENCY (THz)
PHONON WAVE NUMBER (CM⁻¹)
WAVE VECTOR
E2g,E1u
A2u,A2g
50
40
30
20
10
0
1600
1200
800
400
0
A
Γ
M
K
Γ

Figure 3

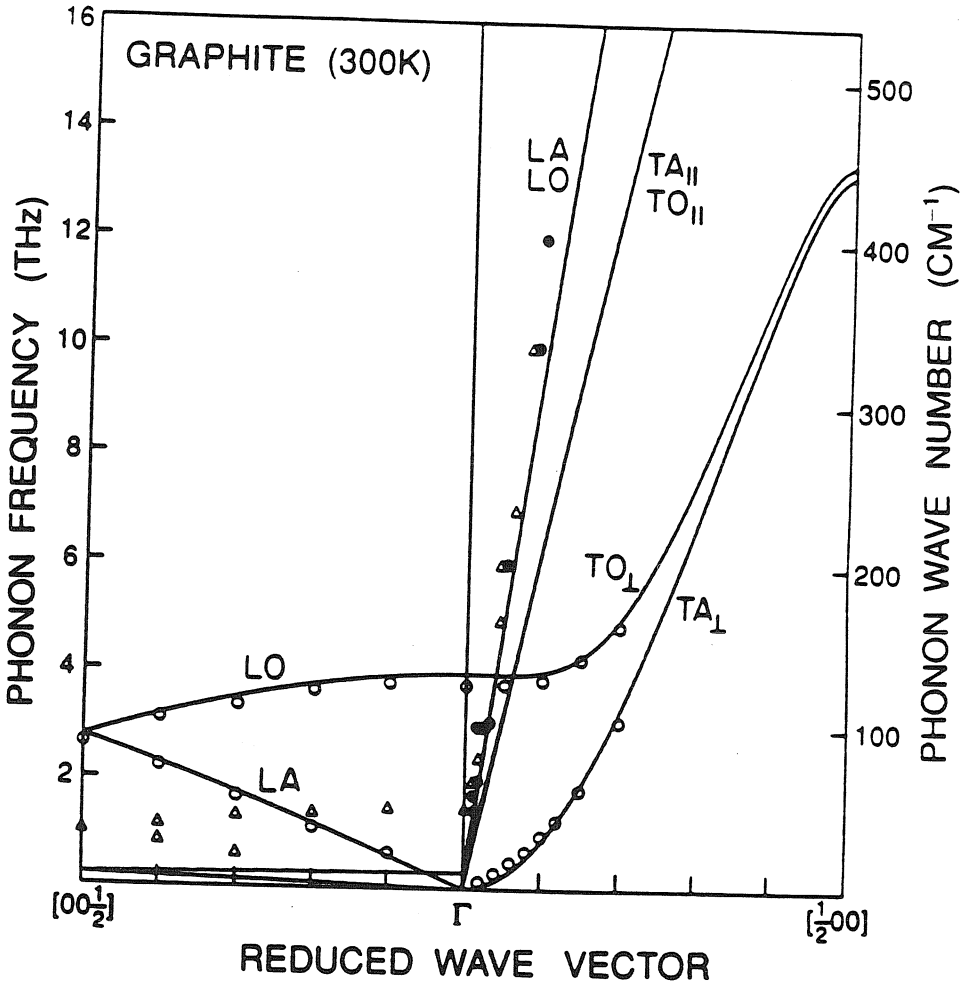
GRAPHITE (300K)
PHONON FREQUENCY (THz)
PHONON WAVE NUMBER (CM⁻¹)
REDUCED WAVE VECTOR
LA
LO
TA∥
TO∥
TO⊥
TA⊥
LO
LA
[00½]
Γ
[½00]
16
14
12
10
8
6
4
2
500
400
300
200
100

Figure 4

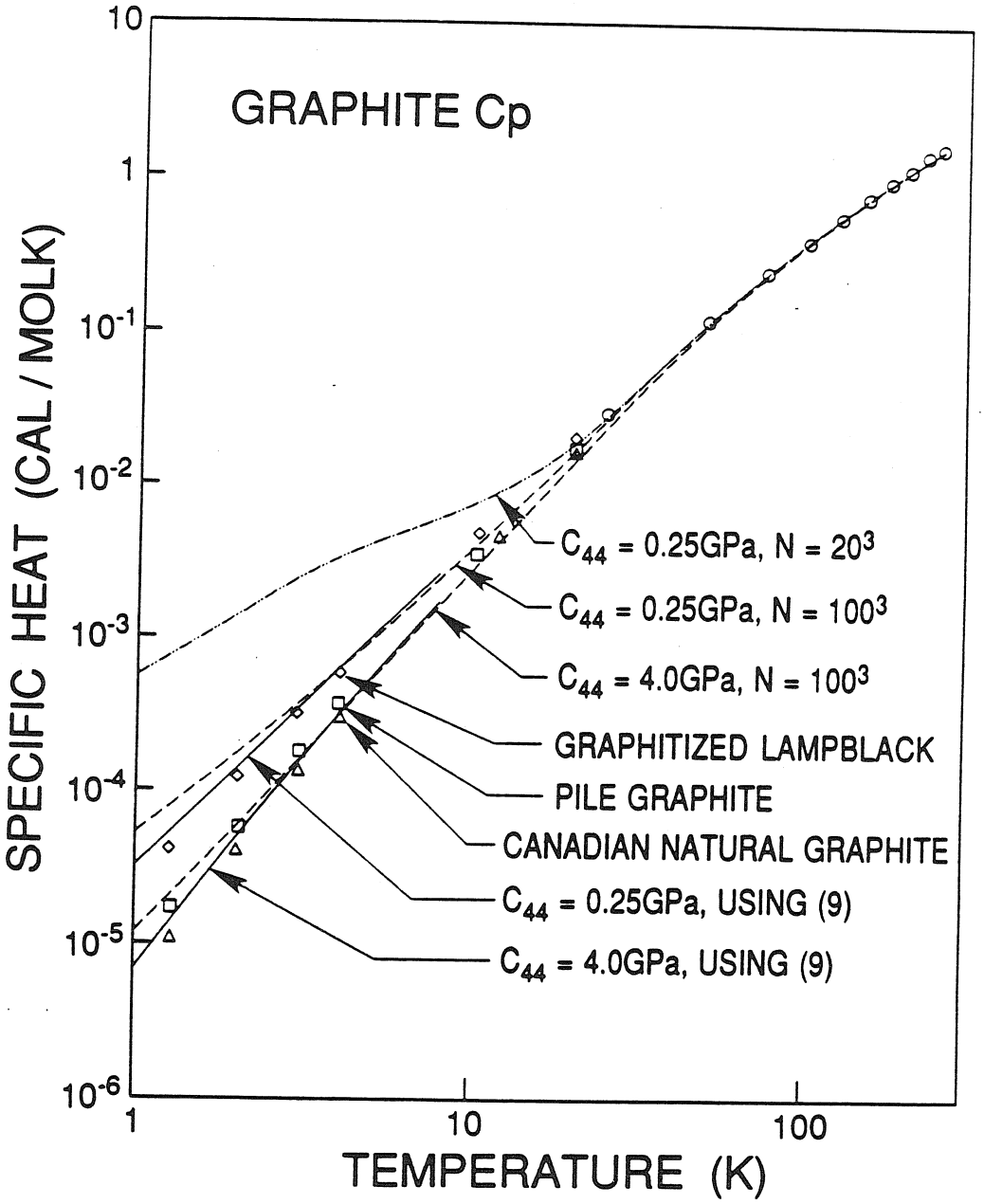
GRAPHITE Cp
SPECIFIC HEAT (CAL / MOLK)
TEMPERATURE (K)
10
1
10^{-1}
10^{-2}
10^{-3}
10^{-4}
10^{-5}
10^{-6}
1
10
100
C_{44} = 0.25GPa, N = 20^3
C_{44} = 0.25GPa, N = 100^3
C_{44} = 4.0GPa, N = 100^3
GRAPHITIZED LAMPBLACK
PILE GRAPHITE
CANADIAN NATURAL GRAPHITE
C_{44} = 0.25GPa, USING (9)
C_{44} = 4.0GPa, USING (9)

Figure 5

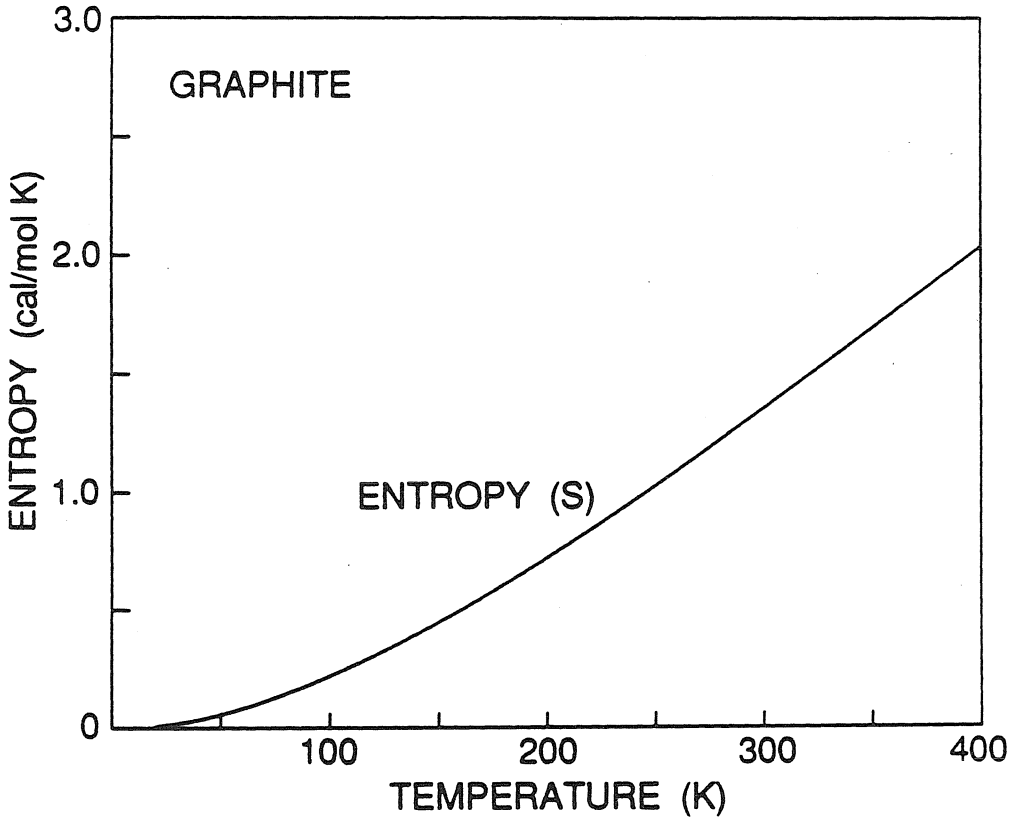
3.0
GRAPHITE
2.0
1.0
ENTROPY (S)
0
ENTROPY (cal/mol K)
100
200
300
400
TEMPERATURE (K)

Figure 6a

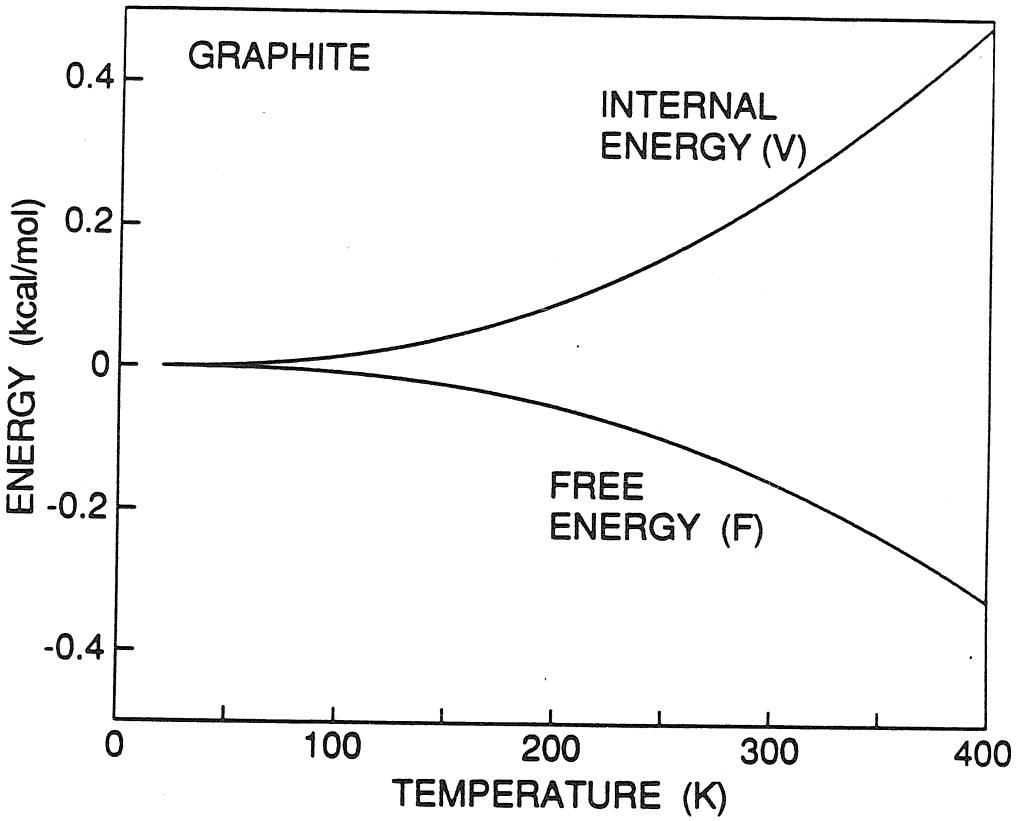
GRAPHITE
INTERNAL
ENERGY (V)
FREE
ENERGY (F)
ENERGY (kcal/mol)
0.4
0.2
0
-0.2
-0.4
0
100
200
300
400
TEMPERATURE (K)

Figure 6b

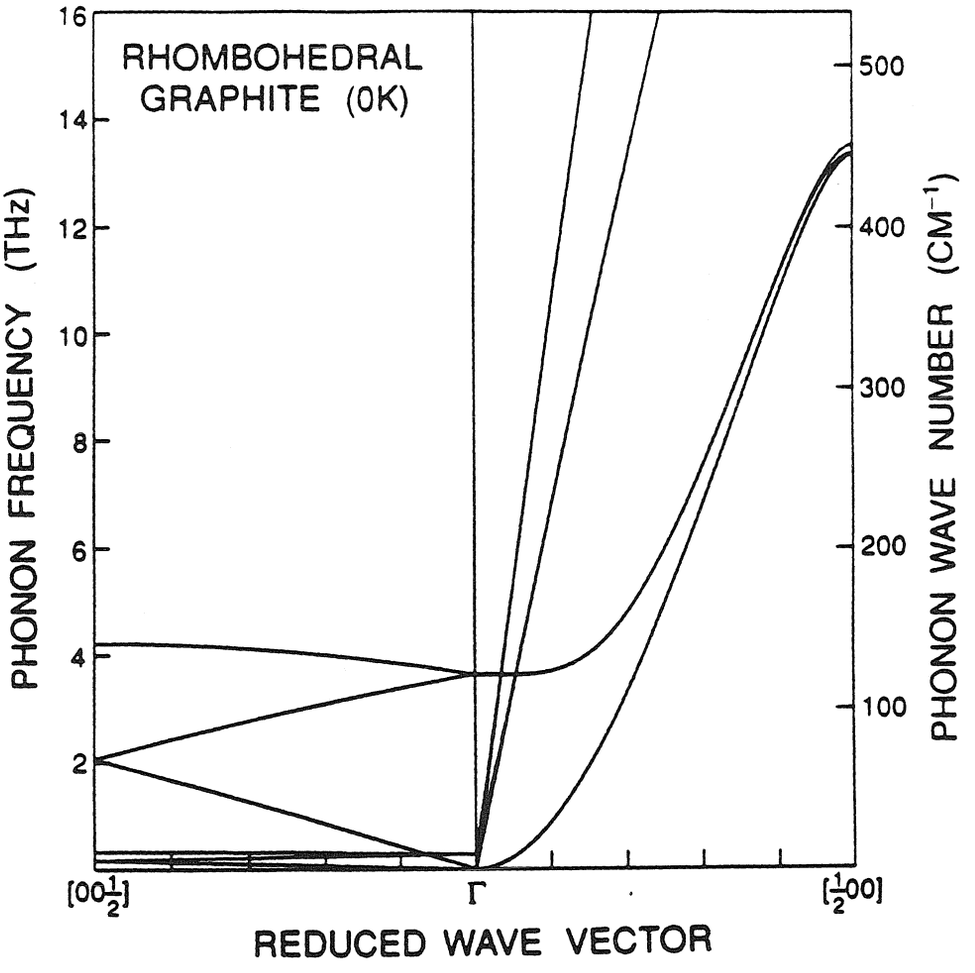
RHOMBOHEDRAL
GRAPHITE (0K)
PHONON FREQUENCY (THz)
PHONON WAVE NUMBER (CM⁻¹)
REDUCED WAVE VECTOR
[00½]
Γ
[½00]
16
14
12
10
8
6
4
2
500
400
300
200
100

Figure 7

Appendix II

Properties for Hydrocarbon Crystals Using New, Nonbond, Force-Field Parameters

Abstract

Nonbond, force-field parameters, derived for molecular-mechanics calculations of polyethylene crystal, are used to calculate properties of various hydrocarbon crystals. Cell parameters, cohesive energy, lattice frequencies and elastic constants are calculated for n-hexane, n-octane, benzene, naphthalene, and anthracene. Lattice frequencies of polyethylene crystal were fitted when van der Waals parameters were determined, leading to a good agreement of calculated, vibrational frequencies and elastic constants with experimental values for these hydrocarbon crystals.

I. Introduction

We developed force-field parameters for molecular-mechanics calculations of polyethylene crystal[1]. In this study, carbon van der Waals (vdW) parameters are derived from graphite and hydrogen vdW parameters are derived to fit cohesive energy, cell parameters and lattice frequencies of polyethylene crystal. Here we use parameters thus derived to calculate properties of hydrocarbon molecular crystals. Since a scaling parameter (ζ) of hydrogen vdW parameters was adjusted to reproduce lattice frequencies of polyethylene crystal, it is of particular interest to calculate lattice frequencies of these crystals and to compare them with observed values.

Hydrocarbon, nonbond, force-field parameters have been derived by Williams and Starr[2] In their study, the exp-6-1 form was used and parameters were determined by using 18 hydrocarbon molecular crystals. Recently, these parameters have been slightly modified by using azahydrocarbon crystals[3]. In their studies, cohesive energy and structure were used to determine vdW parameters and charges. It was shown that electrostatic terms were important, and the charge of hydrogen atom was set to be 0.153e. Also it was shown that geometric mean law could be used for vdW parameters between carbon and hydrogen. Shortenings of 0.07Å for C-H covalent bonds were used in these calculations. Lattice frequencies of molecular crystals were used to optimize the vdW parameters but no significant changes were obtained[4].

One restriction in the parameter-optimization procedure in these studies is that C (a factor in e^{-CR}) in the exp-6-1 potential is not optimized but is obtained from the structure of the elements or theoretically fixed in the parameter optimization. We found that this factor has significant effects on lattice frequencies, and we used polyethylene lattice frequencies to optimize it. Also, we do not use the shortening of C-H covalent bonds in the calculation.

Here we calculate structure, cohesive energy, lattice frequencies and elastic constants for n-hexane, n-octane, benzene, naphthalene, and anthracene by using vdW parameters obtained for polyethylene crystal, and *no* adjustment of the vdW parameters was made for each crystal. The main purpose of this study is to see if these parameters give properties that agree with experimental values. Also, it should be a good test of transferability of vdW parameters. These crystals are chosen because many of the calculated properties can be compared with experimental values.

II. Method

The nonbond potential energy is given by the sum of van der Waals terms and electrostatic terms. The electrostatic term between atoms i and j is given by $C_{unit}q_iq_j/\epsilon R$, where q_i and q_j are charges of atoms, R is a distance between atoms, ϵ is a dielectric constant which we take as one, and $C_{unit} = 332.0647$ converts the energy in kcal/mol, if charges are in electrons and R is in Å. Similarly, the van der Waals term between atoms i and j is given by

$$E(R) = Be^{-CR} - AR^{-6} = \frac{D_0}{\zeta - 6}\left[6e^{\zeta(1-R/R_0)} - \zeta\left(\frac{R_0}{R}\right)^6\right], \qquad (1)$$

where D_0 is a well depth, R_0 is a well distance and ζ is a scaling factor. In terms of these, A, B and C are given by

$$A = D_0\frac{\zeta}{\zeta - 6}R_0^6, \qquad (2a)$$

$$B = D_0\frac{6}{\zeta - 6}e^{\zeta}, \qquad (2b)$$

$$C = \frac{\zeta}{R_0}. \qquad (2c)$$

From Eq.(1), we have

$$E(R_0) = -D_0, \qquad (3a)$$

$$\left(\frac{dE}{dR}\right)_{R_0} = 0, \tag{3b}$$

$$k = \left(\frac{d^2E}{dR^2}\right)_{R_0} = \frac{D_0}{R_0^2}\frac{6\zeta(\zeta-7)}{\zeta-6}. \tag{3c}$$

From these equations, it is seen that the scaling factor ζ is directly related to a force constant (k); thus, lattice frequencies and elastic constants depend on this value. We have three parameters for carbon and hydrogen, respectively. For the parameters between carbon and hydrogen, geometric, mean-combination laws are used; that is

$$A_{CH} = (A_{CC}A_{HH})^{1/2}, \tag{4a}$$

$$B_{CH} = (B_{CC}B_{HH})^{1/2}, \tag{4b}$$

$$C_{CH} = (C_{CC} + C_{HH})/2, \tag{4c}$$

where for the parameter C_{CH}, the arithmetic mean is used, since the function is exponential.

Carbon parameters are determined from graphite crystal[5], where R_0 is determined from an interlayer distance, and D_0 is determined from an elastic constant C_{33}. The scaling factor was not determined directly, and parameters were obtained for three different values of ζ, 11,12, and 13. By using these carbon parameters, hydrogen parameters are determined from cohesive energy, cell parameters, and lattice frequencies of polyethylene crystal[1]. In these calculations, the charge of hydrogen is set to be 0.144e, based on various calculations of small hydrocarbon molecules[1]. Parameters thus obtained (which we call the PE set) are listed in Table I. In this table, Williams' parameters are also shown. A different set with $\zeta_C = 12$ and $\zeta_H = 11.8$ was tested[1] but gave quite similar results. Here, results of calculations with $\zeta_C = 13$ and $\zeta_H = 11.2$ are shown except for n-hexane and benzene crystals. When these parameters are determined, only polyethylene crystal is used in the fitting because accurate experimental data at low temperature are available only for this crystal.

In this study, we used valence force-field parameters to reproduce geometries of molecules. For n-hexane and n-octane, we used valence force-field parameters obtained for n-butane[1], which include all cross terms to reproduce correctly vibrational frequencies as well as a geometry of n-butane. For benzene, naphthalene, and anthracene, force-field parameters based on DREIDING[6],but slightly modified for each crystal, were used. In these calculations, values of force constants are unchanged, but values for equilibrium constants are adjusted to reproduce the average bond distances and angles of the experimental geometries for benzene[7], naphthalene[8], and anthracene[9], respectively. These force-field parameters reproduce experimental geometries after atomic positions are optimized at experimental cell parameters. After optimizing atomic positions, geometries of molecules are experimental ones within experimental errors. C-H bond lengths of these aromatic systems are set to be 1.09Å in calculations using the PE set. We also obtain valence force-field parameters by using the Williams' vdW parameters[3], which reproduce experimental molecular geometries of these crystals. When the Williams' vdW parameters are used, C-H bond lengths are set to be 1.027 Å for aromatic crystals.

In calculations of energy, force, stress and curvature for electrostatic and dispersion terms, Accuracy- Bounded Convergence Acceleration (ABCA) with accuracy parameters of 0.005 kcal/mol for electrostatic energy and 0.001 kcal/mol for dispersion energy is used[10]. Optimization of atomic coordinates at experimental cell parameters is performed and energy, stress, lattice frequencies and elastic constants are calculated. Also, simultaneous optimizations of atomic coordinates and cell parameters are performed and above properties are calculated. The optimization is stopped when the R.M.S. atomic force becomes less than 0.02 kcal/mol Å , and the R.M.S. first derivative of energy with respect to strain becomes less than 0.002 kcal/mol. The cohesive energy is calculated from the difference of energy between an isolated molecule and that of a crystal. Zero-point energy of an isolated molecule

and a crystal is calculated (for crystals, only frequencies at the Γ point are used) and corrections are made. All calculations are performed by using a POLYGRAF[11] software package.

III. Results and Discussion

A. Cohesive Energy and Crystal Structure

Cohesive energy of these crystals is compared with experimental sublimation energy in Table II. The differences between calculated and experimental cohesive energy using the PE parameters are within 0.5 kcal/mol in all the cases studied here, which we believe are within experimental errors. Williams' parameters are fitted to reproduce cohesive energy of n-hexane and benzene since these are known accurately, but for zero-point energy corrections, estimated values are used[12](0.50 kcal/mol for n-hexane and 0.66 kcal/mol for benzene), which are about 0.5 kcal/mol smaller than our calculated values. Cohesive energy obtained by Williams' parameters is similar for n-hexane, n-octane and benzene. But for naphthalene and anthracene, cohesive energy seems to be higher than the experimental value. Accurate experimental data of these systems may determine whether these are real differences.

Optimized crystal structure and densities are shown in Table III. In this table, experimental and calculated cell parameters are also shown. The agreement of calculated and observed values is satisfactory, although Williams' parameters seem to give a slightly better agreement. This is because we fitted cell parameters of polyethylene at low temperature (4K). On the other hand, Williams' parameters are fitted with structure at room temperature, since for most of the systems, structure is not measured at low temperature. In the table, we also show densities of calculated and experimental crystals. Calculated densities using the PE parameters are systematically higher than experimental densities in all the cases shown here

because crystals are expanded at the temperature where experiments are done.

B. Lattice frequencies

Lattice frequencies are shown in Table IV. These are calculated at observed cell parameters, since these values depend on cell dimensions, hence strongly on temperature. For n-hexane and n-octane, lattice frequencies are measured[17] at various temperatures and three frequencies are found at low temperature. But only two frequencies are observed at the temperature at which structure is determined. Here we show calculated frequencies at the optimized structure. The frequencies at the optimized structure correspond to those at 0 K, and these are compared with experimental values at 20 K.

In all the cases shown here, the PE parameters give a better fit than Williams' parameters. Williams' parameters usually overestimate vibrational frequencies. In Table I, it is shown that a force constant of carbon vdW parameters of the Williams' set is larger than that of the PE set. On the other hand, a force constant of hydrogen parameters of the Williams' set is smaller than that of the PE set. This suggests that the force constant of carbon has a larger effect than that of hydrogen on lattice vibrational frequencies for these crystals.

For n-hexane and benzene, we show results calculated by using two different PE parameters. Vibrational frequencies calculated by PE parameters with $\zeta_C = 12$ and $\zeta_H = 11.8$ are slightly smaller than those calculated by using parameters with $\zeta_C = 13$ and $\zeta_H = 11.2$ for most cases but differences are quite small, and both sets give similar R.M.S. errors. It is because the force constants (k) of these parameters do not differ much (see Table I). Force constants of parameters with $\zeta_C = 12$ and $\zeta_H = 11.8$ are about 10% smaller than parameters with $\zeta_C = 13$ and $\zeta_H = 11.2$, and this makes vibrational frequencies of the former set smaller than that of the latter set.

C. Elastic Constants

Elastic constants are shown in Table V. These values depend on cell parameters strongly similar to lattice frequencies. We show these values at experimental cell parameters. Experimental elastic constants are shown for benzene, naphthalene and anthracene (experimental elastic constants of n-hexane and n-octane have not been reported). For benzene, a,b, and c axes correspond to x_1, x_2, and x_3 axes, respectively. For naphthalene and anthracene, the b axis is a unique axis and it is parallel to the x_2 axis. x_1 axis in these cases is taken to be parallel to the a axis to compare with experimental values. For n-hexane and n-octane, experimental values are not reported. In these cases, the convention here is that the x_3 axis is parallel to the c axis and the x_2 axis is in a plane formed by b and c axes.

For benzene, the PE parameters give an R.M.S. error of 0.79 GPa compared with experimental values obtained by Brillouin scattering[22]. Independent experimental values obtained by sound-velocity measurements are reported[23], and these two experimental values agree within experimental errors except for C_{11}, C_{22} and C_{33}. The extrapolated values at 270K by sound-velocity measurements reported in Ref. 22 are C_{11}=5.63 GPa, C_{22}=5.77 GPa and C_{33} = 5.31 GPa. If we compare these values with calculated values by the PE parameters, the agreement becomes even better. Elastic constants calculated by using different PE parameters are again similar. Elastic constants of parameters with $\zeta_C = 12$ and $\zeta_H = 11.8$ are slightly smaller than those with $\zeta_C = 13$ and $\zeta_H = 11.2$ except for C_{66}. It is because force constants of the former set are slightly smaller than those of the latter set.

For naphthalene, experimental values obtained by sound-velocity measurements are reported[24]. In this case again, an R.M.S. error is less than 1 GPa when the PE parameters are used. The experimental errors of this crystal are large, especially for off-diagonal constants[24](less than 5 % for diagonal terms and C_{13}, 15 % for C_{12} and C_{23}, and 50 % for other terms). Hamamsy et al.[25] refined these values

by using experimental compressibilities, but their values are not listed in a table, since each term is not uniquely determined by their method.

For anthracene, experimental values obtained by sound-velocity measurements[26,27,28] as well as values by Brillouin scattering[29] are available. In a table here, values obtained by Brillouin scattering are shown, since an overall error seems to be the lowest in this method. In this case also, the PE parameters give a better agreement with experimental values than Williams' parameters, but an R.M.S. error in this case is much larger than in previous cases. If we use experimental values by Afanaseva et al.[26], which presumably have similar accuracy as in a naphthalene case, we get an R.M.S. error of 1.51 GPa, which is still larger than in previous cases. The largest discrepancy occurs for C_{25}, where the experimental value is negative, but calculated values are positive. Calculation by Pawley[30] also gives a positive value for C_{25}. Also, calculated values for C_{35} are always lower than experimental values. This suggests that calculations using pairwise atom-atom interactions have difficulty in reproducing these experimental values. It may be possible to use these differences to improve the form of nonbond, potential functions.

IV. Summary

van der Waals parameters, obtained by fitting low-temperature structure, cohesive energy and lattice frequencies of polyethylene crystal, are used to calculate various properties of hydrocarbon crystals. The calculated vibrational frequencies and elastic constants agree well with experimental values. For anthracene, calculated elastic constants show systematic deviations, which may be used to improve the functional form of nonbonding interactions.

References

(1) Karasawa, N.; Dasgupta, S. ; Goddard III, W. A. *J. Chem. Phys.* **1991,** *95,* 2260.

(2) Williams, D. E.;Starr, T. L. *Computers & Chemistry* **1977,** *1,* 173.

(3) Williams, D. E.; Cox, S. R. *Acta Cryst.* **1984,** *B40,* 404.

(4) Starr, T. L.; Williams, D. E. *Acta Cryst.* **1977,** *A33,* 771.

(5) Goddard III, W. A.; Karasawa, N. *J. Phys. Chem.*, submitted.

(6) Mayo, S. L.; Olafson, B. D.; Goddard III, W. A. *J. Phys. Chem.*, **1990,** *94,* 8897.

(7) Bacon, G. E.;Curry, N. A.; Wilson, S. A. *Proc. Roy. Soc.*, **1964,** *A279,* 98.

(8) Cruickshank, D. W. J. *Acta Crystallogr.*, **1957,** *10,* 504.

(9) Mason, R. *Acta Crystallogr.*, **1964,** *17,* 547.

(10) Karasawa, N.; Goddard III, W. A. *J. Phys. Chem.*, **1989,** *93,* 7320.

(11) POLYGRAF^{TM} is an interactive, molecular simulation/three-dimensional graphics program from Molecular Simulations Inc. (Biodesign), Pasadena, California 91101.

(12) Williams, D. E. *Acta Crystallogr.*, **1974,** *A30,* 71.

(13) Warshell, A.; Lifson, S. *J. Chem. Phys.*, **1970,** *53,* 582.

(14) Bradley, R. S.; Cleasby, T. G. *J. Chem. Soc.*,**1953,** 1690.

(15) Norman, N.; Mathisen, H. *Acta Chem. Scand.*, **1961,** *15,* 1755.

(16) Mathisen, H.; Norman, N.; Pedersen, B. F. *Acta Chem. Scand.*, **1967,** *21,* 127.

(17) Brunel, L-C.; Dows, D. A. *Spectrochim. Acta, Part A*, **1974,** *30,* 929.

(18) Sataty, Y. A.; Ron, A.; Brith, M. *Chem. Phys. Lett.*, **1973,** *23,* 500.

(19) Sataty, Y. A.; Ron, A. *J. Chem. Phys.*, **1976,** *65,* 1578.

(20) Bazhulin, P. A.; Rakhimov, A. A. *Sov. Phys. Solid State*, **1967,** *8,* 1719.

(21) Suzuki, M.; Yokoyama, T.; Ito, M. *Spectrochim. Acta, Part A*, **1968**, *24*, 1091.

(22) Brunel, L-C. *Chem. Phys.*, **1979**, *37*, 201.

(23) Heseltine, J. C. W.; Elliott, D. W.; Wilson, Jr., O. B. *J. Chem. Phys.*, **1964**, *40*, 2584.

(24) Afanaseva, G. K. *Sov. Phys.- Crystallogr.*,**1969**, *13*, 892.

(25) Hamamsy, M. E.; Elnahwy, S.; Damask, A. C.; Taub H.; Daniels, W. B. *J. Chem. Phys.*, **1977**, *67*, 5501.

(26) Afanaseva, G. K.; Aleksandrov, K. S.; Kitaigorodskii, A. I. *Phys. Status Solidi*, **1967**, *24*, K61.

(27) Danno, T.; Inokuchi, H.*Bull. Chem. Soc. Jpn.*,**1968**, *41*, 1783.

(28) Huntington, H. B.; Gangoli, S. G.; Mills, J. L. *J. Chem. Phys.*, **1969**, *50*, 3844.

(29) Dye, R. C.; Eckhardt, C. J. *J. Chem. Phys.*, **1989**, *90*, 2090.

(30) Pawley, G. S. *Phys. Status Solidi*, **1967**, *20*, 347.

Table I. van der Waals parameters of carbon and hydrogen. Units are kcal/mol for energy and Å for distance. k is the second derivative at an equilibrium distance (Eq.(3)).

(a) polyethylene (PE) van der Waals parameters. Two different sets are shown.

	R_0	D_0	ζ	k
C	3.8410	0.0792	13.0	0.3589
H	3.1665	0.0200	11.2	0.1083
C	3.8837	0.0844	12.0	0.3359
H	3.1975	0.0160	11.8	0.0917

(b) Williams' van der waals parameters[a].

	R_0	D_0	ζ	k
C	3.8983	0.0951	14.0340	0.4614
H	3.3107	0.0128	12.3822	0.0732

[a] Ref. 3.

Table II. Sublimation energy E_{sub} of hydrocarbon crystals. E_{0d} is a lattice energy at the optimized cell parameters, and $\Delta\ E_{zp}$ is a difference of zero-point energy between an isolated molecule and a crystal. Energy is in kcal/mol.

	exp.	PE			Williams[a]		
	E_{sub}	E_{0d}	$\Delta\ E_{zp}$	E_{sub}	E_{0d}	$\Delta\ E_{zp}$	E_{sub}
n-hexane	12.14[b]	13.37[d]	-1.25[d]	12.12[d]	12.95	-1.17	11.78
		13.33[e]	-1.41[e]	11.92[e]			
n-octane	15.88[b]	17.46	-1.48	15.98	16.99	-1.44	15.55
benzene	11.84[a]	12.37[d]	-1.02[d]	11.35[d]	12.53	-1.02	11.52
		13.23[e]	-1.05[e]	12.18[e]			
naphthalene	17.30[c]	18.79	-1.15	17.64	19.44	-1.16	18.28
anthracene	24.40[c]	25.58	-1.37	24.21	26.64	-1.40	25.25

[a] Ref. 3, [b] Ref. 13, [c] Ref. 14, [d] $\zeta_C = 13$, [e] $\zeta_C = 12$.

Table III. Calculated and experimental cell parameters and densities (ρ) of hydrocarbon crystals. In calculations, van der Waals parameters derived for polyethylene (PE) and those by Williams[a] are used. a, b and c are in Å, α, β, and γ are in degrees, ρ is in g/cm^3.

		a	b	c	α	β	γ	ρ
n-hexane	PE($\zeta_C = 13$)	4.19	4.48	8.60	97.2	88.7	103.3	0.9162
	PE($\zeta_C = 12$)	4.20	4.48	8.60	97.2	88.8	103.3	0.9155
	Williams	4.17	4.51	8.70	96.3	87.8	103.9	0.8965
	exp.(T=160K)[b]	4.17	4.70	8.57	96.6	87.2	105.0	0.8881
n-octane	PE	4.20	4.48	11.03	95.4	85.0	103.4	0.9465
	Williams	4.21	4.51	11.15	94.7	84.2	104.0	0.9289
	exp.(T=190K)[c]	4.22	4.79	11.02	94.7	84.3	105.8	0.8909
benzene	PE($\zeta_C = 13$)	7.44	9.23	6.80	89.9	90.0	90.1	1.1118
	PE($\zeta_C = 12$)	7.43	9.18	6.76	90.0	90.0	90.2	1.1240
	Williams	7.41	9.35	6.96	90.0	90.0	89.9	1.0774
	exp.(T=77K)[d]	7.37	9.35	6.77	90.0	90.0	90.0	1.1122
naphthalene	PE	8.02	5.89	8.63	90.0	123.4	90.0	1.2500
	Williams	8.16	5.93	8.65	90.1	122.9	89.9	1.2110
	exp.(T=300K)[e]	8.24	6.00	8.66	90.0	122.9	90.0	1.1848
anthracene	PE	8.39	5.95	11.19	90.1	125.4	90.0	1.2993
	Williams	8.52	6.01	11.22	90.3	125.1	89.8	1.2594
	exp.(T=290K)[f]	8.56	6.04	11.18	90.0	124.7	90.0	1.2453

[a]Ref. 3, [b]Ref. 15, [c]Ref. 16, [d]Ref. 17, [e]Ref. 18 [f]Ref 9.

Table IV. Calculated and experimental lattice frequencies (cm^{-1}) of hydrocarbon crystals. In calculations, van der Waals parameters derived for polyethylene (PE) and those by Williams[a] are used.

(a) n-hexane, calculated at optimized cell parameters.

mode	exp. (T=20K)[b]	PE ($\zeta_C = 13$)	PE ($\zeta_C = 12$)	Williams
A	53	71	70	71
	74	78	78	73
	87	91	92	91
	R.M.S. error	10.9	10.5	11.0

(b) n-octane, calculated at optimized cell parameters.

mode	exp. (T=20K)[b]	PE	Williams
A	47.5	58	63
	65	64	70
	72	76	83
	R.M.S. error	6.5	19.7

(c) benzene, calculated at experimental cell parameters.

mode	exp. (T=77 K)[c]	PE ($\zeta_C = 13$)	PE ($\zeta_C = 12$)	Williams
A_g	97.5	94	93	103
	83.0	82	81	91
	61.0	47	45	50
B_{1g}	132.0	146	145	162
	87.0	111	109	122
	67.0	54	51	62
B_{2g}	—	117	115	127
	94.0	95	93	106
	83.0	87	86	95
B_{3g}	132.0	145	143	161
	105.0	90	89	98
	65.0	63	63	65
A_u	—	108	105	123
	—	67	66	76
	—	61	60	70
B_{1u}	102.0	92	90	106
	71.0	76	75	89
B_{2u}	105.0	112	109	130
	59.0	58	57	67
B_{3u}	91.5	107	103	123
	76.0	57	55	67
	R.M.S. error	11.7	11.7	18.2

(d) naphthalene, calculated at experimental cell parameters.

mode	exp. (T=300 K)[d]	PE	Williams
A_g	109	119	134
	74	83	91
	51	49	54
B_g	125	121	138
	71	72	78
	46	39	47
A_u	98	91	109
	39	40	45
B_u	73	61	68
	R.M.S. error	7.0	12.1

(e) anthracene, calculated at experimental cell parameters.

mode	exp. (T=293 K)[e]	PE	Williams
A_g	121	133	149
	70	77	87
	39	37	40
B_g	125	129	148
	65	63	71
	45	42	48
A_u	—	94	112
	—	34	38
B_u	—	58	66
	R.M.S. error	7.9	16.6

[a]Ref. 3, [b]Ref. 17, [c]Ref. 18,19, [d]Ref. 20,21, [e]Ref. 21.

Table V. Elastic stiffness constants (GPa) of hydrocarbon crystals at experimental cell parameters. In calculations, van der Waals parameters derived for polyethylene (PE) and those by Williams[a] are used.

(a) n-hexane, calculated at cell parameters at T=160 K.

	Exp.	PE ($\zeta_C = 13$)	PE ($\zeta_C = 12$)	Williams
C_{11}	—	11.9	12.1	13.2
C_{12}	—	2.8	2.9	3.8
C_{13}	—	3.8	3.7	6.3
C_{14}	—	0.053	-0.079	0.91
C_{15}	—	0.18	0.17	-0.055
C_{16}	—	-2.3	-2.4	-2.0
C_{22}	—	7.3	7.3	7.9
C_{23}	—	3.4	3.4	5.8
C_{24}	—	-0.69	-0.74	-0.44
C_{25}	—	-0.52	-0.56	0.15
C_{26}	—	1.4	1.5	1.3
C_{33}	—	16.4	16.4	20.9
C_{34}	—	3.0	2.9	4.9
C_{35}	—	0.67	0.47	3.6
C_{36}	—	0.47	0.41	1.4
C_{44}	—	3.1	3.0	3.8
C_{45}	—	0.26	0.18	0.78
C_{46}	—	-0.084	-0.11	-0.17
C_{55}	—	2.8	2.8	4.3
C_{56}	—	0.33	0.29	0.92
C_{66}	—	2.1	2.2	2.6

(b) n-octane, calculated at cell parameters at T=190K.

	Exp.	PE	Williams
C_{11}	—	10.0	11.2
C_{12}	—	2.3	3.0
C_{13}	—	3.5	5.6
C_{14}	—	-0.091	0.65
C_{15}	—	0.19	-0.074
C_{16}	—	-2.2	-2.1
C_{22}	—	5.6	5.9
C_{23}	—	2.4	4.6
C_{24}	—	-0.59	-0.44
C_{25}	—	-0.37	0.20
C_{26}	—	1.4	1.3
C_{33}	—	17.3	25.3
C_{34}	—	3.1	4.8
C_{35}	—	1.1	4.4
C_{36}	—	0.37	1.3
C_{44}	—	2.2	2.4
C_{45}	—	-0.040	0.43
C_{46}	—	-0.14	-0.22
C_{55}	—	2.4	3.3
C_{56}	—	0.13	0.56
C_{66}	—	1.8	2.1

(c) benzene, calculated at cell parameters at T=270K[b].

	Exp.[c]	PE ($\zeta_C = 13$)	PE ($\zeta_C = 12$)	Williams
C_{11}	6.4	5.2	4.8	6.8
C_{12}	3.3	3.5	3.4	4.9
C_{13}	4.1	4.3	4.0	5.9
C_{22}	6.81	5.9	5.5	8.2
C_{23}	3.4	3.4	3.3	4.8
C_{33}	6.08	4.9	4.5	6.9
C_{44}	1.83	1.7	1.7	2.1
C_{55}	3.9	5.2	4.9	6.6
C_{66}	1.43	0.46	0.49	0.74
	R.M.S. error	0.79	0.98	1.43

(d) naphthalene, calculated at cell parameters at T=300K.

	Exp.[d]	PE	Williams
C_{11}	8.19	6.7	9.6
C_{12}	5.56	5.3	7.9
C_{13}	3.22	4.1	6.1
C_{15}	0.2	0.55	0.85
C_{22}	10.02	8.3	12.4
C_{23}	3.48	4.0	5.3
C_{25}	1.9	1.2	1.9
C_{33}	12.43	14.2	18.6
C_{35}	-2.9	-3.2	-4.0
C_{44}	3.44	3.3	4.2
C_{46}	0.7	1.0	1.2
C_{55}	2.34	1.8	2.7
C_{66}	4.43	3.6	4.7
	R.M.S. error	0.93	2.24

(e) anthracene, calculated at cell parameters at T=293K.

	Exp.[e]	PE	Williams
C_{11}	9.17	7.2	10.5
C_{12}	4.10	6.4	9.4
C_{13}	5.68	5.6	8.2
C_{15}	-0.73	0.33	0.49
C_{22}	9.79	9.6	14.0
C_{23}	4.12	5.4	7.4
C_{25}	-3.35	1.3	2.0
C_{33}	17.88	14.4	19.4
C_{35}	-0.51	-3.8	-4.9
C_{44}	2.18	2.3	2.8
C_{46}	1.06	1.5	2.0
C_{55}	1.95	3.0	4.3
C_{66}	3.98	2.8	3.7
	R.M.S. error	2.14	3.08

[a]Ref. 3, [b]Cell parameters at 270 K are extrapolated values from Ref. 7, [c]Ref. 22, [d]Ref. 24, [e]Ref. 29.

Appendix III

Phase Transitions in Polymethylene Single Chains from Monte Carlo Simulated Annealing

Reprinted from The Journal of Physical Chemistry, 1988, 92, 5828.

Phase Transitions in Polymethylene Single Chains from Monte Carlo Simulated Annealing

Naoki Karasawa and William A. Goddard III*

Arthur Amos Noyes Laboratory of Chemical Physics,† California Institute of Technology, Pasadena, California 91125 *(Received: January 8, 1988; In Final Form: April 21, 1988)*

Folding of single isolated polymethylene chains was examined with Monte Carlo simulated annealing. All carbon and hydrogen atoms were considered explicitly by using van der Waals plus torsional potential functions. The calculations allowed continuous variation in each torsional degree of freedom. In addition, we examined the consequences of simplifying the calculations by restricting the carbons to be on a diamond lattice. Ensembles of conformations for larger chains (C_NH_{2N+2}, with N = 16, 32, 64) all show a transition from a random coil at high temperature to a globular form at low temperature. For longer chains ($N \geq 64$), this globularization transition is well described by the mean-field theory of Sanchez.

Introduction

The self-condensation transition behavior (collapse transition) of a chain molecule in dilute solution has been studied extensively by theory[1-3] and computer simulations.[4-7] Most studies have examined the asymptotic properties of very long chains ($N \rightarrow \infty$, where N is the number of segments), finding in this limit that the properties of the chain do not depend on the local stiffness of the chain. Recent Monte Carlo simulations by Kolinski et al.[6] show, however, that the transition behavior of the chain is highly dependent on the local stiffness of the chain as well as on the size of the chain. If the chain is too short or the temperature too low, the properties of the chain should become more dependent on the particular parameters of the chain. To examine the effect of the local properties of the chain on the transition behavior and structure, we used polymethylene as a specific model and carried out simulated annealing studies from 2100 to 100 K. We find a distinct globularization transition for larger chains ($N \geq 16$), which for $N \geq 32$ is well described by the one-parameter mean-field theory of Sanchez.[1]

Most previous simulations have used lattice models (simple cubic,[5] face-centered cubic,[5] diamond[6,7]), but in this study we allowed continuous variation in each torsional degree of freedom and calculated all nonbonding and torsional interactions. Comparisons with equivalent lattice calculations indicate systematic errors from use of such lattices.

Since solvent effects are not included, these simulations of isolated chains apply only to cases in which the solvent interactions are weak and the chain is immiscible.

Model and Sampling Procedure

We generated the polymethylene conformations using fixed bond distances and bond angles but allowing continuous variation of torsion angles. The potential function was chosen to reproduce the torsional potential function of *n*-butane (Abe et al.[8]) with R_{C-C} = 1.53 Å, R_{C-H} = 1.10 Å, θ_{C-C-C} = 112°, θ_{H-C-C} = 109.5°, and θ_{H-C-H} = 109.5°. The total energy of the system is given by the sum of the torsional energy and nonbonding interactions:

$$E = \sum_{i=3}^{N-1} (V_0/2)(1 - \cos 3\phi_i) + \sum_{\text{allpair}} U_{ij} \qquad (1)$$

where V_0 = 2.8 kcal/mol and ϕ_i is the torsional angle of the ith bond. The van der Waals or nonbonded energy between atoms i and j is given by

$$U_{ij} = Be^{-CR_{ij}} - A/R_{ij}^6 \qquad (2)$$

where R_{ij} is the distance between atoms i and j. The sum is taken for all pairs of atoms except those involved directly in a bond stretching or bending interaction. van der Waals parameters are given in Table I.

TABLE I: Nonbonding Energy Parameters[a,b]

	A, Å^6 kcal/mol	B, kcal/mol	C, Å^{-1}	ϵ_0, kcal/mol	R_0, Å	γ
H–H	45.2	9950	4.54	0.072	2.6	11.8
H–C	127	86 100	4.57	0.083	3.1	14.3
C–C	363	908 600	4.59	0.106	3.6	16.5

[a] Reference 8. [b] ϵ_0 is the well depth, R_0 is the distance corresponding to the energy minimum, and γ is the normalized scale factor. The energy U is given by $U = Be^{-CR} - A/R^6 = [\epsilon_0/(\gamma - 6)][6e^{\gamma(1-\rho)} - \gamma\rho^{-6}]$, where $\rho = R/R_0$.

A simplification that reduces computer time is to precalculate all nonbonding energies as a function of R^2 with step size 0.005 Å^2. In the simulations, the value in the list corresponding to the nearest value of the desired R is used. This decreases the time by a factor of 3 but leads to the same energy within 0.1 kcal/mol when $R \geq 0.65R_0$. When $R \leq 0.65R_0$, each nonbonding potential energy is more then 10 kcal/mol, so that the error in this region should not have a large effect on the results.

Various methods have been suggested for trial movement in the Monte Carlo simulation of a polymer chain.[4] The reptation method[9] is used in this study because of its high efficiency and small calculational time. In this approach (see Figure 1), a terminal C–H bond to atom N is replaced with a new C–C bond to the $(N + 1)$ CH_3 group, while the first CH_3 group is contracted to an H (keeping a total of N carbons). When a C–C bond is replaced, the torsional angle (ϕ) of the new bond is chosen randomly. The trial movement is accepted with the probability

$$P_{\Gamma c} = \min\,(1, e^{-\Delta E_{\Gamma c}/k_B T}) \qquad (3)$$

where $\Delta E_{\Gamma c} = E_\Gamma - E_c$, E_Γ is the energy of the trial conformation and E_c is the energy of the current conformation.

During the simulation, the following values are sampled and averaged at each temperature. Internal energy:

$$\langle E \rangle \qquad (4)$$

Specific heat:

$$\langle C \rangle = (\langle E^2 \rangle - \langle E \rangle^2)/k_B T^2 \qquad (5)$$

End-to-end length squared:

$$\langle R^2 \rangle = \langle (\vec{R}_1 - \vec{R}_N)^2 \rangle \qquad (6)$$

† Contribution No. 7723.

(1) Sanchez, I. C. *Macromolecules* **1979**, *12*, 980.
(2) Post, C. B.; Zimm, B. H. *Biopolymers* **1979**, *18*, 1487.
(3) Muthukumar, M. *J. Chem. Phys.* **1984**, *81*, 6272.
(4) Baumgärtner, A. In *Application of the Monte Carlo Method in Statistical Physics*; Binder, K., Ed.; Springer-Verlag: Berlin, 1984; pp 145–180
(5) McCrackin, F. L.; Mazur, J.; Guttman, C. M. *Macromolecules* **1973**, *6*, 859.
(6) Kolinski, A.; Skolnick, J.; Yaris, R. *J. Chem. Phys.* **1986**, *85*, 3583
(7) Kremer, K.; Baumgärtner, A.; Binder, K. *J. Phys. A: Gen. Math.* **1981**, *15*, 2879.
(8) Abe, A.; Jernigan, R. L.; Flory, P. J. *J. Am. Chem. Soc.* **1966**, *88*, 631
(9) Wall, F. T.; Mandel, F. *J. Chem. Phys.* **1975**, *63*, 4592.

0022-3654/88/2092-5828$01.50/0

Radius of gyration:

$$\langle S^2 \rangle = (1/N^2)\sum_{i=1}^{N-1}\sum_{j=i+1}^{N}\langle(\vec{R}_i - \vec{R}_j)^2\rangle = (1/N)\sum_{i=1}^{N}\langle(\vec{R}_i - \vec{R}_{CM})^2\rangle \quad (7)$$

where $\vec{R}_{CM}$ is the center-of-mass coordinate:

$$\vec{R}_{CM} = (1/N)\sum_{i=1}^{N}\vec{R}_i$$

The internal energy is the total potential energy, (1), while the specific heat is the fluctuation of the internal energy. Before beginning a simulated annealing sequence, we did a "melting run" of about 80 000 steps. During this stage, the temperature was set very high ($k_BT = 10^6$ kcal/mol) to allow the chain to sample all parts of configuration space. In doing this, we allowed the segments to pass each other by setting $U_{ij}(R_{ij} = 0) = L$, where L is a large but finite number (generally $L = 10^6$ kcal/mol).

The temperaure was decreased according to a predefined annealing schedule. At each temperature, the system was equilibrated (using multiple reptation steps) until the energy became nearly constant. The criteria for equilibration was

$$\bar{E}_n - 2C \le \bar{E}_m \le \bar{E}_n + 2C$$

where $\bar{E}_m$ is the average energy of the previous m steps, and C is the energy fluctuation (standard deviation) of the last n steps. For $N = 32$, n was chosen as 3000 and m was chosen as 900 000. For $N = 16$ and $N = 64$, n was chosen as 2000 and m was chosen as 400 000. For $N = 8$, n and m were chosen as 1000 and 100 000.

The annealing schedule involved a temperature decrease of 100 K per step for higher temperatures, which was decreased to 50 K per step when the energy fluctuations (specific heat) became large (near the globularization transition temperature, T_c).

Results and Discussion

A. Radius of Gyration versus Temperature. The temperature dependence of the radius of gyration $\langle S^2 \rangle$ is shown in Figure 2 for differing numbers of carbon atoms (N). In the case of $N = 8$ (Figure 2a), the radius of gyration becomes larger as the temperature is decreased, leading to an all-trans structure at low temperature. In the case of $N = 16$ (Figure 2b), $\langle S^2 \rangle$ becomes larger as the temperature is decreased to about 400 K and suddenly drops for temperaures below 300 K. In the case of $N = 32$ (Figure 2c), $\langle S^2 \rangle$ starts dropping below 1050 K, becoming a constant at about 300 K. In the case of $N = 64$ (Figure 2d), $\langle S^2 \rangle$ starts dropping below 1500 K, becoming a constant at about 400 K. End-to-end length versus temperature exhibits very similar tendencies.

To analyze the results, we used rotational isomeric state (RIS) theory[10] to calculate the radius of gyration as a function of temperature, as shown in Figure 2 (dotted line). In RIS theory, only nearest-neighbor interactions between atoms are considered, and no long-range interactions are taken into account. Also, the torsional angles of each bond are assumed to take only three discrete values: (1) trans (t, torsional angle $\phi = 0°$); (2) gauche plus (g^+, $\phi = 112.5°$); (3) gauche minus (g^-, $\phi = -112.5°$). The energy difference between trans and gauche is set to be $E_g - E_t = 0.5$ kcal/mol, and the energy difference between $g^{\pm}g^{\mp}$ and $g^{\pm}g^{\pm}$ is set to be $E(g^{\pm}g^{\pm}) - E(g^{\pm}g^{\mp}) = 2.7$ kcal/mol. Also, the C–C bond lengths are set to be 1.53 Å, and the C–C–C angles are set to be 112°. With the above two assumptions, RIS theory leads to analytic results for all N.

In the case of $N = 8$, the result of the simulation is described well by RIS theory except at high temperature. In the high-temperature region, the dimension of the chain is larger in the simulation than in RIS theory. This is due to the volume exclusion effect, which is neglected in RIS. When $N = 16$ and larger, the chains collapse in the low-temperature region. This is not explained by RIS theory due to the lack of long-range attractive interactions. In addition, the volume exclusion discrepancy at high temperature increases as the chain becomes larger.

(10) Flory, P. J. *Statistical Mechanics of Chain Molecules*; Interscience: New York, 1969.

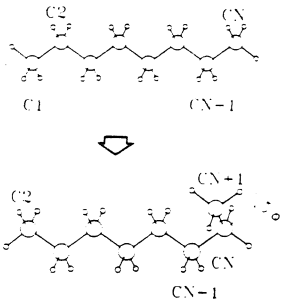

Figure 1. Trial movements used in this study. Here C_8H_{18} ($N = 8$) is shown.

In analyzing the results of the simulations, we find it useful to define an expansion factor α^2:

$$\alpha^2 = \langle S^2 \rangle / \langle S^2 \rangle_0 \quad (8)$$

as the ratio of the radius of gyration for the real chain $\langle S^2 \rangle$ to that of the free chain, $\langle S^2 \rangle_0$ (as given by RIS theory).

B. Comparisons of Lattice and Nonlattice Models. In polymer simulations it is common to use a lattice model in which all carbon atoms must be at sites on a diamond lattice. This considerably simplifies the programming and reduces the calculation time. In this model, all angles are tetrahedral, and the C–C and C–H bond lengths are set to be 1.53 and 1.10 Å, respectively (our calculation treated hydrogen atoms explicitly). We used the same potential energy parameters as for the continuously variable chain (nonlattice), but extra energy was added to each gauche conformation relative to a trans conformation to reproduce the same gauche-trans energy difference. To make a direct comparison with the lattice model, we did nonlattice calculations for a model with free torsional angles (as in section A) but with only three allowed torsional angles ($\phi = 0°, \pm 112.5°$) as in the diamond lattice (and RIS theory).

The temperature dependence of the radius of gyration for a lattice model and nonlattice models for the case $N = 64$ is shown in Figure 3. The temperature dependence of $\langle S^2 \rangle$ with a lattice model shows a globular transition as for the nonlattice models, but $\langle S^2 \rangle$ in the lattice model is smaller than in the nonlattice models, especially in the high-temperature region. On the other hand, the temperature dependence of $\langle S^2 \rangle$ in both nonlattice models is very similar. This suggests that the discrepancy in the lattice model is not due to the discreteness of the torsional angles allowed but rather to the effect of discreteness on the entropies of extended versus globular configurations.

C. Specific Heat versus Temperature. The temperature dependence of specific heat is shown in Figure 4 for differing values of N. In the case of $N = 32$ (Figure 4c) and $N = 64$ (Figure 4d), sharp peaks in the specific heat (at $T = 400$ and 600 K, respectively) mark the transition from random coil to globule. In the case of $N = 16$ (Figure 4b), a sharp peak is observed at $T = 150$ K, indicating the globular transition. The transition temperature increases as N becomes larger, as expected from the increased favorability of intermolecular interactions. However, for $N = 8$ (Figure 4a) no globular transition is observed, and the specific heat increases monotonically as the temperature is decreased to 100 K.

D. Estimation of the Flory Θ Temperature. The mean-field theory predicts the following scaling behavior for a flexible chain molecule as $N \to \infty$:[1]

$T > \Theta$, $\langle R^2 \rangle \propto \langle S^2 \rangle \propto N^{2\nu}$, where $\nu = 3/5$, $\langle R^2/N \rangle \propto N^{0.2}$

$T = \Theta$, $\langle R^2 \rangle \propto \langle S^2 \rangle \propto N^{2\nu}$, where $\nu = 1/2$, $\langle R^2/N \rangle \propto N^0$

$T < \Theta$, $\langle R^2 \rangle \propto \langle S^2 \rangle \propto N^{2\nu}$, where $\nu = 1/3$, $\langle R^2/N \rangle \propto N^{-0.33}$

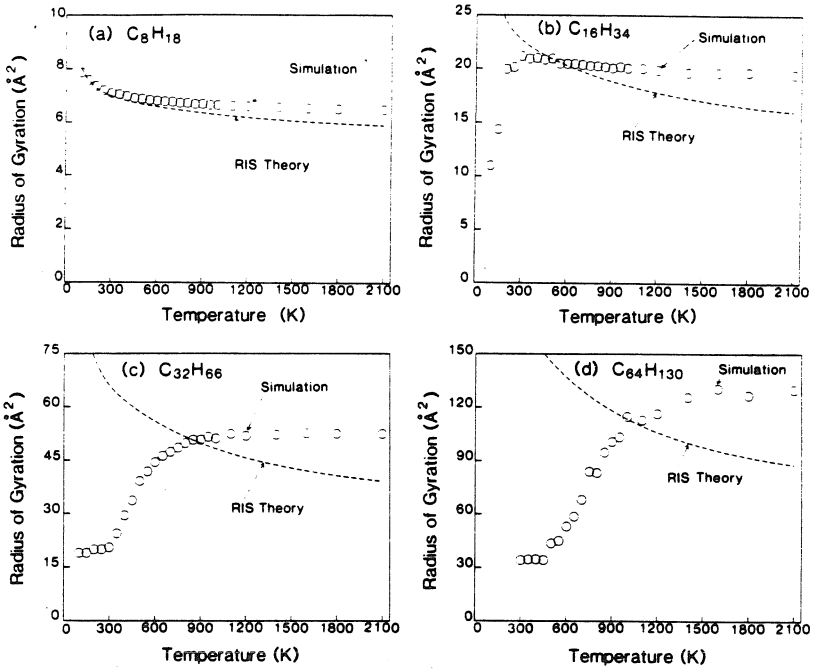

Figure 2. Radius of gyration, $\langle S^2 \rangle$, as a function of temperature (nonlattice, free torsion). Dashed line shows RIS theory.

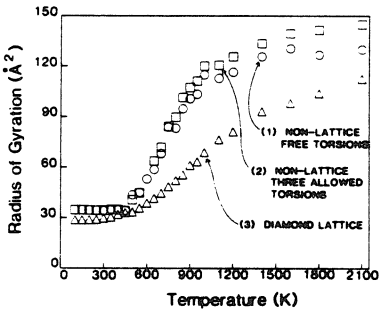

Figure 3. Temperature dependence of radius of gyration, $\langle S^2 \rangle$, for $C_{64}H_{130}$ with use of three different models: (1) nonlattice, free torsions; (2) nonlattice, three allowed torsions (ϕ = 0°, ±112.5°), (3) diamond lattice.

where the Flory temperature Θ is a measure of interatomic interactions versus rigidity.

To determine the value of Θ from our simulations, we plot $\langle R^2 \rangle / N$ and $\langle S^2 \rangle / N$ versus N in Figure 5. The expected slope at high temperature is indicated by the $N^{0.2}$ line. For 1600 K we see that N = 32 and 64 lead to results close to this slope. The expected slope at low temperature is indicated by the $N^{-0.33}$ line. Here we see that N = 32 and 64 give the correct trend but greater deviation. At the Θ temperature, both plots should have zero slope as $N \to \infty$. From Figure 5 we see the Θ ≈ 1100 K. In these simulations, interactions with solvent are ignored, so that our model assumes a *very* poor solvent in which polymethylene is immiscible. This leads to a high Θ and a high globularization temperature. When the chain is in a good solvent, the attractive energy *between* different polymer units will stabilize more extended structures and decrease the Θ temperature.

Including the excluded volume effect and attractive interactions of nearest-neighbor lattice sites on the diamond lattice model, Kremer et al.[7] obtained $k_B\Theta/\epsilon_a = 2.25 \pm 0.10$, where ϵ_a is the attractive nearest-neighbor energy. In our model, the attractive interaction is not between nearest neighbors as in these lattice simulations; rather we include a larger range corresponding to the tail of the van der Waals interaction. Consequently the effective ϵ_a is not just the depth of C–C van der Waals interaction (0.1 kcal/mol) but rather is $\epsilon_a \approx 0.5$ kcal/mol. This ϵ_a is obtained by calculating the total nonbonded attractive interaction between carbons and dividing by 2. Using ϵ_a = 0.5 for Kremer's lattice simulation would lead to Θ = 570 K, much smaller than our estimated value of 1100 K. The same lattice model was used by Kolinski et al.[6] but included the gauche–trans energy difference ϵ_g. For N = 200 they estimated Θ for differeing values of the chain flexibility parameter $|\epsilon_g/\epsilon_a|$. They obtained $k_B\Theta/\epsilon_a = 2.22$ when $|\epsilon_g/\epsilon_a| = 1$ and $k_B\Theta/\epsilon_a = 2.50$ when $|\epsilon_g/\epsilon_a| = 4$. Using Θ from their simulation with $|\epsilon_g/\epsilon_a| = 4$ and assuming ϵ_a = 0.5 kcal/mol lead to Θ = 630 K. This value is also smaller than our value (our calculations use $|\epsilon_g/\epsilon_a| \sim 5$). Both of these lattice estimations of Θ ignored H–H and C–H attractive interactions, whereas they are included in our studies. Also, the number of pairs of units attracting each other in lattice models is smaller than that in our model. These effects would both tend to make the estimated Θ temperature smaller than ours.

Experimentally, the Θ temperature of polymethylene in diphenyl ether solvent is Θ = 434 K,[11] and this is considerably smaller than our estimated value. The main reason for this discrepancy is the stabilization of extended structures because of attractive energy between polymethylene and solvent.

E. Comparison with Mean-Field Theory. Using mean-field theory, Sanchez[1] has shown that in the limit of large N, the expansion factor α^2 of (8) is given by

$$(7\phi_\alpha/3N)(1 - \alpha^2) = \tfrac{1}{2}(\Theta/T)\phi_\alpha^2 + \ln(1 - \phi_\alpha) + \phi_\alpha \quad (9)$$

where

$$\phi_\alpha = \phi_0/\alpha^3$$

$$\phi_0 = (19/27)^{1/2}N^{-1/2}$$

In the derivation of this equation, the chain is assumed to be completely flexible, and long-range interactions between atoms (volume exclusion and van der Waals attraction) are taken into

(11) Seymour, R. B. *Introduction to Polymer Chemistry*; Robert E. Krieger: New York, 1978; p 41.

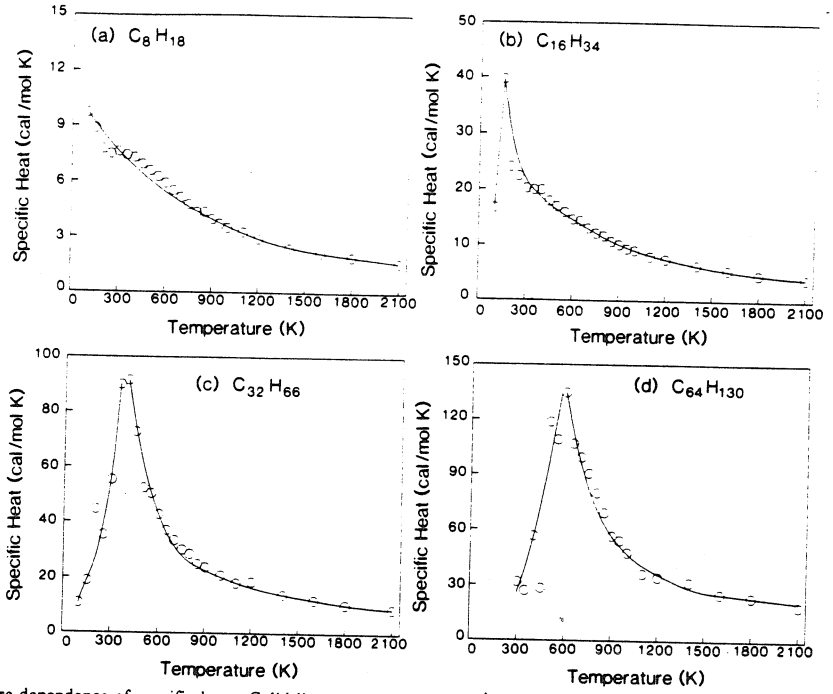

Figure 4. Temperature dependence of specific heat. Solid lines are visual fits of the data.

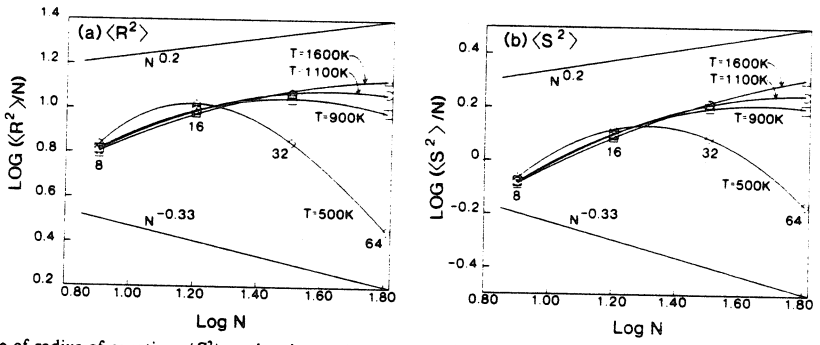

Figure 5. Dependence of radius of gyration, $\langle S^2 \rangle$, and end-to-end distance, $\langle R^2 \rangle$, upon chain length for various temperatures. The Θ temperature is determined by requiring zero slope for large N.

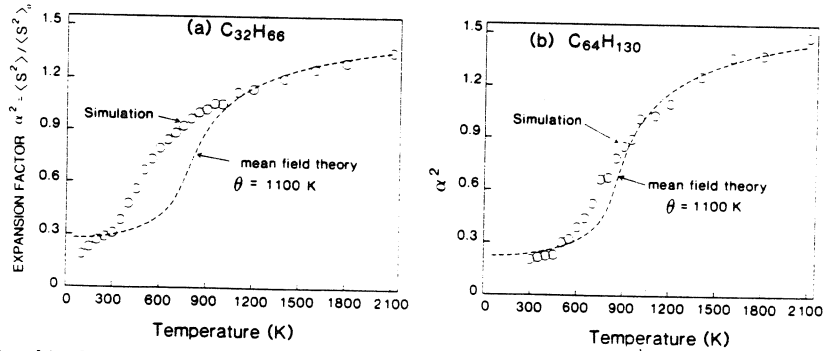

Figure 6. Relative size of (a) $C_{32}H_{66}$ and (b) $C_{64}H_{130}$ as a function of temperature. The expansion factor α^2 is the ratio of the calculated radius of gyration to that expected for a random coil. The dotted line shows how well the simulations are fit in terms of a one-parameter mean-field theory.

account by using average values (average density of atoms and average energy between atoms). Therefore, no correlation effects are considered. It is valid in the limit of large N and, as indicated in Figure 6, provides a good fit to the results of the simulations for $N = 64$. For $N = 32$, the fit is good at high temperature but not at low temperature. For smaller chains ($N = 8, 16$), the fit is poor (as expected, since N is not large).

F. Most Stable Structure of the Chain. During the simulation, the actual conformation of the chain is sampled periodically and displayed by using the BIOGRAF molecular modeling package[12]

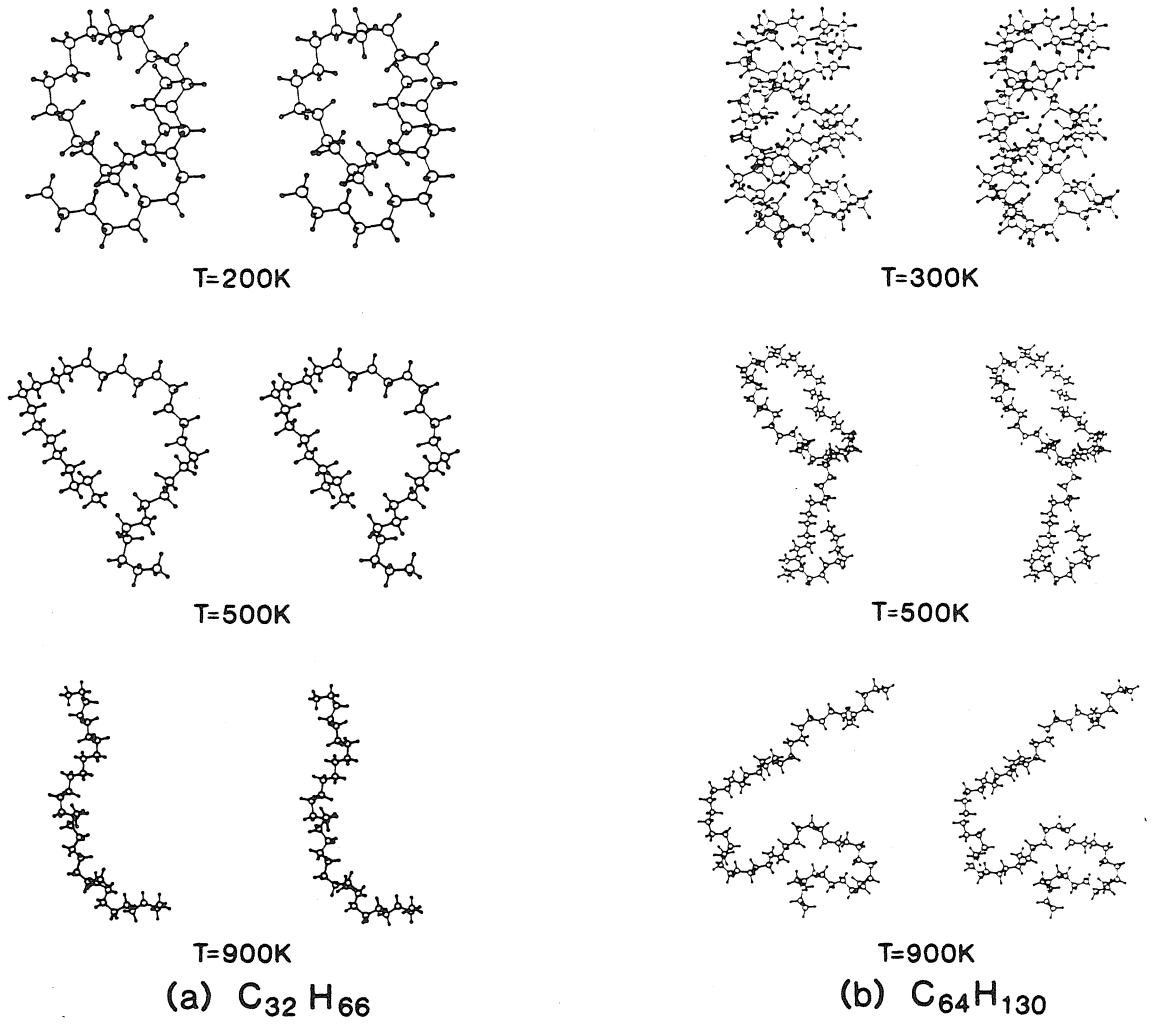

Figure 7. Stereoplots of the equilibrated conformations of polymethylene at various temperatures (selected randomly from the equilibrated set of configurations): (a) $C_{32}H_{66}$; (b) $C_{64}H_{130}$.

on an Evans and Sutherland PS 330 graphics system. This is a useful aid to understanding the conformation changes in the systems under study. Snapshots of conformations at various temperature are shown in Figure 7 for $N = 32$ and $N = 64$. Simulations are carried out at each temperature until thermal equilibrium is reached; the temperature is then lowered, and the system reequilibrated (this process can be thought of as simulated annealing[13]). We find that this procedure leads at low temperature to the most stable structure. As shown in Figure 7, the stable structure is folded or pseudoglobular. To make a globular structure, the chain must have multiple gauche interactions causing unfavorable local interactions. For sufficiently long chains, this unfavorable conformation is compensated by the favorable van der Waals interactions between chains, leading to globular formation.

(12) BIOGRAF is an interactive molecular simulation three-dimensional graphics program from BioDesign Inc., Pasadena, CA.
(13) Kirkpatrick, S.; Gelatt, Jr., C. D.; Vecchi, M. P. *Science (Washington, D.C.)* **1983**, *220*, 671.

Summary

Computer simulations of realistic isolated polymethylene chains have been used to characterize the transitions between random coil at high temperature and globular conformations at low temperature. For longer chains, the random coil–globularization transition is well characterized in terms of a single-parameter mean-field theory. We find that lattice models lead to significant errors in characterizing this system.

Acknowledgment. This research has been partially funded by the Office of Naval Research/Defense Advanced Research Projects Agency (Contract No. N00014-86-K-0735) and by the Imperial Chemical Ind. PLC of the United Kingdom. The calculations were carried out on DEC VAX 8650 and Alliant FX8/8 computers that were funded by an ONR/DARPA contract and a grant from the Division of Materials Research (Materials Research Groups) of the National Science Foundation (Grant No. DMR84-21119). We thank BioDesign Inc. for use of the BIOGRAF molecular simulation program.